EXPERIMENTAL AND NUMERICAL STUDIES OF FLOW STRUCTURE AND ALLUVIAL PROCESSES IN PARTIALLY-OBSTRUCTED OPEN CHANNEL WITH VEGETATION CANOPY

YAN XUFENG

PhD

The Hong Kong Polytechnic University

2018

The Hong Kong Polytechnic University

Department of Civil and Environmental Engineering

Experimental and Numerical Studies of Flow Structure and Alluvial Processes in Partially-obstructed Open Channel with Vegetation Canopy

YAN Xufeng

A thesis submitted in partial fulfillment

of the requirements for the

degree of Doctor of Philosophy

Feb 2018

Certificate of Originality

I hereby declare that this thesis is my own work and that, to the best of my knowledge and belief, it reproduces no material previously published or written, nor material that has been accepted for the award of any other degree or diploma, except where due acknowledgement has been made in the text

________________________ (Signed)

YAN Xufeng (Name of student)

Table of Content

Abstract

The study described in this dissertation presents two key contributions: 1. an experimental investigation and numerical simulation of three-dimensional flow characteristics in a partially-obstructed channel with a vegetation canopy (POCVC); 2. an experimental investigation and two-dimensional numerical simulation of bed morphology evolution in the POCVC.

By means of the measurement of flow characteristics in the POCVC, the adjustment of flow entering the vegetation canopy was determined and further examined. Regarding the depth-averaged longitudinal velocity, the flow adjustment distance in the vegetation region is approximately 70% of the canopy length, given the same vegetation density. However, in the neighboring open water region (NOWR), the flow adjustment distance is much shorter, particularly in areas of high-submergence canopy. It was also observed that the vertical profile of longitudinal velocity could become fully-developed within the same flow adjustment distance. Significantly, in the junction region, as the flow propagates downstream the vertical profile of longitudinal velocity is deflected in the near-bed region. Correspondingly, vertical Reynolds stress is negative in that region. It is suggested that velocity deflection and vertical Reynolds stress negativity are induced by the generation of horizontal coherent vortices, enabling the low momentum from the vegetation canopy to be transported into the neighboring open water. The bed resistance, however, plays a negative role in the

generation of those vortices. This is confirmed by transverse Reynolds stress in the upper layer region being found to be larger than that in the near-bed region. This new finding encouraged a hydrodynamic model to be subsequently proposed to give a description of the vortex pattern arising from the flow-vegetation interaction in the POCVC. This model can be used to understand flow behaviors in POCVC areas.

The turbulent kinetic energy (TKE) budget of fully-developed flow in the POCVC was evaluated. The shear production and turbulent transport both in the vertical and transverse directions are considered. It is shown that within the deeper vegetation canopy TKE is produced by the vegetation stem wake which is balanced by a combination of dissipation and pressure transport. The lower vegetation density promotes the role of vegetation stem wake as the larger stem space tends to support wake development. In the junction region, the shear production due to the vertical/transverse coherent vortices contributes positively to a large proportion of TKE together with the wake production (inside the vegetation canopy). Apart from the energy dissipation and pressure transport, the turbulent transport negatively contributes to TKE. In the NOWR further away from the canopy edges, the turbulent transport becomes dominant.

The Spalart-Allamrus (SA) model was improved to model the surface flow in the POCVC. The concept of the coherent vortices generated in the POCVC was introduced in the numerical model. The turbulence length scale of dominant local vortices is specified so that the transport equation of eddy viscosity becomes anisotropic due to spatial variations of vortices. Results show that the improved vortex-based SA model is able to simulate the flow characteristics of the inner vegetation region except at the entry of the vegetation canopy. In the junction region, the flow velocity deflection and the negative vertical Reynolds stress in the near-bed region can be well reproduced by the improved model, while the standard SA model fails to reproduce the above flow and turbulence properties due to being unable to characterize the horizontal coherent vortices in the POCVC. The parameter study shows that the parameters associated with the horizontal coherent vortices are critical to the particular flow behavior in the junction region.

Clean water scour experiments were conducted to investigate the characteristics of bed-load transport and bed morphologic evolution in the POCVC. It was observed that the massive sediment transport that occurs in the NOWR produces a significant peak of the sediment transport rate. It appears that the sediment sorting must occur during the sediment transport process. As the equilibrium bed is reached, characteristic bedforms can be recognized in the POCVC. Such bed features include (A) water pool induced by flow convergence in the NOWR, (B) slightly-eroded bed protected by the vegetation canopy in the VR, (C) slightly-eroded bed at upstream of the vegetation canopy, (D) local bed scouring near the leading edge of the vegetation canopy, (E) sediment bar with surface fining, and (F) a riffle downstream of the vegetated reach. Of significance is that the scour pool and the downstream riffle compose the famous pool-riffle morphology beneficial for aquatic habitat. Over the generated bed morphology, flow characteristics were measured to gain a better understanding of the bed morphology formation mechanism in the POCVC. The relationship existing between flow characteristics and bed morphology was examined. Results showed that linear relations exist among the longitudinal bed profile, longitudinal flow propagation distance, mean flow velocity and transverse inner extension of bed erosion. At the vegetated reach, the transverse bed profile follows the curve of the tangent hyperbolic function. With the well-defined transverse extension lengths the proposed tangent hyperbolic formulas can well predict the transverse bed profile.

A two-dimensional morphological model, namely Nays2DH-IRRIC, was employed to model the alluvial process in the POCVC. The validation of the numerical model was carried out with the experimental depth-averaged flow velocity and bed morphology. Then factors including angle of repose (RAV), vegetation density (VD), canopy length (CL) and canopy width (CW) (representing the canopy blockage effect) of the vegetation canopy were adopted in the parameter study. It is found that above factors all have significant influence on bed morphology evolution. Numerical Results show that RAV parameterized in the slope failure model only dominates the transverse bed profile in the junction. Larger RAV leads to steeper transverse bed profile. The increase in VD, CL and CW is able to induce deeper pool region at the vegetated reach. Besides above, larger VD tends to induce upstream expansion in pool and bed erosion inside vegetation canopy. Larger CL induces larger pool region along vegetation canopy in the longitudinal dimension. With the increase in CW, the location of the deepest core in the pool tends to shift upstream.

Acknowledgement

My sincere gratitude needs to be expressed to my supervisor, Prof. Wai Wing Hong, Onyx. His wise supervision and patience play significant roles in the completion of my Ph.D study and more importantly the dissertation. Special thanks to my supervisor are for offering me an opportunity of joining his research group and for always trying to create a free space so that I could feel the beauty of scientific research during my Ph.D period. I would like to express sincere thanks to my co-supervisor, Prof. Li Chi Wai. Under his patient guidance, I could be taken into the wonderful world of the flow numerical modeling.

Thanks are to Mr. Leung Kowk Hing for the technical support of the laboratory experimental setups, contributing to the experiment part of the dissertation. Thanks are expressed to Dr. Liu Yaohui, Keane for showing his Ph.D experience to me without reservation. Special thanks are shown to Dr. Tam Wai Cheong and Ms. Anson Elaine for helping improve my English writing skills. In addition, I would like to thank Ms. Tang Lian and Ms. Wang Yao for their special assists.

Also, I would like to thank the Hong Kong Polytechnic University to offer such a good academic platform for my research study, particularly the scholarship to support my finance in Hong Kong.

My family as the spiritual pillar always supported and encouraged me so that I could get through hard moments in these years.

List of Figures

List of Tables

List of Symbols

Alphabetical Symbols

A	=	cross section area for flow passage
C_d	=	drag coefficient of vegetation
F_i	=	resistance force components (F_x, F_y, F_z) by vegetation per unit volume in the *x, y, z* directions
L_0	=	zero-placement length
L_c	=	drag length scale of vegetation canopy
L_d	=	length of downstream reach
L_p	=	length of vegetated reach
L_u	=	length of upstream reach
L_t, L_y, L_z	=	characteristic turbulence length, *y*-component and *z*-component
N	=	number of vegetation element per unit area
P_{sy}, P_{sz}, P_w	=	transverse and vertical shear and wake production of turbulent kinetic energy
Q	=	flow rate
R	=	residual of turbulent kinetic energy budget
Re	=	Reynolds number

S_{uu}	=	energy spectral
T	=	integral period
T_{ty}, T_{sz}, T_p	=	transverse, vertical and pressure transport of turbulent kinetic energy
T, T_{in}, T_{out}	=	erosion thickness of bed and erosion thicknesses in the VR and NOWR
U, V	=	depth averaged velocities
U_m	=	cross sectional averaged longitudinal velocity
Z_b	=	bed elevation
a	=	density of vegetation canopy
b	=	channel width
b_v	=	vegetation canopy width
$\overline{c}_b$	=	averaged sediment concentration of bed-load layer
d	=	sediment diameter
d_{50}	=	median diameter of non-uniform sediment
d_{86}	=	86 percent finer than the given diameter
d_{16}	=	16 percent finer than the given diameter
d_v	=	vegetation stem diameter
f	=	frequency
f_{rk}	=	array resistance parameter
p	=	porosity of bed materials
h	=	water depth

h_l, h_t = water depths at the leading edge and trailing edge

h_v = vegetation canopy height

k = turbulent kinetic energy

l_m = mixing length

q_b = bed-load transport rate

q_{b*} = normalized bed-load transport rate

t = time

t_{ml} = thickness of mixing layer

u, v, w = instantaneous longitudinal velocities

u', v', w' = fluctuating longitudinal velocities

$\bar{u}, \bar{v}, \bar{w}$ = time-averaged longitudinal velocities

$\overline{u'w'}, \overline{u'v'}, \overline{v'w'}$ = Reynolds stresses

$\bar{u}_m$ = average of the maximum longitudinal velocity for hyperbolic tangent velocity profile

$\bar{u}_{\max}$ = maximum longitudinal velocity at the free surface

$\bar{u}_{veg}$ = uniform deep-vegetation-layer longitudinal velocity

u_* = friction velocity

x, y, z = Cartesian coordinates, m

y_p = maximum penetration location of transverse coherent vortices

$y*$ = penetration location of transverse coherent vortices for different vertical layers

z_0 = regression constant parameter for derivation of zero-placement length

z_m = half thickness of mixing layer

z_p = penetration location of vertical coherent vortices

Greek Symbols

θ = momentum thickness of the mixing layer

ς = constant parameter empirically approximating 7.0

κ = Karman constant equal to 0.41

Ω = secondary flow intensity

Θ, Θ_{cr} = Shields number and critical Shields number

$\Delta_{in}, \Delta_{out}$ = inner length scale and outer length scale of transverse bed profile

Φ_b = dimensionless bed-load transport rate

τ_b, τ_{cr} = bed shear stress and critical bed shear stress

ρ, ρ_s = bulk water density and dry bulk sediment density

ϕ = solid volume fraction of vegetation canopy

ϕ_1, ϕ_2 = proportional constant and exponent index to derive Φ_b

ε = dissipation rate of turbulent kinetic energy

$\nu_m, \nu_t, \tilde{\nu}$ = molecular viscosity, eddy viscosity and to-be-solved

		viscosity variable in SA model
$\alpha_y, \beta_y, \delta_y$	=	coefficients characterizing the characteristic turbulence length in the transverse direction
$\alpha_z, \beta_z, \delta_z$	=	coefficients characterizing the characteristic turbulence length in the vertical direction
σ_g	=	geometric standard deviation

Abbreviations

1D	one-dimensional
2D	two-dimensional
3D	three-dimensional
ADV	acoustic Doppler velocimetry
CGSTAB	conjugate gradient squared stabilized
CTL	canopy top level
DA	depth-averaged
FOCVC	fully-obstructed channel with vegetation canopy
LES	large eddy simulation
POCVC	partially-obstructed channel with vegetation canopy
PIV	particle-image velocimetry
RANS	Reynolds averaged Navier-Stokes
SA	Spalart-Allmaras

SNR	signal-to-noise ratio
TKE	turbulent kinetic energy
VR	vegetation region

Chapter 1 Introduction

1.1 Background

Vegetation is one of the critical features of the earth surface. Its physical, chemical and biological effects on environmental systems both directly and indirectly determine the evolution of the earth surface. This, in turn, feeds variability of spatial and temporal boundary effects back to the geometric growth pattern of vegetation species. Riparian vegetation frequently colonizes in river beds in dry seasons when water discharge is low (Figure 1.1). Hence, owing to the flow-sediment-vegetation interaction, corresponding significant roles of riparian vegetation become evident in river network development (Dunn et al., 2011; Fetherston et al., 1995), alluvial processes (Hupp and Osterkamp, 1996; Millar, 2000), river rehabilitation (Ward et al., 2001; Wohl et al., 2005) and water quality (Messina et al., 1997; Osborne and Kovacic, 1993).

Figure 1.1 Riparian vegetation colonization in channels under an emergent condition in Yuen Long area, Hong Kong.

In-channel vegetation has different manners of growth, in accordance with natural flow configurations. When vegetation is emergent under low flow conditions, flow is often characterized by simple hydrodynamics. The vegetation acting as transport-like medium marginally depresses the flow momentum by transferring kinetic energy to potential energy with a scale of energy dissipation. In addition, the existence of the vegetation decreases the conveyance capability of the channel and increases the flood risk. However, it is seen that aquatic vegetation plays a role both in hydrologic resources and hydrologic storage (Harvey et al., 2003). Under the emergent vegetation condition, the flow interacts with vegetation over the entire water depth, resulting in a rather uniform mean flow structure and turbulence field.

Under high flow conditions (e.g., rainstorms and floods), short vegetation varieties (e.g., reeds and shrubs) are submerged by water flow so that the entire depth is divided into a vegetation layer and an overflow layer (see Figure 1.2). The hydrodynamics of the entire water become sophisticated due to the complexity of the geometric boundary. The interface between vegetation layer and overflow layer is sheared by both low- and high-speed flows. When water discharge increases to a critical value, the shear interface may lose the instability and oscillate periodically in space and time, leading to vertical coherent vortices, thus motivating the mass and momentum exchange of flow against the interface. This physical process enables flow with better mixing and dispersion capabilities in the streamwise direction (Nepf et al., 2007) but leads to difficulties regarding estimation in flow dynamics and associated sediment transport characteristics.

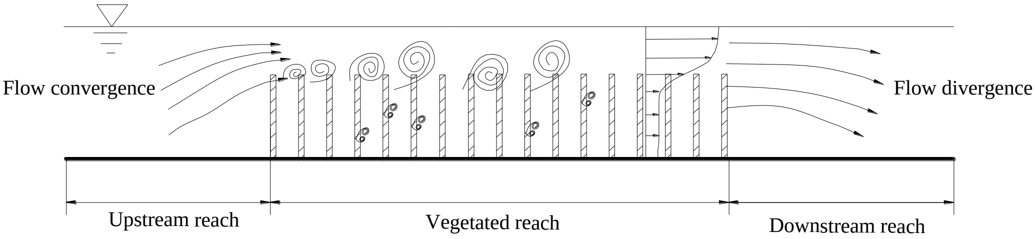

Figure 1.2 Side view of flow configuration in the channel with a vegetation canopy.

Riparian vegetation is another distribution pattern, which can be ubiquitously observed on the flood plain and river bank under flood. As wholly demonstrated in the geometric configuration, vegetation is partially distributed on the channel bed (see Figure 1.3). Due to the reduction of the cross-section area, the existing vegetation redirects the original flow on the vegetated side to the neighboring open water region or the upper overflow layer (if submerged vegetation condition), creating a vertical shear interface between the low- and high-speed flow regions. Meanwhile, the periodically oscillating large-scale coherent vortices are triggered by the instability of flow interface, thus driving transverse momentum exchange and matter dispersion (such as suspended sediment, seed dispersion and chemical mixing) between the inner vegetation region and the neighboring or outer open water region.

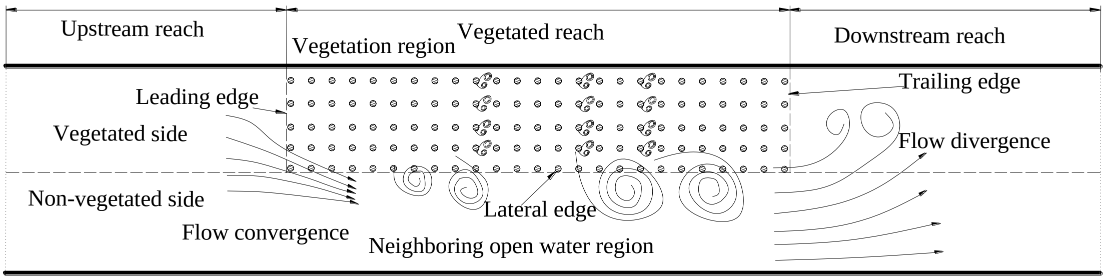

Figure 1.3 Horizontal view of flow configuration in the partially-obstructed channel with a vegetation canopy (POCVC).

In fact, vegetation roots are known to be capable of protecting channel beds and banks (Pollen - Bankhead and Simon, 2009; Pollen and Simon, 2005). Aquatic vegetation, however, can also decrease bed shear stress by dramatically decreasing the near-bed flow velocity. The near-bed related sediment motions, including the bed-load transport and sediment re-suspension, tend to be depressed and hence enhancing bed stability. The pattern, distribution and abundance of vegetation substantially impact channel scale and bed morphology pattern (Bennett et al., 2008; Follett and Nepf, 2012; Kim et al., 2015). These evolved geometric boundaries, in turn, impact the flow structure. Therefore, a better understanding of water-sediment-vegetation interaction mechanism is valuable in water management, channel restoration and biological rehabilitation.

In this thesis, all experiments were conducted in a narrow flume. Because of the narrow width, the aspect ratio of experimental configurations range roughly from 1.0 to 3.0. This suggests that the measured flow characteristics are from a 'narrow-deep' channel. Previous studies have suggested that in a non-vegetated channel of small aspect ratio, sidewalls may play an important role in determining the patterns of mean flow, turbulence and secondary flow (Nezu and Nakagawa, 1993; Yang et al., 2014), and the patterns are different from those channels of large aspect ratio. Nevertheless, there are a variety of narrow open channels, in which the aspect ratio becomes small under high flows in the real life, such as creeks, brooks and streams as well as some urban artificial conduits (see Figure 1.4). Demands of ecological restoration and rehabilitation for these small-aspect-ratio open channels have been increasing in recent years. In this regard, hydrodynamic and sediment dynamic knowledge applicable to narrow open channels is important particularly for urban artificial conduits which are desired to be ecologically functional.

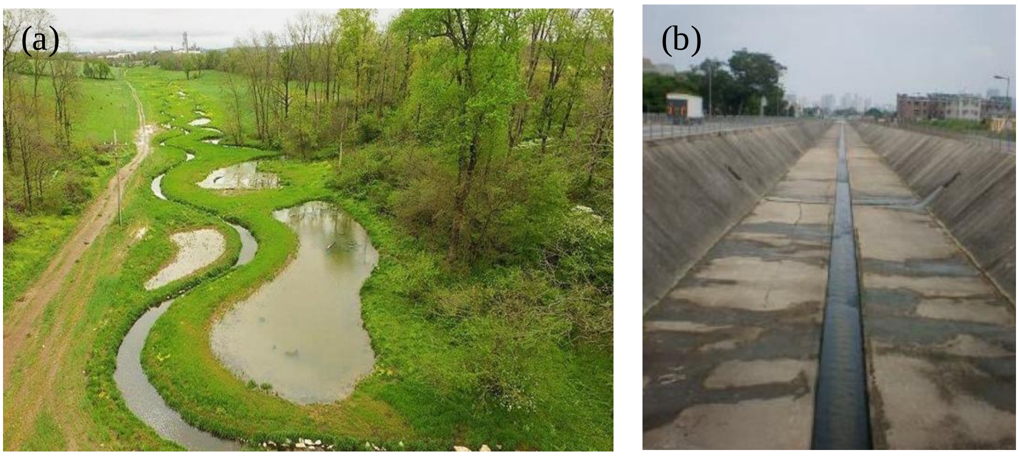

Figure 1.4 Narrow open channels in the real life. (a) A natural creek (source: Bayland Consultants & Designers, Inc.); (b) A reach in Yuen Long Main Nullah, Hong Kong.

1.2 Research objectives

Flow characteristics through aquatic vegetation have been extensively discussed over past decades. Manual simplifications of flow configurations are often utilized for vegetated flow mechanics analysis theoretically, physically and numerically. For instance, by neglecting the transverse effect, the submerged vegetation flow is simplified to be vertically two-dimensional; the partially-vegetated flow is simplified under shallow water flow assumption owing to the simplex vertical flow structure. Therefore, a knowledge gap exists in the three-dimensional description of both flow behavior as well as the associated sediment motion. With the above in mind, the objectives of the dissertation are as follows.

1) To investigate three-dimensional hydrodynamics of flows in a partially-obstructed channel with a vegetation canopy (POCVC) to gain a better understanding of the physical exchange mechanism of mass, momentum and energy between the vegetation region (VR) and neighboring open water region (NOWR).

2) To develop a three-dimensional (3D) Reynolds-averaged Navier-Stokes (RANS) model with the vortex-based Spalart-Allmaras turbulence closure to simulate flow in the POCVC.

3) To observe the characteristics of bed-load transport and bed morphology evolution in the POCVC, and to measure flow characteristics over the equilibrium bed morphology to better enable understanding of the flow-vegetation-sediment interaction in the POCVC.

4) To conduct numerical experiments with a two-dimensional depth-averaged morphological model to investigate the impacts of different flow-vegetation configurations on bed morphology evolution in the POCVC.

1.3 Scope of the dissertation

The dissertation includes seven chapters in total. Apart from the present chapter, that is the first introductory chapter, another six chapters are presented as follows:

- Chapter 2 reviews the up-to-date experimental and numerical work on flow characteristics, sediment transport and bed morphology evolution in both fully-obstructed and partially-obstructed channels with vegetation canopies. The significance of three-dimensional hydrodynamics and the associated alluvial process is emphasized for the present research work.

- Chapter 3 demonstrates details of laboratory experiments to investigate flow behaviors in the POCVC. The flow adjustment before getting fully developed is evaluated according to spatial variations of mean flow velocity, Reynolds stresses and turbulent kinetic energy (TKE). The detailed three-dimensional distribution of mean flow velocity and turbulence are presented. TKE is analyzed term by term to explore the different mechanisms in producing, transporting and dissipating TKE for the thorough understanding of flow behaviors in the POCVC.
- Chapter 4 describes the establishment of the vortex-based Spalart-Allmaras closure incorporated in the RANS model. The concept of dominant characteristic turbulence length among vertical and horizontal coherent vortices and vegetation stem wake in the POCVC is introduced in the standard SA model. The simulation shows that the vortex-based model is able to reproduce the velocity deflection and negativity of vertical Reynolds stress in the near-bed region of the junction while the standard SA model fails to do so. Important parameters in the model are evaluated in additional numerical experiments.
- Chapter 5 demonstrates the bed-load transport characteristics and bed morphology evolution in the POCVC. Characteristic bed morphologies are identified and flow characteristics over the equilibrium bed are measured. The spatial relation between flow characteristics and bed morphology is analyzed. The

transverse bed profile is fitted by the hyperbolic tangent equation with the scaling method. The above investigation and analysis are meaningful for understanding the flow-vegetation-sediment interaction and alluvial process pattern in the POCVC.

- In Chapter 6, the morphological model coupled in the depth-averaged shallow water flow model is used to compute bed morphology evolution induced by the presence of the partial-distributed vegetation canopy. Additional numerical experiments are conducted to evaluate impacts of different flow-vegetation configurations on the bed morphology evolution.
- Chapter 7 presents the conclusions based on the results of the experimental and numerical works. It also proposes unsolved problems and makes recommendations for future work.

The structure of the dissertation and relationship between chapters are shown in the following flowchart as shown in Figure 1.5.

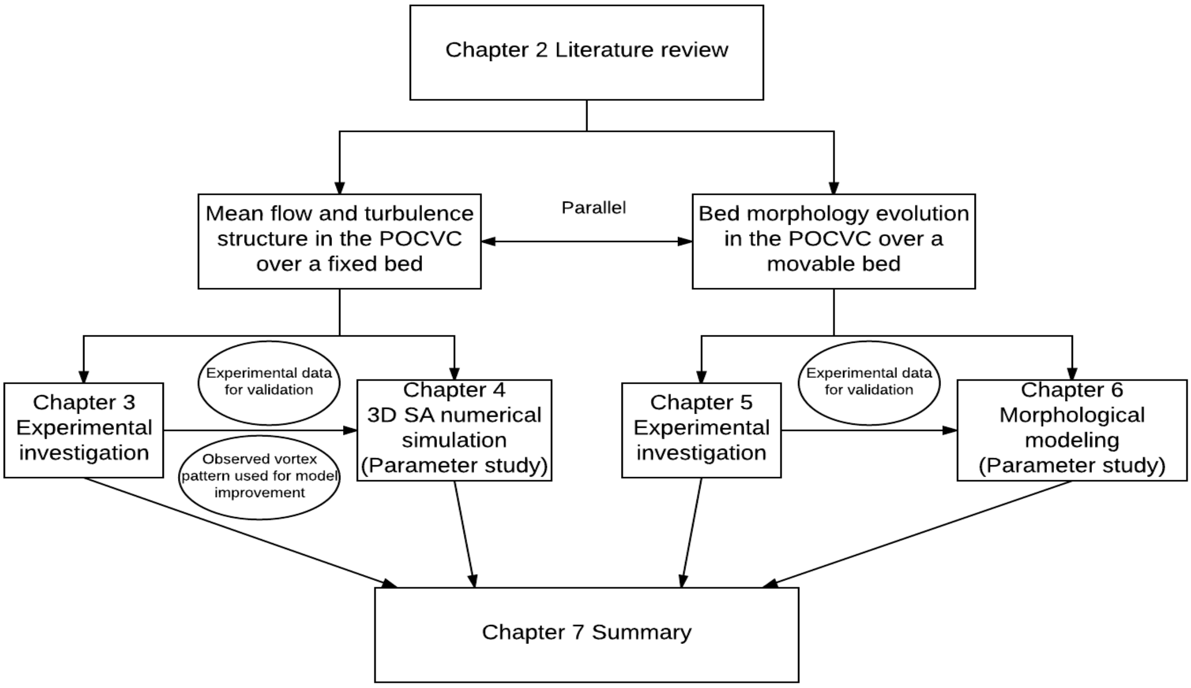

Figure 1.5 Flowchart demonstration of dissertation structure and chapter relationship

Chapter 2 Literature Review

2.1 Introduction

It is well-known that vegetation plays various important roles in all water environments. The interaction between water flow and vegetation elements is highly complex. Frequently, sediment motions accompany flow processes in natural streams, which create additional flow complexity by changing alluvial boundaries. Consequently, an integrated and sophisticated flow-vegetation-sediment system is generated.

In the natural situations, vegetation canopies often partially occur in water flows due to vegetation colonization on flood plains or water-flooding flowing over banks. A lateral interface stands between the vegetation canopy and the neighboring open water. When a partially-distributed vegetation canopy is submerged due to a high-flow condition (in wet seasons), another interface occurs at the canopy top. The strong flow shear at the interface(s) drives mass, momentum and energy exchange between the vegetation canopy and the outer open water. Physical processes in multiple-interface flows are expected to be more complex than those in single-interface flows. The hydro- and sediment-dynamics in the partially-obstructed water flow system are important for practical applications such as water management, river restoration and species rehabilitation. To date, this relevant knowledge is still not fully understood and is the basis for further exploratory work.

2.2 Studies on flows in vegetated channels

2.2.1 Flow in fully-obstructed channels

Investigations on the interaction between flow and vegetation can be broadly found in atmospheric flow through terrestrial vegetation (Brunet et al., 1994; Finnigan, 2000; Gao et al., 1989). One important study by Raupach et al. (1996) demonstrated that the characteristics of wind flow through a terrestrial vegetation canopy are analogous to the turbulent mixing flow such as jet flows, stratification flows and density flows. Raupach et al. (1996) reported that the flow instability at the vegetation top owing to strong flow shear can lead to downstream-propagating vertical coherent vortices which are analogous to the well-known Kelvin-Helmholz (KH) vortices in turbulent mixing flows.

The knowledge acquired from such as the work of the above regarding atmospheric flow through the terrestrial vegetation canopy has been extended to water flows. It has been observed that similar vertical coherent vortices can assemble at the interface between the vegetation canopy and the overflow layer (Ghisalberti, 2002; Nezu and Sanjou, 2008; Poggi et al., 2004). A schematic diagram describing flow and vortex pattern in a fully-obstructed channel with a submerged vegetation canopy (FOCVC) is shown in Figure 2.1.

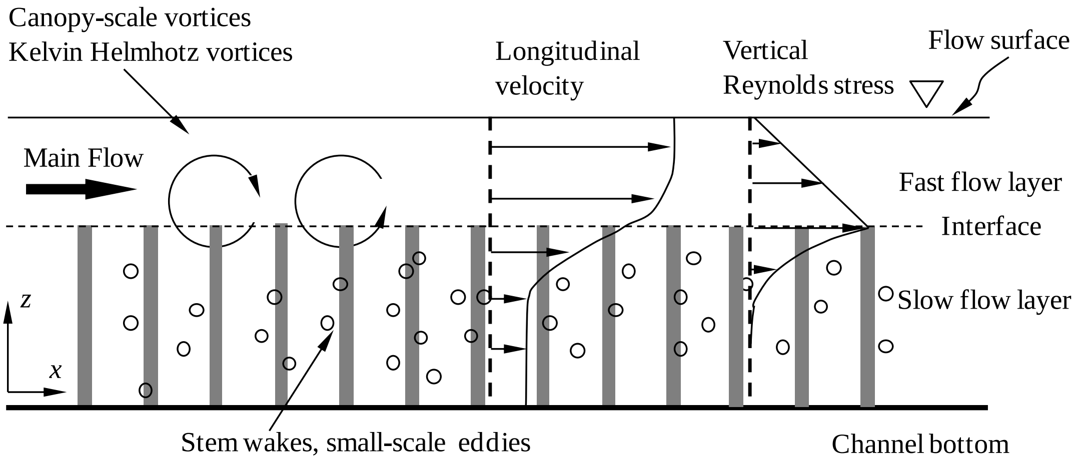

Figure 2.1 Vertical pattern of Flow and vortex developed in a fully-obstructed channel with a submerged vegetation canopy (FOCVC). Under this configuration, the variation of flow characteristics in transverse dimension is insignificant and negligible.

On the basis of the flow pattern and vortex feature, the hyperbolic tangent curve as sketched in Figure 2.2 is proposed to describe the vertical profile of longitudinal velocity,

$$\frac{\overline{u}-\overline{u}_m}{\Delta\overline{u}} = 0.5\tanh\left(\frac{z-z_m}{2\theta}\right) \tag{2.1}$$

where $\overline{u}$ is the time-averaged longitudinal velocity, $\overline{u}_m = \left(\overline{u}_{\max} + \overline{u}_{veg}\right)/2$ is the average of the maximum velocity at the free surface $\overline{u}_{\max}$ and the uniform deep-vegetation-layer velocity $\overline{u}_{veg}$. z_m is half of the thickness of the mixing layer. θ is the momentum thickness of the mixing layer defined as,

$$\theta = \int_{z_1}^{z_2} \left[\frac{1}{4} - \left(\frac{\overline{u} - \overline{u}_m}{\Delta \overline{u}} \right)^2 \right] dz \tag{2.2}$$

By using the thickness of mixing layer to substitute the momentum thickness, $t_{ml} = 2\varsigma\theta$, gives,

$$\frac{\overline{u} - \overline{u}_m}{\Delta \overline{u}} = 0.5 \tanh\left(\varsigma \frac{z - z_m}{t_{ml}} \right) \tag{2.3}$$

where ς is a constant parameter empirically approximating to 7.0.

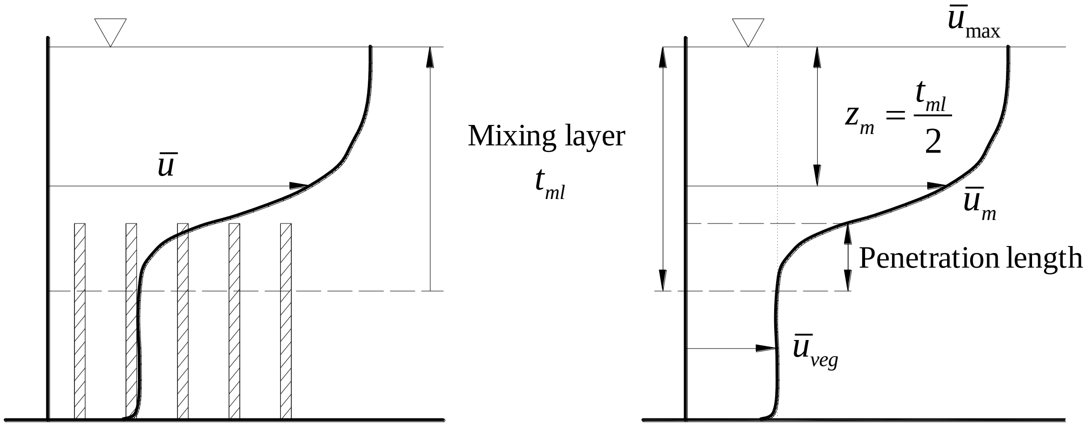

Figure 2.2 Sketch description of the hyperbolic tangent $\overline{u}$-profile of longitudinal velocity in submerged-vegetation flow (after Cheng et al. (2012)).

Another interpretation of flow through a submerged vegetation canopy suggests that an analogous boundary flow forms above the rough vegetation canopy (see Figure 2.3). Nepf and Vivoni (2000) studied the mean flow and turbulence structure under different vegetation emergence ratios. For submerged canopies, due to the generation of vertical coherent vortices, high momentum from the overflow layer is transported within the vegetation canopy. The transport distance is known as the momentum penetration length. The overflow above the vegetation canopy is treated as a boundary layer by Nepf and Vivoni (2000). By employing mixing length theory, a logarithmic profile is derived to describe the vertical distribution of longitudinal velocity with a zero-placement length (L_0) below the vegetation canopy top. This approximation, however, is relatively rough since it fails to describe the velocity inflection at the vegetation top.

$$\frac{\overline{u}}{u_*} = \frac{1}{\kappa} \ln\left(\frac{z - L_0}{z_0} \right) \tag{2.4}$$

$$L_0 = \int_0^h \frac{d\overline{u'w'}}{dz} z dz \Bigg/ \int_0^h \frac{d\overline{u'w'}}{dz} dz \tag{2.5}$$

where u_* is the friction velocity, κ is the Karman constant equal to 0.41, z_0 is a regression constant parameter, and h is the water depth and $\overline{u'w'}$ is the vertical Reynolds stress.

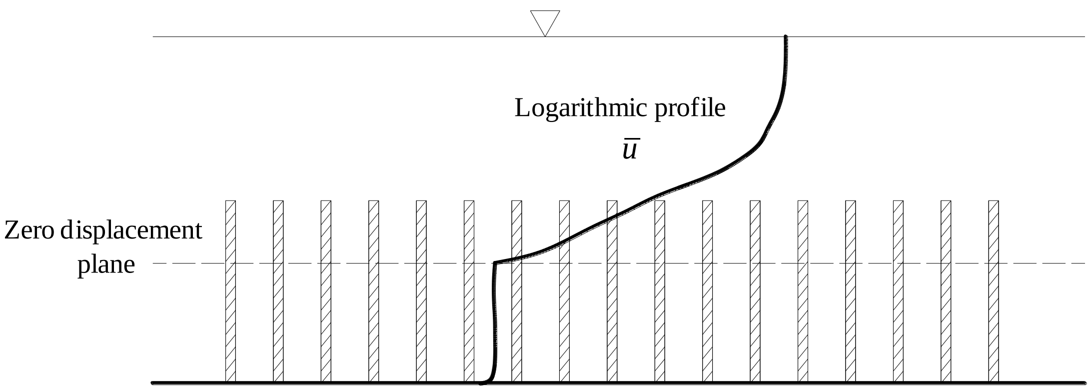

Figure 2.3 Sketch of the logarithmic $\overline{u}$-profile in submerged-vegetation flow (Nepf and Vivoni, 2000).

For emergent canopies, flow is simply driven by hydraulic pressure and dominated by longitudinal exchange without the vertical momentum exchange demonstrated by Nepf and Vivoni (2000). Consequently, the vertical velocity profile almost appears as a straight curve and vertical Reynolds stress approximates to zero as a result of the combined gravitational force of the water body and vegetative drag.

On the basis of the above background knowledge, extensive efforts have been made to understand the flow-vegetation interaction mechanism in the fully-obstructed channel with a vegetation canopy (FOCVC).

Ghisalberti (2002) reported that coherent vortices play an additional role in the flexible vegetation in addition to momentum exchange. The frequency of the vortex passage matches the waving frequency of flexible vegetation and this phenomenon is referred to as "Monami". The agreement between "Monami" motion and vortex evolution was also confirmed by Okamoto and Nezu (2009).

Ghisalberti and Nepf (2004) observed that the generated vertical coherent vortices are limited to a certain size. This differs from the free shear layer growing continuously in turbulent mixing flow. The maximum size of vortices is reached once the shear production of turbulent kinetic energy (TKE) is balanced by dissipation within the canopy.

Liu et al. (2008) carefully examined spatial patterns of the velocity profile between vegetation stems of both submerged and emergent canopies. A flow velocity deflection has been observed in the near-bed region. The authors attributed the reason to counterclockwise rolling vortices. A similar phenomenon, say velocity deflection in the near-bed region, was also observed by Yang et al. (2015). However, currently, there is no theoretical or direct experimental evidence to account for this phenomenon.

The similarity of flow velocity in the submerged-vegetation flow has been widely studied. The scaling analysis method has been shown to be powerful in describing the flow velocity. Cheng et al. (2012), Ghisalberti (2002) and Ghisalberti (2009) according to the mixing layer thickness found that the hyperbolic tangent profile can well fit the velocity under different flow-vegetation configurations as shown in Figure 2.2.

Many studies, however, suggest that the analytical solution of longitudinal velocity can be obtained by assuming the submerged vegetation flow as roughness boundary layer flow. Nepf and Vivoni (2000) used a logarithmic curve to fit the experimental data and good agreement was found at the upper overflow layer. However, near the canopy top, the velocity was underestimated. Huai et al. (2009) starting from the streamwise momentum equation developed a three-layer model to derive the analytical solution of longitudinal velocity in the entire water depth. In addition, regarding the momentum penetration region, a simple exponential model was proposed to describe vertical Reynolds stress hence enabling the differential equation to be resolved.

Recently, the importance of flow behavior though finite-length vegetation canopies has drawn increasing attention. Sukhodolova and Sukhodolov (2012) developed an analytical model to describe the entire region along the vegetation patch. With appropriate assumptions in the momentum equation, the analytical solution of mean flow velocity can be derived. The theory is well supported by experimental data. In a twin paper, Sukhodolov and Sukhodolova (2012) theoretically developed a perturbed boundary layer model for describing turbulence of vegetation patch using the scaling technique. The comparison observed between the field data and the model confirmed the validity of the proposed model.

Siniscalchi et al. (2012) observed that turbulent kinetic energy greatly increases at the leading edge of the vegetation patch. The observed great variation of the vegetative drag along the vegetation patch suggests that the traditional uniform vegetative drag specification in numerical modeling may be inappropriate.

Zeng and Li (2013) using the acoustic Doppler velocimetry (ADV) investigated the hydrodynamics of flow past a submerged vegetation patch. It was revealed that the flow adjustment region and fully-developed region along the entire vegetation patch was able to be clearly classified. The high vegetation density leads to shorter flow adjustment prior to the full development of flow.

Moltchanov et al. (2015) employed Particle Image Velocimetry (PIV) to ensure an accurate instantaneous velocity measurement at the leading edge of the vegetation canopy and the downstream fully-developed region of flow. By conducting the streamwise momentum budget analysis, the contribution of normal dispersive stresses to the streamwise momentum balance was found to be pronounced. The dispersive stress initially acts as a sink term at the leading edge and then changes the sign to act as the source term at the downstream fully-developed region.

Numerical simulations with different mathematical models have been carried out to simulate flow characteristics in the FOCVC. López and García (2001) by incorporating the vegetation canopy into a sink vegetative drag term. To achieve this both 1D *k*-*ε* model and 1D *k*-*ω* model were simply employed to simulate the mean flow and turbulence characteristics for fully-developed flows. The numerical results agree with measured data, including the mean flow velocity, turbulence intensity and Reynolds stress.

Choi and Kang (2004) compared the ability of the following models: the *k*-*ε* model, algebraic stress model (ASM) and Reynolds stress model (RSM) to studying mean flow and turbulence characteristics. Results show that each of these three turbulent models could, to some extent, simulate the flow characteristics. However, by comparison, RSM gives a more accurate calculation of flow velocity and Reynolds stresses by employing high computational consumption.

Xie et al. (2008) examined the capability of large-eddy simulation (LES) to model flows past submerged canopies. The vegetation resistance on flow was modeled by a sink with a drag force term. The simulated results confirmed by existing experimental data show validated the capability of LES and reasonably described the vertical mixing process at the canopy top.

Stoesser et al. (2010) used LES to numerically measure the detailed turbulence of wake flow around the vegetation stems. Instead of the sink term for the vegetative drag, several million grids were built on individual stems. Results showed that the stem spacing influences the wake pattern and hence the vegetative drag. The velocity deflection in the near-bed region was also shown in consistency with the experimental observation.

Zeng and Li (2013) employed the Reynolds averaged Spalart-Allmaras (SA) model to simulate flow past a finite vegetation patch. The SA model can effectively reduce the computational time. The nature of the characteristic turbulence length of the SA model efficiently characterizes the vertical turbulent flow mixing.

2.2.2 Flow in partially-obstructed channels

Another group of studies focused on flows in a channel partially-obstructed by vegetation canopies (POCVC). The majority of existing studies show that the flow is simplified by shallow water flow assumption so that the vertically distributed flow information is averaged over the entire water depth. Thus only the horizontal two-dimension variation in space needs to be considered, greatly simplifying the flow complexity in partially-obstructed channels. Similar to FOCVC, horizontal coherent vortices assembles at the lateral edge of vegetation canopy due to great flow shear between the vegetation canopy and the neighboring open water (see Figure 2.4).

Horizontal coherent vortices carrying high-momentum flow laterally penetrate the vegetation canopy, leading to strong flow mixing in the junction region. White and Nepf (2007) by means of the approximation scaling of shallow water equations demonstrated that the maximum transverse penetration length (also referred to as inner scaling length) can also be expressed as the linear function of the flow resistance length while the outer scaling length is determined by the bed friction.

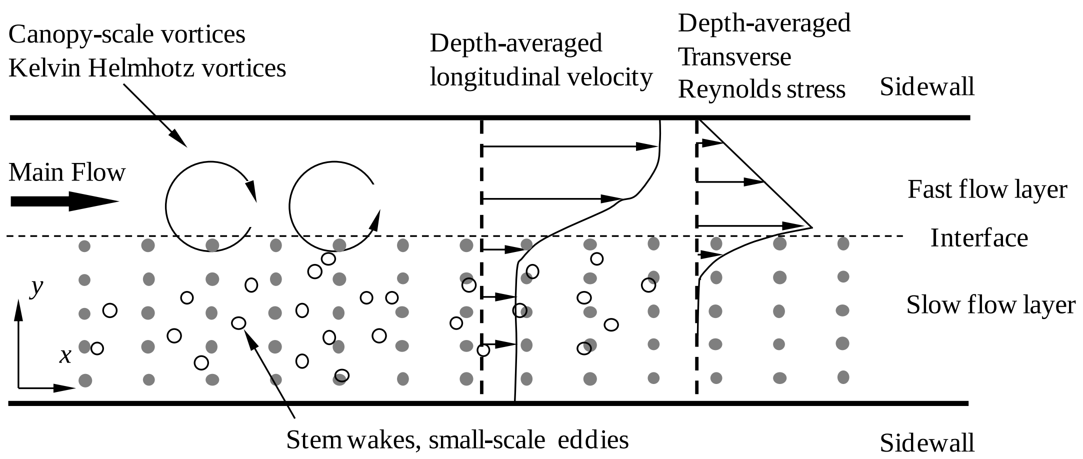

Figure 2.4 Plan view of patterns of flow and vortex developed in a partially-obstructed channel with an emergent vegetation canopy (POCVC). Under this configuration, the variation of flow characteristics in the vertical dimension is uniform and averaged over the water depth.

Hydrodynamics in the POCVC are extensively demonstrated. By conducting experiments in a POCVC (water depth=7cm) with PIV and LDA, Nezu and Onitsuka (2001) investigated transverse distributions of depth-averaged flow velocities and turbulence for fully-developed flows. Significant flow mixing was observed in the junction between the vegetation canopy and neighboring open water. The existence of horizontal coherent vortices was indicated by various perspectives (longitudinal velocity, transverse Reynolds stress and energy spectral). In addition, the authors investigated vertical distribution of flow velocities and turbulence and a linear vertical profile of longitudinal velocity occurs in the shallow flow configuration in the junction region.

White and Nepf (2007) carefully measured the instantaneous velocities in a partially-obstructed channel using ADV. With the well-defined inner and outer scaling lengths of horizontal coherent vortices, the depth-averaged flow velocity and transverse Reynolds stress showed good similarities under different flow-vegetation configurations. Based on that, White and Nepf (2008) further analyzed the flow characteristics and then developed a vortex-based model to describe the flow velocity and transverse Reynolds stress with the mixing length theory.

The above-mentioned near-bank rectangular vegetation canopy is commonly seen. However, the morphology of the vegetation canopy is an important factor affecting flow characteristics in the POCVC and its diversity is broadly concerned. The impact has been well addressed by previous studies.

Bennett et al. (2002) evaluated the flow response and flow structure by installing finite vegetation patches with different morphologies in a laboratory flume. The ecological value of vegetation patches to river restoration was well emphasized by results. The research showed that the vegetation installation in the channel can efficiently alter the original straight flow pattern, changing it to the meandering flow pattern, thus making the natural water flow system a suitable residence for diverse species.

Rominger and Nepf (2011) investigated the effect of near-bank vegetation on bank instability. It was found that the added near-bank vegetation can develop a sandy point bar near the convex bank of a meander. The vegetation on the sandy point bar was seen to effectively suppress the transverse extension of secondary currents over the sediment bar and limit the secondary currents in the neighboring open water region. The flow adjustment due to the near-bank vegetation efficiently protected the bank from erosion by the helical flow generated in meanders.

Zong and Nepf (2012) carefully studied the wake property of a circular array of cylinders. The wake or vortex street behind the cylinder patch is generated further downstream than those generated behind the solid cylinder. Two characteristic lengths were identified downstream the array, and are associated with the cylinder density. Later on, Chen et al. (2012b) then analyzed the experimental data under different flow-vegetation configurations and used the scaling technique to enable the prediction of the mean flow velocity of downstream flow.

Numerically, Xiaohui and Li (2002) used LES to simulate flow in the POCVC. The vegetation resistance effect was adopted as the drag force term in the momentum governing equations. The periodic boundary condition was applied, greatly reducing the grid number, hence enabling the flow in the entire computational domain to be fully developed. The modeling of LES with vegetation effect as the drag force term well produced the horizontal coherent vortices.

Choi and Kang (2006) presented a fully-dimensional modeling of partially-obstructed channels with submerged vegetation canopy, using the Reynolds stress model. The model was validated by experiments by Nezu and Onitsuka (2001). Results show that the mean flow properties are well comparable, while the turbulence anisotropy and secondary currents seem to be overestimated by the Reynolds stress model.

Li and Zeng (2009) used the SA model to investigate the effect of an emergent canopy patch added in a T-junction confluence. The SA model quantitatively predicts the trend of increasing flow in the branch channel with an increase in the branch channel width and/or a decrease in vegetation density. It is shown that due to the presence of the vegetation, the overall energy loss coefficient of the channel system decreases, directly influenced by the amount of flow in the branch channel.

Li and Zhang (2010) used LES to produce the vortex evolution behind a square patch of an emergent canopy. The drag-force method representing the vegetation was confirmed to produce the right property of wake. However, the bed resistance tends to suppress the initiation of vortex behind the vegetation patch. Therefore, the free-slip condition at the bottom boundary was suggested for the successful simulation of vortex street behind vegetation patches using LES.

Huai et al. (2015) built a numerical channel with a large number of grids with a rectangular emergent canopy patch. Individual vegetation stems were treated as the solid boundary. A complete finite vegetation patch was put in the computation domain. The computed results compared well with the experimental measurement. The complete spatial flow evolution was well visualized, including the initial flow zone at the upstream, the diverging flow zone, the developing zone and also the fully developed zone along the vegetation patch.

2.3 Studies on sediment transport and bed morphology evolution in vegetated channels

2.3.1 Sediment transport under uniform flow

The pioneering work (Einstein, 1950; Shields, 1936) on the incipient sediment motion established the solid theoretical foundation of sediment transport. The external fluid force exerted on a sediment particle and the gravity force of the particle as the mobilizing and stabilizing forces determine the motion status of the sediment particle. Their ratio referred to as the Shields parameter is expressed as,

$$\Theta = \frac{\tau_b}{(\rho_s - \rho)gd} \tag{2.6}$$

where τ_b is the bed shear stress, ρ_s is the dry bulk sediment density, ρ is the water density, g is the gravitational acceleration, and d is the particle diameter.

Under different flow configurations, each particle size corresponds to a critical Shields number, over which the initiation of the sediment is enabled. Those critical Shields numbers collapse into the Shields curve estimating the incipient motion for continuous particle size as shown in Figure 2.5. According to the transport mode, the moving sediment status can be categorized into bed loads, suspended loads and wash loads. The latter two sediment types normally occur with fine sediment, floating in the water flow enabled by the buoyancy and lifting effects. Bed-load transport plays a significant role in generating the earth surface landscape for terrenes and river networks. In this current study, bed-load transport is considered only in relation to the large sediment size, and is referred to as equilibrium sediment transport (Van Rijn, 1987). Bed loads can be sliding, rolling and saltation as a result of the action of exerting forces. The de-synchroneity between flow and bed-load motion always occurs due to the above complex motion status. Motions of suspended and wash loads, however, can be simply related to intensities of mean flow and turbulence.

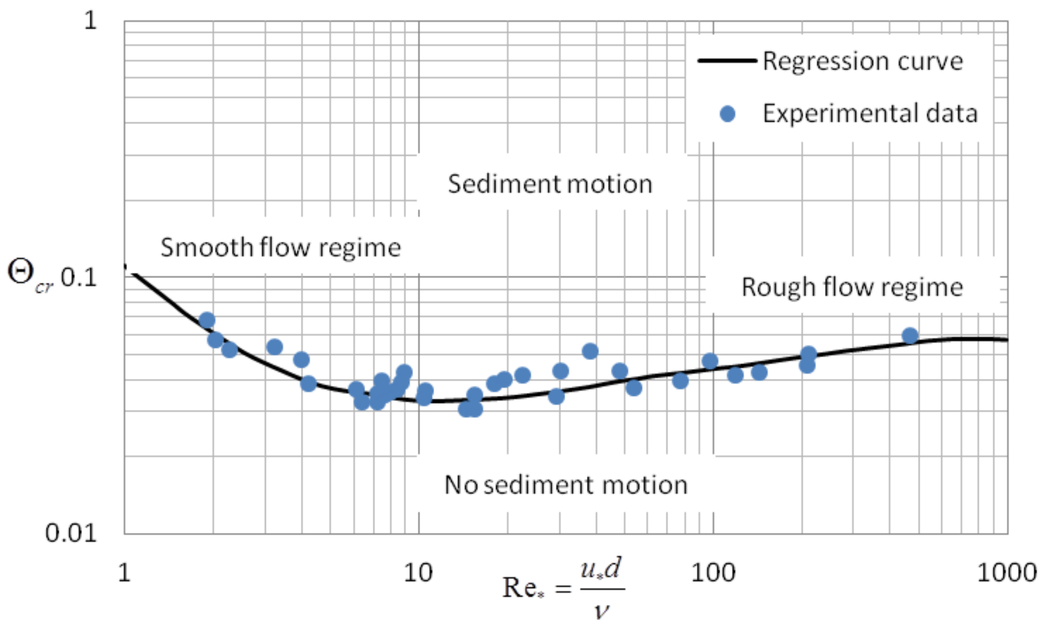

Figure 2.5 Shields diagram determining sediment motion (Shields, 1936).

According to the Shields diagram, Berenbrock and Tranmer (2008) have summarized

Shields number and critical bed shear stress for various classes of particles with different diameters as shown in Table 2.1, and as presented in the book by Julien (2002).

Table 2.1 Critical shear stress by particle-size classification for determining approximate condition for sediment mobility at 20 degrees.

Particle classification name	**Ranges of particle diameters (mm)**	**Shields parameter (dimensionless)**	**Critical bed shear stress (τ_c) (N/m^2)**
Coarse cobble	128 – 256	0.054 – 0.054	112 – 223
Fine cobble	64 – 128	0.052 – 0.054	53.8 – 112
Very coarse gravel	32 – 64	0.05 – 0.052	25.9 – 53.8
Coarse gravel	16 – 32	0.047 – 0.05	12.2 – 25.9
Medium gravel	8 – 16	0.044 – 0.047	5.7 – 12.2
Fine gravel	4 – 8	0.042 – 0.044	2.7 – 5.7
Very fine gravel	2 – 4	0.039 – 0.042	1.3 – 2.7
Very coarse sand	1 – 2	0.029 – 0.039	0.47 – 1.3
Coarse sand	0.5 – 1	0.033 – 0.029	0.27 – 0.47
Medium sand	0.25 – 0.5	0.048 – 0.033	0.194 – 0.27
Fine sand	0.125 – 0.25	0.072 – 0.048	0.145 – 0.194
Very fine sand	0.0625 – 0.125	0.109 – 0.072	0.110 – 0.145
Coarse silt	0.0310 – 0.0625	0.165 – 0.109	0.0826 – 0.110
Medium silt	0.0156 – 0.0310	0.25 – 0.165	0.0630 – 0.0826
Fine silt	0.0078 – 0.0156	0.3 – 0.25	0.0378 – 0.0630

Knowledge of the bed shear stress is critical in the judgment of the particle motion status. It is defined as follow,

$$\tau_b = \rho u_*^2 \tag{2.7}$$

where u_* is the particle skin friction velocity and ρ is the water density.

A few approaches to calculate the friction velocity are known. Two commonly-used are presented as follows. According to the physic definition, bed shear stress is the shear force on particles exerted by water flow. It gives

$$\tau_b = \left(\tau_{yx} + \tau_{zx} + \tau_{yz}\right)_{\text{near bed}} \tag{2.8}$$

where $\left(\tau_{yx}, \tau_{zx}, \tau_{yz}\right)_{\text{near bed}}$ are Reynolds shear stresses near the bed.

Thus the bed shear stress is determined once flow velocity information has been obtained. Another approach to determine the bed shear stress is to calculate the friction velocity by fitting measured data to the logarithmic velocity profile

$$\bar{u} = \frac{u_*}{\kappa} \ln\left(\frac{z}{z_0}\right) \tag{2.9}$$

where κ is the Karman constant equal to 0.41, z_0 is the regression constant parameter.

Einstein (1950) contributed significantly to both the theoretical and laboratory work of bed-load transport. He first considered the effect of flow randomness and particle number in motion in bed-load transport with the probability function. In the study, the dimensionless bed-load transport rate was defined as

$$\Phi_b = \frac{q_b}{\sqrt{(\rho_s - \rho) g d^3}} \tag{2.10}$$

where q_b is the volumetric rate of bed-load transport.

Extensive laboratory experiments have been conducted to evaluate the relation between Φ_b and fluid force (e.g., bed shear stress or Shields number). Empirically, the relation is identified between the two parameters as

$$\Phi_b = \phi_1(\Theta - \Theta_{cr})^{\phi_2} \tag{2.11}$$

where ϕ_1 is the proportional constant related to flow and sediment properties, ϕ_2 is the exponent index, derived empirically by the fitting experimental data to the formula, and Θ_{cr} is the critical Shields number. Physically, Φ_b cannot be negative so $\Phi_b = 0$ when $\Theta < \Theta_{cr}$. Eq.2.11 can be used to calculate the local bed-load transport rate with associated flow characteristics. Table 2.2 presents commonly-quoted bed-load transport relations on the basis of the forehead physical mechanism.

Table 2.2 Common bed-load transport rate formulas.

Authors	Formulas
Meyer-Peter and Müller (1948)	$\Phi_b = 8(\Theta - \Theta_{cr})^{1.5}, \Theta_{cr} = 0.047$
Einstein (1950)	$\dfrac{43.5\Phi_b}{1+43.5\Phi_b} = 1 - \dfrac{1}{\sqrt{\pi}}\int_{-(0.143/\Theta)-2}^{+(0.143/\Theta)-2} e^{-t^2}\,dt$
Ashida & Michiue (1972)	$\Phi_b = 17(\Theta - \Theta_{cr})(\sqrt{\Theta} - \sqrt{\Theta_{cr}}), \Theta_{cr} = 0.05$
Engelund & Fredsoe (1976)	$\Phi_b = 18.74(\Theta - \Theta_{cr})(\sqrt{\Theta} - \sqrt{\Theta_{cr}}), \Theta_{cr} = 0.05$
Fernandez Luque & van Beek (1976)	$\Phi_b = 5.7(\Theta - \Theta_{cr})^{1.5}, \Theta_{cr} = 0.037 - 0.0455$
Parker (1979)	$\Phi_b = 11.2\Theta^{1.5}\left(1 - \dfrac{\Theta_{cr}}{\Theta}\right), \Theta_{cr} = 0.03$
Wong and Parker (2006)	$\Phi_b = 3.97(\Theta - \Theta_{cr})^{1.5}, \Theta_{cr} = 0.0495$

Another way of estimating the bed-load transport rate is by solving the partial differential equation of sediment mass with the pre-calculated velocity field in numerical modeling.

Bed loads balance equation

$$(1-p)\frac{\partial z_b}{\partial t}+\frac{\partial(\delta_b\bar{c}_b)}{\partial t}+\frac{\partial q_{bx}}{\partial x}+\frac{\partial q_{by}}{\partial y}=0 \tag{2.12}$$

where z_b is the bed elevation, q_{bx} and q_{by} are the bed-load transport rates in longitudinal and transverse directions, t is the time, x and y are the longitudinal and transverse coordinates, p is the porosity of bed materials, δ_b is the thickness of the bed-load layer, and $\bar{c}_b$ is the averaged sediment concentration of the bed-load layer. q_{bx} and q_{by} can be calculated in terms of the resultant transport rate q_b. With the further assumption

$$(1-p)\frac{\partial z_b}{\partial t}=\frac{1}{L_s}(q_b-q_{b*}) \tag{2.13}$$

where L_s is the non-equilibrium adaptation length for bed-load transport, and q_{b*} is the bed-load transport rate under equilibrium conditions. Both are empirical parameters related to the flow and sediment properties. With the substitution of Eq.2.13, Eq.2.12 only has one unknown variable (q_b) to be solved.

2.3.2 Sediment transport and bed morphology evolution in vegetated channels

Vegetation effectively resists flow motion so that the bed shear stress enabling the incipient motion of sediment dramatically decreases. The bed-load transport rate in vegetated channels is identified to still comply with the proportionality relation (Baptist, 2005; Jordanova and James, 2003). Jordanova and James (2003) calculated the bed shear stress by subtracting the vegetative drag from the momentum equation regarding equilibrium flow through an emergent canopy. It was shown that the bed shear stress significantly reduces due to the existing vegetation stems. The bed-load transport rate formula can be also expressed by the reduced bed shear stress but it was suggested that further validation is needed by the addition of more data under different flow-vegetation configurations.

$$q_b = 0.017(\tau_b - \tau_{cr})^{1.05} \tag{2.14}$$

where τ_{cr} is the critical bed shear stress. Compared with the sediment transport formula in non-vegetated flows, the exponent index obviously decreases (referred to Table 2.1).

To date, numerous laboratory experiments have been conducted to investigate characteristics of sediment transport and bed morphology evolution in vegetated channels.

James et al. (2002) used the flume data of flow through the emergent canopy to reveal that the bed-load transport rate is substantially influenced by the stem drag. Experiments show the occurrence of sediment deposition in the short vegetation patch. The volume of sediment deposition was proved to be directly affected by the flow rate and patch length.

Yager and Schmeeckle (2013) measured the micro bed topography around individual stems due to local erosion and deposition in the fully-obstructed emergent canopy. The 2D velocity fields were measured to gain further understanding of the flow-vegetation-sediment interaction. The bed-load transport rate in the vegetated flow has been shown to be erratic (increase or decrease), depending on the turbulence intensity, mean flow velocity and the vegetation distribution pattern.

Tang et al. (2013) expanded the principle of the incipient motion of sediment from bare bed to vegetated bed by considering the spatial property of flow. They observed that it is even easier to initiate sediment in vegetated channels due to minor secondary fluid motions induced by vegetation stems.

Le Bouteiller and Venditti (2015) observed that the bed elevation in the vegetation region tended to rise in line with upstream sediment deposition in that region. The authors attributed the morphological response to a compensation of the reduced bed shear stress.

Recently, attention has been moved to the alluvial process in the POCVC. However, it should be noted that the majority of existing literature focus on the suspension pattern of sediment transport. Zong and Nepf (2010) investigated the effect of partially-obstructed vegetation on the deposition of sediment in the water flow (suspended loads). Both dispersion and advection processes, each essentially associated with the flow field, were identified to determine the deposition pattern in the vegetation patch. Follett and Nepf (2012) presented the sediment patterns around a patch of reedy emergent canopy. They asserted that such patterns were well explained by the flow structure and turbulence caused by the vegetation patch.

The pattern of bed morphological change in the POCVC was observed by Kim et al. (2015). The canopy resistance contributed by the combination of canopy width and vegetation density was altered in that study. It was shown that the sediment deposition volume near the trailing edge of the vegetation canopy is influenced by flow intensity and canopy resistance. Linear relations were found to occur between flow intensity and sediment erosion or deposition in different regions.

In comparison, the numerical simulation of alluvial processes in the vegetated channel including sediment transport and bed morphology evolution is difficult. The reason for this lacking might be the uncertainty in calculating the bed shear stress at the junction between the vegetation region and the neighboring open water region. Another limiting factor to the numerical simulation of the vegetated bed is caused by computer capability. It is known that the time lag between water flow and sediment transport (mainly bed loads) is of great significance (Phillips and Sutherland, 1989; Wu et al., 2000). Specifically, the evolution duration of sediment transport and bed morphology evolution greatly exceeds that of water flow. Therefore, the simulation of the flow-sediment co-evolution requires great computational expense, particularly for 3D flow modeling.

Tsujimoto (1999) employed 2D horizontal scheme by depth-averaging to simulate the alluvial processes including bed-load transport, bed morphology evolution and surface sorting. A simple case of a partially-obstructed channel with a short vegetation patch was demonstrated and the importance of vegetation patch on the alluvial processes was discussed. The author proposed two perspectives of alluvial processes in the POCVC, including that the existence of vegetation canopy enables (i) the narrowing process of a stream with severe degradation, widening vegetation zone and multi-terrace formation, and (ii) development of the sand island.

A series of numerical modeling work has been done by Wu and Wang (2004), Wu et al. (2005) and Wu and He (2009) for restoration purposes of rivers and ecosystem. Wu and Wang (2004) described procedures of 2D depth-averaged simulation of sediment transport and bed morphology in vegetated channels in detail. Using the finite volume method, sediment transport and bed deformation were predicted with the pre-calculated flow fields, and the boundary was modified by the simulated results of sediment transport and bed deformation for a next time step. The simulated results of bed morphology in the POCVC agree with the experimental data with acceptable accuracy. Wu et al. (2005) improved the previous model to simulate unsteady flow and non-uniform total-load transport and the model calibration was made in terms of a partially-obstructed channel with alternate vegetation patches. The changes in bed topography, bank retreat, and thalweg meandering were well predicted. Wu and He (2009) applied the existing morphological model to study the effect of vegetation on the capability of flow conveyance and sediment transport in partially-obstructed channels with rigid and flexible vegetation.

Crosato and Saleh (2011) numerically evaluated the effects of floodplain vegetation on a medium-sized river using a 2D morphodynamic model with submodels of flow resistance and plant colonization. The simulated results show that the presence of vegetation tends to produce a single channel rather than braided channels frequently formed on the bare floodplain, since the vegetation regulates the flow path.

As stated, the computation of sediment transport and bed deformation in the POCVC in the above studies all employed the 2D flow-sediment coupled model, which can correctly produce the sediment dynamic phenomena regardless of the high accuracy.

2.4 Summary

The recognition of the significance of vegetation canopies on the water management, alluvial process, and river restoration has been raised by the public for decades. Extensive efforts have been made for understanding the flow-vegetation and flow-vegetation-sediment interaction mechanism. Particularly, investigations of mean flow and turbulence characteristics due solely to the flow-vegetation interaction solely have been extended to a variety of vegetation canopy configurations. The variety of observations offer appropriate directions for practical exploratory activities.

Relatively complete experimental knowledge and theoretical analysis are presently available to illustrate the flow-vegetation interaction mechanism. The knowledge also contributes to the development of the modeling perspectives of vegetative flows. Different modeling methods focus on how to model eddies due to the flow-vegetation interaction. k-ε model, k-w model and RSM and SA model have been employed to conduct numerical simulations of flow evolution through vegetation canopies.

The existing knowledge for the flow-vegetation interaction mechanism is still limited to simple boundaries. Particularly, the junction between the vegetation region and the neighboring open water region in the POCVC lacks detailed three-dimensional flow description, since the majority of previous research studies focused on the depth-averaged flow characteristics. In the junction region, however, the turbulence is highly anisotropic, leading to uncertainty when applying existing two-dimensional depth-averaged flow knowledge in practice. Therefore, it is of significance to investigate the fully-dimensional flow and turbulence properties for a complete understanding of flow behaviors in the POCVC.

Certainly, knowledge of the fully-dimensional flow enables more reasonable and accurate understanding of sediment transport and bed morphology evolution, since bed-load-dominated transport needs the care of flow velocity and turbulence in the near-bed region. In addition, such accurate knowledge is more important for improving numerical simulations. So far, studies including experimental investigations and numerical simulations on three-dimensional flow characteristics and the associated sediment transport and bed morphology evolution of flow in the POCVC are insufficient and incomplete, which should limit or even make misunderstanding of flow-vegetation-sediment interaction processes.

Chapter 3 Characteristics of Mean Flow and Turbulence Structure in the Partially-obstructed Open Channel with Vegetation Canopy

3.1 Introduction

Riparian vegetation plays a significant role in water management, stream restoration and river rehabilitation. It can promote biodiversity by providing food and habitats for aquatic life reproduction (Stoesser et al., 2005; Sweeney et al., 2004; Wu and He, 2009). Heavy metals and contaminants are detained due to the vegetative drag, which further reduces downstream flow entrainment (Simpson et al., 1983; Windham et al., 2003). Sediment transport and bed scour are hindered, as bed shear is significantly reduced by the vegetation blockage. Therefore, planting vegetation on the river bank is taken as one of the common engineering measures for river bank protection.

Raupach et al. (1996) first reported that the characteristics of wind flow over terrestrial canopy are very close to the turbulent mixing flow. It is also observed that similar coherent vortices tend to resemble at the interface between the vegetation layer and outer open water layer in the aquatic vegetated flow. For example, Ghisalberti (2002) observed coherent vortices over submerged flexible vegetation. Poggi et al. (2004) demonstrated that vegetation density is one of the significant factors in the generation of coherent vortices.

Recently, knowledge of flow structure within partially-obstructed open channels with vegetation canopies (POCVC) has gained attention, since vegetation partly distributed near wetlands banks and on floodplains is commonly observed in real situations. Certainly, hydrodynamics in the POCVC is more complex. Horizontal coherent vortices motivate the momentum exchange between the vegetation region and non-vegetation region (Nezu and Onitsuka, 2001; Rominger and Nepf, 2011; White and Nepf, 2007, 2008), resulting in a hyperbolic transverse profile of longitudinal velocity. The profile of longitudinal velocity can be analyzed by dimensional scaling technique based on the momentum exchange characteristics which are affected by the resistive nature of the porous vegetation canopy (White and Nepf, 2007, 2008). With characteristic scaling lengths, the transverse profile of longitudinal velocity can be concisely expressed (White and Nepf, 2008).

The above studies approximate the flow structure in the POCVC to be bi-dimensional (i.e. longitudinal and transverse). This treatment is appropriate when the transverse characteristic length scale (i.e. channel width) greatly exceeds the vertical length scale (i.e. water depth) in a relatively large-aspect-ratio channel. Table 3.1 shows the majority of experimental work for POCVC. The aspect ratio for most of the other cases is larger than 5, under which the flow can be treated as shallow water flow. Similar to submerged vegetation flow with negligible lateral boundary influence (Hu et al., 2013; Liu et al., 2012), the analytical solution of the transverse profile of longitudinal velocity is derived based on the basic flow information (Huai et al., 2008; Tang et al., 2011) with a simple eddy viscosity model.

Table 3.1 Experimental works in literatures for partially-obstructed open channels with vegetation canopy

Authors	Canopy geometric configuration				
	Water depth	Channel width	Aspect ratio	Arrangement	Emergent
Tsujimoto and Kitamura (1992)			8	Sided on 1/8 channel bed	Emergent
Nezu and Onitsuka (2001)	7cm	40cm	5.71	Sided on 1/4 channel bed	Submerged
White and Nepf (2007)	5.5-15cm	120cm	8.7-22.6	Sided on 1/4 channel bed	Emergent
Rominger and Nepf (2011)	14cm	120cm	8.6	Centered on 1/15-2/3 channel bed	Emergent
Chen et al. (2012b)	13.3cm	120cm	9.0	Circle patch centerd on channel bed	Emergent
Meftah et al. (2014)	14-25cm	400cm	16.0-28.6	Centered on 3/4 channel bed	Emergent
Shimizu and Tsujimoto (1993)	12.8cm	40cm	3.125	Sided on 1/2 channel bed	Submerged

This chapter aims to study the flow structure and turbulence in the POCVC, which can provide a good perspective of three-dimensional flow behaviors in the POCVC. Also, it is expected that the obtained knowledge can be used to improve the 3D mathematical model to rationally reproduce the flow characteristics in the POCVC. Experimental measurement of the fully-dimensional (3D) instantaneous flow velocities is carried out in a rectangular POVCV with a small channel aspect ratio (=width/depth). The latest generation of 3D NORTEX acoustic Doppler velocimeter (ADV), namely Vectrino-II, is used for velocity measurement due to its high efficiency. The Reynolds-averaged technique is applied to calculate mean flow velocities and turbulence, including flow velocity, Reynolds stresses and turbulent kinetic energy (TKE). The evaluation includes the following points.

- Flow adjustment through the POCVC. The longitudinal variation of flow characteristics in the vegetation region, junction and neighboring open water region, including water depth, longitudinal velocity and Reynolds stresses are presented;

- The pattern of those flow characteristics for the fully-developed flow is presented. Vegetation density and vegetation submergence are changed to obtain a more general pattern.
- A term-by-term analysis of TKE transport equation is conducted to make a deep understanding of the role of partially-distributed vegetation canopy in TKE transport;
- A qualitative hydrodynamic model for describing the generated vortex pattern in the POCVC is proposed, which is beneficial to the further improvement of the numerical model for flow in the POCVC.

3.2 Experiment

3.2.1 Laboratory flume

A flume is set up in the Hydraulics Laboratory at The Hong Kong Polytechnic University. Figure 3.1 shows the overall structure of the flume. The flume has a length, width, and depth of 12.5m, 0.31m, and 0.4m, respectively. Its sidewalls are made out of glass and its bottom is made out of steel. The flume bed is built with an initial slope of 1/300m and it can vary continuously from 0.83% to 2%. Honeycomb is installed at the entrance of the flume such that large-scale eddies can be filtered to straighten the flow. Water depth can be adjusted by the tailgate at the flume exit. Four water tanks are set to close the entire system. A Pump is installed to provide water recirculation. The flow rate is capable to range from 0 to 100 liter per hour (l/h) and it is monitored by using a PROMAG type electromagnetic flow meter. As shown in the figure, the flow meter is attached to the two-wheel holder which is located on the flow recirculation pipe. This helps to make flow measurement at various locations of the flume. While other measurements are needed, different equipment can be mounted on the holder. During the experiment, a point gauge is used to measure the water depth and it has the accuracy of +/- 1mm.

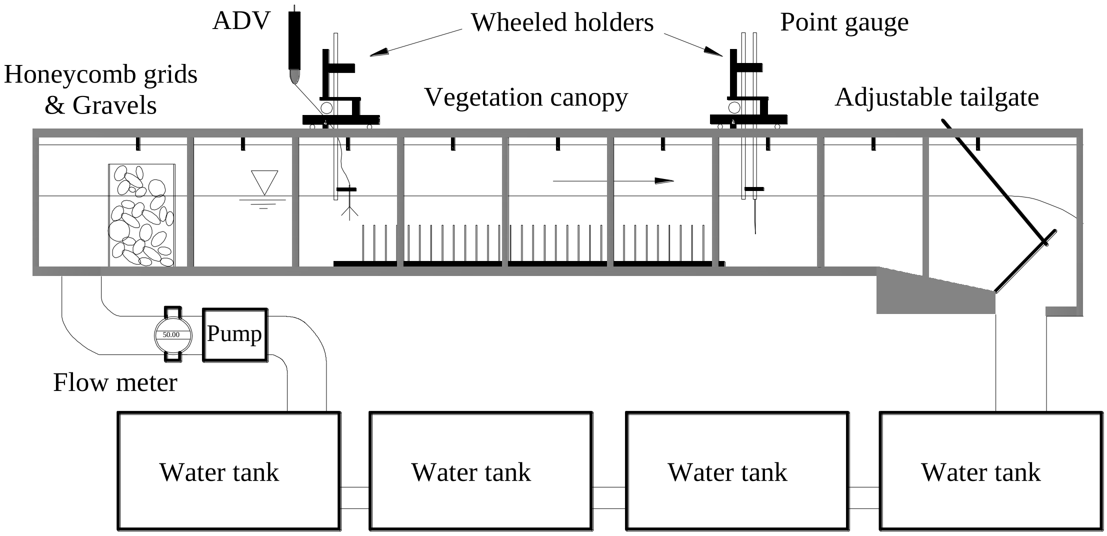

Figure 3.1 Sketch of the recirculation flume system and flow measurement setup in the vegetated flow.

Figure 3.2 shows the sketch of the reach of interest, including (a) plan view, (b) side view and (c) cross section view. Plastic cylinders used to mimic vegetation elements are of height h_v=15cm and diameter d_v=0.5cm. They are mounted onto a PVC board with a rectilinear grid pattern for conciseness and certainty. The vegetation canopy is distributed on half of the bed (canopy width, b_v=0.155m). The cylinder density is defined as the number of vegetation element per unit area, N. The frontal area per unit volume is calculated by the product of effective width (in this case equivalent to the cylinder diameter) and density as $a=nd_v$ (m^{-1}). The solid volume fraction is given as $\phi=\pi ad/4$. It is suggested that C_d is determined to be about 1.2 for the present vegetation canopy configuration (Cheng, 2013; Tanino and Nepf, 2008). The array resistance parameter $f_{rk}=C_d a$, which is used as an input of the drag force term in the numerical model. The drag length scale is $L_c=(C_d a)^{-1}$. The present vegetation canopy can be classified as a dense condition ($C_d ah>0.1$) according to Luhar et al. (2008), since $C_d ah=0.25\text{-}1.0$ for current canopy configurations.

It is difficult to locate specific regions due to such complex geometric configuration in the POCVC. For convenience, the entire channel is partitioned as shown in Figure 3.3. The channel includes the upstream of vegetation canopy, the vegetated reach and the downstream of vegetation canopy. Specifically, the vegetated reach consists of the vegetation region (VR, $y/b_v<1$) and the neighboring open water region (NOWR, $y/b_v>1$). The two regions are linked by the junction. It should be noted that the junction partially occurs in the VR and partially in the NOWR. The former part is named inner-side junction and the latter is named outer-side junction. In order to avoid confusion, VR is referred to as the region inside vegetation canopy far away from the lateral edge and NOWR is referred to as the neighboring region far away from the lateral edge. The above partition way will be used in the entire rest of the dissertation. Finally, the downstream of vegetation canopy also includes two parts: the canopy wake region and the region adjacent to canopy wake.

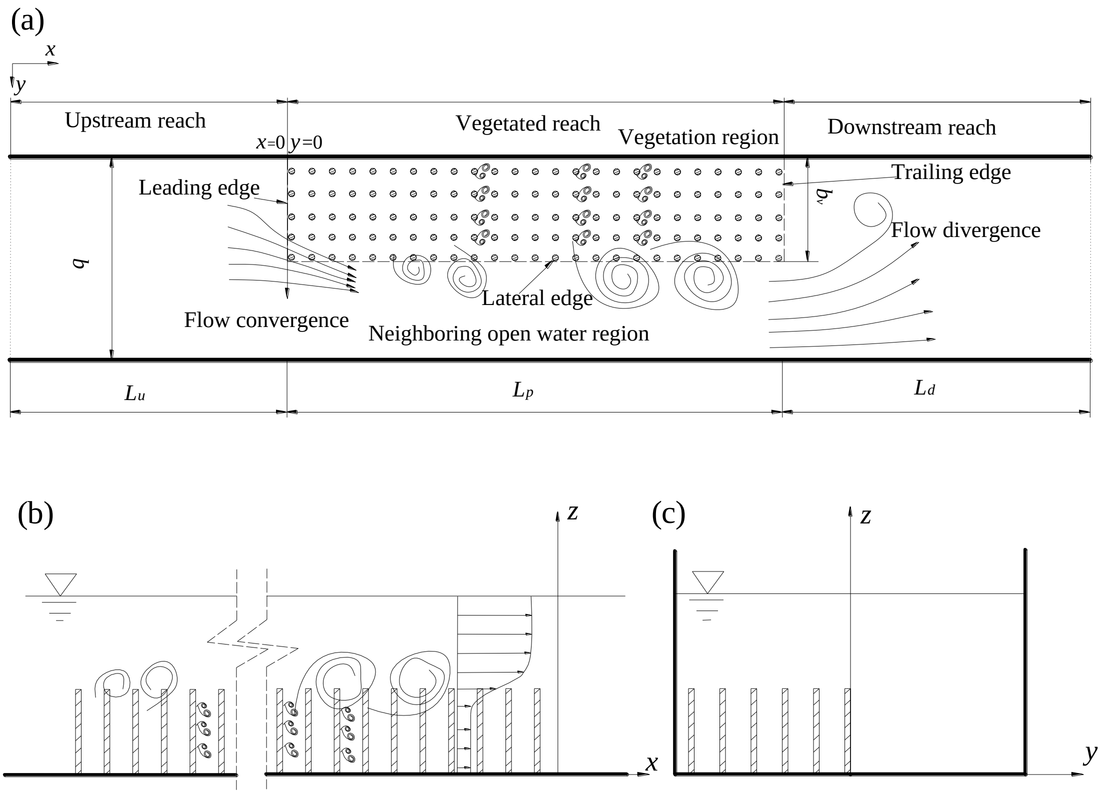

Figure 3.2 Sketch of the reach of interest according to descriptions. (a) Plan view; (b) side view; (c) front view. The coordinate is x=0 defined at the leading edge, y = 0 at the side wall and z=0 at the bottom.

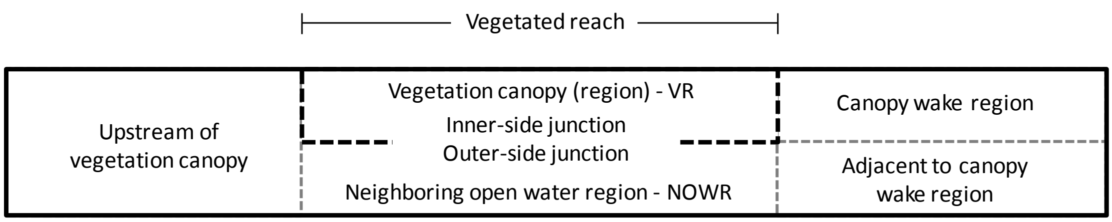

Figure 3.3 Partition of the entire open channel

In the experiment, both submergence and emergence conditions are investigated by varying the flow rate and adjusting the tail gate. In the case of submergence condition, the vegetation density is decreased by removing half of the cylinders.The information of the flow conditions is summarized in Table 3.2.

Table 3.2 Summary of experimental flow configurations

Case	Q (m^3/hour)	H (m)	U_m (m/s)	Re_H U_mH/ν	N	ϕ	a (m^{-1})	Aspect ratio b/H	H/h_v	$(C_da)^{-1}$ (m)	C_dah_v
Q75H30N1	75	0.302	0.223	67204	1111	0.022	5.56	1.03	2.01	0.15	1.00
Q50H25N1	50	0.256	0.175	44803	1111	0.022	5.56	1.21	1.71	0.15	1.00
Q50H25N2	50	0.251	0.178	44803	555	0.011	2.78	1.24	1.67	0.30	0.50
Q50H25N3	50	0.253	0.177	44803	278	0.005	1.39	1.23	1.69	0.60	0.25
Q35H15N1	35	0.145	0.22	31900	1111	0.022	5.56	2.14	0.97	0.15	1.00

Note: Q - flow rate, H - water depth at the fully-developed flow, U_m - cross sectional averaged velocity for the fully-developed flow, Re_H - depth-related Reynolds number, N - cylinder density, b/H - aspect ratio (width/depth), H/h_v - depth/cylinder height.

As shown in Figure 3.4, measurements of longitudinal variation of flow characteristics were carried out along three longitudinal transects, respectively, y/b_v=0.47, y/b_v=1.04 and y/b_v=1.53. Such transects respond to the VR, the outer-side junction and the NOWR. This measurement is to evaluate flow adjustment through the partially-distributed vegetation canopy. In addition, measurements at the cross section of x/L_p=0.832 are conducted to determine the lateral variation of flow characteristics for fully-developed flow. Different flow-vegetation configurations by changing flow rate, water depth and vegetation density are taken into account to generalize flow characteristics.

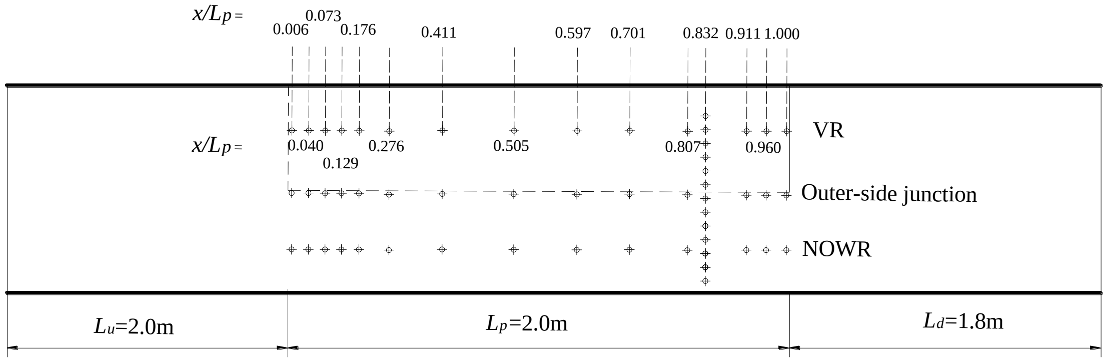

Figure 3.4 Arrangement of measurement verticals.

3.2.2 Reynolds averaging procedures

In real situations, the flow cannot be definitely steady even if the incoming flow rate is definite as a constant. Fluctuations can be observed in regard to the relevant properties of the flow. Particularly, unsteady eddies are induced in vegetated flows. The phenomenon is referred to as flow turbulence. Turbulence is significant for understanding the physical process of flow since it governs parts of mass, momentum and energy transport and transfer besides the main flow. Since fluctuations happen in the flow process with time, the time averaging technique of flow properties is employed for flow description. This statistical approach was first introduced by Reynolds (1894), so the time averaging is also called as the Reynolds averaging.

Assuming the flow is considered to be three-dimensional, the instantaneous velocity of flow is divided into three components (u,v,w) with respect to the longitudinal, transverse and vertical coordinates (x,y,z). Taking u as the example, by time averaging we have,

$$\overline{u} = \frac{1}{T}\int_0^T u dt \tag{3.1}$$

where $\overline{u}$ is the time-averaged longitudinal velocity; T is the integral period; t is the time.

The fluctuating velocity u' is expressed as,

$$u' = \overline{u} - u \tag{3.2}$$

The longitudinal turbulence intensity is then derived,

$$\overline{u'} = \sqrt{\overline{u'u'}} \tag{3.3}$$

With $\overline{u'}$, $\overline{v'}$ and $\overline{w'}$ all derived, TKE can be derived,

$$k = \frac{1}{2}(\overline{u'}^2 + \overline{v'}^2 + \overline{w'}^2) \tag{3.4}$$

With similar mathematical operation of time averaging, the Reynolds stresses ($-\overline{u'w'}$, $-\overline{u'v'}$, $-\overline{v'w'}$) are obtained.

3.2.3 Instantaneous flow velocities measurement

Vectrino-II (ADV profiler)

The latest generation acoustic Doppler velocimetry, i.e., Vectrino-II (ADV profiler), manufactured by the Nortex company was employed to measure three-dimensional instantaneous flow velocities. With measured instantaneous flow velocities, mean velocities and generated vortices can be statistically obtained to show flow characteristics under a given flow configuration.

Different from Vectrino and Vectrino Plus measuring one-point three-dimensional information at once, Vectrino-II (ADV profiler) can provide a profiling region of approximately 40-80 mm in height away from the central transducer. The profiling region consists of up to 35 sampling points with the accuracy of 1mm. This upgrade enables high-resolution measurements of flow velocities with much reduction of time consumption of experiments. The density of sampling points in the profiling region can be configured in MIDAS (Multiple Instrument Data Acquisition System) software. The detailed description of Vectrino-II can be found in Appendix A. Instantaneous velocity components (u, v, w) are measured. In order to refine the quality of the measured data such as temporal velocity spikes, the phase-space thresholding technique developed by Goring and Nikora (2002) is employed. Meanwhile, the forward-backward three-point smoothing technique is used to refine spatial fluctuation of data for better presentation of flow information. The details of above two techniques can also be found in Appendix A. To ensure the capture of high-frequency turbulence, the sampling rate and number were set to 75 Hz and 5000, respectively (Chanson et al., 2007; Nezu and Nakagawa, 1993).

3.3 Results and discussion

3.3.1 Instantaneous velocity characteristics

The significant nature of the flow motion through vegetation canopy is the generation of large-scale vortices at the interfaces (canopy edges) between the vegetation canopy and the outer open water owing to losing stability of flow at the interfaces. The generated vortices are known to be coherent and characterized with relatively-low frequency. In order to directly observe the existence of large-scale coherent vortices in the present experiments, instantaneous three-dimensional velocities with time are presented. As shown in Figure 3.5, two locations (i.e., Location A and Location B) are selected at the middle range on the canopy top and the middle range very close to the lateral edge, respectively. It is expected that coherent vortices would be generated owing to strong flow shear on the two locations.

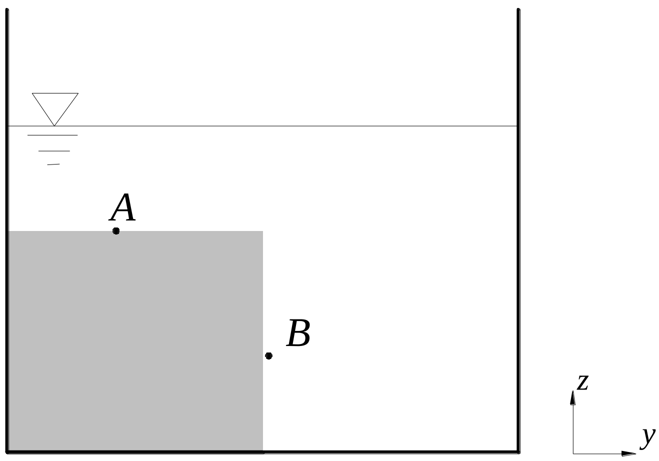

Figure 3.5 Two locations selected for examining the generation of large-scale coherent vortices.

Figure 3.6 presents the evolution of three-dimensional instantaneous velocities in time. In order to observe the large-scale (low-frequency) fluctuations of velocities clearly, the majority of small-scale (high-frequency) fluctuations (induced by, e.g., vegetation stem wake or measurement noises) are filtered. It is clearly noted that the velocities at the two locations fluctuate in time. At Location A, the coherence can be observed between u and w, indicating the generation of vertical coherent vortices. It is also noted that the v-fluctuation is somewhat equivalent to the w-fluctuation in terms of the magnitude but their coherence is nearly negligible. Similarly, at Location B, the obvious coherent fluctuations occur between u and v, indicating the generation of horizontal coherent vortices. In comparison with Location A, here the mean levels and amplitudes of velocities are greater. Again, the w-fluctuation is also pronounced, which is comparable to the v-fluctuation. However, the u-fluctuation is negligibly coherent to the w-fluctuation.

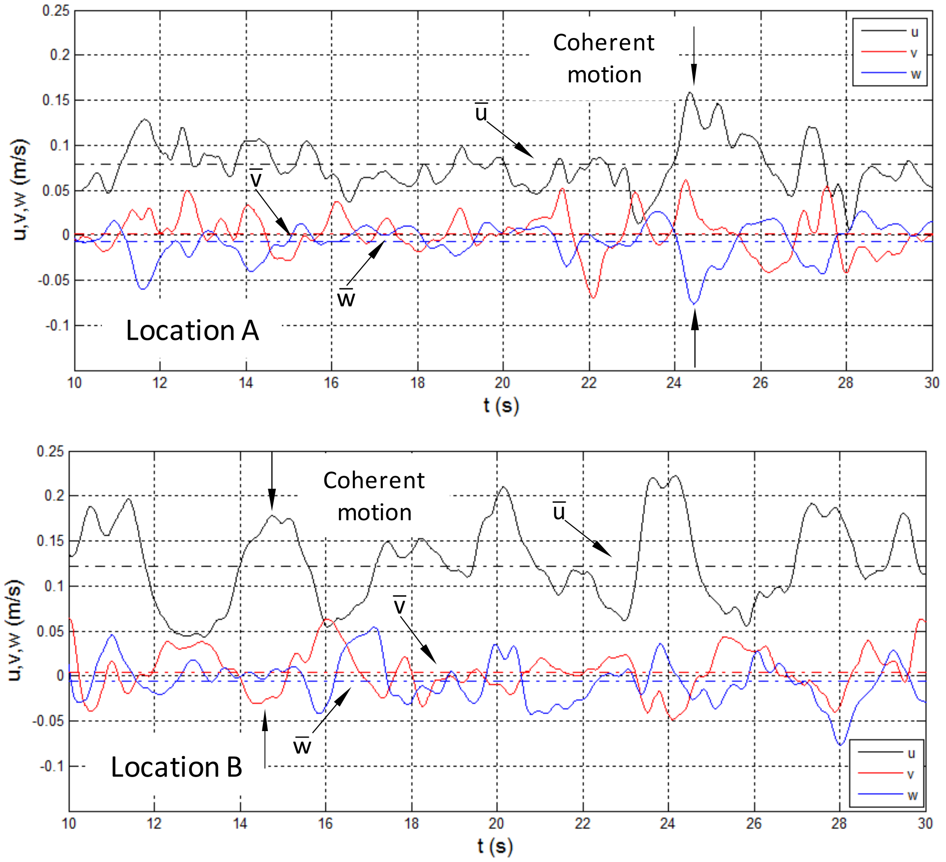

Figure 3.6 Three-dimensional instantaneous velocities

With the recorded instantaneous velocities, power spectral density (PSD) distribution for each dimension can be calculated by applying the Fast Fourier Transform (FFT) Algorithm to transform flow velocity information from the time space to the spectral space. Then, vortex information with various scales can be clearly observed. Figure 3.7 shows PSD distribution for three-dimensional velocities. It is clearly shown that at the two locations high peaks with low frequencies occur on the PSD distribution for all velocity components. At Location A, the peak magnitude for *w* exceeds that for *v* while the contrary is noted at Location B. This suggests that vertical coherent vortices are dominant at Location A and horizontal coherent vortices dominant at Location B.

However, it is uncertain what causes the pronounced but non-coherent fluctuation of flow in the third dimension.

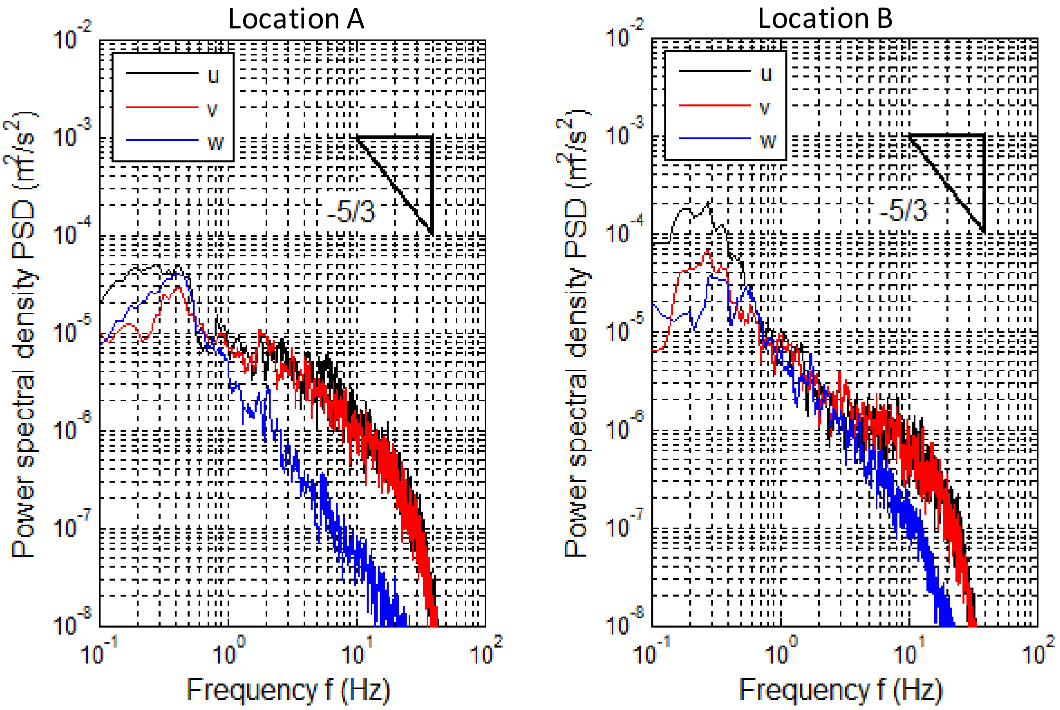

Figure 3.7 Power spectral density.

3.3.2 Flow adjustment in the partially-obstructed channel with vegetation canopy

In this section, flow adjustment in terms of different flow characteristics is evaluated. Three longitudinal transects at y/b_v=0.47, y/b_v=1.04 and y/b_v=1.53 are considered. The three transverse locations are referred to the VR, outer-side junction and NOWR, respectively.

3.3.2.1 Water depth adjustment

Figure 3.8a shows the longitudinal distribution of water depth in the VR and NOWR, and Figure 3.8b shows the transverse surface slope along the channel. For a bi-dimensional flow with transverse effect neglected, the acceleration of fluid is balanced by the longitudinal component of gravitational force, bed shear stress, vegetative drag and hydraulic slope. Clearly as shown in Figure 3.8b, the transverse hydraulic slope plays an important role in force balance in the case of POCVC. The effect, however, significantly decreases and even vanishes at the downstream of vegetation canopy. The location where the transverse surface slope approaches to zero is regarded as where equilibrium flow is reached. Of interest is that the equilibrium location (x/L_p=0.7) for the submerged case is moved downstream as compared to that (x/L_p=0.6) for the emergent case. This observation is firstly demonstrated by experimental work.

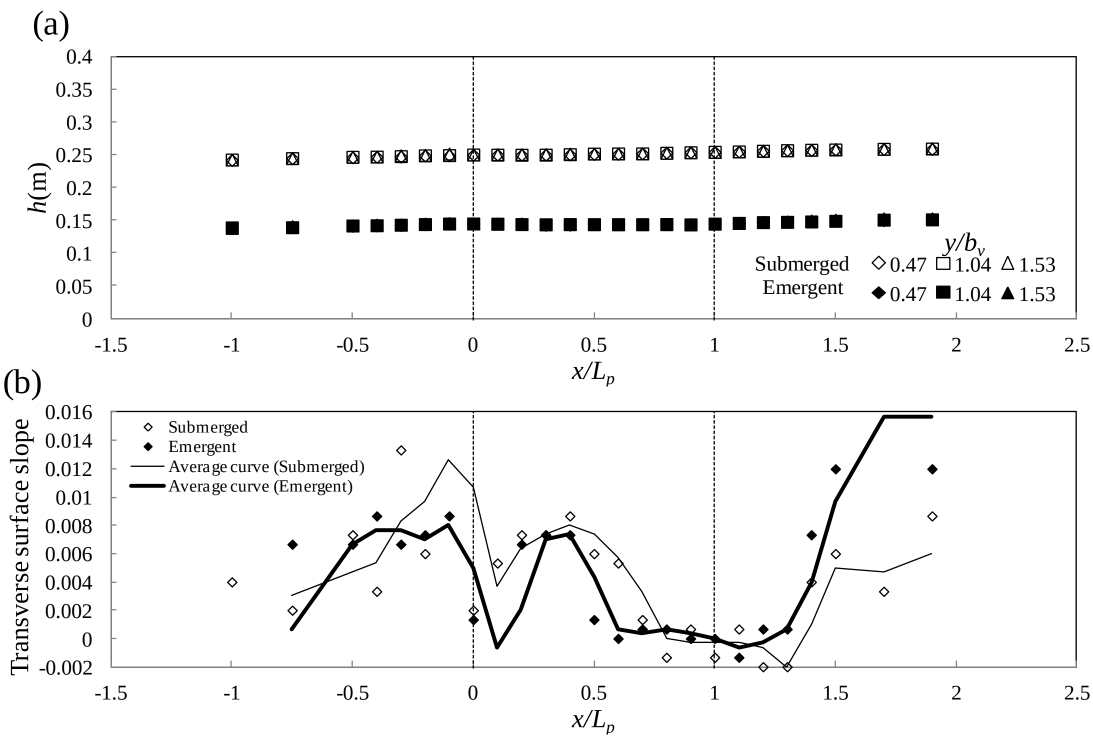

Figure 3.8 Measured water depths of flow and (b) transverse surface slope along the

POCVC of n=1111m^{-2}. The two dashed lines indicate the leading edge (left, x/L_p=0) and trailing edge (right, x/L_p=1).

3.3.2.2 Depth-averaged longitudinal velocity *U*

Figure 3.9 presents the depth-averaged (DA) longitudinal velocity for three cases: a), b), and c). Three curves are included in each case and they are velocity profiles recorded in the VR (black circle line), outer-side junction (red circle line), and NOWR (black circle line). As seen in the figure, different flow behaviors are observed. In all cases, the DA longitudinal velocity in the VR decreases while in the NOWR increases along the stream. This suggests that the adjustment distance in the VR is larger than the counterpart in the NOWR. Based on results as shown in figures, the adjustment distance is found to be constant and is located at x/L_p=0.7. For adjustment distance in the NOWR, it varies with flow conditions (i.e. flow rate and channel width) and the adjustment distance in the NOWR is found to be x/L_p=0.41, x/L_p=0.28 and x/L_p=0.7 for Q75H30N1, Q50H25N1 and Q35H15N1, respectively. This result indicates that the flow could be completely adjusted once the flow adjustment is completed in the VR.

The adjustment of DA longitudinal velocity is consistent with the observation of the adjustment of water depth. The flow adjustment in the junction (y/b_v=1.04) is of interest. The velocity declines quickly in a short distance (x/L_p<0.2) for three cases and then slowly increases as the flow propagates downstream. But the increase is not great and the velocity might be treated as constant.

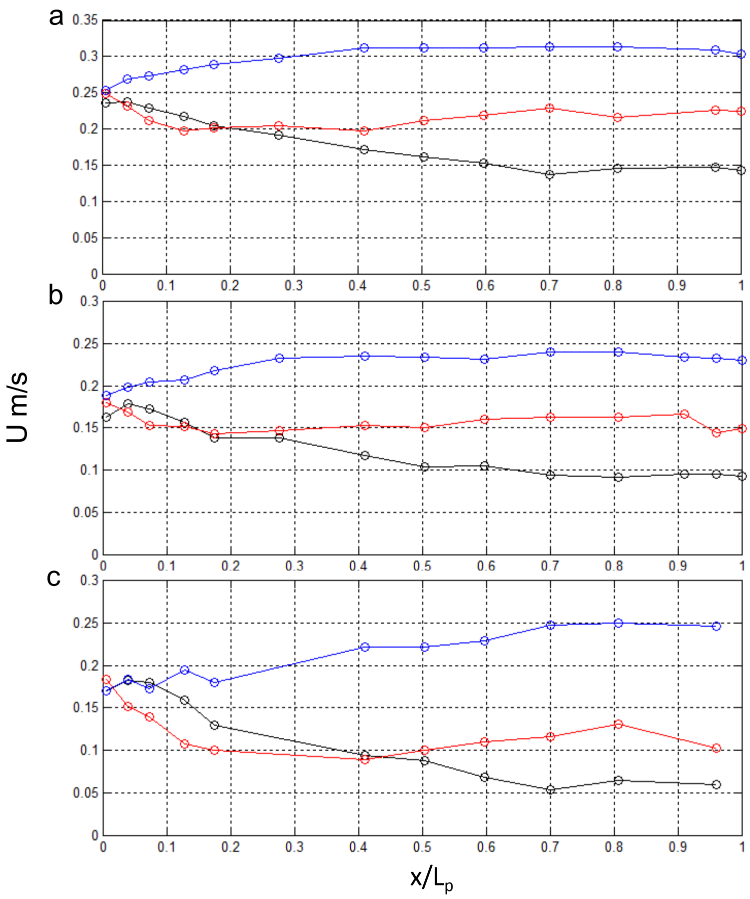

Figure 3.9 Spatial evolution of DA longitudinal velocity along the vegetated reach. Black circle line (VR, y/b_v=0.47), red circle line (outer-side junction y/b_v=1.04) and blue circle line (NOWR, y/b_v=1.53).

3.3.2.3 $\bar{u}$ -profile

Figure 3.10 shows the longitudinal velocity evolution along the vegetation canopy for different canopy submergence ratios (Q75H30N1, Q50H25N1 and Q35H15N1). Results in the VR, junction and NOWR are presented to observe the flow adjustment in terms of the vertical $\bar{u}$ -profile. At the entry region of vegetation canopy (x/L_p=0.006), $\bar{u}$ -profiles across the channel comply with the logarithmic law for all cases. As flow propagates downstream, the $\bar{u}$ -profile continuously adjusts due to the vegetative drag. Specifically, $\bar{u}$ quickly decreases below the canopy top level (CTL) while increases above the CTL in the VR. Meanwhile, $\bar{u}$ in the NOWR also increases due to water transversely redistributed into this region. It can be found that $\bar{u}$ in the VR requires a longer distance for full development compared with the NOWR. In the VR, the $\bar{u}$-profile roughly remains stable after x/L_p=0.597 and evolves into a hyperbolic tangent curve while the $\bar{u}$-profile in the NOWR remains stable after x/L_p=0.0175 except for the slight change in the near-bed region. The adjustment of the $\bar{u}$-profile is basically consistent with adjustment of U at the different transverse locations (see Figure 3.9).

Of significance is the evolution pattern of longitudinal velocity in the junction. Similar to the VR, the $\bar{u}$-profile above the CTL keeps the tangent hyperbolic shape. However, the profile below the CTL displays a particular shape that is hardly presented in the existing laboratory flume work. Beginning with x/L_p=0.073, the $\bar{u}$-profile is deflected below the CTL and the velocity deflection is enhanced as flow propagates downstream. Velocity deflection was reported by Nepf and Vivoni (2000) investigating leafed vegetation. The cause for the velocity deflection is the reduction of vegetative drag force on water body when the vegetation density increases as the vertical distance increases. In this study, the most relevant reason is the generation of the horizontal coherent vortices in the junction. The detailed discussion will be elaborated in later sections.

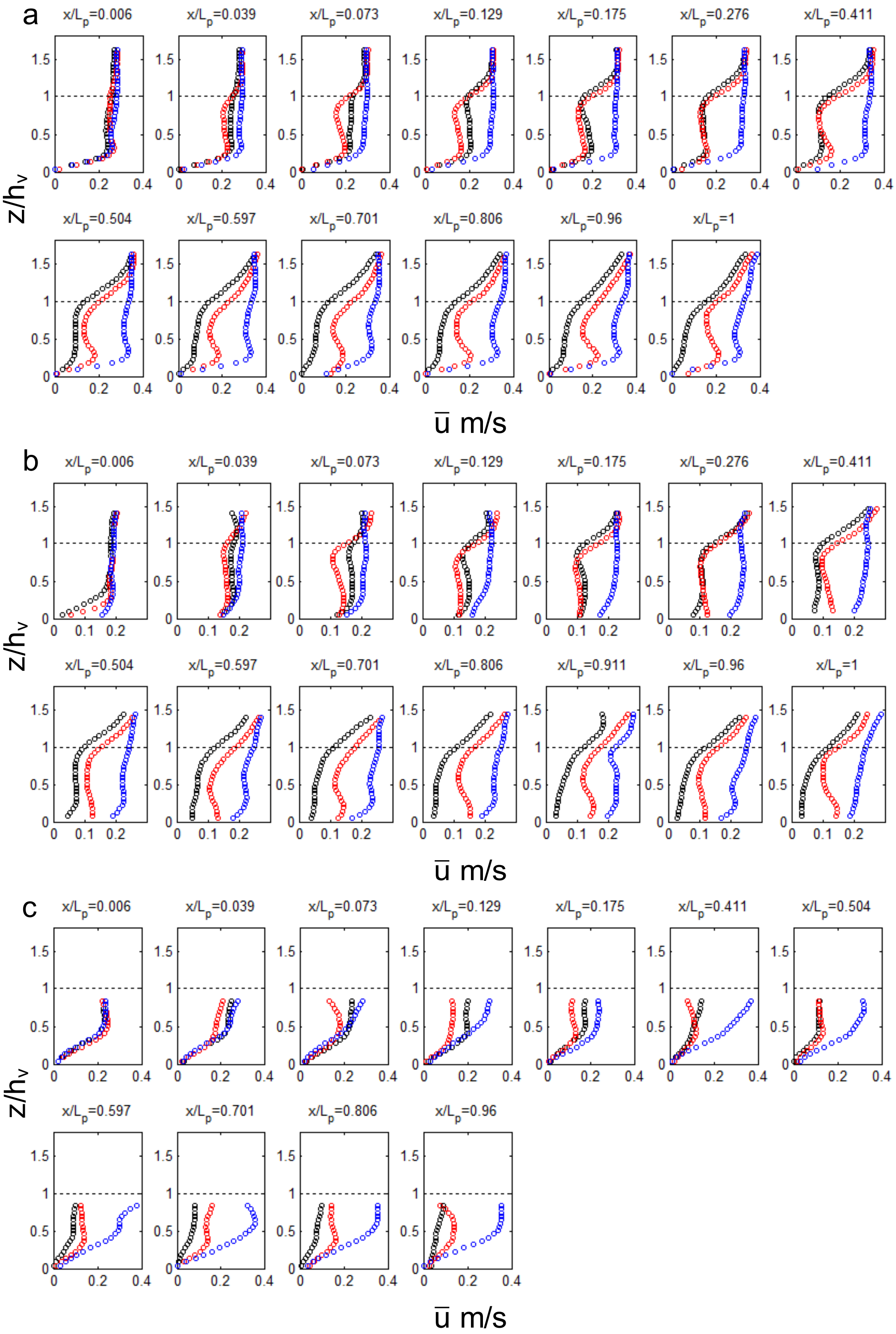

Figure 3.10 Evolution of the $\bar{u}$ -profile along the vegetated reach. Black circle (VR, y/b_v=0.47), red circle (outer-side junction, y/b_v=1.04) and blue circle (NOWR,

y/b_v=1.53). The black dashed line indicates CTL.

3.3.2.4 $-\overline{u'w'}$ -profile

Figure 3.11 shows the vertical distribution of $-\overline{u'w'}$ along the vegetation canopy, which characterizes the longitudinal evolution of turbulent momentum exchange in the vertical direction. For submerged canopy (Q75H30N1 and Q50H25N1), $-\overline{u'w'}$ In the VR and junction grows above the CTL as flow propagates downstream due to the generation of horizontal coherent vortices. At the same time, the momentum penetrates into the vegetation canopy leading to the increase in vertical Reynolds stress below the CTL. In the NOWR, $-\overline{u'w'}$ keeps decreasing above the bed like that in the straight open channel. This means that the effect of vegetation canopy is negligible for regions far away from the lateral edge. Compared with the $\overline{u}$ -profile, a longer distance is required for the adjustment of the $-\overline{u'w'}$-profile. For the emergent canopy, $-\overline{u'w'}$ remains constant close to zero due to the existence of vegetation canopy. The particular attention should be paid to the junction region. It can be observed that $-\overline{u'w'}$ evolves to be negative in the near-bed region. This negativity corresponds to the deflection of the $\overline{u}$ -profile in the same region and happens for both submerged and emergent canopies.

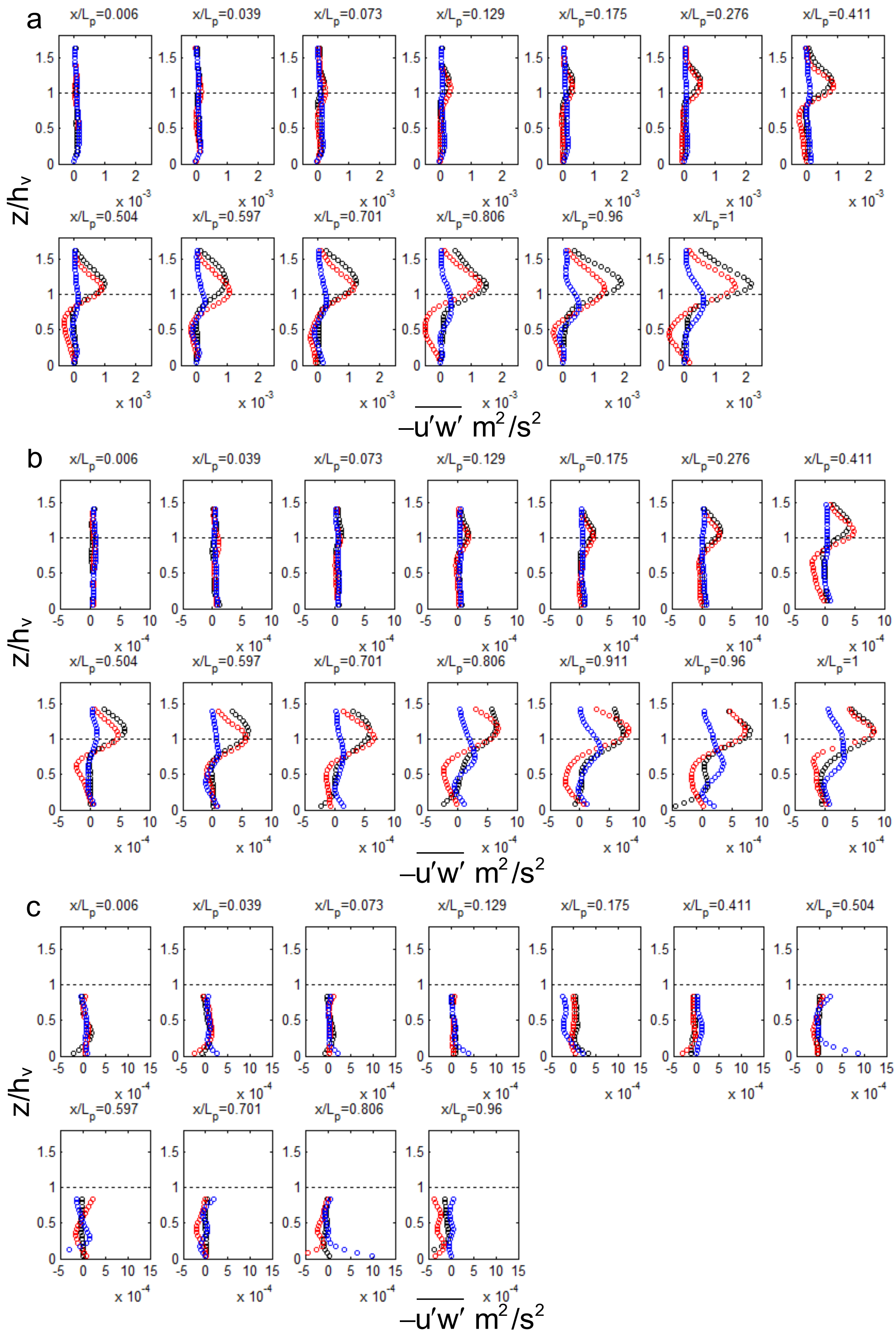

Figure 3.11 Evolution of the $-\overline{u'w'}$-profile along the vegetated reach. Black circle (VR, y/b_v=0.47), red circle (outer-side junction, y/b_v=1.04) and blue circle (NOWR,

y/b_v=1.53). The black dashed line indicates CTL.

3.3.2.5 $-\overline{u'v'}$-profile

Figure 3.12 shows the vertical distribution of $-\overline{u'v'}$ along the vegetation canopy, which characterizes the longitudinal evolution of turbulent momentum exchange in the transverse direction. The lateral edge of vegetation canopy also triggers the generation of horizontal coherent vortices like the vegetation top triggering the generation of vertical coherent vortices. In the VR, $-\overline{u'v'}$ almost remains negligible as flow propagates downstream indicating a negligible impact of the transverse coherent vortices on flow deep inside the vegetation canopy. However, $-\overline{u'v'}$ is observed to be significant in the junction. The value quickly increases above the bed bottom and then remains a large magnitude except for the region near the exit of vegetation canopy. The near-bed increase in $-\overline{u'v'}$ suggests the generation of horizontal coherent vortices. In addition, $-\overline{u'v'}$ declines quickly to zero in a short vertical distance above the CTL. This indicates that the upper-layer water body enables the quick destruction of horizontal coherent vortices. In the NOWR far away from the lateral edge, $-\overline{u'v'}$ significantly decreases compared with that in the junction.

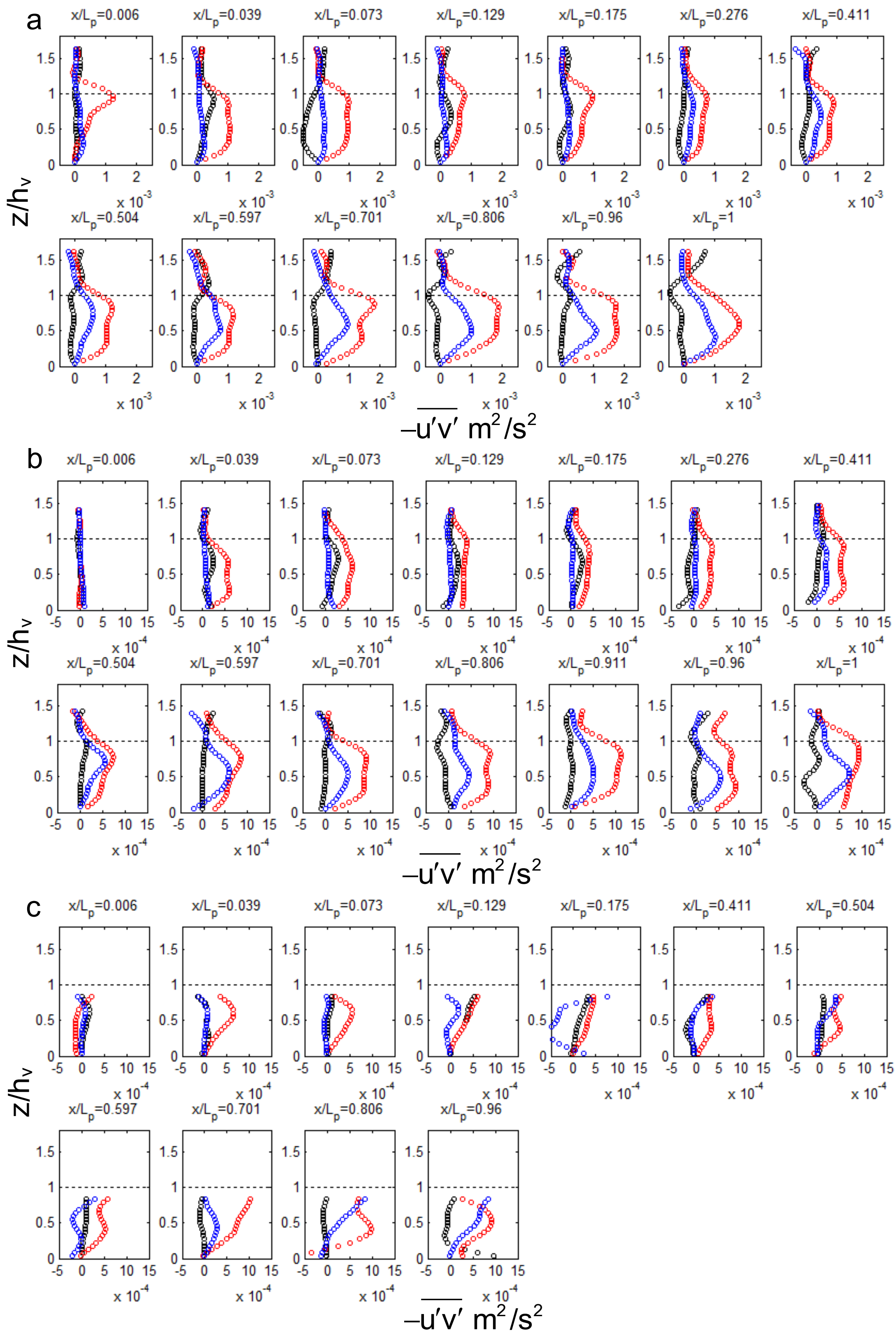

Figure 3.12 Evolution of the $-\overline{u'v'}$-profile along the vegetated reach. Black circle (VR, y/b_v=0.47), red circle (outer-side junction, y/b_v=1.04) and blue circle (NOWR,

y/b_v=1.53). The black dashed line indicates CTL.

3.3.3 3D pattern of mean flow and turbulence structure of fully-developed flow

3.3.3.1 Effect of vegetation density and vegetation submergence on flow characteristics

Extensive studies have demonstrated that flow characteristics in vegetated channels are influenced by numerous factors. Among them, vegetation density and water depth play significant roles reported by Raupach et al. (1996), Poggi et al. (2004), Nepf and Vivoni (2000), Ghisalberti and Nepf (2004), White and Nepf (2007) and Neary et al. (2012). In this section, vegetation density and water depth are changed to investigate the impact of flow-vegetation configuration variation on the flow characteristics in the POCVC. Different transverse locations are considered in the investigation, which are y/b_v=0.516, y/b_v=0.968, y/b_v=1.097 and y/b_v=1.419 corresponding to VR, inner-side junction, outer-side junction and NOWR.

Longitudinal velocity $\bar{u}$

The vertical $\bar{u}$-profile at different transverse locations is shown in Figure 3.13. Scenarios for submerged and emergent canopies are presented for understanding the general pattern of longitudinal velocity. For convenient comparison, $\bar{u}$ is normalized by the cross-section-averaged velocity, U_m (=water discharge/cross-section area). As seen in Figure 3.13a, for submerged vegetation, $\bar{u}$ in the VR clearly performs the general flow manner in the FOCVC meaning that the $\bar{u}$ -profile is developed into the hyperbolic tangent curve. It can be observed that the vegetation density is influential to the magnitude of $\bar{u}$ (Q50H25N1, Q50H25N2, Q50H25N3). Increasing vegetation density leads to the decrease in $\bar{u}$ nearly for the entire water depth. In comparison, the $\bar{u}$ -profile pattern under the varied vegetation density in the current flow-vegetation configurations differs from the counterpart in the FOCVC. In the FOCVC, As reported by Poggi et al. (2004), below the CTL $\bar{u}$ becomes smaller while above the CTL $\bar{u}$ becomes larger under a high vegetation density. The possible cause is that the water flow through fully-distributed vegetation canopy is solely directed to the upper overflow region while water flow through the partially-distributed vegetation canopy is partially directed to the NOWR. Therefore, the flow conveyance capacity of the upper overflow region in the POCVC might decreases, also resulting in the decrease in $\bar{u}$. Also, water depth is critical to the $\bar{u}$ -profile. For the submerged canopy, larger water depth leads to stronger inflection of the profile (see Q75H30N1 and Q50H25N1). The emergence of vegetation canopy (submergence ratio=1.0) only leads to a vertical straight $\bar{u}$ -profile.

In the junction region, the $\bar{u}$ -profile becomes complicated owing to strong flow mixing effect arising from the generated horizontal and vertical coherent vortices. In the inner-side junction, due to the vegetative drag still acting on the flow body, the $\bar{u}$ -profile pattern is similar to that in the VR except the increase in magnitude. Importantly in the outer-side junction, the $\bar{u}$ -profile is deflected in the near-bed region for both submerged and emergent canopies. Specifically, the velocity above the bed initially increases within a very short vertical distance (around z/h_v=0.2 for all cases), and then decreases as the vertical distance increases. The velocity deflection leads to the negative gradient on the $\overline{u}$ -profile, which inverses the mass and momentum transfer from the lower to the upper. Above the deflection region, the $\overline{u}$ -profile again displays the hyperbolic tangent pattern. For the emergent canopy, the deflected $\overline{u}$ -profile is also observed. But in the upper region the $\overline{u}$ -profile remains the vertical straight curve as there is no vertical turbulent mixing of vertical coherent vortices. It is clear that the vegetation density tends to enhance the effect of velocity deflection (Q50H25N1, Q50H25N2, Q50H25N3). The deflection event disappears for the smallest vegetation density.

In the NOWR, the velocity deflection effect decreases further away from the junction and the $\overline{u}$ -profile tends to return to the manner of the wall-bounded flow. But $\overline{u}$ -profile still slightly deviates from the logarithmic curve probably owing to the small aspect ratio (=width/depth), where flow mixing tends to expand to the NOWR. In the work of Nezu and Onitsuka (2001), the $\overline{u}$ -profile is examined to comply with the logarithmic law in the open channel with a small aspect ratio.

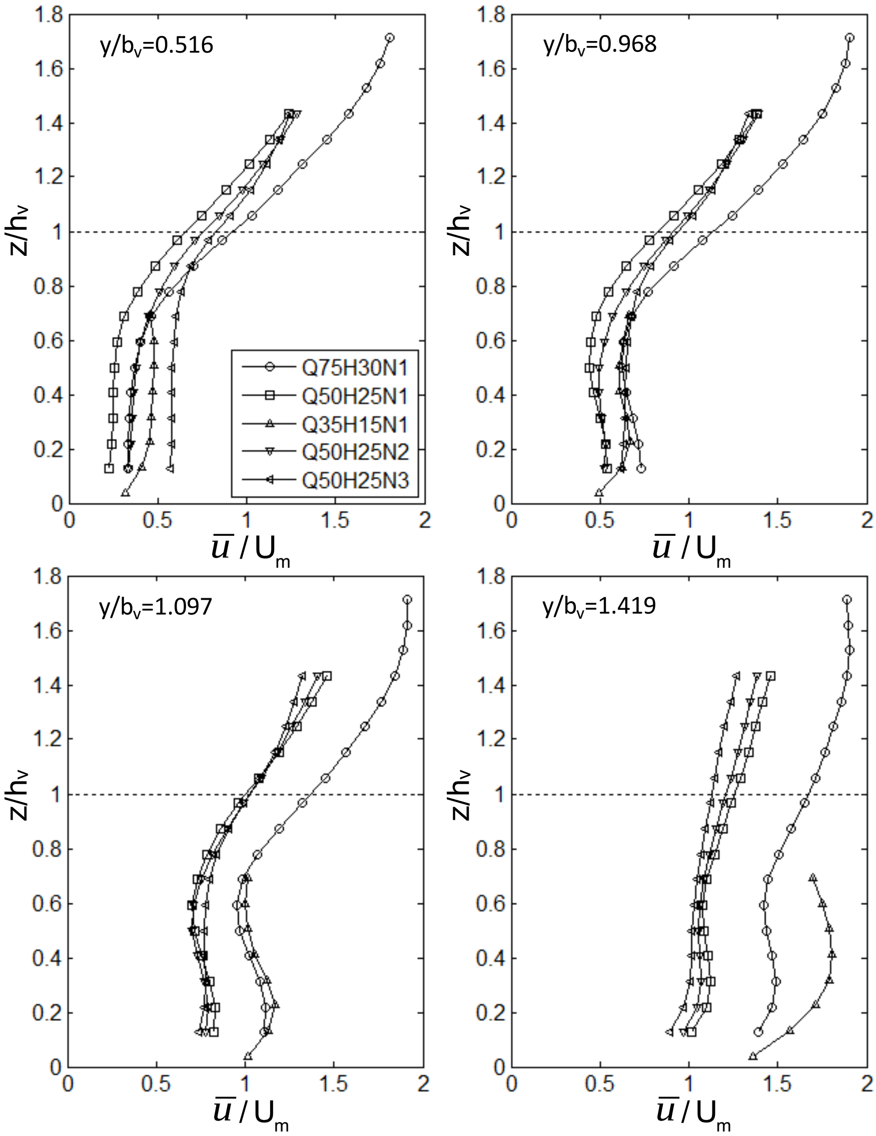

Figure 3.13 Velocity profiles of fully-developed flows at different transverse locations.

Vertical Reynolds stress $-\overline{u'w'}$

Figure 3.14 shows the vertical profile of $-\overline{u'w'}$ at different transverse locations under different flow-vegetation configurations. Again, in the VR the $-\overline{u'w'}$-profile takes after the pattern in FOCVC. $-\overline{u'w'}$ initially increases from a lower vertical location in the vegetation canopy and becomes maximum at the CTL, and then $-\overline{u'w'}$ decreases linearly toward the free surface. The $-\overline{u'w'}$-profile is well known to be induced by the generated vertical coherent vortices. The distance between the onset increase point and the CTL is referred to as the vertical momentum penetration length, which has been extensively explored in literatures (Ghisalberti, 2002; Ghisalberti and Nepf, 2006; Nepf and Vivoni, 2000). The effect of vegetation density on the vertical penetration length is shown to be not strong. This differs from the observation in Nepf et al. (2007) that the penetration length is inversely related to vegetation density ($\delta_e = \frac{0.23 \pm 0.06}{C_d a}$). The possible reason is also that partial redirection of the water flow toward the NOWR changes the characteristics of vertical penetration length. However, more experimental data under different flow-vegetation configurations in the POCVC should be provided to confirm this variation. The submergence status of vegetation canopy determines the pattern of the $-\overline{u'w'}$-profile. Negligible $-\overline{u'w'}$ is observed for the emergent canopy. For the submerged canopy, it can be noted that larger water depth leads to larger vertical penetration length (Q75H30N1), which is consistent with the observation in Nepf and Vivoni (2000).

In the junction, the similar pattern of the $-\overline{u'w'}$-profile can be seen on the inner side. However, $-\overline{u'w'}$ becomes negative in the near-bed region, which is coincident with the deflection of the $\bar{u}$-profile in the same region. From the viewpoint of physics, $-\overline{u'w'}$ being negative indicates the momentum transport from the lower layer to the upper by turbulence. As known, the momentum transfer is always from the high-speed flow to the low-speed flow. Thus it is reasonable that the deflection of the $\bar{u}$-profile and the negativity of the $-\overline{u'w'}$-profile occur in the same region, where horizontal coherent vortices are generated. Therefore, the distribution pattern of horizontal coherent vortices is inferred to be inherently related to the above abnormal longitudinal velocity and vertical Reynolds stress. The preliminary interpretation is that the generated horizontal coherent vortices transport the low momentum from the vegetation canopy to the neighboring open water, resulting in the reduction of flow velocity. Also, the negativity of the $-\overline{u'w'}$-profile is seen to be enhanced the vegetation density. As the vertical distance increases, $-\overline{u'w'}$ becomes zero for the emergent canopies, while becomes positive and peaks at z/h_v=1for the submerged canopies. This reflects the vertical turbulent flow mixing from significant flow shear at the vegetation top can be diffused toward the NOWR and maintain the relatively same intensity in the VR.

In the NOWR, the negativity of $-\overline{u'w'}$ in the near-bed region disappears. Owing to the absence of vegetation canopy, $-\overline{u'w'}$ obviously decays and the downward-shift maximum of the $-\overline{u'w'}$-profile indicates the decayed vortices might shift close to the bed.

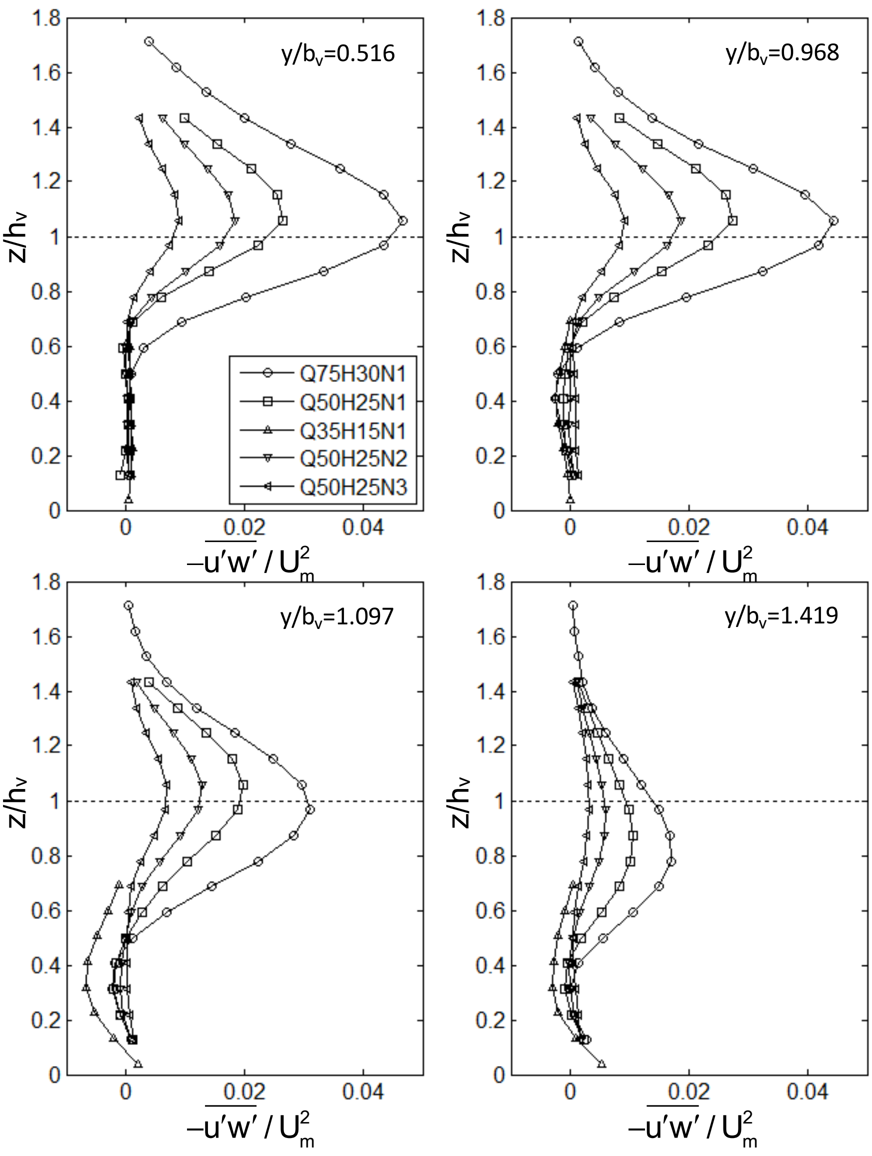

Figure 3.14 Vertical Reynolds stress of fully-developed flows at different transverse locations.

Transverse Reynolds stress $-\overline{u'v'}$

Figure 3.15 shows the vertical profile of $-\overline{u'v'}$ at different transverse cross-sections. $-\overline{u'v'}$ remains roughly zero in the entire water depth in the VR, while $-\overline{u'v'}$ becomes pronounced below the CTL In the junction indicating significant momentum exchange in the transverse direction driven by the generated horizontal coherent vortices. A remarkable increase of $-\overline{u'v'}$ can be observed in the near-bed region. Importantly, such increase directly suggests the growth of horizontal coherent vortices above the bed. In another word, the existence of bed tends to inhibit the generation of horizontal coherent vortices in spite of flow still sheared in the near-bed region. The maximum of $-\overline{u'v'}$ is observed to be vertically maintained for a while. Then decrease happens below the CTL and continues toward the free surface. In the NOWR, the $-\overline{u'v'}$-profile takes after its counterpart in the junction, while the magnitude obviously decreases. As expected, the vegetation density strongly affects the magnitude of $-\overline{u'v'}$ (Q50H25N1, Q50H25N2 and Q50H25N3). It can be observed that the larger vegetation density leads to the larger magnitude. However, It is also observed that the decrease onset location of the $-\overline{u'v'}$-profile occurs at lower water level under larger vegetation density.

The concept that the bed plays an inhabited role in the generation of horizontal coherent vortices can be found in other literature. Theoretically, Ghidaoui and Kolyshkin (1999) analyzed flow instability in the compound channel and de Lima and Izumi (2013) analyzed the flow instability in the POCVC. Both studies show that a bed resistance parameter accounting for the flow shallowness and bed roughness inhibits the generation of horizontal coherent vortices. This concept is of such importance that the turbulence in the junction becomes highly anisotropic. It suggests that the isotropic turbulence model might not be suitable for the modeling of flow characteristics at this region. Also, this finding shows the direction for improving numerical models to reasonably describe the turbulence pattern in this region.

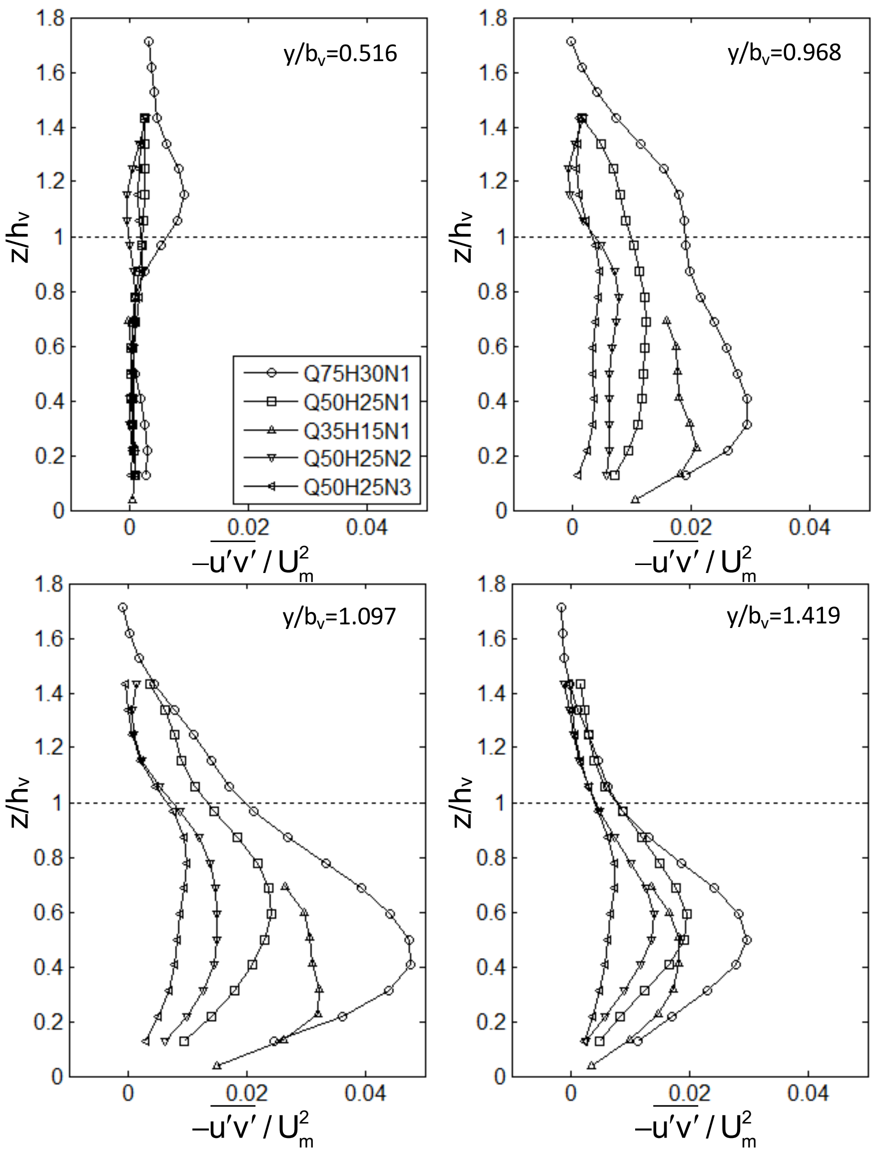

Figure 3.15 $-\overline{u'v'}$-profile for fully-developed flows at different transverse locations.

Turbulent kinetic energy TKE

Now, we know that significant turbulent activities occur at the top and lateral edge of the vegetation canopy. It is worth seeing the distribution of TKE indicating the overall effect of those turbulence activities. Figure 3.16 shows the TKE-profile at different transverse locations. In the VR, TKE becomes very small far below the CTL since its source is mainly from the wake of individual vegetation stems. Its maximum occurs at the CTL and then it continuously decreases above the CTL. The TKE-profile is similar to the $-\overline{u'w'}$-profile, since their contributors are all the vertical coherent vortices. In the outer-side junction, TKE becomes pronounced below the CTL owing to the contribution of the horizontal coherent vortices. It is found that its global maximum is reached below the CTL in the canopy corner region, suggesting the existing the most dramatic energy exchange due to the presence of vegetation canopy. Also, it is shown that the bed inhibits the growth of TKE in the near-bed region. Unlike the $-\overline{u'v'}$-profile, the TKE-profile remains a large magnitude below the CTL. This is because TKE arising from the vertical coherent vortices contributes to total TKE. In the NOWR, TKE decreases as well while its profile is still similar to that in the outer-side junction.

The increase in vegetation density, on one hand, enhances both vertical and horizontal coherent vortices, resulting in pronounced TKE at the top and lateral edge of vegetation canopy. On the other hand, increasing vegetation density leads to the decrease in TKE deep inside the canopy, where TKE under the smallest vegetation density (Q50H25N3) obviously exceeds TKE under the other two vegetation densities (Q50H25N1 and Q50H25N2). A possible reason is that closer spacing inhibits the development of vegetation stem wake.

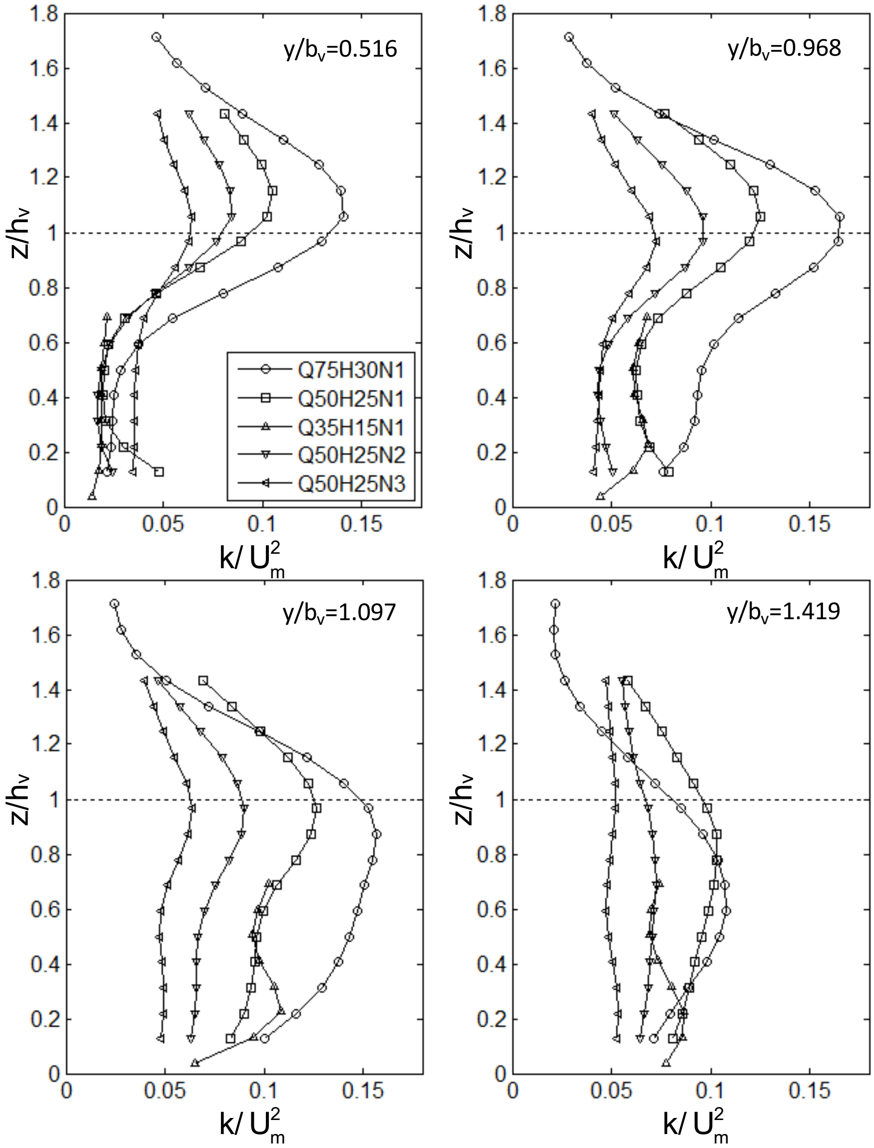

Figure 3.16 TKE of fully-developed flows at different transverse locations.

3.3.3.2 Contour of flow characteristics for fully-vegetated flow

Figure 3.17 shows the mean longitudinal velocity for different flow configurations. Expectedly, the smallest velocity zone occurs deep inside vegetation canopy for all flow configurations. In comparison, the largest velocity zone occurs at the corner of the open water region, which is farthest from the vegetation canopy. Exception can be observed for the smallest density of vegetation canopy (Q50H25N3). The largest velocity zone is right above the open channel bed. This might be a result of reduced flow resistance due to reduced vegetation density.

For submerged canopies, it is clear that above the CTL the isoline density is larger in the vertical direction, while in the outer-side junction the isoline density is larger in the transverse direction. In the near-bed region of junction, a clear bulge of velocity isoline can be observed for all cases except for the smallest vegetation density (Q50H25N3). The velocity bulge indicates a smaller velocity in the upper-layer than the lower-layer which is equivalent to the velocity deflection of the $\bar{u}$ -profile. The velocity bulge is spanning to the NOWR. Vegetation density has a critical impact on the behavior of the velocity bulge. Specifically, larger vegetation density positively contributes to the degree of the velocity bulge. The extreme case is that the smallest vegetation density nearly fails to produce the velocity bulge

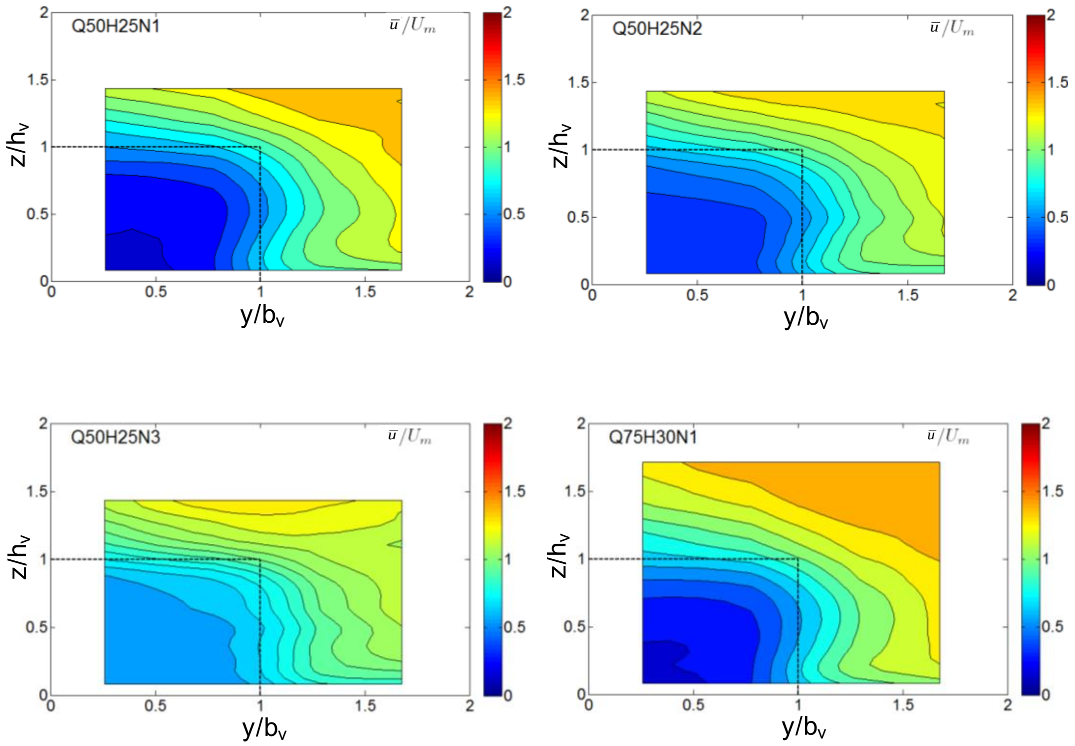

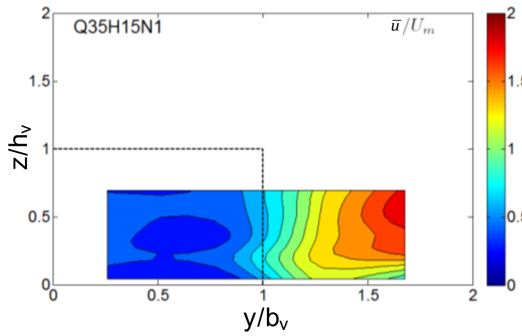

Figure 3.17 Contour of longitudinal velocity of the fully-developed flow

Figure 3.18 shows the contour of $-\overline{u'w'}$ for different flow configurations. It is clearly observed that the maximum core of $-\overline{u'w'}$ occurs above vegetation top for the submerged vegetation, which indicates the strongest momentum exchange and flow mixing. For the emergent canopy, no apparent $-\overline{u'w'}$ is produced in the entire cross section.

The maximum of $-\overline{u'w'}$ is near the canopy corner (e.g., y/b_v=0.75) rather than the center of canopy top (e.g., y/b_v=0.5). The behavior is valid for all flow configurations. This is probably because flow shear gradient in the vertical direction is the greatest in that region. The larger vegetation density can produce larger $-\overline{u'w'}$. Different water depths have no obvious impact on the pattern of $-\overline{u'w'}$ except that larger water depth might lead to a deeper penetration into vegetation canopy. A small but negative zone of $-\overline{u'w'}$ occurs in the near-bed region of outer-side junction. As vegetation density becomes smaller (Q50H25N3), the negative zone disappears as the velocity bulge disappears. The interpretation of negative $-\overline{u'w'}$ has been elaborated and can be referred to the last section.

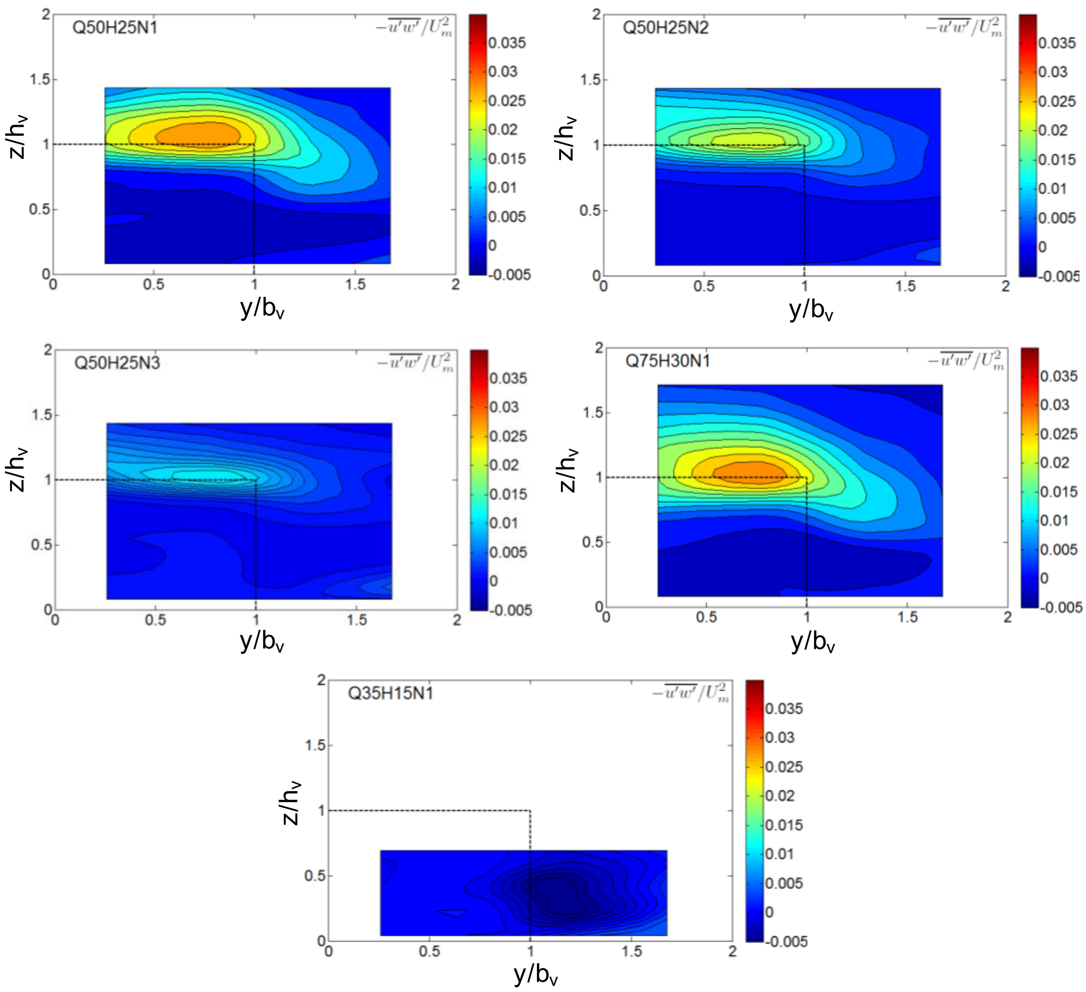

Figure 3.18 Contour of vertical Reynolds stress of the fully-developed flow

Due to flow shear at the lateral edge of vegetation canopy, transverse Reynolds stress ($-\overline{u'v'}$) is produced, which drives the transverse exchange of momentum between VR and NOWR. Figure 3.19 shows the contour of $-\overline{u'v'}$ for different flow configurations. Unlike $-\overline{u'w'}$ peaking right at the canopy top, the maximum core of $-\overline{u'v'}$ is shifted to the NOWR rather than the lateral edge. The shift of $-\overline{u'v'}$ in the present study is consistent with observation of Meftah et al. (2014) who provided negative evidence for the conventional presentation of Reynolds stresses peaking at canopy edges. This suggests the inflection point of the transverse flow velocity profile might be shifted to the NOWR, since the inflection point of the flow velocity profile is coincident with the maximum Reynolds stress. This finding is significant in the theoretical analysis of velocity profile in the transverse direction, since with the present finding it is uncertain that previous literatures derives the theoretical transverse flow velocity profile with the treatment of inflection point at the lateral edge of vegetation canopy.

Vegetation density clearly has an essential impact on the pattern of $-\overline{u'v'}$. Larger density can produce larger $-\overline{u'v'}$. Moreover, it is noted that the maximum core of $-\overline{u'v'}$ rises to the layer of the vegetation canopy corner under the smallest vegetation density.

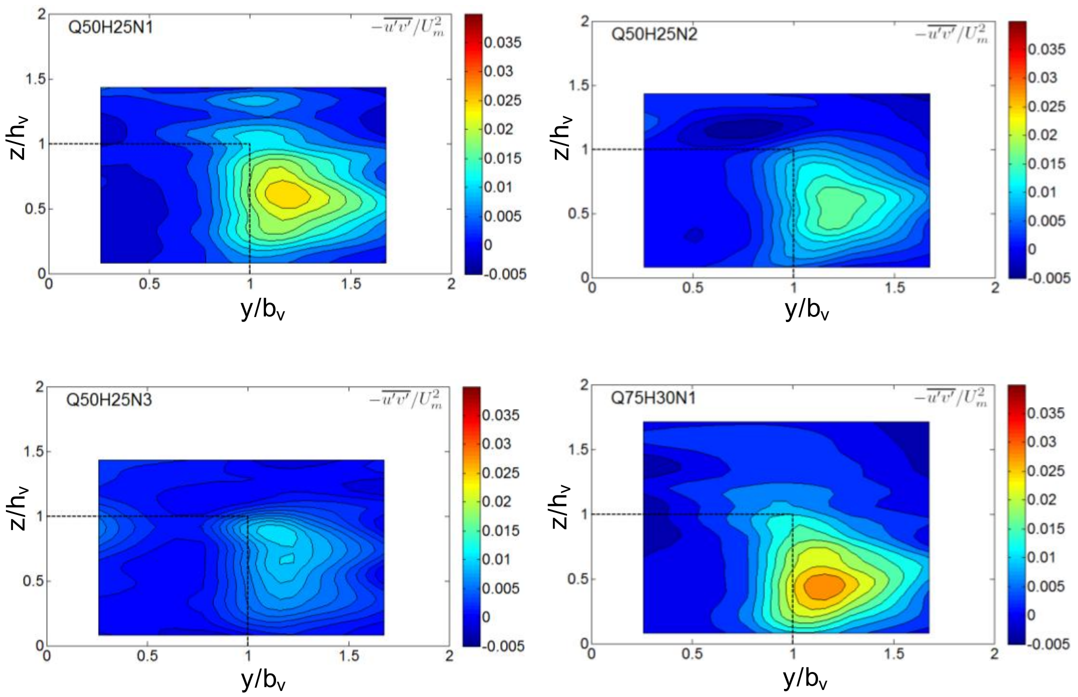

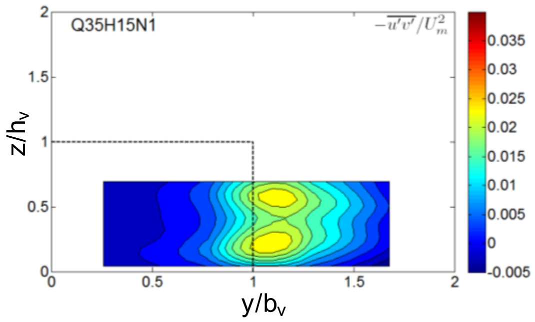

Figure 3.19 Contour of transverse Reynolds stress of the fully-developed flow

Figure 3.20 shows contour of TKE. As understood, the combination of the vertical and horizontal coherent vortices contributes the pattern of TKE. Deep inside vegetation canopy TKE is negligible. The maximum core of TKE occurs at edges of vegetation canopy. Vegetation density is shown to have a significant impact on the pattern of TKE. For the largest vegetation density (Q50H25N1), TKE peaks nearly right at the canopy corner, indicating the comparable intensity of the vertical and horizontal coherent vortices. This can be confirmed by the distribution of Reynolds stresses (see Figure 3.18 and Figure 3.19). As vegetation density decreases, the maximum core of TKE gradually shifts toward the canopy top (y/b_v<1).

For the largest submergence ratio (Q75H30N1), although the normalized TKE is relatively small due to the large normalization factor (U_m), the maximum core of TKE shifts toward the side of VR, suggesting the generated vertical coherent vortices more intensive than the generated horizontal coherent vortices. Submergence ratio, therefore, can benefit the development of vertical coherent vortices. For the emergent canopy, the maximum core of TKE occurs next to the lateral edge of canopy as no vertical coherent vortices are generated in this case.

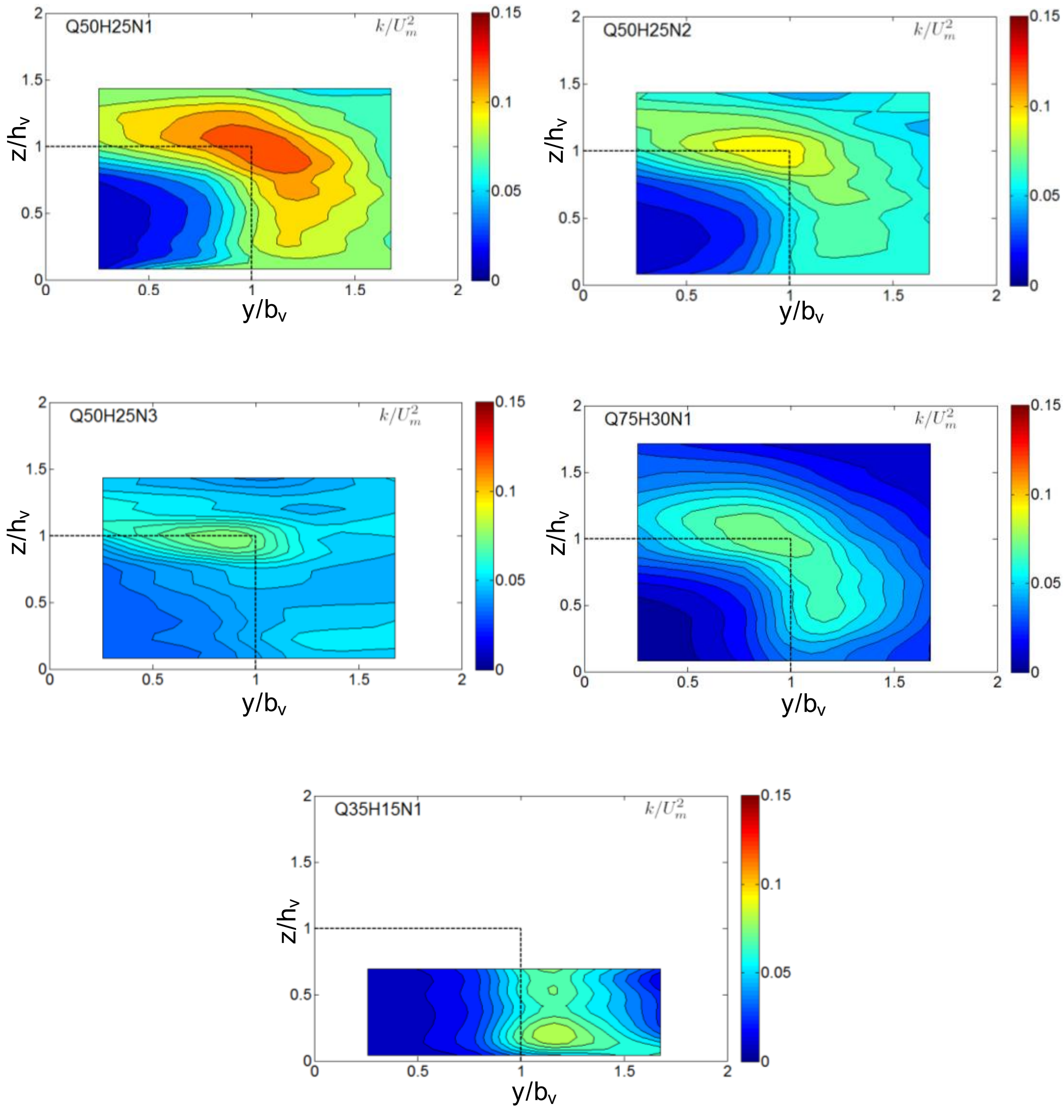

Figure 3.20 Contour of TKE of the fully-developed flow

3.3.2.3 Eddy viscosity

For isotropic or weakly-anisotropic turbulence, eddy viscosity is normally regarded as the scalar and should be equivalent according to Eq.3.5 and Eq.3.7, since the variation of eddy viscosity has no significant effect on flow in the other dimension. This physical consideration is feasible to those flows that large-scale vortices are not generated, and can be found in various Reynolds averaging models such as the Allmurus-Spalart model and the *k*-*ε* model (López and García, 2001; Li and Zeng, 2009; Spalart and Allmaras, 1992). However, in regard to the strongly-anisotropic turbulent flow such as flow around the cylinder or flow past the vegetation canopy in the present study, the single eddy viscosity treatment is non-satisfactory and of limitation in estimating the local exchange of turbulent momentum.

In the present study, vegetation canopy is partially distributed in the open channel. Coherent vortices are generated both in vertical and horizontal dimensions and span within the entire cross section, which enables a more sophisticated flow field. It is certainly more reliable that different vortices should be described by their own characteristic turbulence parameters.

Similar to the molecular diffusion, the mixing or diffusing effect of turbulent flow can be modeled by the eddy viscosity. The turbulent momentum flux represented by the Reynolds stress can be modeled with a linear relation according to the Boussinesq eddy viscosity assumption. Based on the mixing length theory, the mixing length is calculated as,

With respect to vertical Reynolds stress,

$$-\rho\overline{u'w'} = \rho\nu_t\left(\frac{\partial\overline{u}}{\partial z} + \frac{\partial\overline{w}}{\partial x}\right) \tag{3.5}$$

$$l_t = \left(\frac{\nu_t}{\partial\overline{u}/\partial z}\right)^{1/2} \tag{3.6}$$

With respect to transverse Reynolds stress

$$-\rho\overline{u'v'} = \rho\nu_t\left(\frac{\partial\overline{u}}{\partial y} + \frac{\partial\overline{v}}{\partial x}\right) \tag{3.7}$$

$$l_t = \left(\frac{\nu_t}{\partial\overline{u} / \partial y}\right)^{1/2} \tag{3.8}$$

Since the flow is fully developed, theoretically the longitudinal derivative with respect to any variables should be zero (i.e., $\frac{\partial\overline{v}}{\partial x} = \frac{\partial\overline{w}}{\partial x} = 0$). Therefore, the eddy viscosity can be respectively calculated by vertical and transverse Reynolds stresses with the corresponding velocity gradients.

Figure 3.21 illustrates the vertical distribution of eddy viscosity according to Eq.3.5. The eddy viscosity is normalized by the production of water depth (*h*) and mean flow velocity (U_m). In the VR, it is clearly noted that ν_t/hU_m deep inside the vegetation canopy is negligible for the submerged canopy, but increases when approaching the CTL owing to the generation of horizontal coherent vortices. Its maximum can be observed above the CTL and a parabolic profile is formed, consequently. This is consistent with existing observations of flow past the submerged canopy (Nepf and Vivoni, 2000). So, the result that Ghisalberti and Nepf (2004) showed a constant eddy viscosity above the CTL might be debatable. The growth onset point of eddy viscosity is z/h_v=0.4-0.6, which is consistent with the vertical momentum penetration length. For the emergent canopy (Q35H15N1), the eddy viscosity is very small compared with its counterpart for the submerged canopy owing to the absence of vertical coherent vortices. In the NOWR, the pattern of ν_t/hU_m shows a similar manner to that in the VR. The exception is that the growth onset point shifts downward the lower layer. The shifting is more apparent for the largest vegetation density (Q50H25N1 and Q75H30N1). This manner is consistent with the vertical penetration length observed in the $-\overline{u'w'}$-profile, which indicates the vertical coherent vortices shifting downward owing to the absence of the vegetation canopy. It is interestingly noted that, with the normalization of hU_m, the eddy viscosity can collapse into a universe curve roughly. This observation might be useful for the theoretical derivation of the longitudinal velocity.

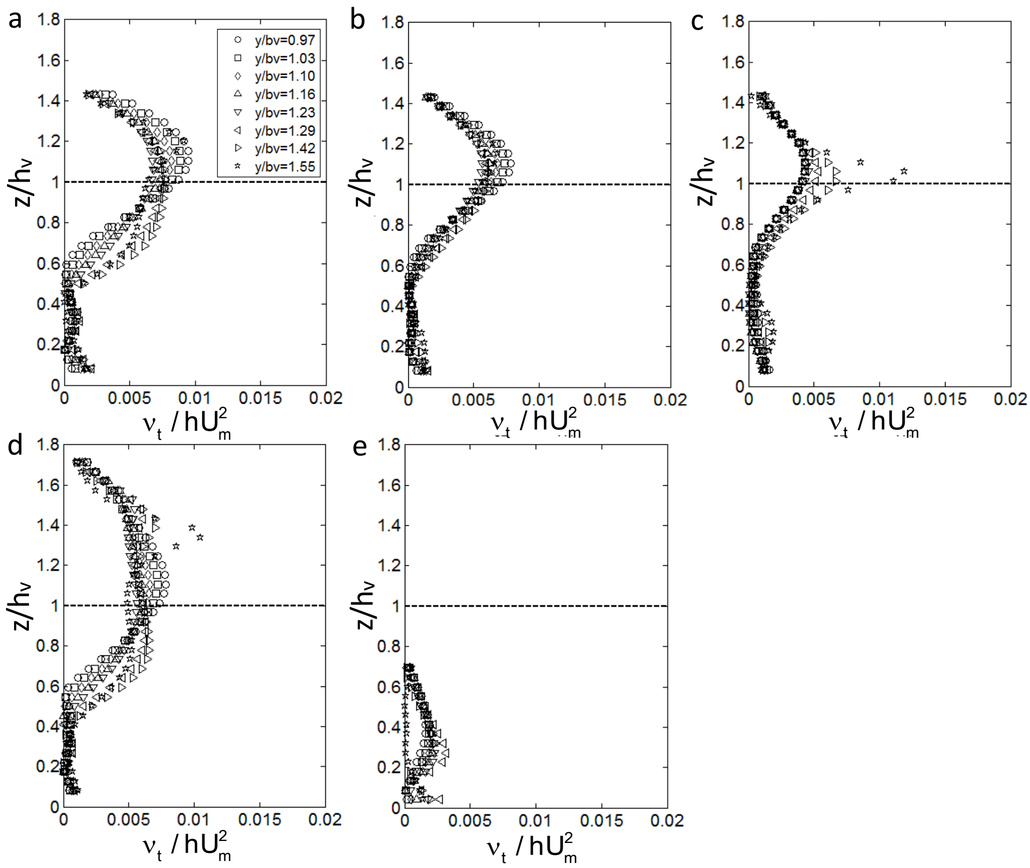

Figure 3.21 Vertical profiles of eddy viscosity derived from Eq.3.5 at different transverse locations. (a) Q50H25N1, (b) Q50H25N2, (c) Q50H25N3, (d) Q50H25N1

and (e) Q50H25N1.

Figure 3.22 illustrates the vertical distribution of ν_t / hU_m calculated by Eq.3.7. The eddy viscosity is related to the generated horizontal coherent vortices, reflecting the flow mixing effect in the transverse direction. Above the channel bed, the eddy viscosity sharply increases as the vertical distance increases. This suggests that the resistance effect of bed essentially suppresses the flow mixing in the horizontal dimension in the near-bed region. With a development distance over the bed, eddy viscosity reaches the maximum and remains a large value below the CTL. This indicates that the flow mixing effect induced by horizontal coherent vortices becomes most pronounced. Then ν_t / hU_m decreases toward the CTL and the decrease onset point tends to rise toward the CTL with the decrease in vegetation density. The normalized ν_t-profile takes after the normalized $-\overline{u'v'}$-profile with the occurrence of the most pronounced horizontal flow mixing in the junction region. In addition, it is clear that the vegetation density can enhance flow mixing.

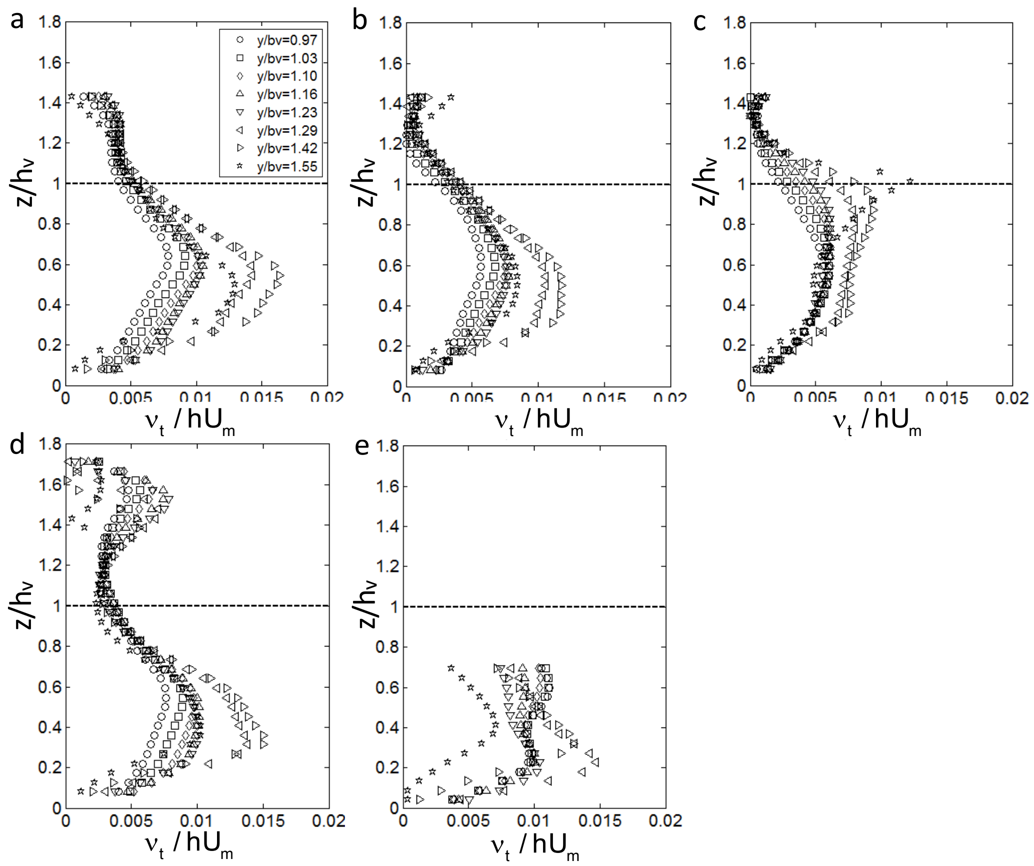

Figure 3.22 Vertical profiles of eddy viscosity derived from Eq.3.7 at different transverse locations. (a) Q50H25N1, (b) Q50H25N2, (c) Q50H25N3, (d) Q50H25N1 and (e) Q50H25N1.

3.3.4 Budget of TKE

The proceeding sections of this chapter describe that three-dimensional flow characteristics in the POCVC fairly differ from those in the FOCVC. Meanwhile, the description of depth-averaging concept arising from the shallow water assumption in the POCVC seems so simplified that the associated prediction might be inaccurate for understanding flow through near-bank or riparian vegetation canopies. The most impressive example is that the vertical profile of longitudinal velocity is deflected in the near-bed region of the outer-side junction.

TKE is an important fundamental parameter for describing flow turbulence. For the fully-developed flow, TKE performs in the process of dynamic equilibrium and is balanced by various characteristic physical processes. For vegetated flows, those processes include shear production, wake production, turbulent transport, pressure transport and turbulent dissipation. Assuming flow being fully-developed, the transport of TKE can be approximately described by equations as below,

$$\frac{Dk}{Dt} = 0 = P_{sy} + P_{sz} + P_w + T_{ty} + T_{tz} + T_p + \varepsilon \tag{3.9}$$

$$\text{Shear production} = P_{sy} + P_{sz} = \overline{u'v'}\frac{\partial \overline{u}}{\partial y} + \overline{u'w'}\frac{\partial \overline{u}}{\partial z} \tag{3.10}$$

$$\text{Wake production} = P_w = \frac{1}{2} C_d N \overline{u}^3 \tag{3.11}$$

$$\text{Turbulent transport} = T_{ty} + T_{tz} = -\frac{\partial \overline{kv'}}{\partial y} - \frac{\partial \overline{kw'}}{\partial z} \tag{3.12}$$

$$\text{Pressure transport} = T_p = -\frac{1}{\rho}\left(\frac{\partial \overline{p'u'}}{\partial x} + \frac{\partial \overline{p'v'}}{\partial y} + \frac{\partial \overline{p'w'}}{\partial z} \right) \tag{3.13}$$

$$\text{Viscous dissipation} = \varepsilon = -\nu_t \begin{pmatrix} \overline{\left(\frac{\partial u'}{\partial x}\right)^2} + \overline{\left(\frac{\partial v'}{\partial x}\right)^2} + \overline{\left(\frac{\partial w'}{\partial x}\right)^2} + \overline{\left(\frac{\partial u'}{\partial y}\right)^2} + \overline{\left(\frac{\partial v'}{\partial y}\right)^2} \\ + \overline{\left(\frac{\partial w'}{\partial y}\right)^2} + \overline{\left(\frac{\partial u'}{\partial z}\right)^2} + \overline{\left(\frac{\partial v'}{\partial z}\right)^2} + \overline{\left(\frac{\partial w'}{\partial z}\right)^2} \end{pmatrix} \tag{3.14}$$

In the POCVC, shear production should be divided into transverse-shear production and vertical-shear production due to the generation of vertical and horizontal coherent vortices (Eq.3.10). The wake production is induced by flow around vegetation stems, and thus is only applicable within the vegetation canopy. The physical interpretation of wake production is the work done by turbulence against drag elements and cannot be measured. Accordingly, the wake production is approximately related to the drag and mean velocity (Nepf and Vivoni, 2000; Raupach et al., 1986). Similarly, the turbulent transport can be divided into the transverse and vertical components due to horizontal vertical coherent vortices (Eq.3.12). The definition of viscous dissipation is also complicated. It is extremely sensitive to the turbulent velocity gradient. The disturbance during measurements might lead to significant error. In order to avoid the uncertainty of measurements, the viscous dissipation is calculated in an alternative way as below (Nepf and Vivoni, 2000),

$$S_{uu} = A\frac{18}{55}\varepsilon^{2/3}\left(\frac{U}{2\pi}\right)^{2/3} f^{-5/3} \tag{3.15}$$

where $A \approx 1.5$ is a constant. The viscous dissipation can be determined by fitting spectra of the longitudinal velocity in the inertial subrange. Due to difficulties in direct measurement, pressure transport is herein estimated as the residual of other total terms,

$$T_p \approx R = -(P_{sy} + P_{sz} + P_w + T_{ty} + T_{tz} + \varepsilon) \tag{3.16}$$

Figure 3.23 shows different components contributing to TKE in the VR (y/b_v=0.516).

In this region flow generally performs in a similar way to that in the FOCVC as demonstrated earlier on. It is clear that transverse-shear production ($P_{sy}h/U_m^3$) is negligible along the vertical for all cases, corresponding to the negligible transverse turbulent transport ($T_{ty}h/U_m^3$). This indicates that horizontal coherent vortices hardly affect flow in the VR far away from the junction. Further, the production of TKE almost all arises from the vertical-shear production ($P_{sz}h/U_m^3$) near the CTL and the wake production P_wh/U_m^3 due to flow around vegetation stems. This is consistent with the observation by Nepf and Vivoni (2000) studying flow in the FOCVC. Farther below the CTL, the main production is contributed by P_wh/U_m^3. It can be noticed that smaller vegetation density leads to larger P_wh/U_m^3. The possible cause is that dense vegetation stems might inhibit the development of stem wake. Both $P_{sz}h/U_m^3$ and P_wh/U_m^3 increase and are comparable. In addition, as the vertical distance from the bed increases, denser vegetation density leads to greater growth of the above two terms. However, vegetation density has negligible influence on the growth onset point of $P_{sz}h/U_m^3$. $T_{tz}h/U_m^3$ also contributes to TKE as a source role. At the CTL, $P_{sz}h/U_m^3$ nearly reaches the maximum while P_wh/U_m^3 becomes zero due to the disappearance of vegetation stems. Finally, Above the CTL, $P_{sz}h/U_m^3$ decreases continuously, while $T_{tz}h/U_m^3$ negatively contributes to TKE as a sink role. The dissipation $\varepsilon h/U_m^3$ is observed to partly balance the production. Particularly over the CTL the dissipation is significant against the significant vertical shear production. However, as vegetation density decreases, $\varepsilon h/U_m^3$ becomes significant in the VR, corresponding to the pronounced P_wh/U_m^3. Pressure transport T_ph/U_m^3 calculated as the residual of all other terms has the negative peak just below the CTL. Generally, $T_p h / U_m^3$ above the CTL positively contributes to total TKE.

Figure 3.24 shows different components contributing to TKE in the inner-side junction (y/b_v=0.903). $P_{sy} h / U_m^3$ becomes significant below the CTL due to the generation of horizontal coherent vortices. It increases from a very small value in the near-bed region to the maximum below z/h_v=0.4 and then decreases when approaching the CTL. $P_{sz} h / U_m^3$ is similar to its counterpart in the VR. $P_w h / U_m^3$ gets more pronounced and particularly at the canopy corner is almost two times of that at the CTL. The possible reason is that the velocity at the edge region is much larger than that in the VR, and the definition of wake production ($P_w = \frac{1}{2} C_d n \bar{u}^3$) simply indicates that the larger local velocity can lead to larger wake production. Though the negative $T_{ty} h / U_m^3$ is observable, turbulent transport is still dominated by $T_{tz} h / U_m^3$. Below the CTL the positive value as the source becomes weaker and is shifted downward. $\varepsilon h / U_m^3$ gradually becomes larger than that far below the CTL, but $T_p h / U_m^3$ with the negative value becomes noticeable.

In the outer-side junction (y/b_v=1.097), $P_{sy} h / U_m^3$ below the CTL clearly exceeds $P_{sz} h / U_m^3$ at the CTL owing to the generation of horizontal coherent vortices and absence of the vegetation canopy (see Figure 3.25). It is inferred that the generated horizontal coherent vortices might replace the partial effect of vegetation canopy on the transverse-shear production. Meanwhile, $P_w h / U_m^3$ becomes zero due to absence of vegetation stem wake. Therefore, TKE production in this region is contributed by the shear production in both the vertical and transverse directions. The turbulent transport is also significant in this region. Farther below the CTL, $T_y h / U_m^3$ is dominant to transport TKE to other regions. Near the CTL, $T_z h / U_m^3$ negatively contributes to TKE. The maximum of $\varepsilon h / U_m^3$ can be observed below the CTL comparable to the maximum over the CTL in the VR. The positive $T_p h / U_m^3$ shifts below the CTL indicating extra TKE added to this region by the hydraulic pressure.

Figure 3.26 shows different components of TKE in the NOWR (y/b_v=1.419), which is far away from the junction. All the forehead-mentioned components contributing to TKE dramatically decay. Particularly, the turbulent transport becomes negligible. The vertical distributions of longitudinal velocity and TKE in this region (see Figure 3.13 and Figure 3.17) support this behavior. However, the dissipation $\varepsilon h / U_m^3$ remains noticeable, particularly below the CTL where horizontal coherent vortices span across the channel. $T_p h / U_m^3$ becomes positive through the entire water depth.

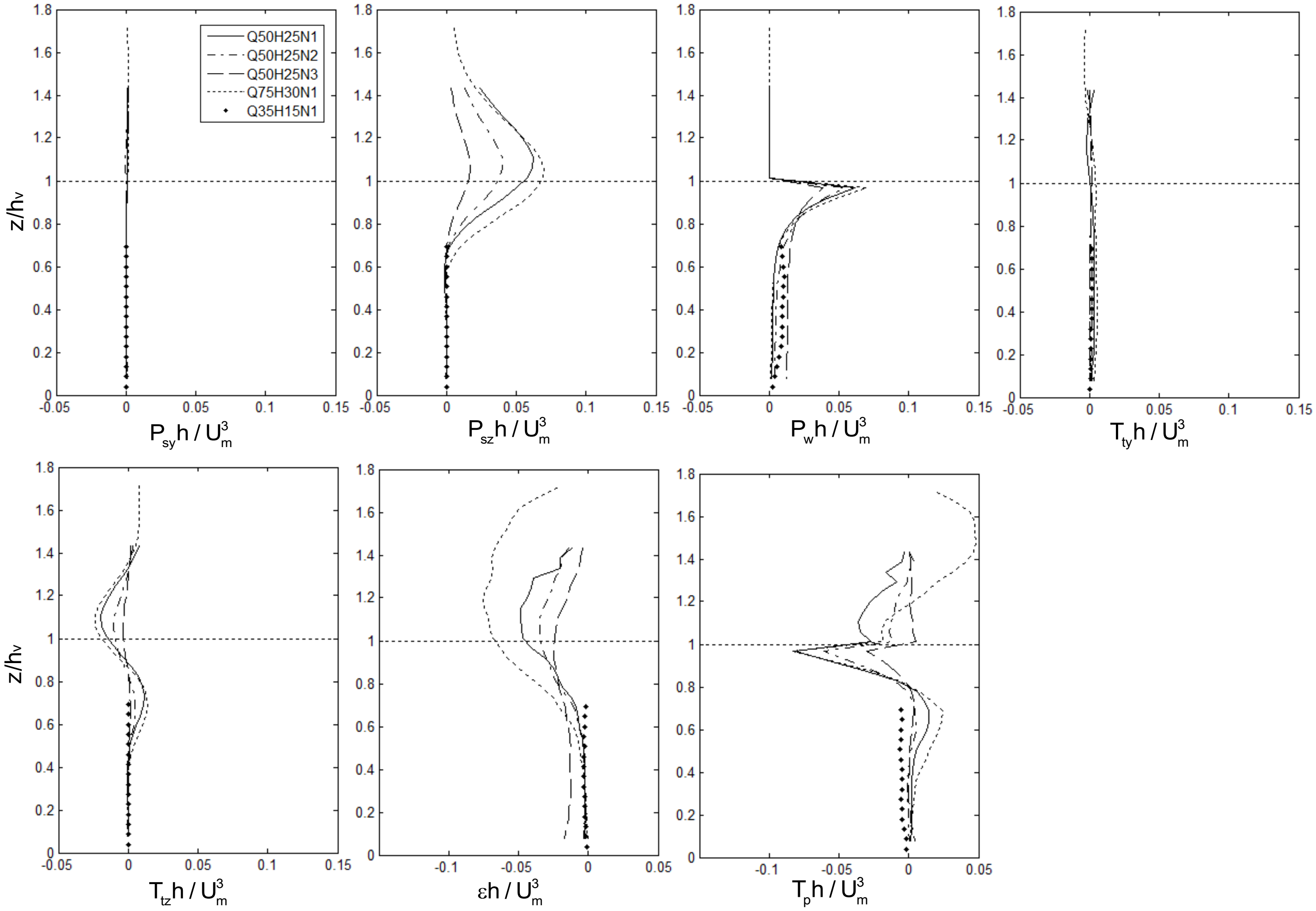

Figure 3.23 Components contributing to TKE in the VR (y/b_v=0.516)

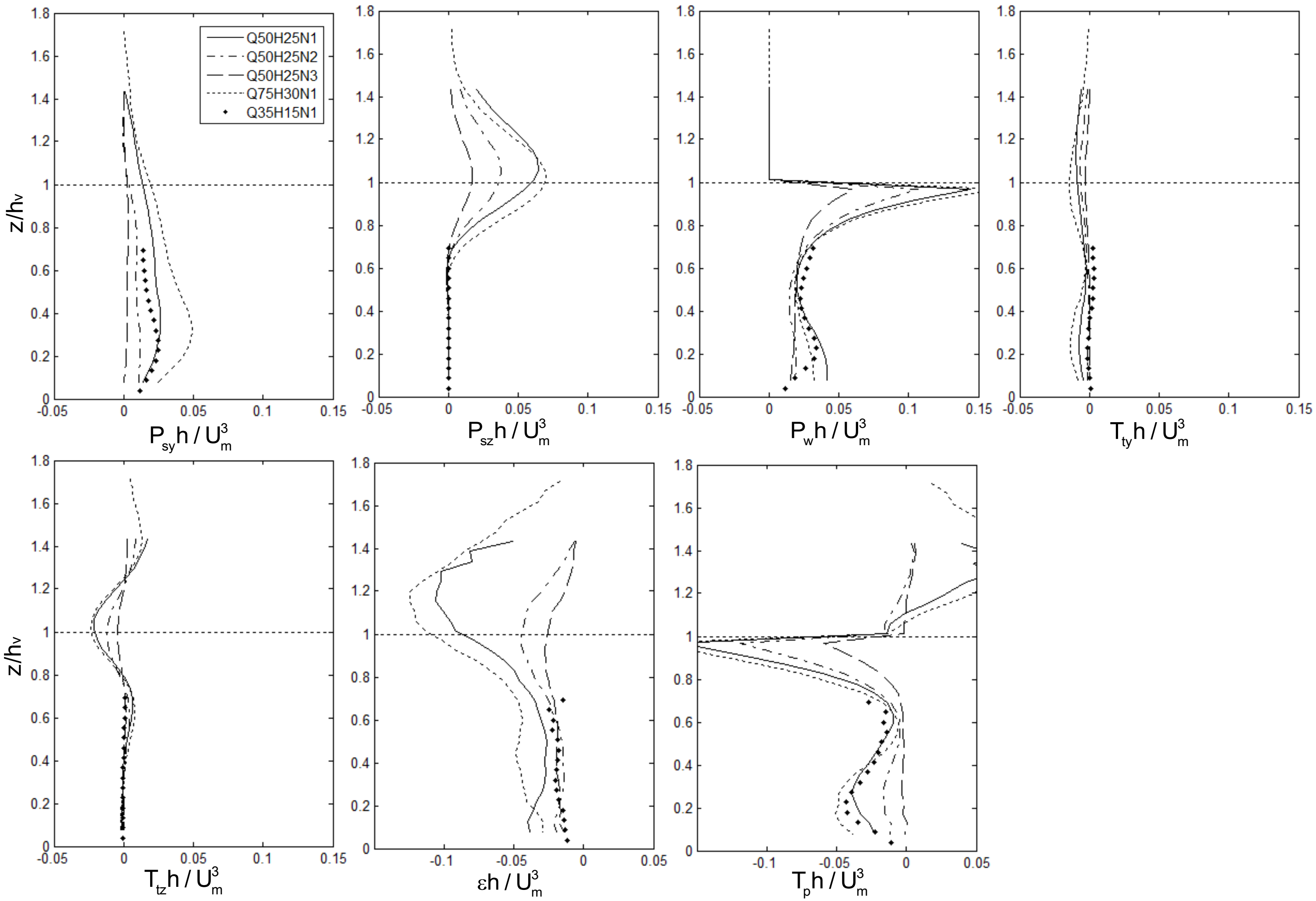

Figure 3.24 Components contributing to TKE in the inner-side junction (y/b_v=0.903)

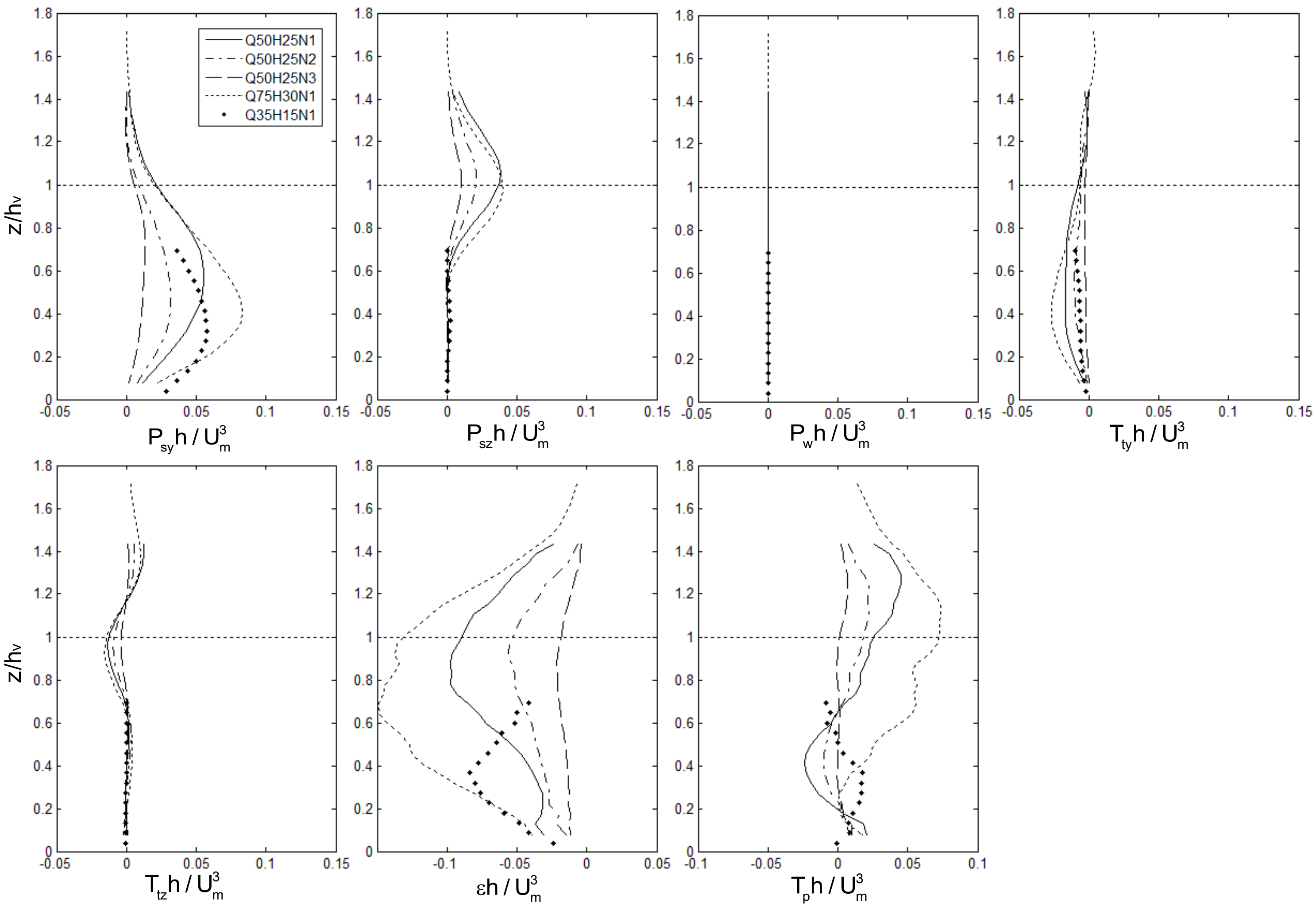

Figure 3.25 Components contributing to TKE in the outer-side junction (y/b_v=1.097).

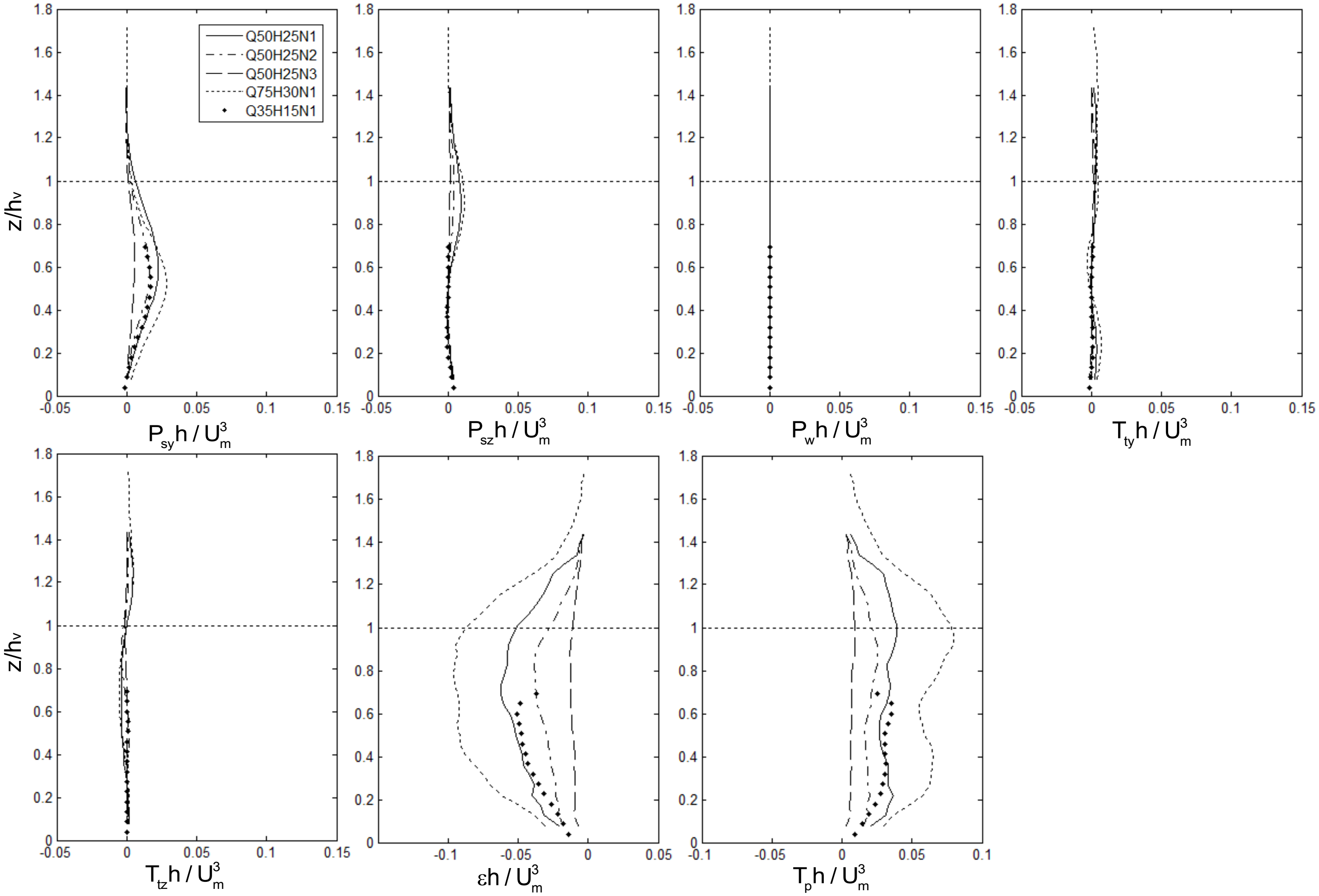

Figure 3.26 Components contributing to TKE in the NOWR (y/b_v=1.419)

3.3.5 Implications on hydrodynamic model for the partially-obstructed channel with vegetation canopy

When the vegetation canopy is partially distributed in the open channel, the interface(s) between the vegetation canopy and outer free water occurs at the edges of vegetation canopy (see Figure 3.27). This results in significant flow instability and subsequently large-scale coherent vortices generated against interfaces. For submerged canopies, two interfaces can be found, respectively, at the top and lateral edge. Vertical and horizontal coherent vortices, therefore, are generated at the top and lateral edge. Due to the generation of those coherent vortices, massive high-momentum flow from outer open water regions is transported into the vegetation canopy in the transverse direction and vertical direction. The physical process is dominated by the sweep event during the evolution of periodic large-scale vortices. Meanwhile, low-momentum flow inside the vegetation canopy is transferred into the outer open water region, which is dominated by the bursting event.

The behavior of mean flow and turbulence becomes particularly complicated in the junction. On one hand, the bed resistance plays a negative role in the development of horizontal coherent vortices. In the outer-side junction, both transverse Reynolds stress and TKE production increase from nothing at the bed to the maximum above the bed. In this subregion, due to the less significant influence of transverse momentum exchange, the flow behavior tends to comply with the wall-bounded theory (or logarithmic law). However, above the subregion, the low-momentum flow from the vegetation region is massively transported inside, leading to deflection of the vertical profile of longitudinal velocity and negativity in vertical Reynolds stress. It means that the high momentum at the lower layer with large velocity is transported to the upper layer with small velocity. As the vertical distance increases, vertical horizontal vortices begin to play an important role due to the penetration. The turbulent flow mixing leads to the vertical increase in longitudinal velocity in a remarkable gradient. As a consequence, a hyperbolic tangent profile of longitudinal velocity can form even though no vegetation canopy obstructs flow there.

On the other hand, the horizontal and vertical coherent vortices join at the canopy corner. According to the term-by-term analysis of transport equation of TKE, the vertical-shear production clearly reduces above the CTL owing to the absence of vegetation canopy, while the turbulent transport stands remarkably to feed the local TKE. But the noticeable value of vertical-shear production indicates that a source of flow shear still exists in that region. It is inferred that horizontal coherent vortices might act as an obstructive role like the vegetation canopy, leading to flow shear near the CTL between the upper high-speed flow and lower low-speed flow. The hyperbolic tangent profile of longitudinal velocity can be a strong evidence. Above the subregion, the transverse-shear production by horizontal coherent vortices tends to decrease as the vertical distance from bed increases. It is inferred that the open water above the CTL might lead horizontal coherent vortices to decay.

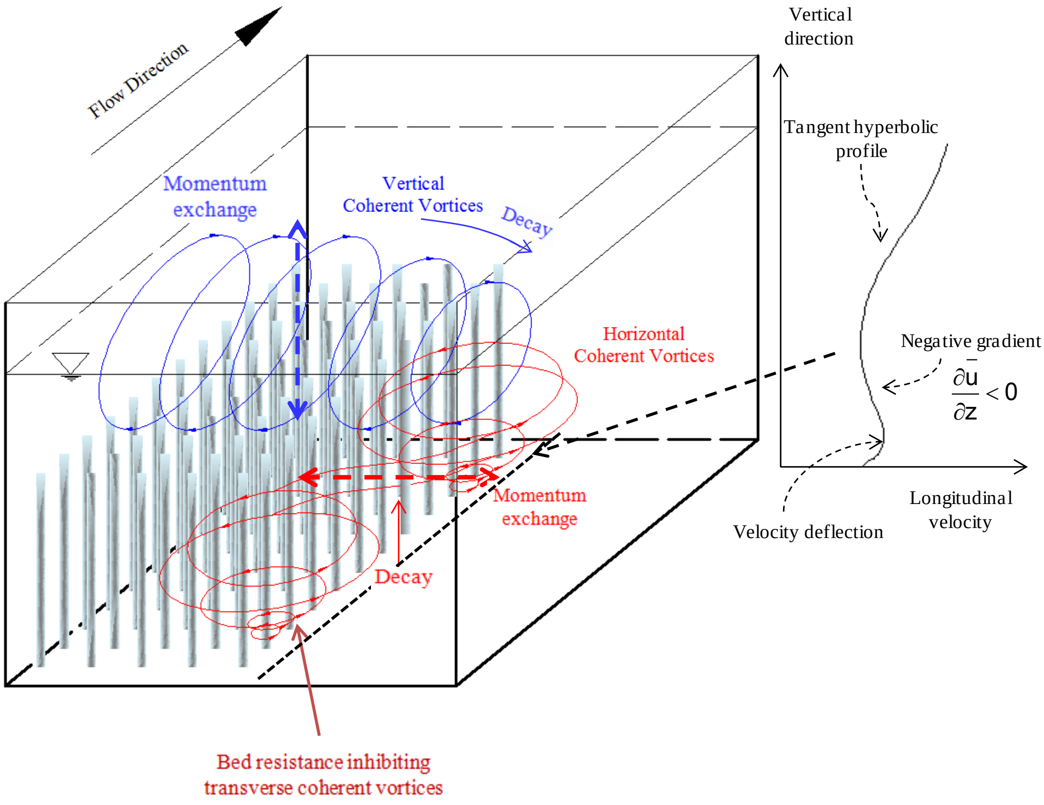

Figure 3.27 Hydrodynamic model describing flow and vortex structure in the POCVC

More qualitatively, In the outer-side junction (taking the example of y/b_v=1.161), as shown in Figure 3.28 the entire water depth can be divided into three subregions according to the vertical profile of longitudinal velocity including the wall subregion, the deflection subregion and the mixing subregion. Each subregion has the following properties.

1 Wall subregion

Vertical Reynolds stress is positive, and transverse Reynolds stress is relatively small, indicating that horizontal coherent vortices are little influential to the flow in this subregion. Thus the flow can be approximately treated as the (quasi) wall-bounded flow. The vertical profile of longitudinal velocity complies with the (quasi) logarithmic law.

2 Deflection subregion

Transverse Reynolds stress due to horizontal coherent vortices becomes pronounced (comparable to the maximum of vertical Reynolds stress). The low momentum is transported from the vegetation region to local flow with high momentum, leading to velocity deflection on the vertical profile. Thus the vertical velocity gradient becomes negative ($\partial \bar{u} / \partial z < 0$). Meanwhile, vertical Reynolds stress becomes negative ($-\overline{u'w'} < 0$).

3 Mixing subregion

Vertical coherent vortices become more important as vertical Reynolds stress becomes positive and increase with the increasing vertical distance, while horizontal coherent vortices become less important as transverse Reynolds stress decreases with the increasing vertical distance. The flow in the mixing subregion nearly complies with the turbulent mixing flow theory, the velocity profile of which might be described by the tangent hyperbolic curve.

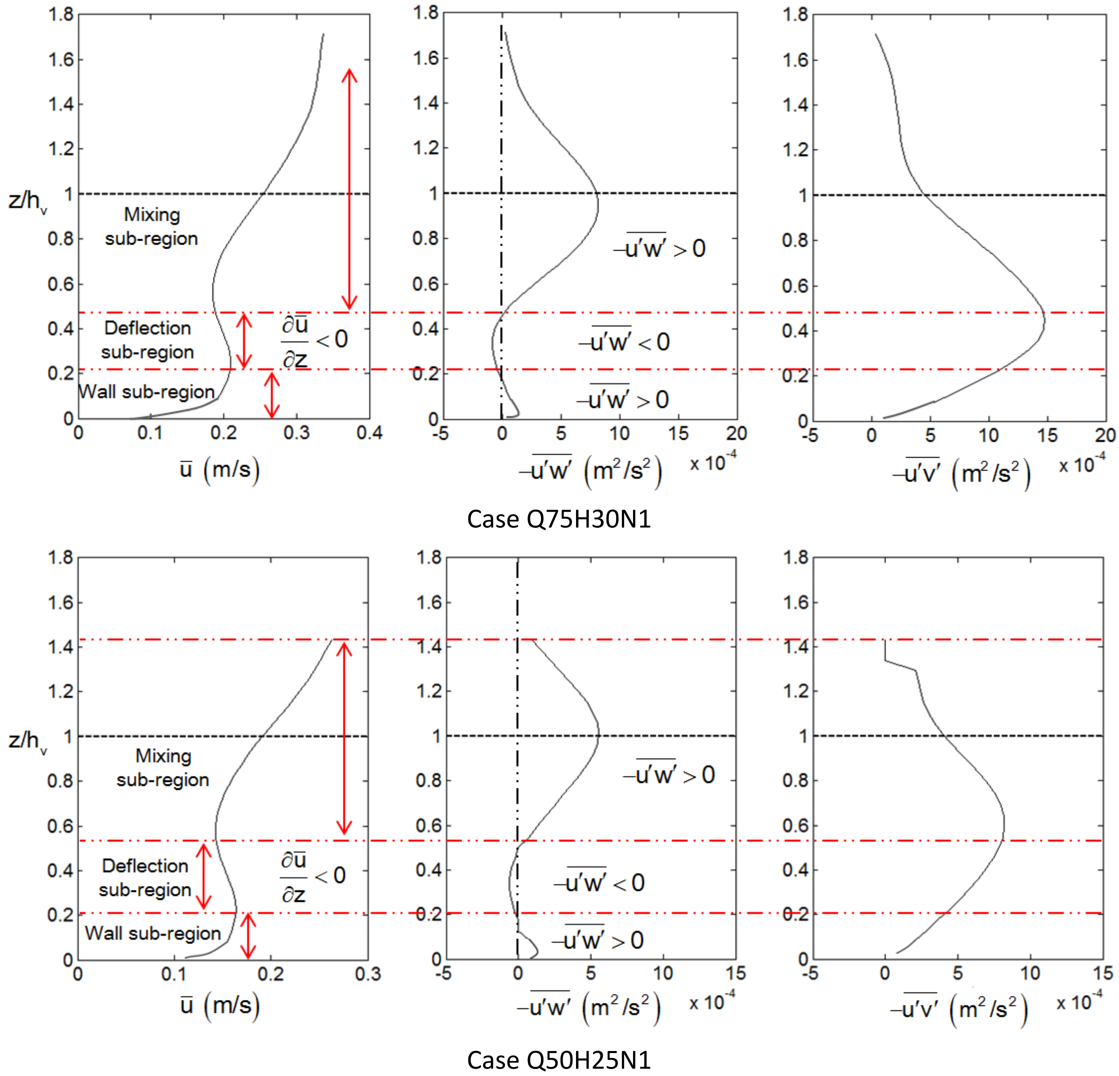

Figure 3.28 Subregions divided in the water depth in the outer-side junction (y/b_v=1.161).

3.4 Conclusions

In this chapter, the flow characteristics in the POCVC under various flow-vegetation configurations were investigated. The latest-generation acoustic Doppler velocimeter (ADV) profiler, namely Vectrino-II, was used to measure three-dimensional instantaneous velocities. Comparing with the traditional ADV, Vectrino-II has the high efficiency for its capability of detecting a vertical profiling. The measured data were refined by despiking technique and smoothing algorithm.

First, the flow adjustment in the POCVC was examined with the depth-averaged longitudinal velocity, longitudinal velocity, vertical Reynolds stress and transverse Reynolds stress. For the depth-averaged longitudinal velocity (U), the flow adjustment distance in the VR ($y/b_v \ll 1$) approximates 70% of canopy length ($0.7L_p$) under the same vegetation density. In the NOWR ($y/b_v \gg 1$), the flow adjustment distance is shortened in particular for the high-submergence canopy. Compared to the depth-averaged longitudinal velocity, the flow adjustment is also suitable for the adjustment of the vertical profile of longitudinal velocity ($\bar{u}$). However, for other turbulent properties such as vertical Reynolds stress ($-\overline{u'w'}$) and transverse Reynolds stress ($-\overline{u'v'}$), longer adjustment distance is required.

Second, the significant finding is that the vertical profile of longitudinal velocity is deflected below the CTL in the junction between the VR and the NOWR. As flow propagates downstream, the velocity profile below the CTL is gradually deflected and evolved to the S-shape curve for the submerged canopy. Correspondingly, vertical Reynolds stress is observed to be negative at the nearby region of velocity deflection. The velocity deflection and negativity in vertical Reynolds stress are suggested to be induced by the generation of horizontal coherent vortices. Essentially, the low-momentum flow from the vegetation canopy is transported into the neighboring open water in the junction. Meanwhile, the bed resistance plays a negative role in the generation of those horizontal coherent vortices, confirmed by that the growth of transverse Reynolds stress. With this new finding of the physical flow process in the POCVC, a hydrodynamic model is proposed for describing the vortex pattern rising from the flow-vegetation interaction in the POCVC, which can be used to better understand the particular generated flow characteristics.

Finally, TKE budget of fully-developed flow was evaluated term by term. The production and turbulent transport both in the vertical and transverse directions are taken into consideration. The result shows inside the deeper vegetation canopy TKE is only produced by the vegetation stem wake balanced by the combination of dissipation and pressure transport. The lower vegetation density is found to promote vegetation stem wake owing to the larger spacing for the wake development. Near the edges of vegetation canopy, the shear production due to the vertical and transverse coherent vortices positively contributes a large proportion together with the wake production (only inside the vegetation canopy). Apart from the energy dissipation and turbulent pressure transport, the turbulent transport negatively contributes to TKE. In the outer open water region farther away from the canopy edges, the pressure transport makes the major contribution to TKE, which is accordingly balanced by the viscous dissipation.

Chapter 4 3D Numerical Simulation of Flow in the Partially-obstructed Channel with Vegetation Canopy

4.1 Introduction

To date, numerous numerical simulations have been carried out to study flow in fully-obstructed channels with vegetation canopy (FOCVC). López and García (2001) incorporated the vegetation canopy into a sink vegetative drag term and employed both 1D k-ε model and 1D k-ω model to simulate the mean flow and turbulence characteristics of a fully-developed flow. Choi and Kang (2004) compared the abilities of the k-ε model, algebraic stress model (ASM) and Reynolds stress model (RSM) in simulating the flow and turbulence characteristics. They found that RSM with high computational expense can give more accurate and detailed flow information such as flow velocity and Reynolds stresses due to the anisotropic nature of the model. Using large-eddy the simulation (LES) model, Xie et al. (2008) treated vegetation resistance as the drag force as a sink and successfully produced vertical coherent vortices, while Stoesser et al. (2010) established adequately fine grids between individual vegetation stems of an emergent canopy to simulate flow structure and a small-scale eddy field. Both methods achieved acceptable results, but the latter requires extraordinary computational effort to solving the many linear equations on the established tremendous grids.

Effort has also been made to study partially-distributed channels with vegetation canopies (POCVC). Xiaohui and Li (2002) used LES to simulate flow through the emergent canopy. Choi and Kang (2006) presented a three-dimensional modeling of flow through the submerged canopy, using RSM. Huai et al. (2015) built a computational domain with numerous grids to create a rectangular emergent canopy patch with LES. The depth-averaged flow information was developed in the analysis from a comparison of existing experimental work.

The Spalart-Allmaras (SA) model has been adopted to simulate water current and wave through an aquatic vegetation canopy for years. Li and Zeng (2009) using the SA model, investigated the effect of an emergent canopy patch added in a T-junction confluence and quantitatively predicted the trend of increasing water discharge in the branch channel with an increase in branch channel width and/or the decrease in vegetation density. Zeng and Li (2013) employed the SA model to simulate flow past a finite vegetation patch. It was found that the one-equation SA model can effectively save computational time and that the nature of characteristic turbulence length in the SA model well characterized the vertical turbulent flow mixing.

Previous studies have not presented particular flow characteristics such as velocity deflection and negative vertical Reynolds stress in the near-bed region in the junction of POCVC, where the vortex pattern is highly anisotropic and complex. It is uncertain whether numerical models, particularly the SA model, can simulate such flow characteristics. The effects of vertical and horizontal coherent vortices and vegetation wake were taken into account. In this chapter, based on experimental observations in Chapter 3, a description of an attempt to improve the standard SA model is attempted so that those flow characteristics observed in the POCVC can be effectively produced. After validation, further numerical experiments are conducted to study effects of the different flow-vegetation configurations on water flow.

4.2 Description of mathematic model

The 3D RANS model incorporating the Spalart-Allmaras (SA) turbulence closure was employed. The grid generation is described by Lin and Li (2002) and the turbulence model was developed by Zeng and Li (2013).

4.2.1 Governing equations of flow motion

The governing equations of the model are as follows,

Continuity equation:

$$\frac{\partial \overline{u}_i}{\partial x_i} = 0 \tag{4.1}$$

Momentum equations:

$$\frac{\partial \overline{u}_i}{\partial t} + \overline{u}_j \frac{\partial \overline{u}_i}{\partial x_j} = \frac{\partial}{\partial x_j}\left[\nu_m \left(\frac{\partial \overline{u}_i}{\partial x_j} + \frac{\partial \overline{u}_j}{\partial x_i} \right) - \overline{u_i' u_j'} \right] - \frac{1}{\rho}\frac{\partial \overline{p}}{\partial x_i} - \frac{F_i}{\rho} + g_i \quad (i=1,2,3;\ j=1,2,3) \tag{4.2}$$

in which x_i denotes the coordinates in x, y and z directions; $\overline{u}_i$ is the time-averaged velocity component (u, v, w); t is the time; ρ is the water density; ν_m is the molecular viscosity; $\overline{u_i'u_j'}$ is the Reynolds stresses (i.e. second-order correlations) calculated by turbulent velocity components; F_i represents the resistance force components (F_x, F_y, F_z) introduced by vegetation per unit volume in the *x, y, z* directions, respectively. By introducing the eddy viscosity ν_t, Reynolds stresses are given by the eddy viscosity model,

$$-\overline{u_i'u_j'} = \nu_t \left(\frac{\partial \overline{u}_i}{\partial x_j} + \frac{\partial \overline{u}_j}{\partial x_i} \right) - \frac{2}{3} k \delta_{ij} \tag{4.3}$$

in which $k = \frac{1}{2}\overline{u_i'u_i'}$ is TKE, δ_{ij} is the Kronecker delta (i.e., $\delta_{ij} = 1$ for $i = j$, $\delta_{ij} = 0$ for $i \neq j$).

The SA model is to directly compute ν_t using one partial differential equation through a new viscosity variable $\tilde{\nu}$,

$$\nu_t = \tilde{\nu} f_{\nu 1} \tag{4.4}$$

$$\frac{\partial \tilde{\nu}}{\partial t} + \overline{u}_j \frac{\partial \tilde{\nu}}{\partial x_j} = c_{b1} \psi_v \tilde{\nu} + \frac{1}{\sigma} \left\{ \frac{\partial}{\partial x_k} \left[\left(\tilde{\nu} + \nu_m \right) \left(\frac{\partial \tilde{\nu}}{\partial x_k} \right) \right] + c_{b2} \left(\frac{\partial \tilde{\nu}}{\partial x_k} \frac{\partial \tilde{\nu}}{\partial x_k} \right) \right\} - c_{w1} f_w \left(\frac{\tilde{\nu}}{L_t} \right)^2 \tag{4.5}$$

where: $f_{\nu 1} = \dfrac{\chi^3}{\chi^3 + c_{\nu 1}^3}$, $f_{\nu 2} = 1 - \dfrac{\chi}{1 + \chi f_{\nu 1}}$, $f_w = g \left[\dfrac{1 + c_{w3}^6}{g^6 + c_{w3}^6} \right]^{1/6}$, $\tilde{S}_v = S_v + \dfrac{\tilde{\nu}}{\kappa^2 L_t^{\,2}} f_{\nu 2}$,

$S_v = \sqrt{\omega_j \omega_j}$, $\chi = \dfrac{\tilde{\nu}}{\nu_m}$, $g = r + c_{w2}\left(r^6 - r\right)$, $r = \dfrac{\tilde{\nu}}{\psi_v \kappa^2 L_t^2}$, $c_{b1} = 0.1355$, $c_{b2} = 0.622$,

$c_{\nu 1} = 7.1$, $\sigma = \dfrac{2}{3}$, $c_{w1} = \dfrac{c_{b1}}{\kappa^2} + \dfrac{1 + c_{b2}}{\sigma}$, $c_{w2} = 0.3$, $c_{w3} = 2$

The left-hand side of the equation determines the rate of change of variable $\tilde{\nu}$ following the mean flow field; on the right-hand side, the terms represent the production, diffusion and destruction rates of eddy viscosity, respectively.

4.2.2 Characteristic turbulence length

Now note the last term on the right side. Physically, Spalart and Allmaras (1992) introduced this term to characterize the inhibitive effect on the eddy viscosity by the wall. L_t is a turbulence length scale essentially characterizing the vortex size. Normally, the value is equal to the distance to the closest wall for the near-wall region. Zeng and Li (2012), however, modified L_t for regions within the range of the roughness height as a constant related to the gravel diameter, and at the outer layer L_t becomes sum of the distance to the wall and the above constant. With respect to vegetated flows, the pattern of turbulence is different from those for smooth and rough walls. The characteristic turbulence length for vegetated flows scales with the stem diameter for vegetation wakes and the size of coherent vortices against the interfaces between the vegetation canopy and outer open water. The turbulence length scale for large eddy is related to the integral length scale of the eddy. According to Pope (2000), the turbulence length scale for large eddy can be taken as half in size of vortices. Therefore, the turbulence length scale L_t within the partly-distributed submerged vegetation is defined as following procedures (see Figure 4.1). Firstly, to simplify the specification of turbulence length scale, the entire cross section is divided into four regions, namely, I (y, 0-b_v; z, 0-h_v), II (y, 0-b_v; z, h_v- h), III (y, b_v-b; z, 0-h_v)

and IV (y, b_v-b; z, h_v- h) (see Figure 4.1a).

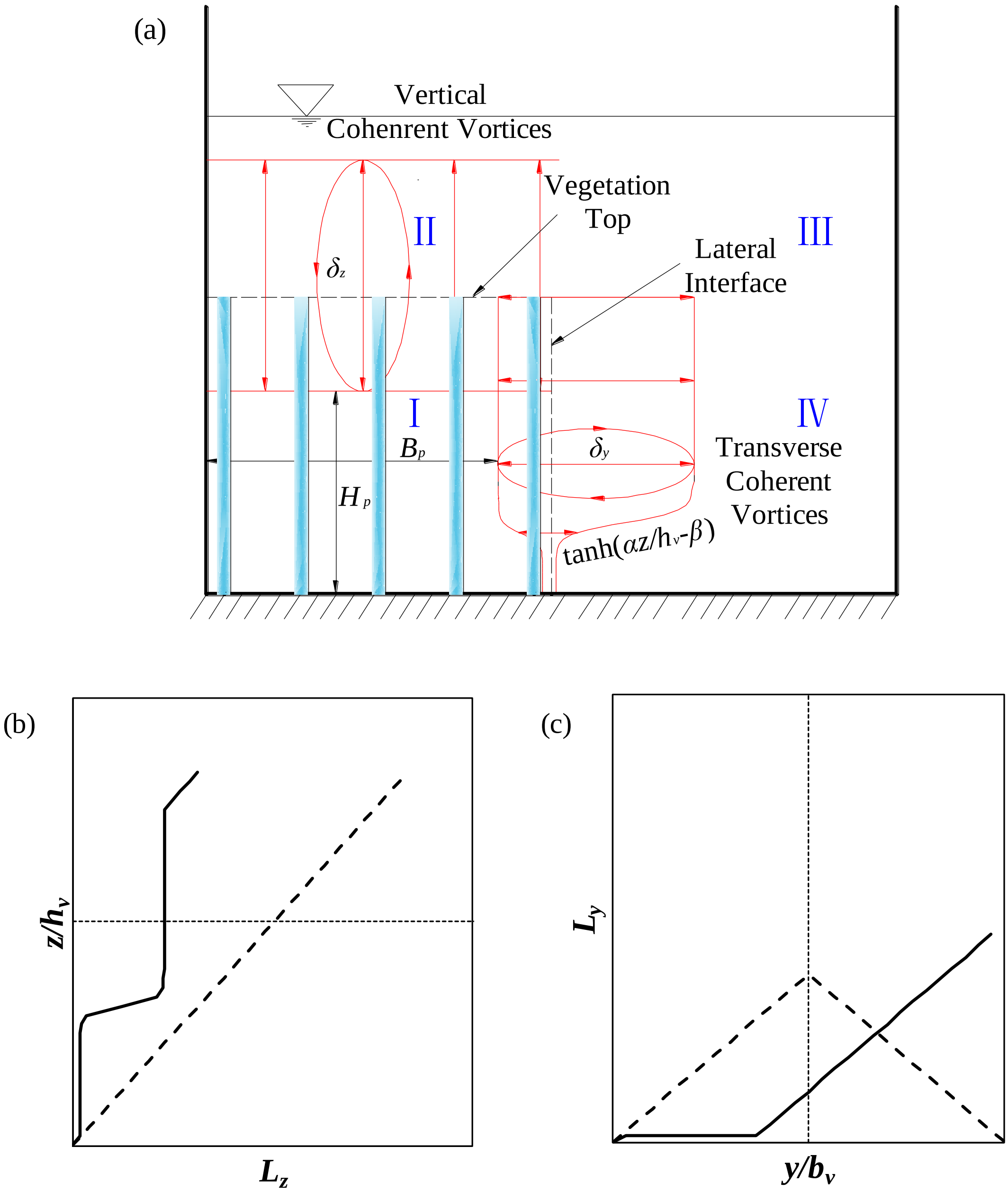

Figure 4.1 Definition of turbulence length scale in both vertical and transverse dimensions. For the vertical dimension (Figure 4.1b), the solid line is for regions I and II, and the dashed line is for regions III and IV. For the transverse dimension (Figure 4.1c), the solid line is for regions I and IV, and the dashed line is for regions II and III. The dotted lines indicate the vegetation top and lateral interface.

It is clearly noted that for regions I and II stem-scale and canopy-scale vortices dominate in the turbulence length scale in the vertical dimension. For regions III and IV the turbulence length scale is simply equal to the distance to the wall. Therefore, the turbulence length scale in the vertical dimension is given,

$$L_z = \begin{cases} d + 0.25\delta_z \left[1 + \tanh\left(\alpha_z \dfrac{z}{h_v} + \beta_z \right) \right] + \max(0, z - z_p) & \text{(for region I and II)} \\ z & \text{(for region III and IV)} \end{cases} \tag{4.6}$$

In the equations, δ_z is the integral length scale of vertical coherent vortices, taken as the size of the vortex and estimated from the vertical velocity profile; z_p the vertical penetration location; coefficients α_z and β_z determine the location of vertical coherent vortices. Substantially, Eq.4.6 reflects the penetration of turbulent momentum and the size of vertical coherent vortices.

With respect to the transverse dimension, the stem-scale and canopy-scale vortices are the main sources of turbulence viscosity for region I and IV. It should be noted that the bed suppresses the generation of horizontal coherent vortices. This physical concept was brought up by Chu et al. (1991) and de Lima and Izumi (2013). The effect, however, reduces as the distance from the bed increases and we presently assume that the evolution of the transverse coherent vortices performs as illustrated in Figure 4.1a characterized by the hyperbolic tangent function. For regions II and III, where vegetation is absent, the turbulence length scale is equal to the distance to the nearest side wall. Thus it gives,

$$L_y = \begin{cases} d \ \ (y \le y^*) & \text{(for region I and IV)} \\ d + 0.25\delta_y \left[1 + \tanh\left(\alpha_y \dfrac{z}{h_v} + \beta_y \right) \right] \ \ (y > y^*) & \text{(for region I and IV)} \\ \min\left(y, b - y \right) & \text{(for region II and III)} \end{cases} \tag{4.7}$$

$$y^* = b_v - \left[b_v - \left(\delta_y - y_p \right) \right] \times \frac{1}{2} \left[1 + \tanh\left(\alpha_y \frac{z}{h_v} + \beta_y \right) \right] \tag{4.8}$$

In the equations, δ_y is the integral length scale of transverse coherent vortices, taken as the size of vortices; y_p is the boundary of transverse coherent vortices in the NOWR; y^* is the boundary of transverse coherent vortices in the vegetation region and it is calculated by Eq.4.8; these values can be estimated from the transverse velocity profile; coefficients α_y and β_y are to determine the evolution of transverse coherent vortices as the distance from the bed increases. In fact, Eq.4.7 reflects the penetration of turbulent momentum, the size of horizontal coherent vortices and the effect of the channel bed on the evolution of transverse coherent vortices.

It should be noted that coefficients α and β in Eq.4.6 and Eq.4.7 carry different physical meanings. Finally, we take the smaller value between L_y and L_z as the local characteristic turbulence length scale except for region I, where the vertical and horizontal coherent vortices coincide at the corner of vegetation canopy. A special treatment in region I is to take the maximum of L_y and L_z. Therefore, the specification of characteristic turbulence length is as follows,

$$L_t = \begin{cases} \max(L_y, L_z) & \text{(for region I)} \\ \min(L_y, L_z) & \text{(for region II,III,IV)} \end{cases} \tag{4.9}$$

The drag force term is resolved by employing the quadratic friction law,

$$F_i = \frac{1}{2} n \rho C_d b_e \bar{u}_i \sqrt{\bar{u}_j \bar{u}_j} \tag{4.10}$$

where C_d denotes the stem drag coefficient; b_e denotes the effective stem width (i.e. the diameter for a cylinder), n is the stem density; C_d in the present simulation is taken as 1.2 mentioned earlier on.

4.2.3 Numerical methods

The σ-coordinate transformation technique is used to transform the calculation domain of the uneven free surface and bottom into a regular cube. The governing equations are resolved using a split-operator finite difference method. The details can be referred to in the study by Lin and Li (2002).

4.2.3.1 σ-coordinate transformation

The Cartesian coordinates are able to characterize irregular bottom and free waving surface so that it is difficult to calculate accurately the free surface using the pressure boundary condition. The problem also affects the calculation of the velocity field. In order to overcome the above difficulty in computation, the σ-coordinate transformation can be employed, which was firstly introduced by Phillips (1957) and has been widely used in computational models for oceanography and meteorology. It maps the varying vertical coordinate of the physical domain to a uniform transformed space where the coordinate σ spans from 0 to 1 (see Figure 4.2). With the assumption that the free surface is a function of the horizontal plane, a slightly modified σ-coordinate developed by Lin and Li (2002) gives,

$$\tau = t \quad \xi^1 = x \quad \xi^2 = y \quad \xi^3 = \sigma = \frac{z + h^*}{D} \tag{4.11}$$

where (x, y, z, t) are space and time coordinates in Cartesian coordinate system; (ξ^1, ξ^2, ξ^3, τ) are space and time coordinates in the σ-coordinate system; D=h^*+η is the entire water depth, h^* is the distance measured from z=0 and η is the surface elevation.

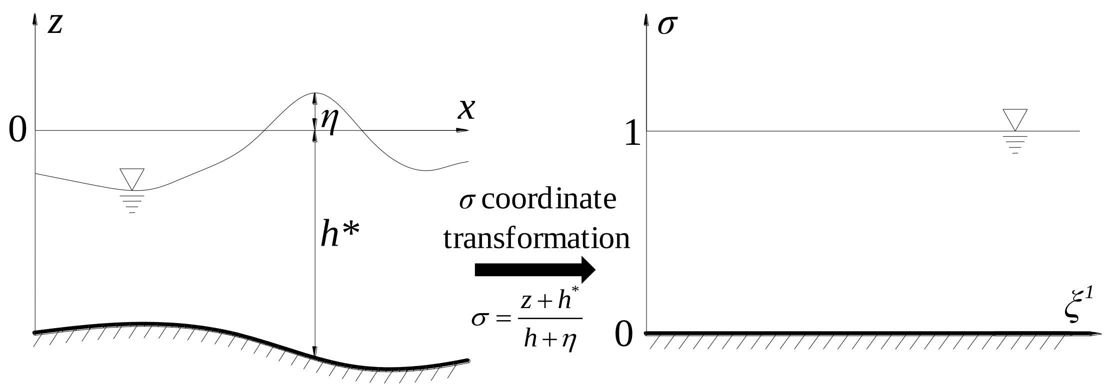

Figure 4.2 σ-coordinate system transformation

With the transformation by Eq.4.11, the governing equations in the new coordinate (ξ^1, ξ^2, ξ^3, τ) can be obtained,

$$\frac{\partial \bar{u}_i}{\partial \xi^k} \frac{\partial \xi^k}{\partial x_i} = 0 \tag{4.12}$$

$$\begin{aligned} &\frac{\partial \bar{u}_i}{\partial \tau} + \frac{\partial \bar{u}_i}{\partial \xi^k} \frac{\partial \xi^k}{\partial t} + \bar{u}_j \frac{\partial \bar{u}_i}{\partial \xi^k} \frac{\partial \xi^k}{\partial x_j} \\ &= \nu \frac{\partial \xi^k}{\partial x_j} \frac{\partial}{\partial \xi^k} \left(\frac{\partial \bar{u}_i}{\partial \xi^m} \frac{\partial \xi^m}{\partial x_j} \right) + \frac{\partial \tau_{ij}}{\partial \xi^k} \frac{\partial \xi^k}{\partial x_j} - \frac{1}{\rho} \frac{\partial \bar{p}}{\partial \xi^k} \frac{\partial \xi^k}{\partial x_i} - \frac{1}{\rho} F_i + g_i \end{aligned} \tag{4.13}$$

$$
\begin{aligned}
&\frac{\partial \nu}{\partial \tau}+\frac{\partial \nu}{\partial \xi^k}\frac{\partial \xi^k}{\partial t}+\bar{u}_j\frac{\partial \nu}{\partial \xi^k}\frac{\partial \xi^k}{\partial x_j}\\
&=c_{b1}\tilde{S}_v\nu+\frac{1}{\sigma}\left\{\frac{\partial \xi^k}{\partial x_j}\frac{\partial}{\partial \xi^k}\left[\frac{\partial \nu}{\partial \xi^m}\frac{\partial \xi^m}{\partial x_j}\right]+c_{b2}\left(\frac{\partial \nu}{\partial \xi^m}\frac{\partial \xi^m}{\partial x_j}\right)\left(\frac{\partial \nu}{\partial \xi^m}\frac{\partial \xi^m}{\partial x_j}\right)\right\}-c_{w1}f_w\left(\frac{\nu}{d}\right)^2
\end{aligned}
\tag{4.14}
$$

With

$$
\begin{aligned}
&\frac{\partial \xi^3}{\partial t}=\frac{\partial \sigma}{\partial t}=-\frac{\sigma}{D}\frac{\partial D}{\partial \tau}\\
&\frac{\partial \xi^3}{\partial x_1}=\frac{\partial \sigma}{\partial x}=\frac{1}{D}\frac{\partial h^*}{\partial \xi^1}-\frac{\sigma}{D}\frac{\partial D}{\partial \xi^1}\\
&\frac{\partial \xi^3}{\partial x_2}=\frac{\partial \sigma}{\partial y}=\frac{1}{D}\frac{\partial h^*}{\partial \xi^2}-\frac{\sigma}{D}\frac{\partial D}{\partial \xi^2}\\
&\frac{\partial \xi^3}{\partial x_3}=\frac{\partial \sigma}{\partial z}=\frac{1}{D}
\end{aligned}
\tag{4.15}
$$

$$
\begin{aligned}
&\tau_{11}=2\nu_t\left(\frac{\partial \bar{u}}{\partial \xi^1}+\frac{\partial \bar{u}}{\partial \sigma}\frac{\partial \sigma}{\partial y}\right) \qquad \tau_{12}=\tau_{21}=\nu_t\left(\frac{\partial \bar{u}}{\partial \xi^2}+\frac{\partial \bar{u}}{\partial \sigma}\frac{\partial \sigma}{\partial y}+\frac{\partial \bar{v}}{\partial \xi^1}+\frac{\partial \bar{v}}{\partial \sigma}\frac{\partial \sigma}{\partial x}\right)\\
&\tau_{22}=2\nu_t\left(\frac{\partial \bar{v}}{\partial \xi^2}+\frac{\partial \bar{v}}{\partial \sigma}\frac{\partial \sigma}{\partial y}\right) \qquad \tau_{13}=\tau_{31}=\nu_t\left(\frac{\partial \bar{u}}{\partial \sigma}\frac{\partial \sigma}{\partial z}+\frac{\partial \bar{w}}{\partial \xi^1}+\frac{\partial \bar{w}}{\partial \sigma}\frac{\partial \sigma}{\partial x}\right)\\
&\tau_{33}=2\nu_t\left(\frac{\partial \bar{w}}{\partial \sigma}\frac{\partial \sigma}{\partial z}\right) \qquad \tau_{23}=\tau_{32}=\nu_t\left(\frac{\partial \bar{v}}{\partial \sigma}\frac{\partial \sigma}{\partial z}+\frac{\partial \bar{w}}{\partial \xi^2}+\frac{\partial \bar{w}}{\partial \sigma}\frac{\partial \sigma}{\partial y}\right)
\end{aligned}
\tag{4.16}
$$

4.2.3.1 Split operator method

For convenience, a split operator method is used to solve the governing equations. At each time interval, the momentum equations are split into three steps, namely, advection, diffusion and pressure propagation,

$$
\frac{\partial \bar{u}_i}{\partial \tau}=A(\bar{u}_i)+D(\bar{u}_i)+P(\bar{p}) \tag{4.17}
$$

where $A(\bar{u}_i)$ denotes the advection operator, $D(\bar{u}_i)$ denotes the diffusion operator and $P(\overline{p})$ denotes the pressure gradient and body force operator.

Advection step

$$\frac{(\overline{u}_i)^{n+1/3}-(\overline{u}_i)^n}{\Delta\tau}=A(\overline{u}_i)^n=-\left(\frac{\partial\overline{u}_i}{\partial\xi^k}\frac{\partial\xi^k}{\partial t}-\overline{u}_j\frac{\partial\overline{u}_i}{\partial\xi^k}\frac{\partial\xi^k}{\partial x_j}\right)^n \tag{4.18}$$

where $\Delta\tau$ is the time step size, and the superscript n+1/3 represents the first intermediate step among these three steps. Similar symbols are also used in the following equations.

The method of characteristics is used to solve the above equation. Assuming the spatial variation of a function (e.g., velocity component) can be decomposed into a series of Fourier wave components, the schemes in this class of method produce an accurate solution for the advection of waves. In particular, the phase accuracy is very high and the amplitude damping is quite small (Leonard, 1979). Under uniform grids, the combination of the quadratic backwards characteristics method and the Lax-Wendroff method gives the Minimax characteristics method (Li, 1990). Lin and Li (2002) successfully implemented this method on non-uniform grids. The Minimax characteristics method is also adopted here.

Diffusion step

$$\frac{(\overline{u}_i)^{n+2/3}-(\overline{u}_i)^{n+1/3}}{\Delta\tau}=D(\overline{u}_i)^{n+1/3}=-\left(\nu_t\frac{\partial\xi^k}{\partial x_j}\frac{\partial}{\partial\xi^k}\left(\frac{\partial\overline{u}_i}{\partial\xi^m}\frac{\partial\xi^m}{\partial x_j}\right)+\frac{\partial\tau_{ij}}{\partial\xi^k}\frac{\partial\xi^k}{\partial x_j}\right)^{n+1/3} \tag{4.19}$$

Propagation step

$$\frac{(\overline{u}_i)^{n+1}-(\overline{u}_i)^{n+2/3}}{\Delta\tau}=p(\overline{p})^{n+1}=\left(-\frac{1}{\rho}\nu_t\frac{\partial\overline{p}}{\partial\xi^k}\frac{\partial\xi^k}{\partial x_i}\right)^{n+1}-\frac{1}{\rho}F_i+g_i \tag{4.20}$$

The central difference scheme in space is used to discretize Eq.4.19 and Eq.4.20. For continuity requirement, Eq.4.20 is substituted into the continuity equation to obtain a Poisson pressure equation.

Similarly, the eddy viscosity transport equation (4.14) is split into two steps: advection and diffusion with source. The same procedures for the solution of the momentum equations are used to solve the eddy viscosity equation, i.e., the Minimax characteristics method and the central difference scheme are adopted in the advection step and diffusion step, respectively.

3.2.3.3 CGSTAB method

The Poisson pressure equation obtained after the σ-coordinate transformation and aforementioned discretization can be written in the following general form:

$$Aq=b \tag{4.21}$$

where A is a sparse matrix which contains information of mesh system, free surface, bottom geometry and boundary conditions; q is the vector of to-be-solved pressure ($\overline{p}^{n+1}$); b is the known vector which contains information of sources and boundary conditions.

In order to solve Eq.4.21, the so-called conjugate gradient squared stabilized (CGSTAB) method was utilized in the present simulations. This method was first proposed by Vorst and Sonneveld (1990) and further modified by Van der Vorst (1992). It can be applied to non-symmetric matrices and to both structured and unstructured meshes. When compared to the classical Gauss-Seidel method, this method was confirmed to be better able to significantly shorten the computational time under the same convergence criterion.

4.2.4 Boundary conditions

At the free surface, both the dynamic and kinematic conditions should be satisfied at the interface of water and air, given as follows,

$$p = 0, \qquad \frac{\partial u_i}{\partial \sigma} = 0 \tag{4.22}$$

$$\frac{\partial \eta}{\partial t} = w - u\frac{\partial \eta}{\partial x} - v\frac{\partial \eta}{\partial y} \tag{4.23}$$

Eq.4.22 is in the form of advection equation and can be resolved by the method of characteristics.

On the solid boundary, the free-slip condition coupled with the wall function replaces the conventional no-slip condition. This treatment enables reasonable results with coarser grids near the solid boundary. For the inflow condition, an assigned velocity distribution is pre-calculated based on flow rate. The water surface slope effect is represented by streamwise component of gravity. For the outflow condition, the water surface elevation is specified and velocity gradients are assumed to be zero.

$$\frac{\bar{u}}{u*} = \frac{1}{\kappa}\ln\left(\frac{Ezu*}{\nu}\right) \tag{4.24}$$

where $u*$ is the shear velocity and E is the logarithmic law constant, recommended as 9.0 for smooth boundaries.

The Newton Raphson's method is used to calculate $u*$ in an iterative algorithm as follow,

$$u* = \frac{\bar{u}\kappa}{\ln\left(\frac{Ezu*}{\nu}\right)} \tag{4.25}$$

4.3 Results

4.3.1 Validation of modified SA model

The grid size is 0.058m×0.01m×0.0065m and 0.058m×0.01m×0.007m for the submerged case and emergent case, respectively. The time step is 0.005s. The convergent calculations reveal that the grids and time step are sufficiently fine. The experimental data presented in the study of White and Nepf (2007) and in the last chapter is used for model validation (summarized in Table 4.1). It should be noted that the former only has the depth-averaged (DA) flow information while the latter can provide a validation of 3D flow information. For the sake of consistency, denotations defined in Chapter 3 such as VR, outer-side junction and NOWR are also used here to describe transverse locations of the channel (see Figure 3.3).

Table 4.1 Parameters and coefficients in simulations.

Case	δ_y (m)	δ_z (m)	y_0 (m)	z_0 (m)	α_z, β_z (Eq.6)	α_y,β_y (Eq.7)
Submerged	0.135	0.135	0.24	0.20	50, 0.625	10, 0.45
Emergent	0.135	/	0.24	/	/	10,0.45
White and Nepf (2007) Case IV	0.193	/	0.57	/	/	10,0.6

Figure 4.3 illustrates the comparison between the measured transverse profile of DA longitudinal velocity and modeling results along the porous array for Case IV by White and Nepf (2007). It is clearly noted that the simulated velocities agree well the experimental data, indicating that the modified SA model can model the partly-obstructed channel flow with a large aspect ratio.

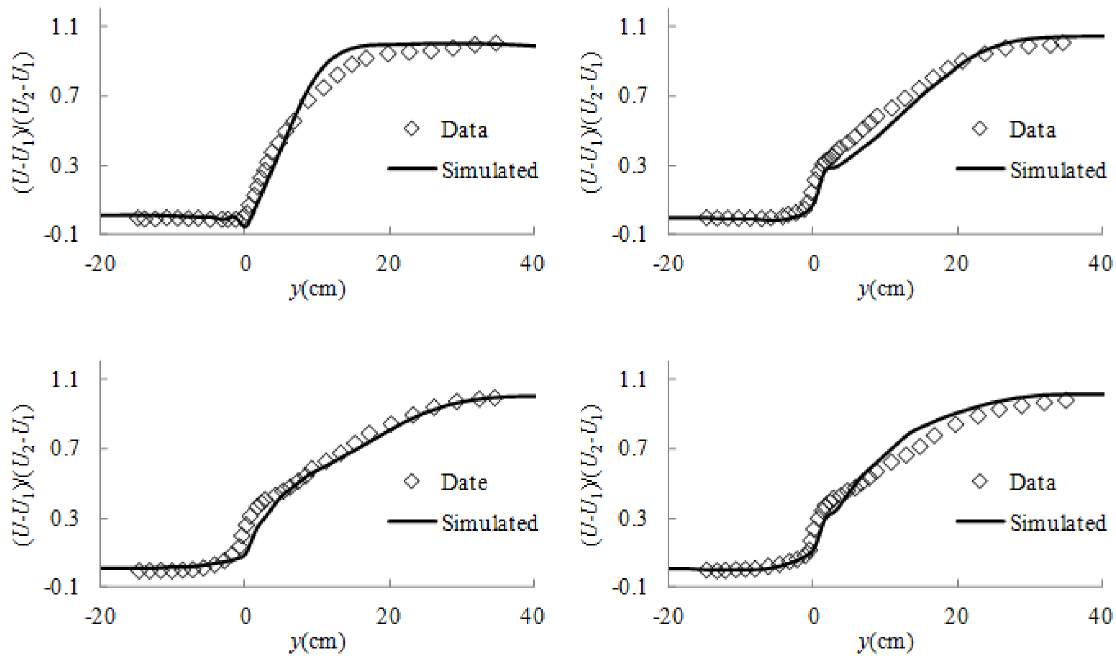

Figure 4.3 Comparison between experimental data of CaseIV in White and Nepf (2007) and simulated results by the modified SA model. The denotations are consistent with the definition in the White and Nepf (2007).

The simulated results of the $\bar{u}$ -profile along the vegetation canopy are illustrated in

Figure 4.4. In the VR, the simulated results agree well with the experimental data of the fully-developed flow for both submerged and emergent cases. However, pronounced deviation occurs in the lower part of the vertical velocity profile for non-fully-developed flow (x/L_p=0.41). Similar results are found in the study of Zeng and Li (2013). The cause for the deviation could be explained as follows. The drag force in the numerical model is averaged over the vegetative cross-section, while in real situations the drag force is discontinuously exerted on the fluid normal to the stem. In the outer-side junction, despite the transitional stage before the full development of flows, the modified SA model has confirmed the existence of the velocity deflection ($\partial\overline{u}/\partial z < 0$) in the near-bed region. In constrast, the standard SA model fails to simulate such phenomenon. Finally, minor difference between experimental data and simulated results can be observed in the NOWR. Still, the performance of the modified SA model is better than that of the standard one. It should be noted that there is still space to improve the simulation accuracy of modified SA model in the POCVC.

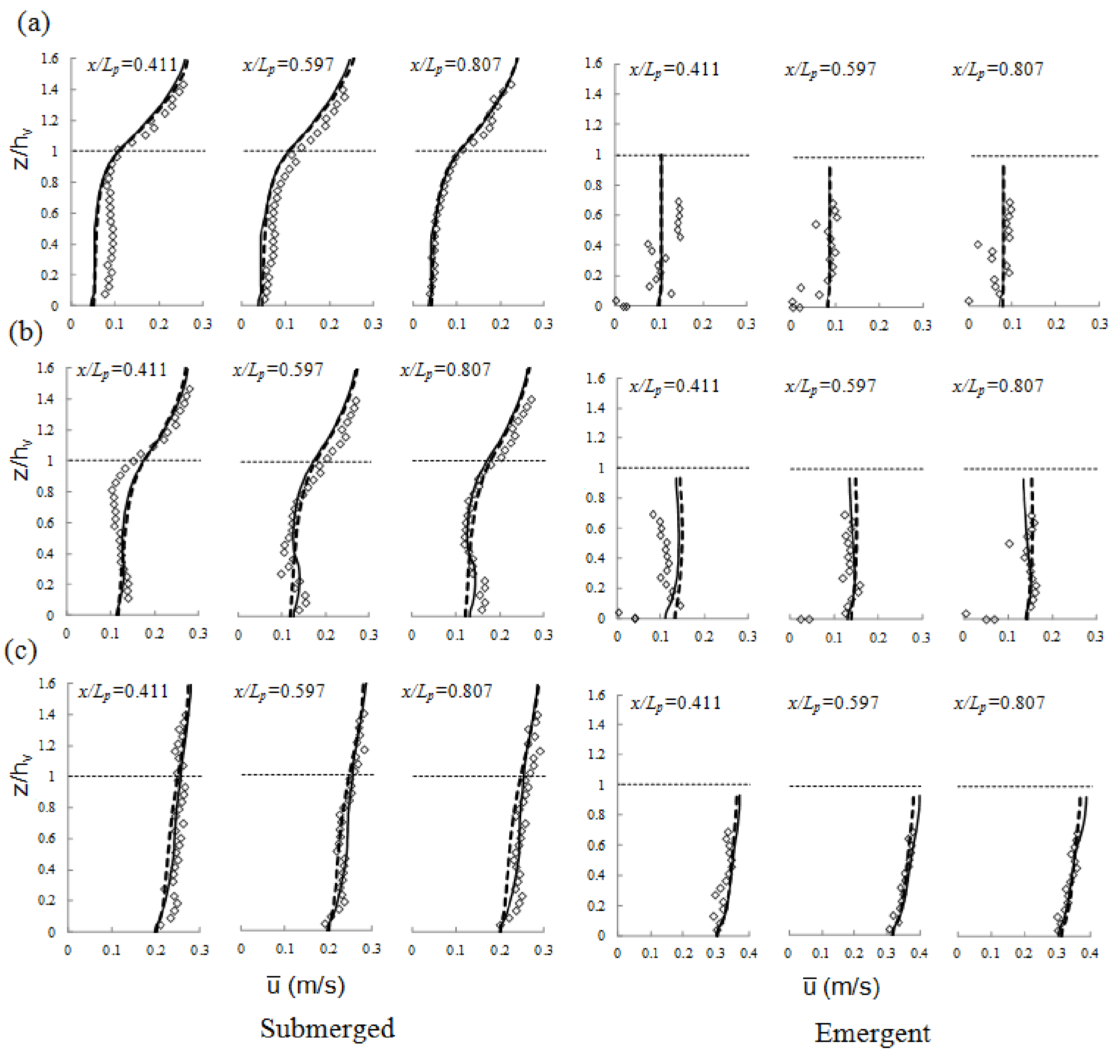

Figure 4.4 Comparison of $\bar{u}$ -profiles along the vegetation canopy between the experiment and simulation for N=1111m^{-2}. (a) VR, y/b_v=0.41; (b) Outer-side junction, y/b_v=1.04; (c) NOWR, y/b_v=1.53. The dashed line indicates the vegetation top and the solid line denotes the simulated results; the empty diamond denotes the experimental data.

The simulated results of $-\overline{u'w'}$-profiles along the vegetation canopy are illustrated in Figure 4.5. The simulated $-\overline{u'w'}$ agree well with the measured ones in the VR for both submerged and emergent cases. No significant difference between the two sets of data is noted except at the lower vegetation layer near the trailing edge, which can be attributed to the spikes produced by velocity sensor of Vectrino-II. Significant difference in $-\overline{u'w'}$ between the standard SA model results and experimental data occur in the outer-side junction. Similar to the vertical velocity profile, the positive simulated $-\overline{u'w'}$ values below the vegetation top deviate from the observed negative Reynolds stress. The modified SA model, however, successfully simulates such negative zone. In the NOWR, $-\overline{u'w'}$ is underestimated by both modified and standard SA models, which means the present modified SA model with the one-equation mode is relatively weak in simulating the anisotropic effect due to the combination of vertical and horizontal coherent vortices. The simulated results for the emergent case, however, agree well with the experimental data probably because the generated horizontal coherent vortices are unable to affect the water flow in this region.

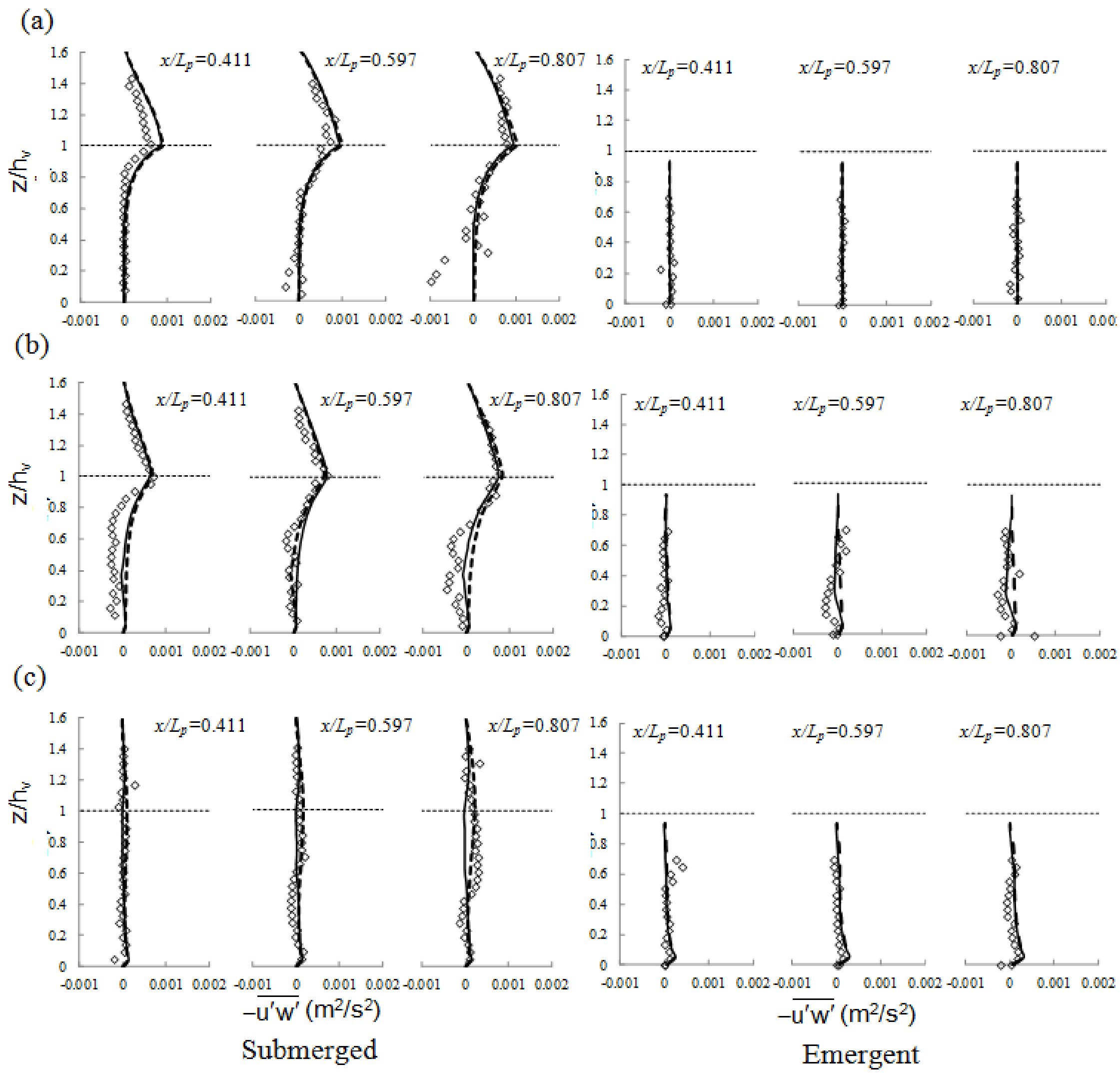

Figure 4.5 Comparison of $-\overline{u'w'}$-profiles along the vegetation canopy between the experiment and simulation for N=1111m^{-2}. (a) VR, y/b_v=0.41; (b) Outer-side, junction y/b_v=1.04; (c) NOWR, y/b_v=1.53. The dashed line indicates the vegetation top. The solid line denotes the simulated results; the empty diamond denotes the experimental data.

4.3.2 Parameter sensitivity study on velocity deflection and negativity of vertical Reynolds stress

In order to evaluate the behavior of the developed vortex-based SA model, main parameters which are probably associated with the deflection of longitudinal velocity and negativity of vertical Reynolds stress in the near-bed region are tested in the parameter sensitivity study. Obviously, such flow phenomena occur in the NOWR. Therefore, the simulated flow characteristics in the NOWR are considered only in the parameter study. The parameters include the spatial distribution parameters a_y and β_y, transverse turbulence length δ_y and the vegetation density n. Tests do not involve the vertical-vortex-related parameters since they are assumed to negligibly affect the flow behavior in the NOWR. The parameter details are listed in Table 4.2.

Table 4.2 Details of tested parameters in the vortex-based SA model

Run	Q (m^3/s)	a_y	β_y	δ_y (m)	N (m^{-2})
PV	**0.0125**	**10**	**0.45**	**0.12**	**5.56**
PVA1	0.0125	**5**	0.45	0.12	5.56
PVA2	0.0125	**16**	0.45	0.12	5.56
PVB1	0.0125	10	**0.3**	0.12	5.56
PVB2	0.0125	10	**0.6**	0.12	5.56
PVL1	0.0125	10	0.45	**0.08**	5.56
PVL2	0.0125	10	0.45	**0.16**	5.56
PVD1	0.0125	10	0.45	0.12	**8.33**
PVD2	0.0125	10	0.45	0.12	**2.08**

Note: PV is the reference case which has been validated with experimental data in the proceeding sections. The underlined bold number is the varied parameter evaluated.

Effect of α_y

The vertical distribution of longitudinal velocity and vertical Reynolds stress under different α_y are shown in Figure 4.6. It is clear that the variation of α_y does not affect the degree of the velocity deflection and negativity of vertical Reynolds stress. α_y characterizes the transitional behavior before the horizontal coherent vortices become fully developed. Thus the transitional behavior of horizontal coherent vortices has a negligible effect on the flow behavior in the region adjacent to the vegetation canopy.

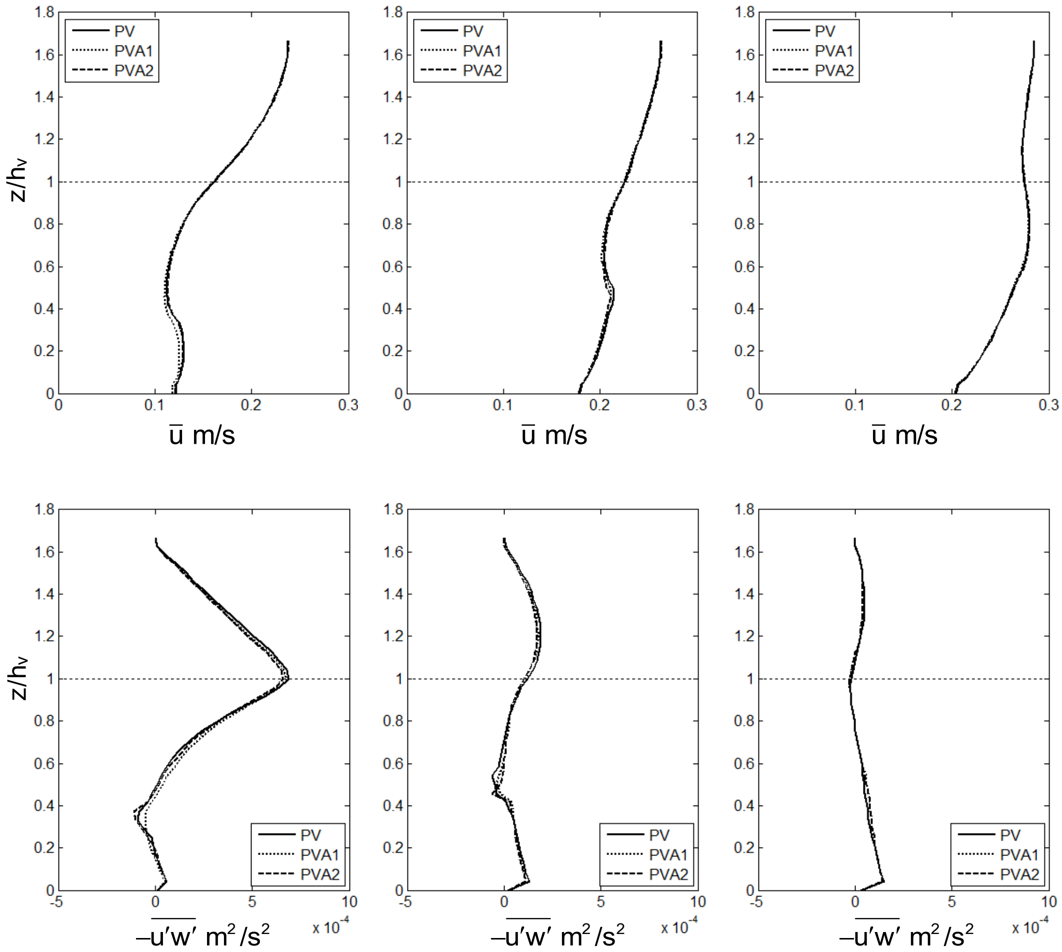

Figure 4.6 Longitudinal velocity and vertical Reynolds stress affected by α_y (from left to right: y/b_v=1.067, 1.333 and 1.600).

Effect of β_y

As shown in Figure 4.7, compared with α_y, the effect of β_y on the flow velocity deflection in the outer-side junction is fairly pronounced. Overall, the larger β_y leads to the greater vertical distance of flow velocity growth in the near-bed region, where the flow tends to comply with the wall-bounded flow theory or logarithmic law. In this region, the transverse momentum exchange is insignificant. Above this region, the flow velocity is deflected to a same local minimum, indicating that the negative gradient of velocity profile is greater for the larger β_y. No difference is observed at the upper flow layer for different β_y. β_y also affects the behavior of vertical Reynolds stress. It is obviously noted that the vertical location of negative peak shifts upward for the larger β_y.

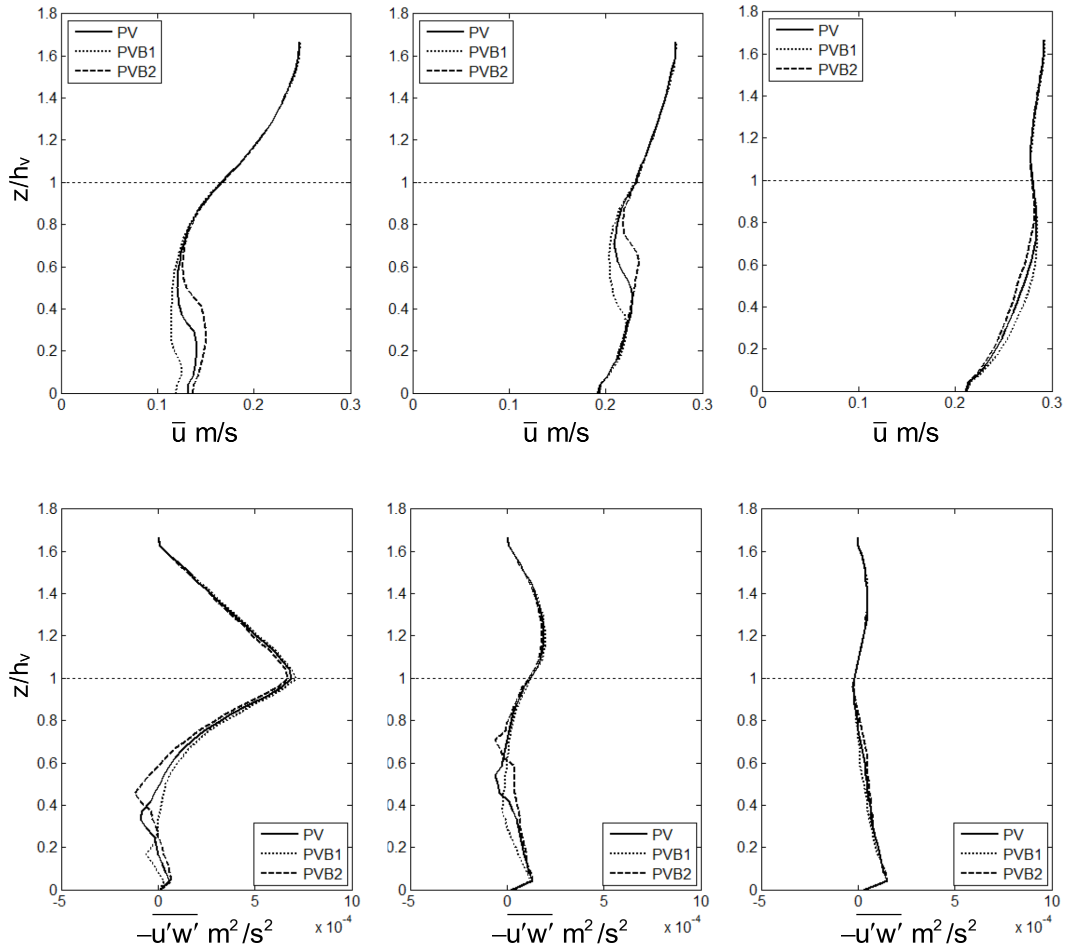

Figure 4.7 Longitudinal velocity and vertical Reynolds stress affected by β_y (from left to right: y/b_v=1.067, 1.333 and 1.600).

Effect of transverse length δ_y

As shown in Figure 4.8, at y/b_v=1.067, the vertical velocity profile is not pronounced under different values of transverse length δ_y. However, it is still noted that the larger δ_y leads to the larger degree of the velocity deflection. The vertical distribution of vertical Reynolds stress is also similar for different δ_y. When farther away from the canopy lateral edge (y/b_v=1.333), the velocity deflection is absent for the smallest δ_y (PVL1 δ_y=0.08m) and is present for the other larger δ_y (PV δ_y=0.12m and PVL2 δ_y =0.16m). This indicates that δ_y =0.08m is so small that the flow at this transverse location cannot be affected by horizontal coherent vortices with the specified short transverse turbulent length. The vertical location of negative vertical Reynolds stress for smallest δ_y increases to the CTL, which differs than the other two cases for larger δ_y. The effect of the transverse coherent effects almost disappears for the outer location in the NOWR (y/b_v=1.600).

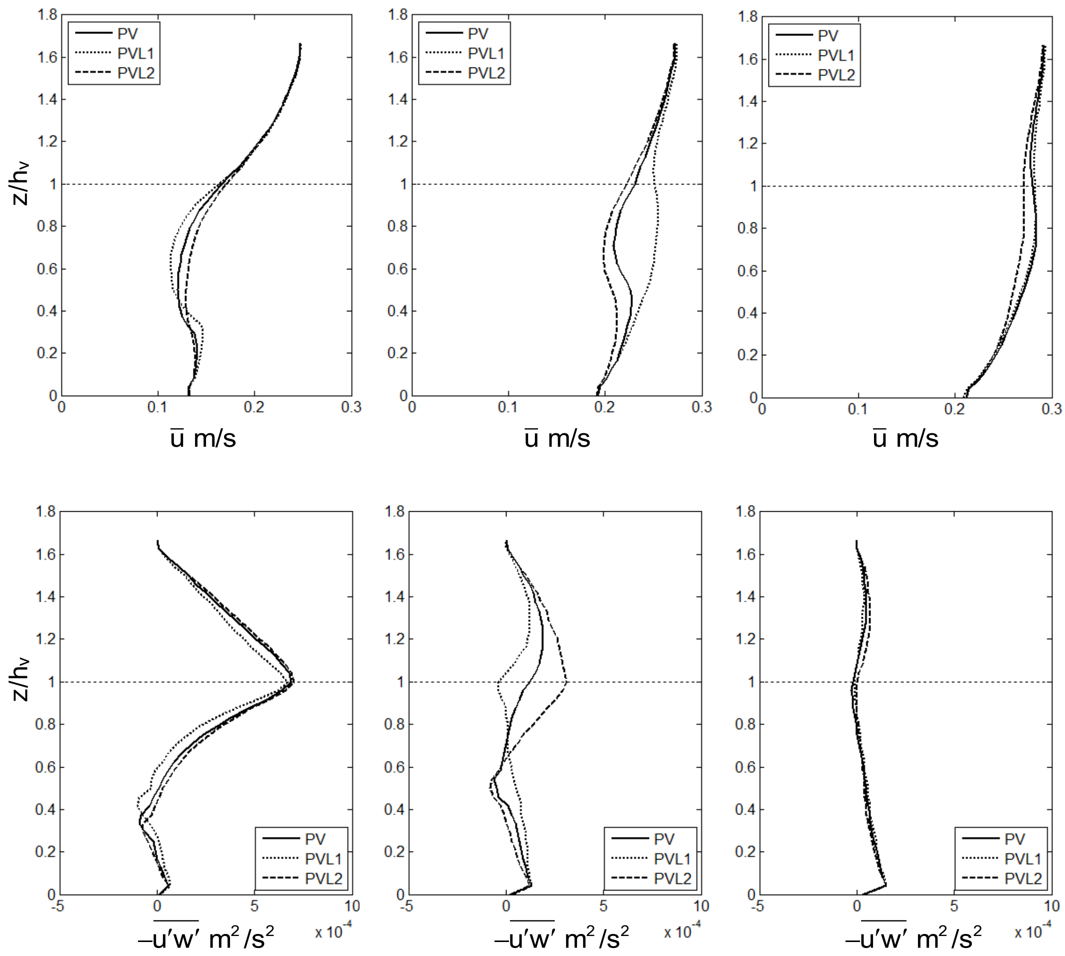

Figure 4.8 Longitudinal velocity and vertical Reynolds stress affected by transverse turbulence length at different transverse locations (from left to right: y/b_v=1.067, 1.333 and 1.600).

Effect of vegetation density *N*

Results show that the vegetation density is an important factor influencing the degree of velocity deflection because the intensity of horizontal coherent vortices is related to the vegetation density. As shown in Figure 4.9, the velocity deflection in the near-bed region clearly becomes more pronounced as the vegetation density increases (y/b_v=1.067). Particularly for the smallest vegetation density (PVD1 n=2.08), the velocity deflection is nearly negligible. At the outer region (y/b_v=1.600), as the vegetation density decreases, the flow velocity, overall, becomes smaller. With the reduction of the vegetation density, the maximum Reynolds stress at the CTL clearly reduces, indicating the reduced intensity of horizontal coherent vortices. However, the vegetation density has no influence on the vertical locations of velocity deflection and the negative peak of vertical Reynolds stress.

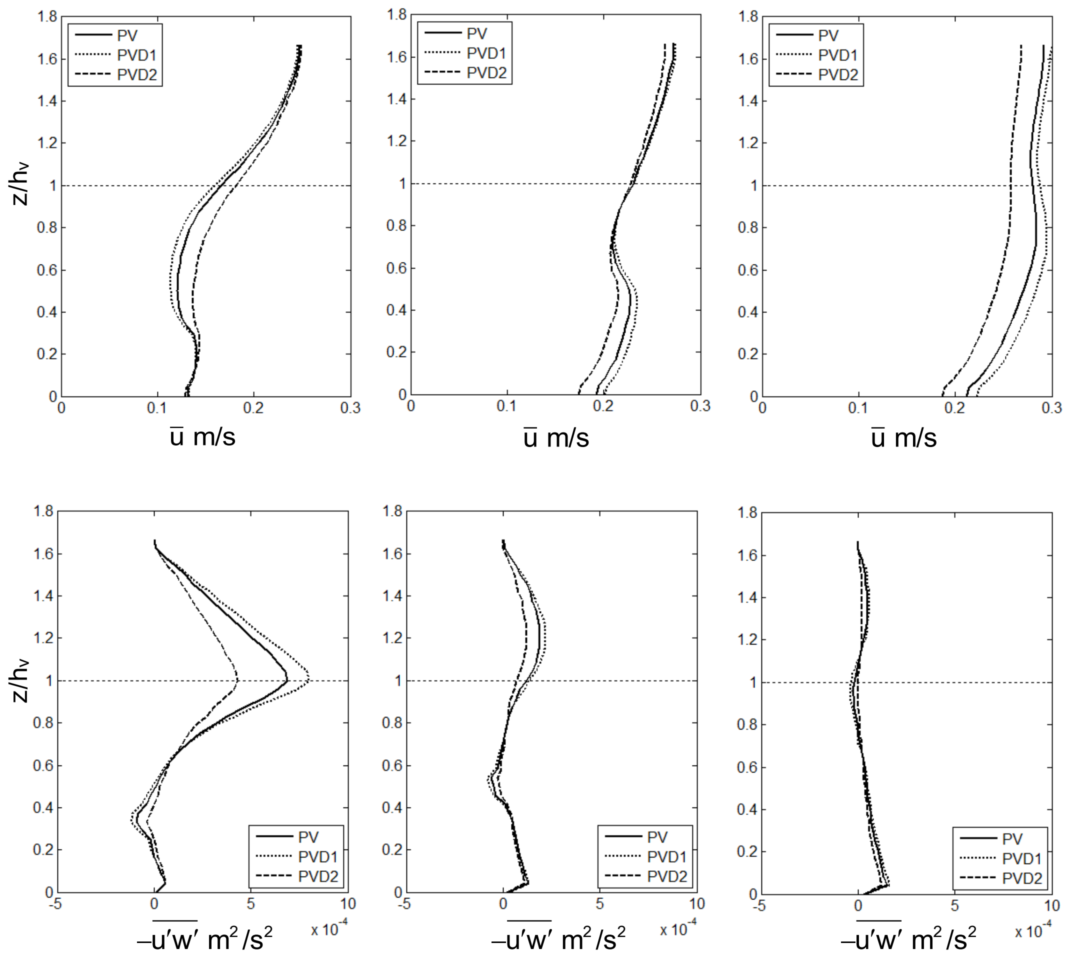

Figure 4.9 Longitudinal velocity and vertical Reynolds stress affected by vegetation density (from left to right: y/b_v=1.067, 1.333 and 1.600).

4.4 Conclusions

The Spalart-Allmaras (SA) model can efficiently model the sheared flow through the vegetation canopy due to the nature of the eddy viscosity transport equation in describing the characteristic turbulence length of large-scale vortices (Zeng and Li, 2013). However, the standard one-equation SA model is isotropic, which is difficult in describing flow characteristics in the partially-obstructed channel with vegetation canopy (POCVC).

Herein, this study improved the SA model on the basis of the vortex pattern generated in the POCVC. The specification of the turbulence length scale of vortex is in terms of the local vortices so that the transport equation of eddy viscosity becomes substantially anisotropic due to the spatial variation of dominant turbulence length scale. Along the vegetation canopy, the vortex-based SA model can still well simulate the flow through the inner vegetation region away from the junction except for the entry region of vegetation canopy. Particularly in the junction, the improved model, for both the submerged and emergent canopy, successfully reproduces the flow velocity deflection and negative vertical Reynolds stress in the near-bed region. The standard SA model, however, fails to reproduce the above flow and turbulence properties owing to being unable to characterize horizontal coherent vortices in the POCVC.

With the sensitive study of parameters, the two parameters α_y and β_y which describe the spatial distribution of horizontal coherent vortices have different influences on the simulated flow behaviors. The difference in α_y hardly affects the degree of velocity deflection and the negativity in vertical Reynolds stress in the near-bed region. The larger β_y leads to flow to develop in the wall-region within a larger vertical distance. As a result, the degree of velocity deflection is more pronounced. The characteristic transverse turbulence length L_y dominates the transverse extension of horizontal coherent vortices in the NOWR. As L_y decreases, the outer region farther away from the lateral edge of vegetation canopy is negligibly affected by horizontal coherent vortices with momentum exchange between the VR and the NOWR. The investigations show that the vegetation density is the rooted influential factor for the coherent vortices generation. As the vegetation density increases, the degree of velocity deflection and negativity in vertical Reynolds stress increases. When the vegetation density becomes fairly small, the degree of velocity deflection and negative vertical Reynolds stress correspondingly becomes negligible.

Chapter 5 Sediment Transport and Bed Morphology in the Partially-obstructed Open Channel with Vegetation Canopy

5.1 Introduction

Vegetation, in real situations, commonly exists near the channel bank with finite length, and in practice is regarded as one ideal measure to restore the aquatic environment. In previous chapters, mean flow characteristics and turbulence structure in the partially-obstructed open channel have been investigated from different aspects. The hydrodynamic knowledge is useful for understanding the alluvial processes under similar flow configurations such as riparian channel and floodplain with colonized vegetation. However, when sediment motion on the channel bed is considered, the boundary becomes the dynamic type, which is not the same as the only pure flow situation with the fixed boundary. It is expected that the bed morphology evolution feeds boundary variation back to the flow, leading to the readjustment of flow structure. Therefore, the flow-sediment-vegetation interaction is more complicated in comparison with the flow-vegetation interaction. For the practical reason, it is more promising to obtain the flow structure and associated bed morphology pattern in the POCVC. It can provide academic fundamental of flow and sediment dynamics for river restoration, species rehabilitation, water management and so on.

The sediment transport characteristics and bed morphology pattern in the vegetated flow have been investigated in decades. James et al. (2002) used flume data characterizing flow through an emergent canopy to reveal that the bed-load transport rate is substantially influenced by the stem drag. Jordanova and James (2003) established the relationship between bed-load transport rate and bed shear stress by partitioning the total flow resistance. Crosato and Saleh (2011) demonstrated that the presence of vegetation tends to produce a single channel rather than braided channel frequently formed on bare floodplains, since the vegetation regulates the flow behavior. Yager and Schmeeckle (2013) experimentally showed that the bed-load transport rate in the vegetated flow is still under uncertainty (increase or decrease), which depends on the intensity of the turbulence and mean flow velocity as well as the vegetation distribution pattern. Tang et al. (2013) extended the principle of incipient motion of sediment on bare beds to that on vegetated beds by considering the spatial property of flow. They observed that it is easier, in regard to the incipient velocity, to initiate sediment in the vegetated channel due to minor secondary fluid motions induced by vegetation stems.

Attention has been extended to the alluvial process under particular flow-vegetation configurations recently. Zong and Nepf (2010) investigated the effect of partially-distributed vegetation on the deposition of suspended loads in water flow. Both dispersion and advection processes were identified to determine the deposition pattern in the vegetation patch essentially associated with the flow field. Follett and Nepf (2012) presented the sediment patterns around a patch of reedy emergent canopy, which was well explained by the flow structure and turbulence caused by the vegetation patch. Chen et al. (2012a) investigated the scour effect and dune characteristics in a FOCVC.

The presence of vegetation is able to protect the sediment bed from flow erosion by decreasing the bed shear stress. Yang et al. (2015) found that the gradient of velocity profile outside the viscous sublayer is much smaller than the gradient of logarithmic profile, which indicates the reduction in the frictional velocity. Le Bouteiller and Venditti (2015) observed that the bed in the vegetation region instead of erosion tends to ascend as the upstream sediment deposits in that region. The authors attributed the morphological response to a compensation of the reduced bed shear stress. Similar sediment deposition was also observed by Kim et al. (2015) in a POCVC.

The difference of the above two studies is that the suspended load transport is dominant for the former while the bed-load transport is for the latter. In both studies, obvious bed scour, however, happens at the entry of vegetation region. This observation suggests that the vegetation can protect the bed except at the entry of vegetation canopy. In fact, this concept local scour of bed is somewhat analogous to the bridge pier scour. When flow encounters obstacles like bridge piers, the downflow in front face of obstacle leads to the growth of scour hole by increasing the effective bed shear stress (Khosronejad et al., 2012). The downflow at the entry of vegetation canopy also might be the cause accounting for the local bed scour.

When vegetation canopy partially obstructs the channel, massive water on the vegetated side is discharged toward the non-vegetated side. As a result, flow velocity on the non-vegetated side increases, leading to enhancement of sediment transport and bed erosion. Therefore, the presence of partially-distributed vegetation canopy meanwhile tends to produce the bed scour on the non-vegetated side. Kim et al. (2015) conducted experimental investigation of bed morphology evolution in a POCVC. Obvious bed scour was observed in the NOWR adjacent to the vegetation canopy. The study shows a positive linear relationship between the maximum scour depth and the blockage effect (defined as production between the vegetation patch width and solid frontal area per unit volume) of vegetation patch across the channel.

As discussed above, partially-distributed vegetation canopies (patches) broadly occur in real situations while only a few experimental investigations of alluvial processes under similar flow-vegetation configurations are seen. Therefore, this chapter aims to carry out an experiment to show the overall characteristics of sediment transport, bed morphology evolution and mean flow and turbulence in a POCVC. The details of methodology and experiment setup are presented in Section 5.2. The results and discussion are presented in Section 5.3, specifically,

- Characteristics of sediment transport in clean water scour experiments are presented. Particular attention is paid to the sorting effect of transported sediment ;
- When the equilibrium bed reached, characteristic bed morphologies around the partially-distributed vegetation canopy are well investigated and the bed surface sediment sorting due to the non-uniformity of bed materials is

measured;

- Flow characteristics over the equilibrium bed morphology, such as mean flow velocities and Reynolds stresses, are measured, which are used to account for the generation of bed morphology as well as the sorting effect of bed surface sediment;
- Scaling analysis is conducted to investigate the underlying relationship between equilibrium bed morphologies and flow characteristics.

Finally, some concluding remarks are presented in Section 5.4.

In comparison with previous studies (Bennett et al., 2008; Follett and Nepf, 2012; Kim et al., 2015), a longer vegetation canopy is selected in the present study. For an adequately-long vegetation canopy, the entire vegetated reach can be partitioned into the flow adjustment region and the fully-developed flow region (White and Nepf, 2007; Yan et al., 2016), in which horizontal coherent vortices tend to form along the vegetation canopy.

5.2 Laboratory experiments

Laboratory experiments were conducted in the same flume system used for investigation of flow characteristics over the flat bed in Chapter 3. The geometric configuration of vegetation canopy was not changed. The vegetation canopy is 2m in length (L_p) and 0.15m in width (b_v); the upstream reach is 1.5m in length (L_u), and the downstream reach is 2m in length (L_d). The height of cylinders is 0.15m (h_v) and the diameter is 0.005m (d). The spacing between adjacent vegetation stems in both the longitudinal and lateral directions is s=0.03m. Therefore, the number of the vegetation cylinders per unit area is N=1111 (m^{-2}) and the solid volume fraction of vegetation canopy is given as $\phi=\pi ad/4$=0.022 and the vegetation density is $a=Nd$=5.56 (m^{-1}). A sediment layer with a thickness of 6.5cm was laid on the bed bottom for clean water scour experiments as illustrated in Figure 5.1. Thus initially the height of vegetation canopy above the bottom is 8.5cm. An inclined buffering upslope made of gravels was used to enable the incoming flow to gradually propagate onto the sediment bed. At the exit of the sediment bed, bricks were set up to establish a control section and a sediment sample filter can be easily installed to collect sediment transported from upstream. Thus, the sediment transport rate from the entire studied reach can be calculated.

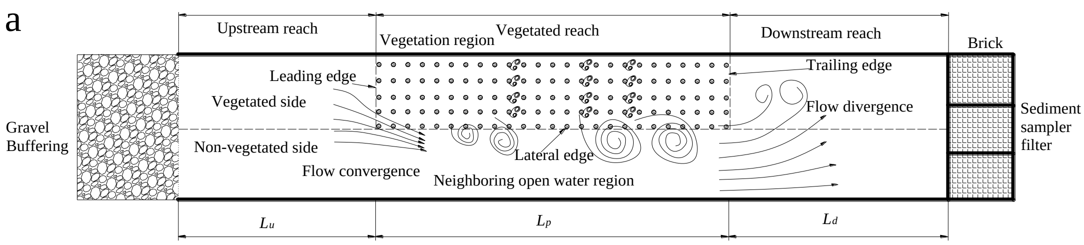

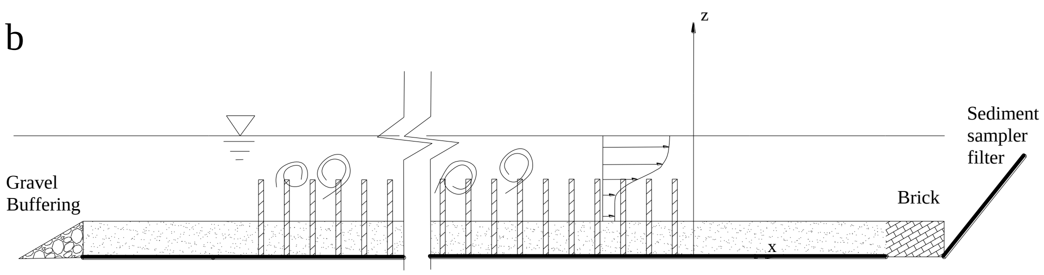

Figure 5.1 Sketch of the sediment flume. (a) Plan view; (b) Side view.

In order to approach a natural condition, sediment with an initial gradation from the field area in Yuan Long, Hong Kong was used and the sediment gradation is shown in Figure 5.2. It is expected that sediment sorting effect might occur in the sediment transport process and on the bed surface. As shown in the figure, the median diameter (d_{50ini}) is 1.42mm and the geometric standard deviation ($\sigma_{gini} = \sqrt{d_{84} / d_{16}}$) is 2.31. Gomez and Church (1989) suggested that bed-load transport is dominant when the sediment diameter is larger than 0.2mm. The bed-load dominated transport is confirmed by the observation during the experiment. Therefore, it is assumed that suspended load transport has the negligible impact on the final results.

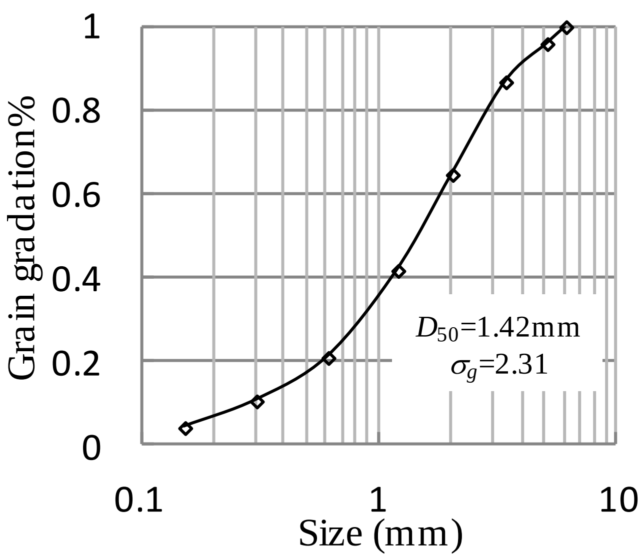

Figure 5.2 Grain gradation of initial bed materials.

In experiments, in order to decrease the interference of large flow velocity due to shallow water depth at the initial stage on the bed, water was slowly pumped into the channel with exit being closed. With this special treatment, the bed scour was observed to be negligible before clean water scour started. As water depth rose to a high level, experimental flow rates were set and the exit was opened to initiate water flow. As bed surface sediment was initiated completely, the sediment sampler filter was put at the control section to collect the sediment transported from upstream. The collection duration was kept as one minute for each sample, and the interval between neighboring samples was set as two minutes. However, according to the sediment transport intensity (by observation), the collection duration was adjusted accordingly. When the equilibrium bed reached (bed-load transport rate significantly decreases to a small value), the flume system was shut down to have water drained out. A point gauge with an accuracy of 0.001m was employed to measure bed deformation. In addition, the surface sediment was carefully sampled to investigate sediment sorting effect over the bed morphology (see Figure 5.3). Samples of transported sediment and bed surface were put into an oven of 105 C^o to completely dry the sediment samples. An electronic scale was used to measure the weight of those samples so that sediment transport rate was calculated. The size distribution was determined by means of sediment sieving test.

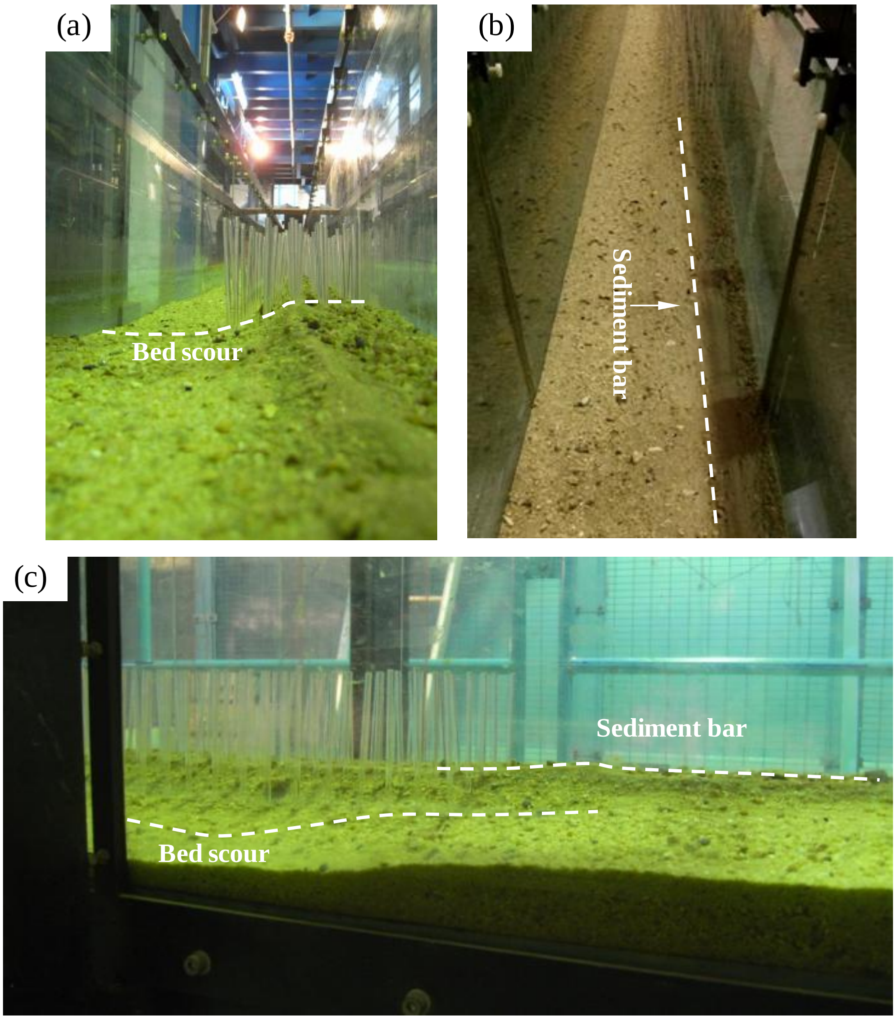

Figure 5.3 Photos of equilibrium bed morphology in clean water scour. On the non-vegetated side, the bed was significantly scoured along the canopy. The bed scour extended to the vegetated side. A long sediment bar formed after the canopy and extended downstream with surface fining.

To understand the role of the flow structure in the sediment transport and bed morphology evolution, Vectrino-II was used to investigate the 3D flow details (such as the primary velocity profile, secondary flow and turbulence) over the equilibrium bed topography for Case1. Details of Vectrino-II can be referred to that in Chapter 3. It should be noted that, even though equilibrium bed is assumed, there are sediment particles moving on the bed due to near-bed turbulence. In order to decrease the disturbance on velocity measurement due to minor bed changes, paint was sprayed to stabilize the bed. The entire channel is partitioned according to the spatial distribution of vegetation canopy, which is consistent with Chapter 3 (see Figure 5.4). The sketch of the measurement arrangement is shown in Figure 5.5. At most cross-sections, measurements on three verticals including VR, junction and NOWR were carried out to observe the flow adjustment over the generated bed. Additional careful measurements including thirteen verticals were made to examine the transverse variation of flow characteristics.

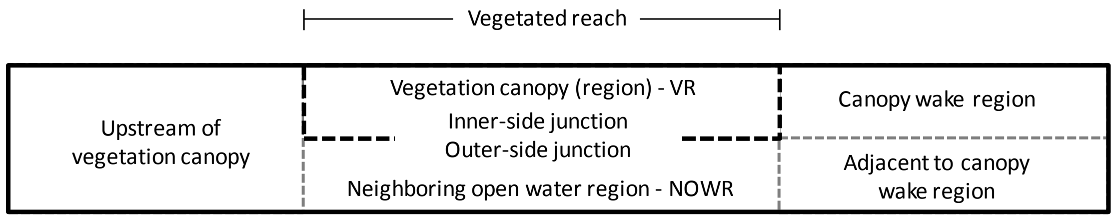

Figure 5.4 Partition of the entire open channel.

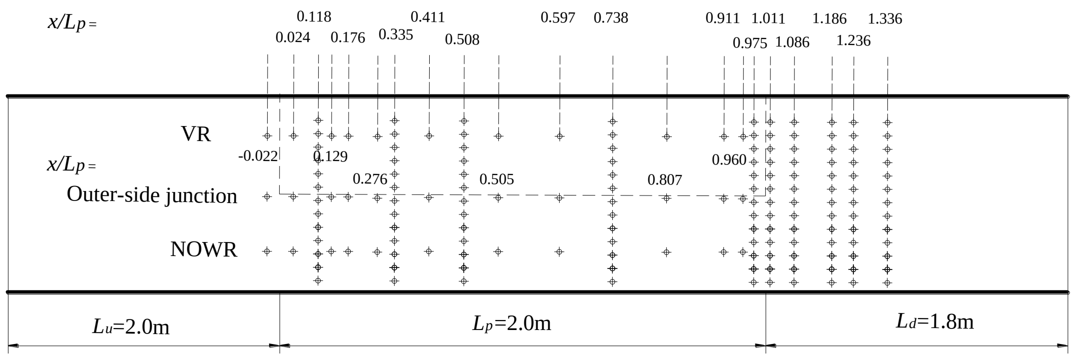

Figure 5.5 Measurement plan in the partially-obstructed channel

Two flow configurations are employed referred to as Case1 and Case2. In Case1, the experimental discharge is roughly 0.0125m^3/s, and the water depth is 0.169m at the leading edge (h_l) and 0.160m at the trailing edge (h_t). In Case2, the discharge is roughly 0.0166m^3/s, and the water depth is 0.198m at the leading edge (h_l) and 0.19m at the trailing edge (h_t). The flow surface slopes are 0.45% and 0.40% for the two cases, and the vegetation canopy is under shallow submergence condition. The details of flow configurations are summarized in Table 5.1.

Table 5.1 Flow configurations for bed morphology evolution in the partly-obstructed channel.

	Q (m^3/s)	h_l (m)	h_t (m)	S_w $(h_l - h_t)/L_p$	U_0 (m/s)	Fr	Re	Vegetation status
Case1	0.0125	0.159	0.150	0.45%	0.238	0.185	40222	Emerged
Case2	0.0166	0.198	0.190	0.40%	0.270	0.194	53460	Submerged

5.3 Experiment results and discussions

5.3.1 Bed-load transport process

5.3.1.1 Bed-load transport rate

Without upstream sediment supply, the bed-load motion was not in equilibrium. The rate of bed-load transport is essentially the rate of scouring of bed sediment. In addition, due to vegetation canopy partially across the channel bed, the bed shear stress was re-adjusted with a high level at the reach adjacent to the canopy and a low level at the reach covered by the canopy. Therefore, the bed-load transport rate should be unsteady and non-uniform in time and space. Figure 5.6 shows the dimensionless bed-load transport rate ($q_{s*} = q_s \big/ \sqrt{\left[\left(\rho_s - \rho\right)/\rho\right] g d_{50ini}}\, d_{50ini}$) in the duration of the clean water scour experiment. It is clear that q_{s*} increases significantly from a small value (close to zero) to maximum after a scour period for both cases. The increasing stage of q_{s*} is t=2345s-3575s for Case1 and t=1950s-3410s for Case2, which is interpreted as the arrival of the first sand wave. It is observed that the bed-load transport intensity is highly non-uniform in the POCVC. For instance, the transport rate in the NOWR of vegetated reach is larger than that at the downstream reach. Consequently, the sand wave tends to be formed at the downstream reach as shown in Figure 5.7. The bed-load transport rate at the downstream of the sand wave is limited due to the discontinuity of sediment transport from upstream. The source of bed loads is mainly from the area between the sand wave and channel exit. When the sand wave propagates close to the channel exit, the bed-load transport rate continuously decays. The extreme case ($q_{s*} \approx 0$) occurs when the sand wave arrives at the channel exit.

Then q_{s*} generally decays with time. It is interesting to note the difference in results between the two cases. For Case2, local peaks of q_{s*} repeatedly occur at t=6290s and 7260s, while similar repeated peaks are not observed for Case1. This suggests that sand waves are closely related to the flow intensity. The intermittent bed-load transport, therefore, is a feature in the POCVC due to high non-uniformity of bed-load transport rate in absence of upstream sediment supply.

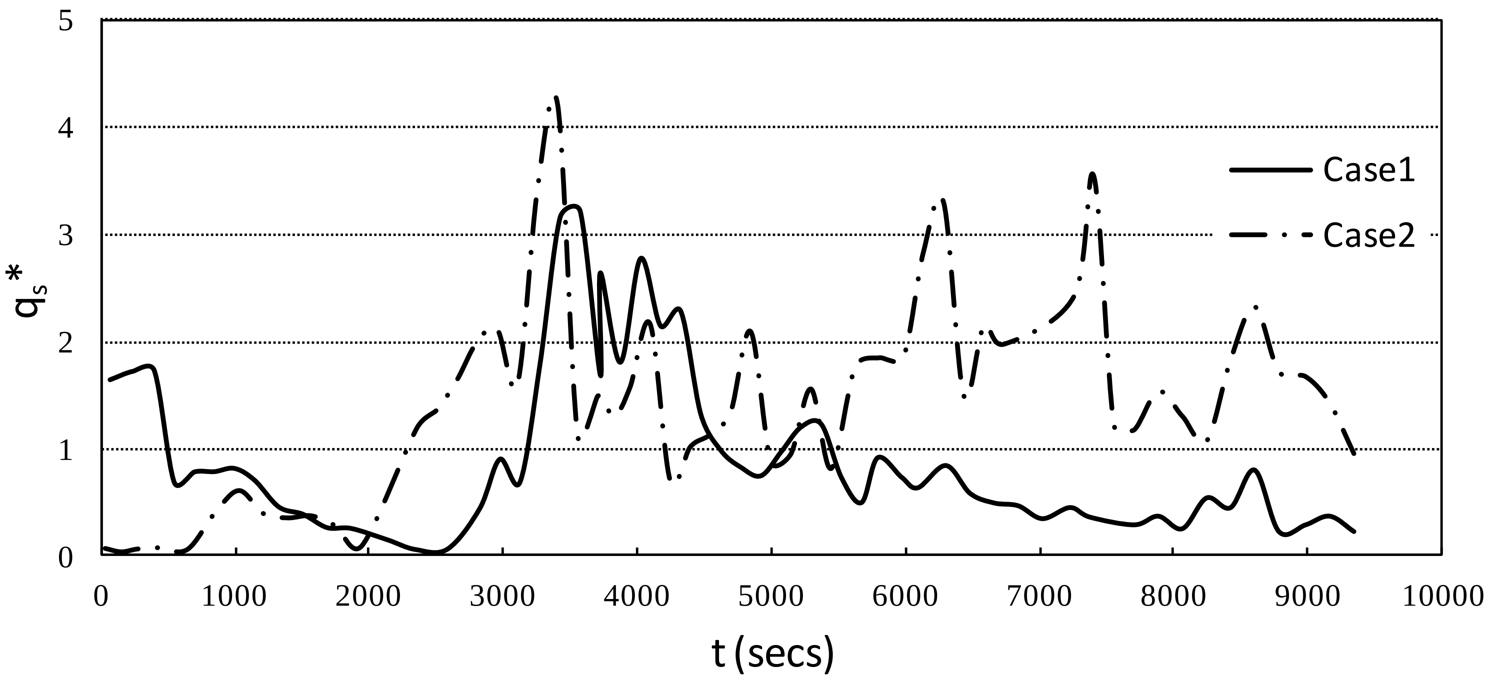

Figure 5.6 Normalized bed-load transport rate during the clean water scour process

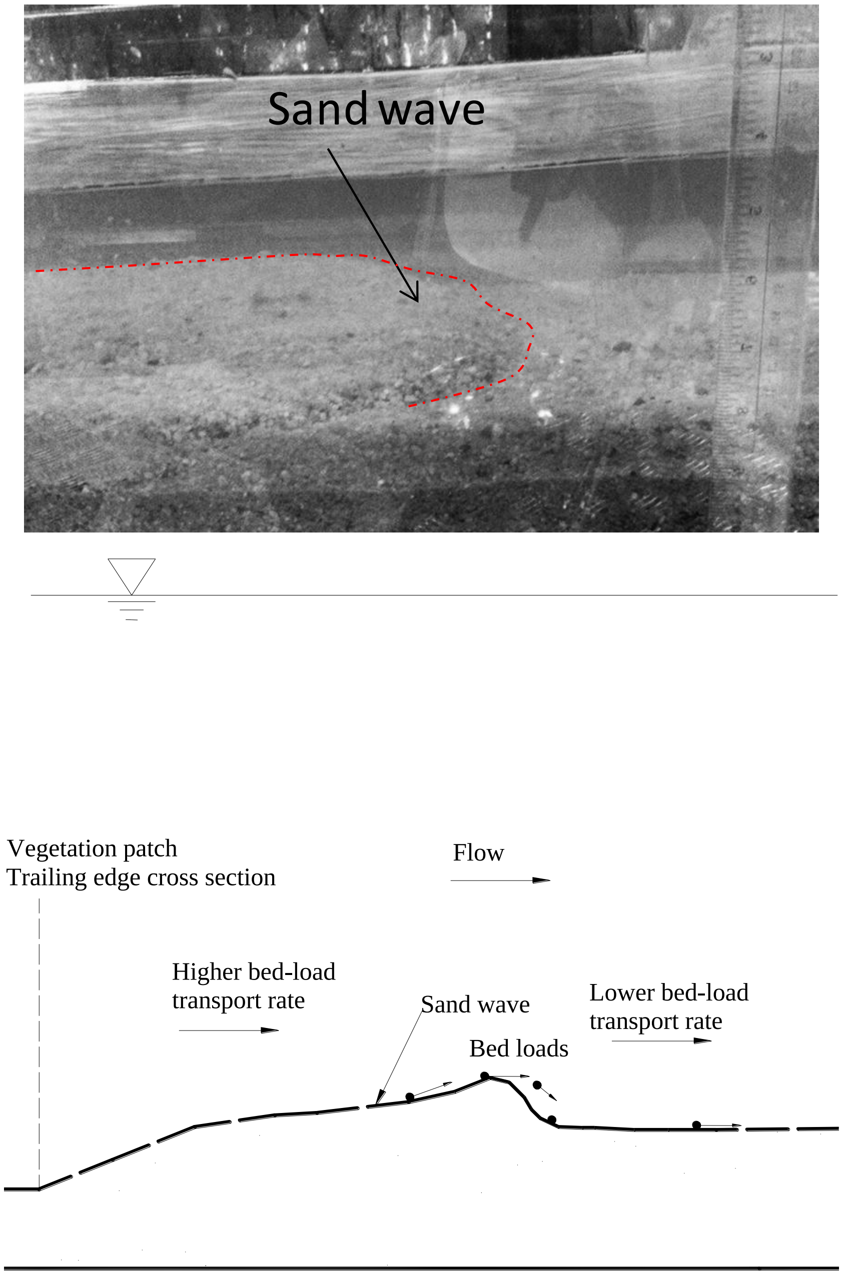

Figure 5.7 Sand wave propagation observed at the downstream reach. At the non-vegetated side, abundant sediment is transported from the vegetated reach. The upstream bed-load transport rate is much larger than the downstream transport rate, resulting in sand waves at the downstream reach.

5.3.1.2 Sediment sorting effect in the bed-load transport process

Due to the non-uniformity effect of bed materials, the temporal sorting phenomenon is expected to occur in bed-load transport. Figure 5.8a shows the proportion of each particle composition in bed-load transport. Compared with the initial sediment mixture, the finest sediment composition (<0.15mm) almost disappears. This agrees well with the suggestion of Gomez and Church (1989) that the finest sediment (<0.15mm) is transported as the suspended loads. It is observed that compositions of sediment mixture are adjusted. In bed-load transport process, the range of 0.6mm-3.25mm is dominant (e.g., t>2825s for Case1, and t>2660s for Case2). The proportion of dominant sediment range at most increases by 50% relative to the initial sediment mixture. The finest range and the coarsest range significantly decrease correspondingly in sediment mixture. However, when the transport rate decreases to the minimum, the proportion of sediment of fine range greatly increases (e.g., t=2585s for Case1, and t=1575s for Case2). This indicates that the sand wave not only suppresses the sediment transport at the downstream but also enhances the fining effect of the transported sediment mixture.

The sorting phenomenon can be further interpreted through the characteristics of transported sediment mixture, which are the variations of median diameter ($d_{50*} = d_{50} / d_{50ini}$) and geometric deviation ($\sigma_{g*} = \sigma_g / \sigma_{gini}$) presented in Figure 5.8b. When the transport rate decreases, d_{50*} greatly decreases, lower than the initial value of the initial sediment mixture. This is consistent with previous observations. The geometric deviation greatly increases, indicating high non-uniformity of sediment mixture. d_{50*} is generally larger than the initial value, which corresponds to the achievement of the global maximum of q_{s*}. This is consistent with the increasing proportion of sediment size in the range of 0.6mm-3.25mm. Clearly as shown in Figure 5.9, d_{50*} and σ_{g*} are essentially coherent with the sand wave propagation. This is because, before the arrival of the sand wave at the channel exit, the small bed shear stress at the downstream reach only can transport fine sediment. Bed-load transport rate would decrease as the sand wave approaches to the sediment collection site. However, after the sand wave passed the sediment collection site, d_{50*} increased again with the increasing bed-load transport rate.

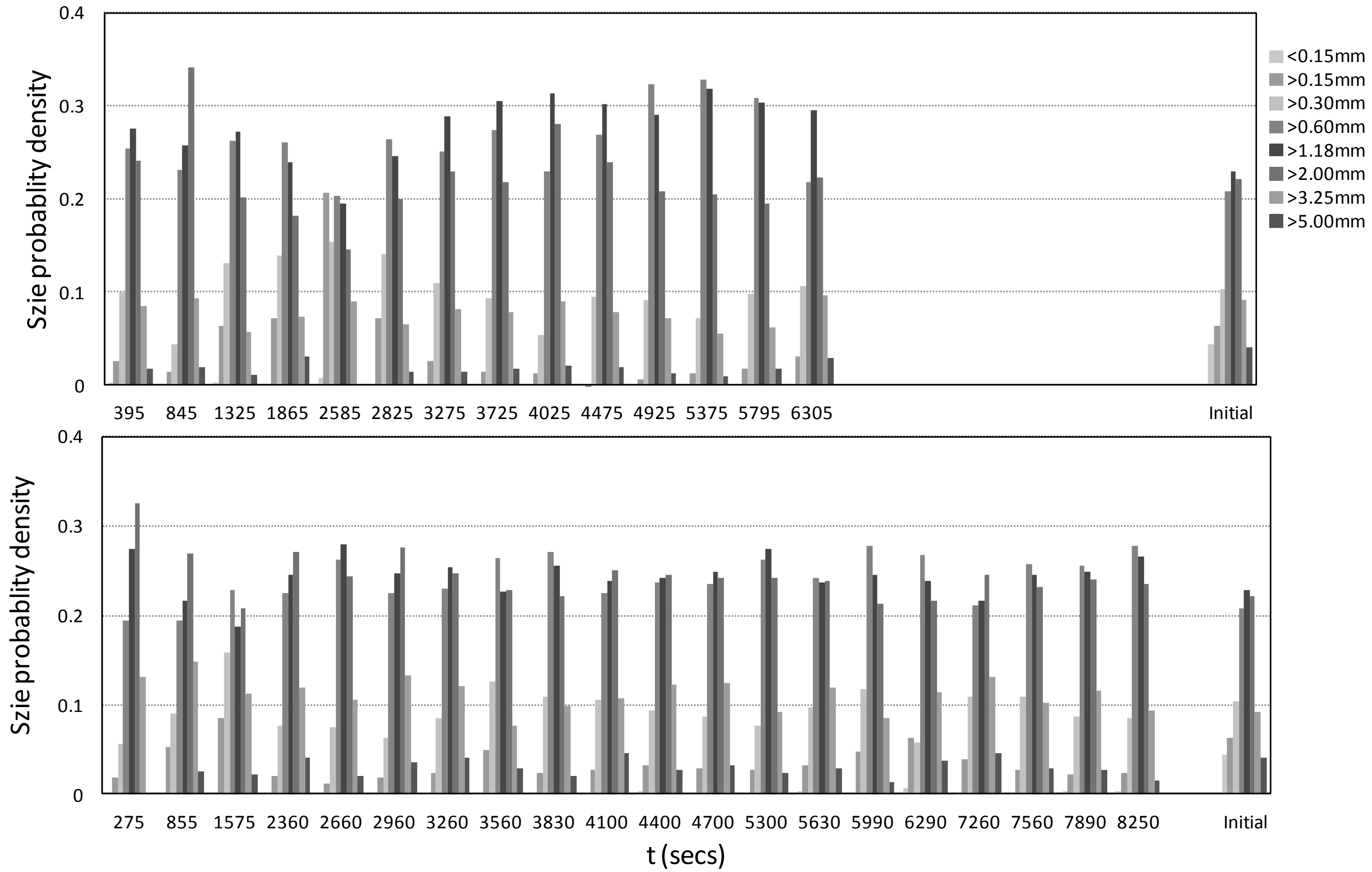

Figure 5.8 Proportion of grain size range in the transported bed loads

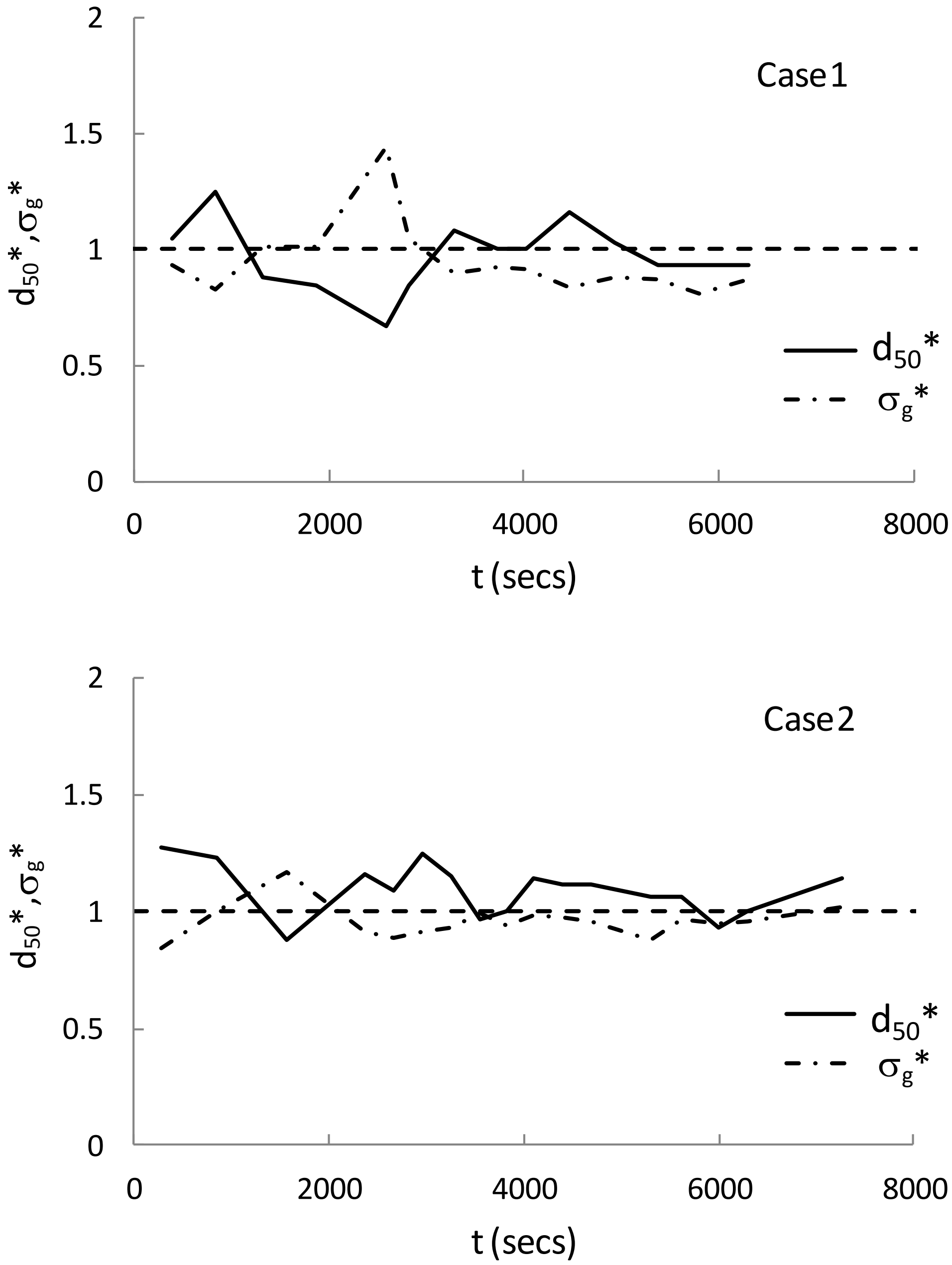

Figure 5.9 Sorting properties of the transported bed loads

5.3.2 Bed morphology

In real simulations, characteristic bed morphology occurs in response to specific flow configuration. The generated bed morphology, besides the flow-vegetation interaction, tends to facilitate the complexity of flow characteristics. Therefore, it is required to recognize the characteristic bed morphology in the POCVC to further benefit the understanding of the flow-vegetation-sediment interaction.

5.3.2.1 Transverse bed profiles

Figure 5.10 shows the transverse bed profiles at the equilibrium state. For Case1 (Q=0.0125m^3/s), there is little bed erosion upstream of the non-vegetated reach. This indicates the given flow condition is below the threshold of incipient motion of bed materials. The greater flow rate (Case2, Q=0.0166m^3/s), however, leads to relatively strong erosion, which is still less than 20% of initial bed layer thickness. At the vegetated reach, the apparent local erosion occurs at the entry of the vegetation canopy (x/L_p=0.025). At that location, for Case1, bed elevation on the vegetated side exceeds that on the non-vegetated side due to local bed scour. For Case2, bed elevation on the two sides is almost equal. The comparison suggests that the large flow rate leads to the great local erosion of non-vegetated side at the entry of vegetation canopy. The occurrence of local erosion at the entry of vegetation canopy agrees with the finding by Kim et al. (2015). The cause of this local erosion has not been explained. There are two possibilities: one, the increasing local flow velocity due to the reduction of the cross-sectional area by the vegetative occupation tends to induce the local bed scour and two, as the flow meets the vegetation canopy, downflow tends to be generated, similar to the flow behavior around the bridge pile. The downflow is able to promote bed scour. It is believed that the above two aspects might both contribute to the local bed scour at the entry of the vegetation canopy.

Taking y/b_v=0.533 as an example, the scour area extends to 0.05L_p and 0.2 L_p for Case1 and Case2, respectively. Therefore, it is inferred that the local erosion longitudinal length is also positively related to the incoming flow intensity (e.g., flow rate) in addition to vegetation density reported by Kim et al. (2015).

As flow propagates downstream, the erosion on the non-vegetated side dominates bed morphology evolution owing to flow convergence in the NOWR. The bed on the vegetated side, however, nearly keeps its initial elevation. The scour depth reaches maximum (Z_b/Z_{bini}=0.35 and 0.15) at x/L_p=0.625 for Case1 and Case2. This location is consistent with that of flow being fully developed in partly-obstructed channels over a flat bed. The transverse bed profile evolves to an analogous tangent parabolic curve. The scour depth for the large flow rate (Case2) generally exceeds that for the small flow rate (Case1). At the downstream, the erosion transversely extends to the bed on the vegetated side for both cases. Larger transverse erosion corresponds to a larger flow rate. In addition, it is clear that the bed on the vegetated side bulges at the boundary (i.e. x/L_p>0.825) between the greatly-eroded bed and less-eroded bed. This bulge extends to the downstream and broadens in the wake region of the vegetation canopy, leading to a sediment bar. In fact, sediment bars can be found after the vegetation canopies in a realistic scenario. Tooth and Nanson (2000) and Euler et al. (2014) observed that a long sediment ridge occurs behind the vegetation canopy in fieldwork.

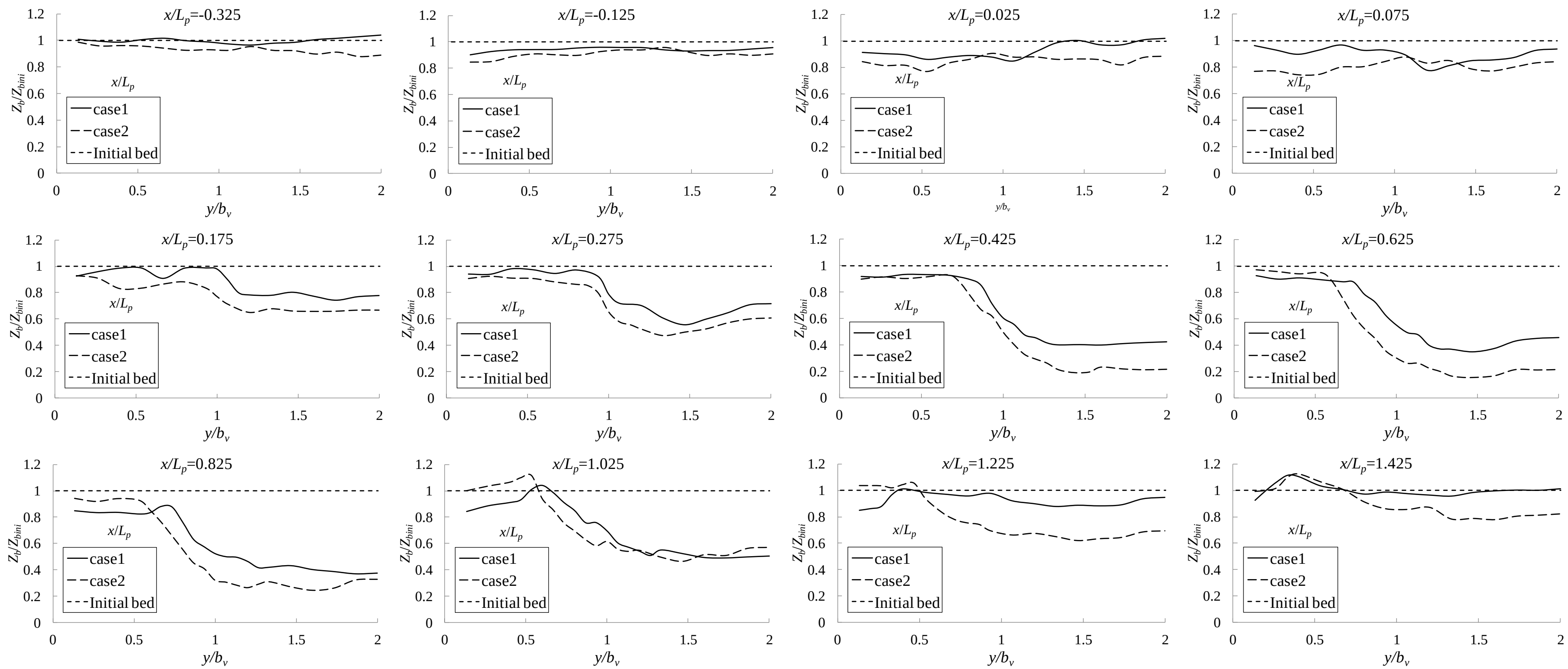

Figure 5.10 Transverse bed profiles after clean water scour along the channel

5.3.2.2 Longitudinal bed profiles

Figure 5.11 shows the longitudinal bed profile of three transects. As can be clearly noted, a large-scale water pool lays in the NOWR because of the significant scour. For the large flow rate (Case2), it can be observed that a shorter distance is required for the water pool to reach the maximum depth (x/L_p=0.375), compared with the small flow rate (Case1, x/L_p=0.625). The scour depth decreases after the vegetated reach resulting in an upslope and a downslope formed between the leading edge and trailing edge, respectively, which may control bed-load transport and sorting effect in the water pool. For y/b_v=0.533, the bed morphology displays a contrary trend of erosion with respect to the two flow rates. For the small flow rate (Case1), the bed morphology is mainly characterized with downstream degradation. For the large flow rate (Case2), despite general erosion, the bed is hardly eroded deep inside the vegetation canopy.

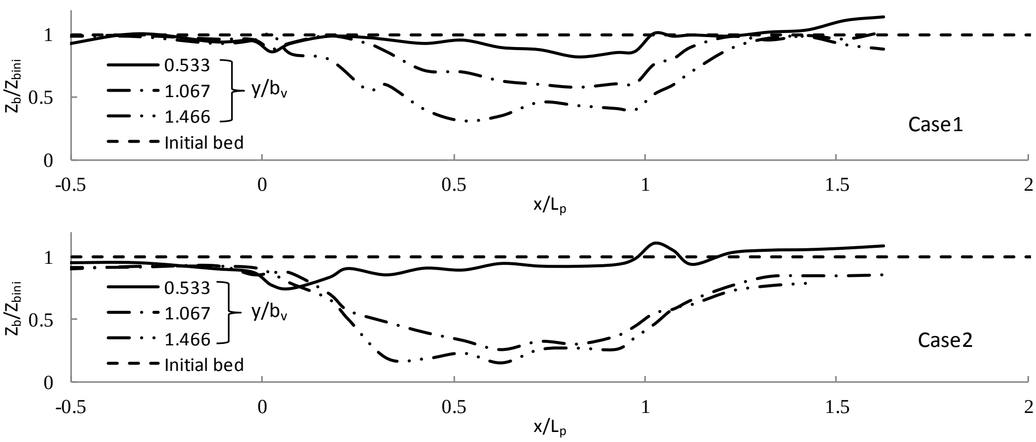

Figure 5.11 Longitudinal bed profiles in clean water scour.

It is worth noting that the spatial position and pattern of the water pool observed in the present study differs from the result of Kim et al (2015) who studied a short vegetation canopy (i.e., L_p=0.6m) as shown in Figure 5.12. In that study, the equilibrium position (i.e., largest scour) of the water pool begins near the trailing edge of the vegetation canopy (i.e., L_p=0.5m) and ends at the downstream (i.e., 1.5L_p=0.75m). The equilibrium position of the water pool in the present study, however, spans from the longitudinal center of the vegetation canopy (i.e., 0.5L_p=1.0m for Case1 and 0.3L_p=0.6m for Case2) to the trailing edge (i.e., L_p=2.0m for both cases). The substantial different spatial patterns of the water pool might be attributed to the different flow patterns. In the present study, since the canopy length is sufficient (i.e., L_p=2m), the flow adjustment distance (i.e., 0.6L_p=1.2m) does not exceed the vegetation canopy length, which means that flow became fully developed within the vegetated reach. With respect to the study of Kim et al. (2015), the canopy length is so short that the according flow adjustment distance is not sufficient for flow to be fully developed before exiting the vegetated reach. The depth-averaged flow velocity property, in terms of the spatial distribution, is found to be consistent with the scour pool for the two studies as discussed above. The flow pattern, therefore, can be used to understand the characteristics of bed morphology due to the presence of the partially-distributed vegetation canopy. This finding is important since the spatial distribution of the pool can be predicted on the basis of the vegetation canopy length. Unquestionably, the influence of canopy length on external flow evolution and associated bed morphology evolution should be further considered by such as varying the geometric configuration of vegetation canopy for a further interpretation of flow-vegetation-sediment interaction.

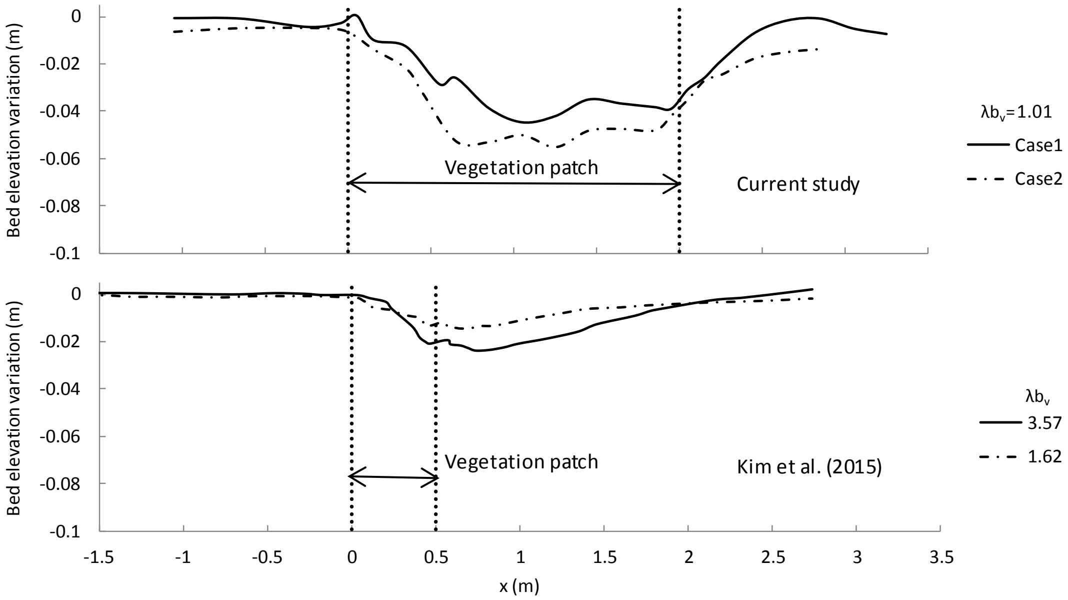

Figure 5.12 Comparison of the spatial distribution of the generated water pool on the vegetated side.

Apart from the water pool as a main feature on the vegetated side, the sediment bar extending from the vegetation region to downstream at the wake of the vegetation canopy is another outstanding bedform. This latter is the result of flow diverging at the downstream reach. Kim et al. (2015) also showed that a very narrow sediment ridge is formed in the wake region of vegetation canopy. The sediment ridge lay on the non-vegetated side close to the channel center. However, Figure 5.13 shows that the sediment bar for the present study is formed on the vegetated side, extending from the VR to the downstream reach. In addition, the sediment bar in the present study is noted to sway toward the channel bank at the downstream, while in the study of Kim et al. (2015) remains nearly straight. It is believed that the difference in the pattern of sediment bar distribution is associated with vegetation canopy configurations. Under similar vegetation density, the length of vegetation canopy for the present study is 2m, which is four times that in Kim et al. (2015).

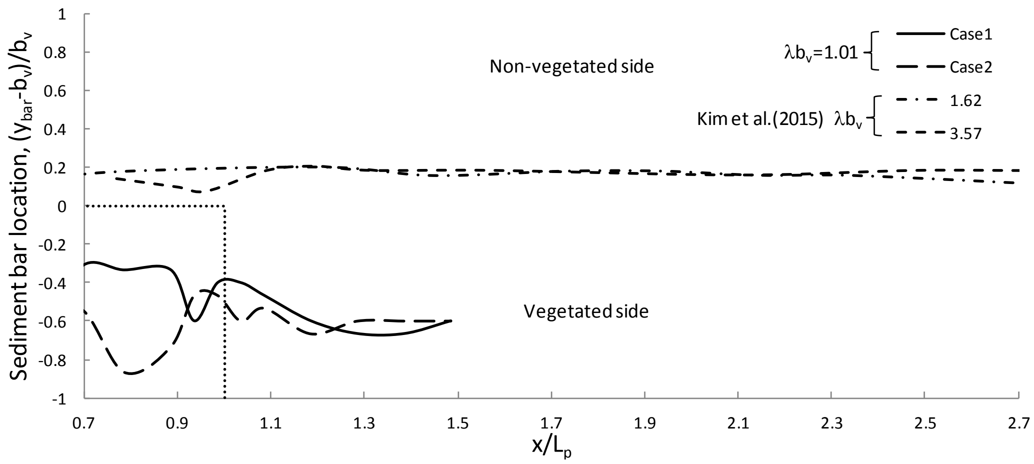

Figure 5.13 Pattern of the sediment bar (bar peak location relative to the vegetation canopy). The dotted line indicates vegetation canopy edges

5.3.2.3 General bed morphology pattern

Figure 5.14 shows the equilibrium bed morphology after a clean water scour in the POCVC. For a convenient identification, characteristic bedforms are labeled from A to F. They are (A) water pool induced by flow convergence in the NOWR, (B) slightly-eroded bed protected by the vegetation canopy in the VR, (C) slightly-eroded bed upstream of the vegetation canopy, (D) local bed scour near the leading edge of the vegetation canopy, (E) sediment bar with surface fining extending downstream after the vegetation canopy, and (F) riffle downstream of the vegetated reach.

The partial blockage by the vegetation canopy induces typical bed morphology similar to the pool-riffle sequence. It is reasonable to believe that complex pool-riffle sequences are produced if repeated or alternative vegetation canopies are introduced in the open channel. When the water level decreases, flow characteristics over the generated pool-riffle sequence morphology should be more outstanding (i.e. the mean flow velocity is larger as flow passes the riffle and smaller as flow passes the pool), compared with flat bed morphology. Pool and riffle sequences are ecologically valuable to river restoration and species rehabilitation, since the heterogeneity in bed morphology can produce diverse habitats and flow conditions which encourage the flourishing of a biodiversity of species (Güneralp et al., 2012; Hauer et al., 2011).

Unlike the formation of pool-riffle sequence due to the presence of a vegetation canopy in this study, the pool-riffle bedforms are self-motivated by complex a flow field, including secondary flows and fluctuating turbulent flows. To some extent, the pool-riffle sequence is the self-adjustment of the channel bed and the generation of the pool-riffle sequence effectively decreases the enlarged flow energy on the non-vegetated side. However, the introduction of vegetation in the open channel (e.g. vegetation colonization or waterflooding) directly alters initial flow structure and bed shear stress. The formation of the pool-riffle sequence is a passive process. This is similar to the method of river restoration, in which deflectors are commonly used in the river to increase the variability of flow pattern and bed morphology (Biron et al., 2004; Jamieson et al., 2013). Compared with introduced deflectors, vegetation is more eco-friendly to the environment (Palmer et al., 2005) since its colonization on channel bed can be normally processed in a more natural way.

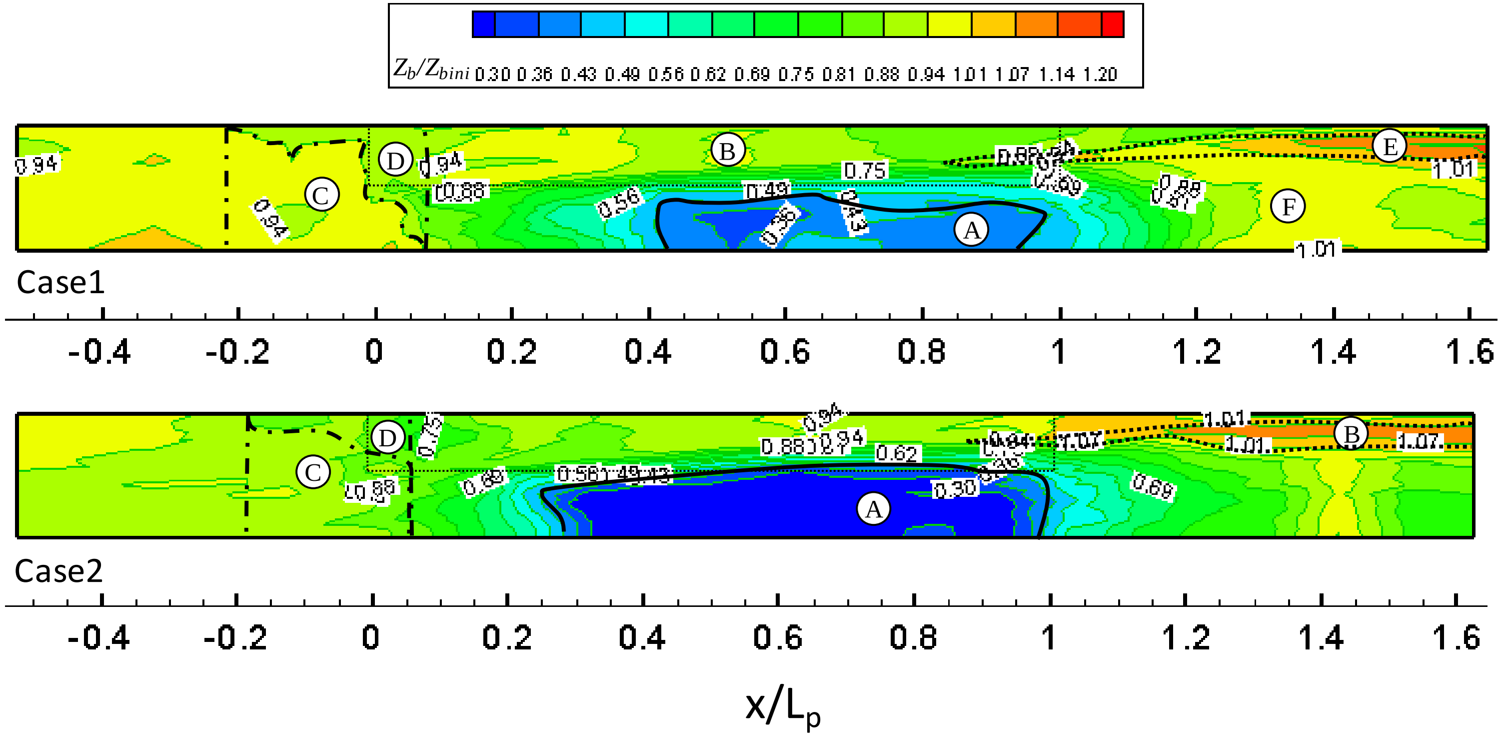

Figure 5.14 Equilibrium bed morphology. The dotted rectangular square indicates the location of vegetation canopy. The origin is located on the left bank wall at the leading edge.

Figure 5.14 shows the spatial variation of bed shear stress (τ_b) for Case2, which is calculated by near-bed Reynolds stresses (see Eq.2.8). It can be observed that two zones for the large magnitude of the bed shear stress clearly occur at the vegetated reach and downstream of the vegetated reach, respectively. In the vegetated reach (x/L_p=0-1), the bed shear stress is overall small and ranges from 0.1 to 0.6. According to the suggested critical bed shear stress (0.47-1.3 N/m^2) by Table 2.1 for current sediment size (d_{50}=1.42mm), the calculated bed shear stress is overall smaller than the critical bed shear stress. This indicates the generation of the bed armor at the vegetated reach. Downstream (x/L_p=1-1.2) particularly in the junction region and NOWR, the bed shear stress greatly increases to a high level (1.6 N/m^2). This longitudinal region in fact forms the exit of the pool, where an adverse bed slope occurs. Therefore, the significant bed form resistance is expected to correct the critical bed shear stress necessary to enable the incipient motion of sediment.

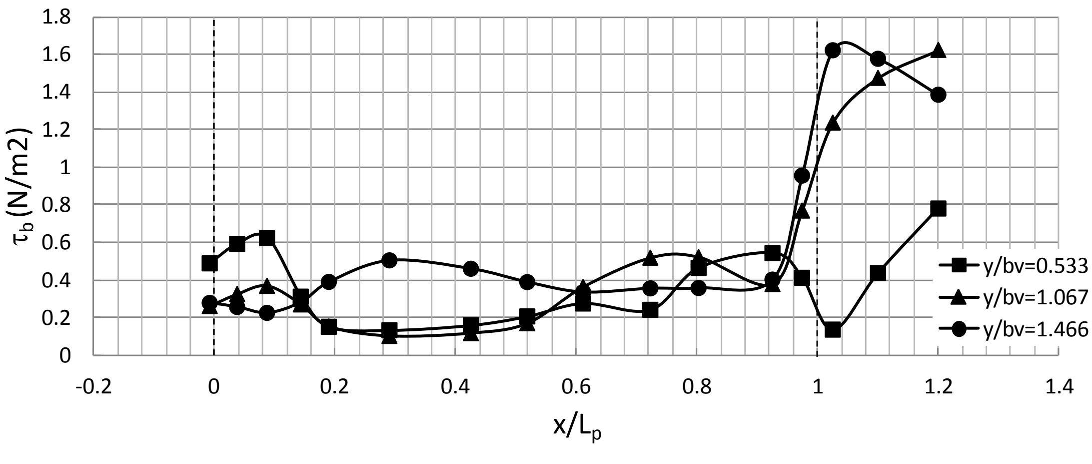

Figure 5.15 Longitudinal distribution of bed shear stress along the channel for Case2. Dashed lines indicate leading and trailing edges of vegetation canopy.

Figure 5.15 shows the transverse variation of the bed shear stress downstream of the channel. At the entry region of the vegetated reach (x/L_p=0.120), high bed shear stress occurs at the junction. As flow propagates downstream, the bed shear stress on the non-vegetated side increases while that on the vegetated side remains small. It should be noted that after x/L_p =0.738, the increase onset of the bed shear stress in the transverse profile gradually extends to the inner vegetation region, corresponding to the same trend in the transverse bed profile (see Figure 5.9).

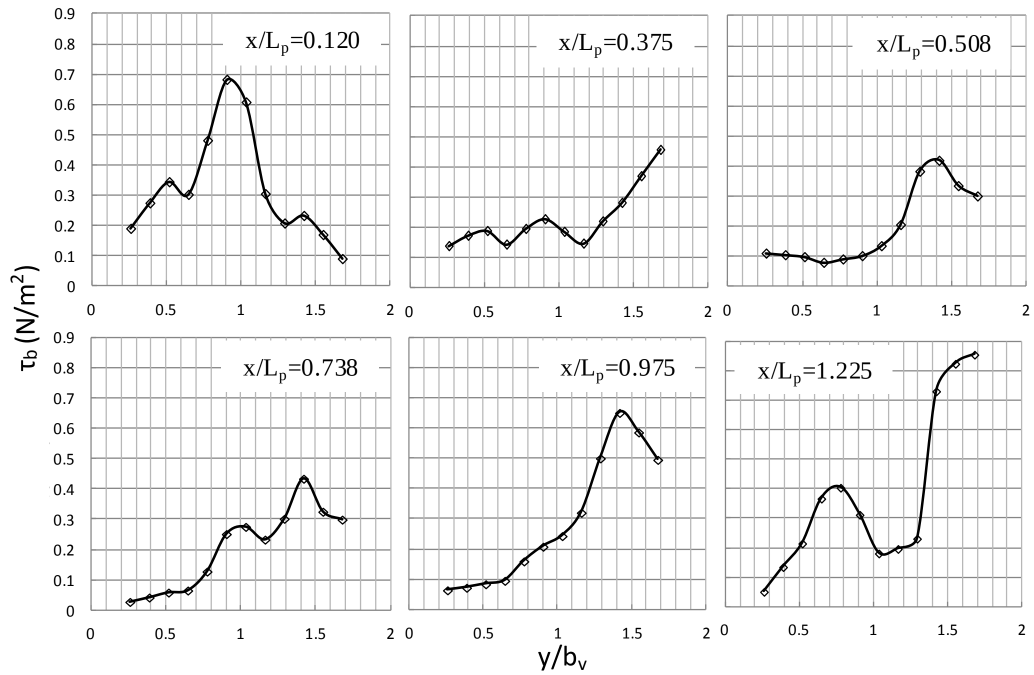

Figure 5.16 Transverse distribution of bed shear stress along the channel for Case2.

5.3.3 Flow characteristics over equilibrium bed morphology

In real situations, flow generally exists over bed morphology due to alluvial process. In the present experiment, the near-bed flow structure motivates bed surface sediment, resulting in various bedforms and sediment sorting. The generated uneven boundary of bed morphology, in turn, impacts the flow structure by exerting resistance force on flow body. Therefore, the mutual processes lead to the ultimate equilibrium bed morphology. It is difficult to achieve the transient flow structure during the evolution of bed morphology owing to the quick boundary change. In the dissertation, investigation of the flow structure over the equilibrium bed was carried out, which is helpful to demonstrate and explain water mass and momentum transport, passive scalar transport characteristics (e.g. suspended load transport and contaminant diffusion) and bed surface sediment conditions (e.g., armor effect and bed surface sorting).

5.3.3.1 Depth-averaged (DA) flow characteristics

Figure 5.17a shows longitudinal profiles of DA longitudinal velocity. It is observed that the locations of flow being fully-developed at the three longitudinal transects are different. The flow adjustment distance reaches L_{in}=0.6L_p in the VR and L_{out}=0.28L_p in the NOWR. The result, with respect to the flat bed, observed by Yan et al. (2016) in the same channel is illustrated in Figure 5.17b. In comparison, the inner flow has the similar adjustment distance (i.e., L_{in}=0.6L_p) over the sediment bed and flat bed. In the NOWR, the outer flow over the flat bed needs a longer distance for adjustment (i.e., L_{out}=0.42L_p for flat bed and L_{out}=0.28L_p for sediment bed), indicating that the degraded bed morphology is capable of fastening the adjustment of external flow by increasing water depth.

Rominger and Nepf (2011) suggested that the adjustment distance of internal flow in the VR for a low-flow blockage vegetation canopy is associated with the vegetation density (a) and canopy width (b_v), $L_{in} = (3.0 \pm 0.3)\left[\frac{2}{C_d a}(1+(C_d a b_v)^2)\right]$. According to the formula, the adjustment distance for the present flow configuration varies in the range of 1.62m-1.98m. This is larger than the observed result (L_{in}=1.2m). Yan et al (2016) demonstrated that the aspect ratio (channel width/water depth) of the channel is the root cause of the difference. The aspect ratio of Yan et al (2016) is 2.153, much smaller than 8.6 of Rominger and Nepf (2011).

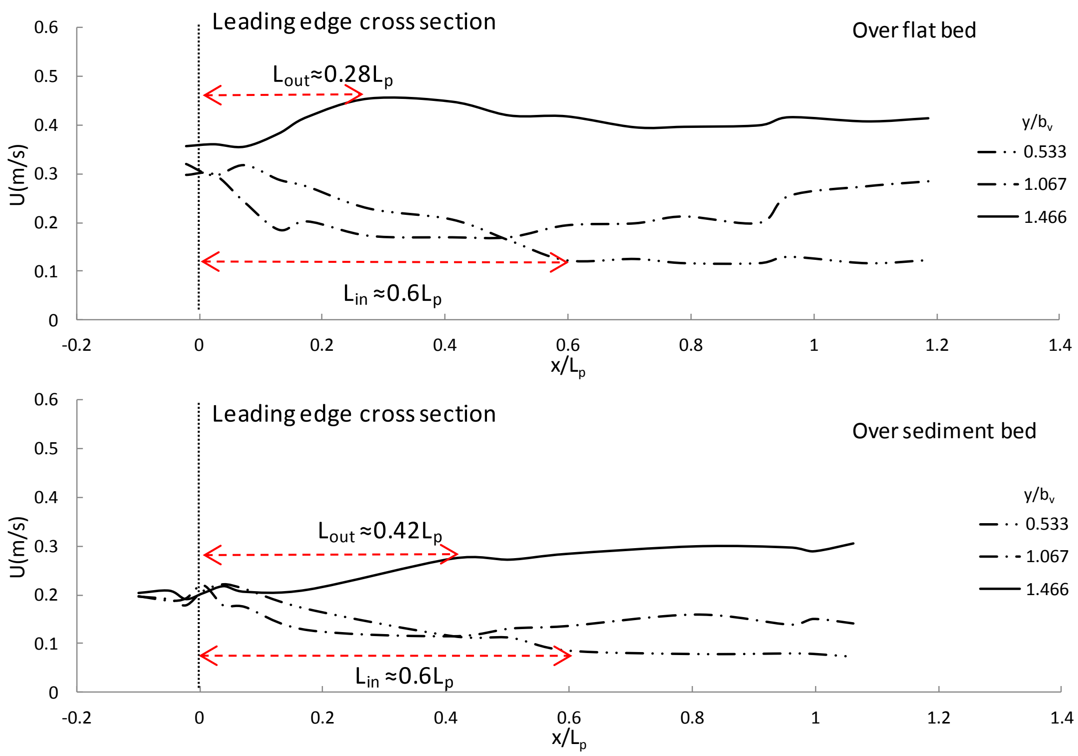

Figure 5.17 Longitudinal profiles of the DA longitudinal velocity.

Interestingly as shown in Figure 5.18, the DA longitudinal velocity of external flow in the NOWR becomes fully-developed at x/L_p=1.3 (approximately the maximum point) in Kim et al. (2015). This essentially disagrees with the result that the maximum occurs at x/L_p=0.28 in the vegetated reach in the present study. In comparison of the two studies, it appears that the difference in geometric configurations of the vegetation canopy is probably the root reason leading to the different results. In the present study, the canopy length is L_p=2.0m, thus exceeding L_p=0.5m given in the study of Kim et al. (2015). It is probable that under the long vegetation canopy in the present study, the flow resistance imparted by the sediment roughness and bed form force is sufficient to allow external flow to evolve to an equilibrium state in the range of vegetation canopy. Nevertheless, the short vegetation canopy in Kim et al. (2015) fails to do so.

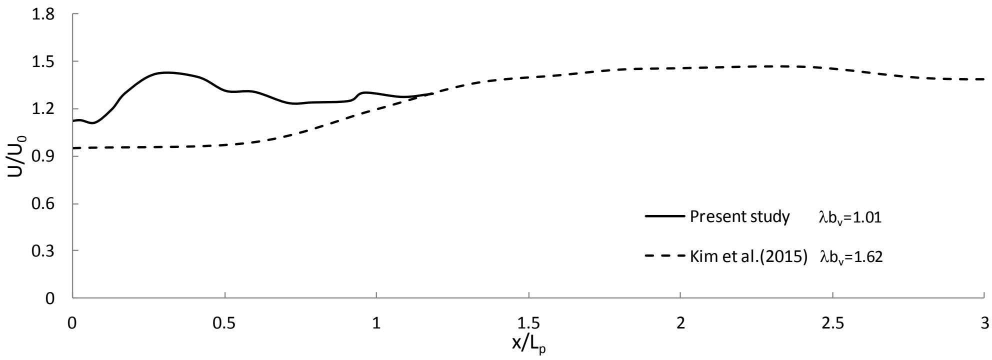

Figure 5.18 Comparison of DA longitudinal velocity between the present study and Kim et al. (2015).

Figure 5.19 shows the transverse profile of DA longitudinal velocity. It is noted that due to partial blockage by the vegetation canopy, the transverse profile of longitudinal velocity gradually adjusts downstream. The velocity profile is nearly fully developed at x=1.402m (0.7L_p) consistent with the flow adjustment over flat bed. When the flow exits the vegetated reach, the DA longitudinal velocity increases in the VR and decreases in the NOWR due to the reattachment of flow.

Figure 5.20 shows the transverse distribution of DA transverse Reynolds stress (τ_{yx}/ρ). As the flow enters the vegetated reach, local maximum is observed in the NOWR (x=0.162m). However, flow quickly adjusts with the local maximum occurring in the junction and continuously growing downstream. It should be noted that the flow adjustment regarding transverse Reynolds stress is consistent with that regarding the longitudinal velocity. At the downstream of the vegetated reach, the maximum of transverse Reynolds stress increases again. In the wake region of the vegetation canopy, the magnitude of transverse Reynolds stress is also noticeable due to the growth of horizontal coherent vortices.

Figure 5.21 shows the transverse distribution of DA turbulent kinetic energy (TKE). It is likely that the generation of horizontal coherent vortices is the main source in generating TKE and its maximum occurs in the junction but remains at a high level in the NOWR differing from τ_{yx}/ρ. This might be attributed to the turbulence induced by the deformed bed. TKE becomes pronounced in the canopy wake where the longitudinal sediment bar is formed.

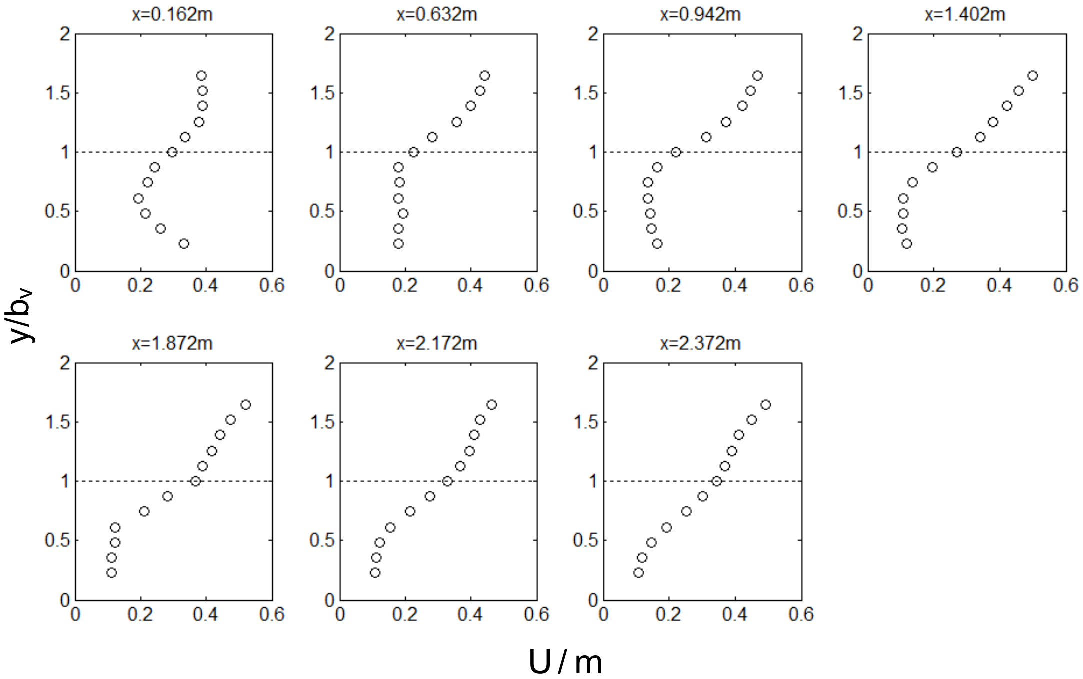

Figure 5.19 Transverse profile of DA longitudinal velocity.

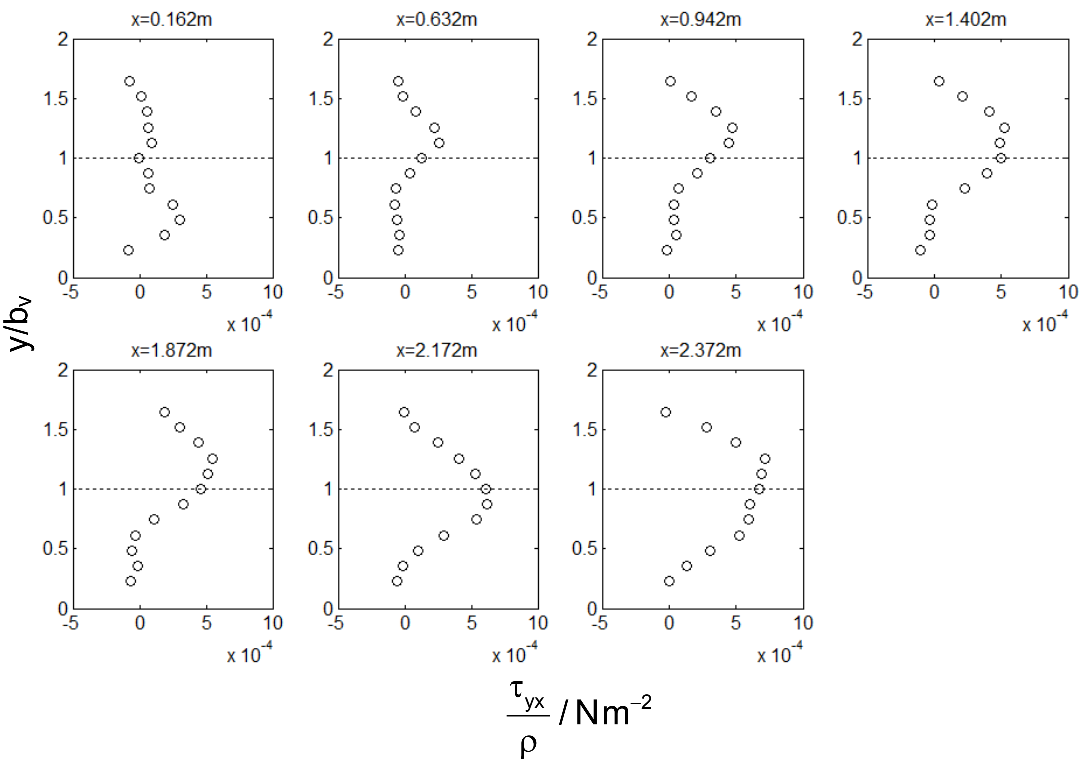

Figure 5.20 Transverse profile of DA transverse Reynolds stress.

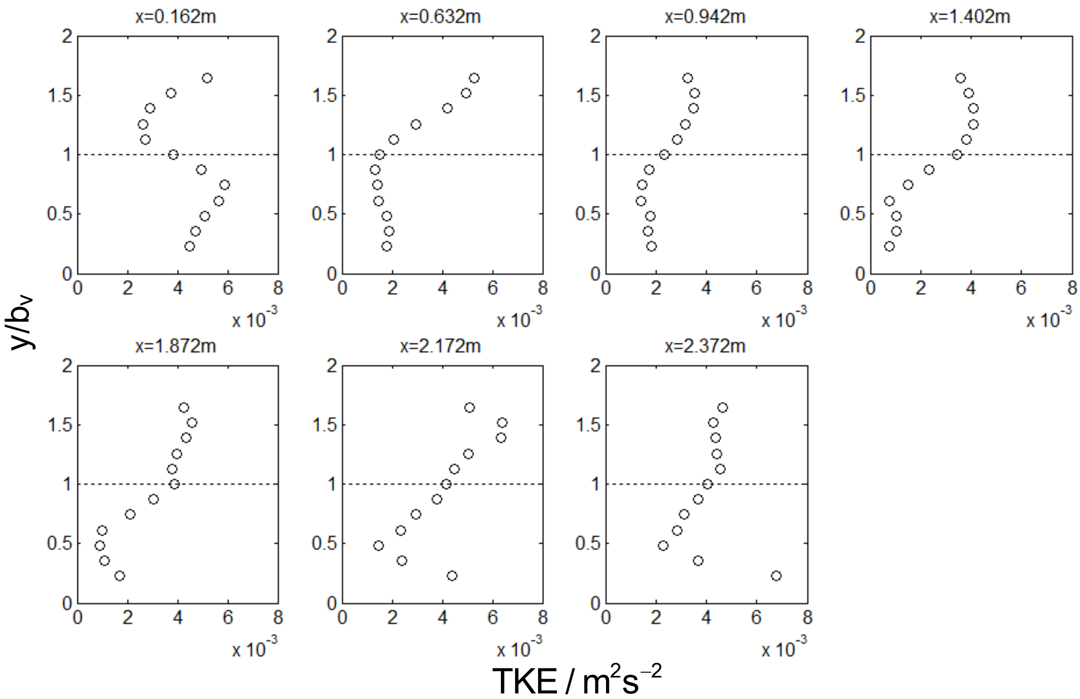

Figure 5.21 Transverse profile of DA turbulent kinetic energy.

5.3.3.2 3D distribution pattern of flow characteristics

$\bar{u}$ -profile

Figure 5.22 shows the $\bar{u}$ -profile over generated transverse bed topography at different cross-sections along the vegetation canopy. Near the entry (x/L_p=0.118), it can be observed that the $\bar{u}$ -profile performs regularly across the channel. $\bar{u}$ on the vegetated side obviously decreases while on the non-vegetated side roughly follows the logarithmic law. As flow propagates downstream, it is clear that the $\bar{u}$ -profile is deflected in the near-bed region of the junction and maximum magnitude occurs near the bed. The same phenomenon occurs over flat bed in the POCVC. The is attributed to the generation of horizontal coherent vortices in the junction. Differently, a two-stage bed topography, analogous to compound channel bed, is developed under current flow configuration. As reported, horizontal coherent vortices can be generated, laterally spanning compound channel beds (Nezu and Nakayama (1997) and Ghidaoui and Kolyshkin (1999). Therefore, it should be expected that the coexistence of vegetation canopy and two-stage channel bed might both enhance the generated horizontal coherent vortices and thus the associated flow characteristics. As flow exits the vegetated reach, the velocity deflection effect shifts to the vegetated side (e.g., x/L_p =1.186 y=0.10m-0.20m). This actually corresponds to horizontal coherent vortices expanding toward the vegetated side owing to the absence of vegetation canopy.

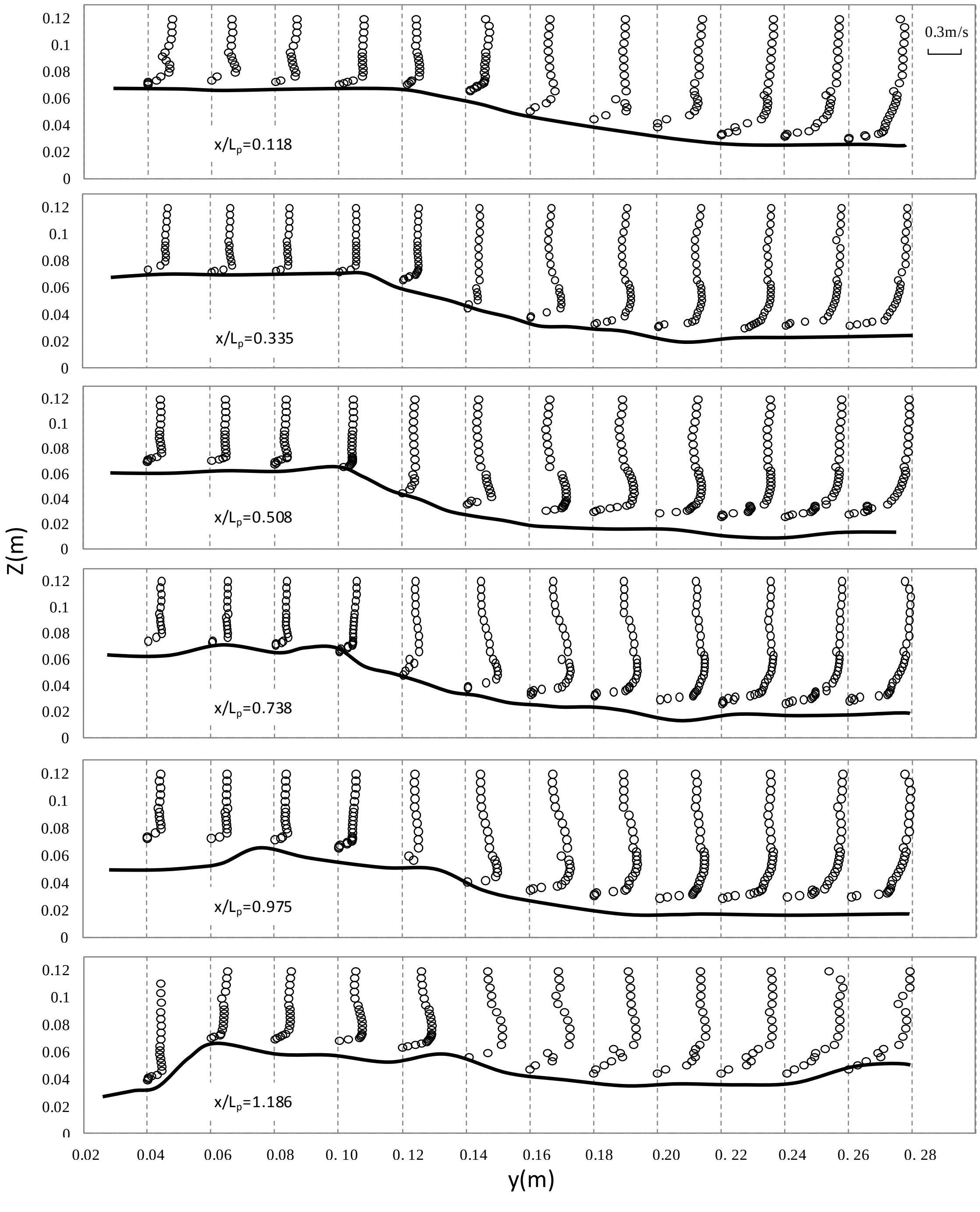

Figure 5.22 Vertical profiles of the longitudinal velocity at different transverse locations.

In the vegetated reach, a scour pool is generated in the NOWR, adjacent to the vegetation canopy. However, the bed deep inside the VR is well protected by the presence of the vegetation canopy. The two-stage bed morphology analogous to the compound channel is generated in the vegetated reach. As is well known, secondary flows triggered by the irregularity of compound bed morphology in transverse direction play a significant role in mass and momentum transport of flow (Liu et al., 2013; Thomas and Williams, 1995), and scalar transport. The transverse bed surface sediment sorting is closely related to secondary flow intensity. This is commonly observed in natural rivers and laboratory channels such as meanders. Often, only fine sediment can respond to and move with the near-bed minor transverse flow motion due to secondary flows. Therefore, it is important to identify the pattern of secondary flows along vegetation canopies for a better understanding of bed surface conditions.

The secondary flow intensity can be expressed as,

$$\Omega = \frac{\partial \overline{w}}{\partial y} - \frac{\partial \overline{v}}{\partial z} \tag{5.1}$$

Figure 5.23 shows secondary flow vectors and intensity at different cross-sections along the channel. Clearly, secondary flows at different cross sections evolve downstream along the channel in terms of magnitude and spatial distribution. At the entry of the vegetated reach, flow is directed toward the NOWR due to partial obstruction of vegetation canopy. "Fluid particles" pointing toward the NOWR indicates positive spanwise velocity. However, $\overline{w}$, much smaller than $\overline{v}$, points upward in the VR and points downward in the NOWR. A significant negative core of secondary flow intensity occurs near the bed of the junction. The significant positive core near the side wall in the vegetation region should be due to the measurement error. Downstream the channel, $\bar{v}$ gradually decreases while $\bar{w}$ increases accompanied with the increase in secondary flow intensity. The transverse velocity meanwhile changes the direction in the near-bed region, corresponding to the upward-pointing vertical velocity in the junction. Consequently, a clockwise flow circulation finally forms near the bed of the junction. Further downstream, the negative core of secondary flows is enhanced and lifts upwards. With the generation of the clockwise secondary flows, the low-momentum flow in the VR is transversely transported to the NOWR at the upper layer, and high-momentum flow in the NOWR is transported to the VR at the lower layer. The generation of secondary flows is expected to transport fine sediment to the inner-side junction. Downstream the vegetated reach, the core of secondary flows transversely shifts toward the vegetated side from the junction owing to the disappearance of the vegetation canopy. The significant transverse velocity component pointing the vegetated side is expected to transport more fine sediment to the canopy wake region, agreeing well with the generation of sediment bar with surface finning.

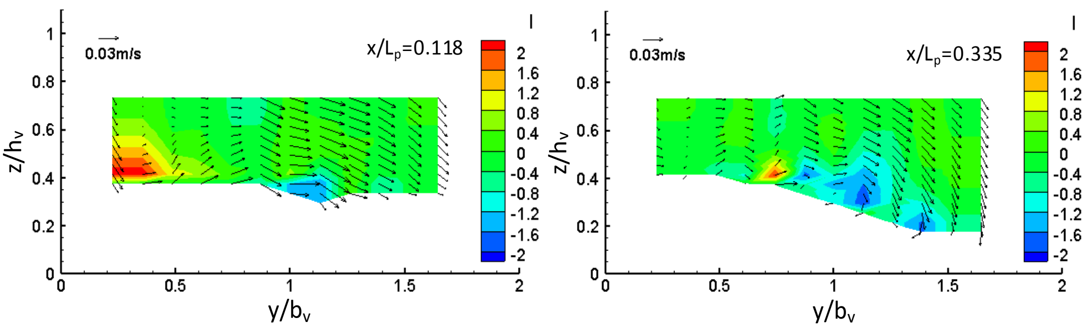

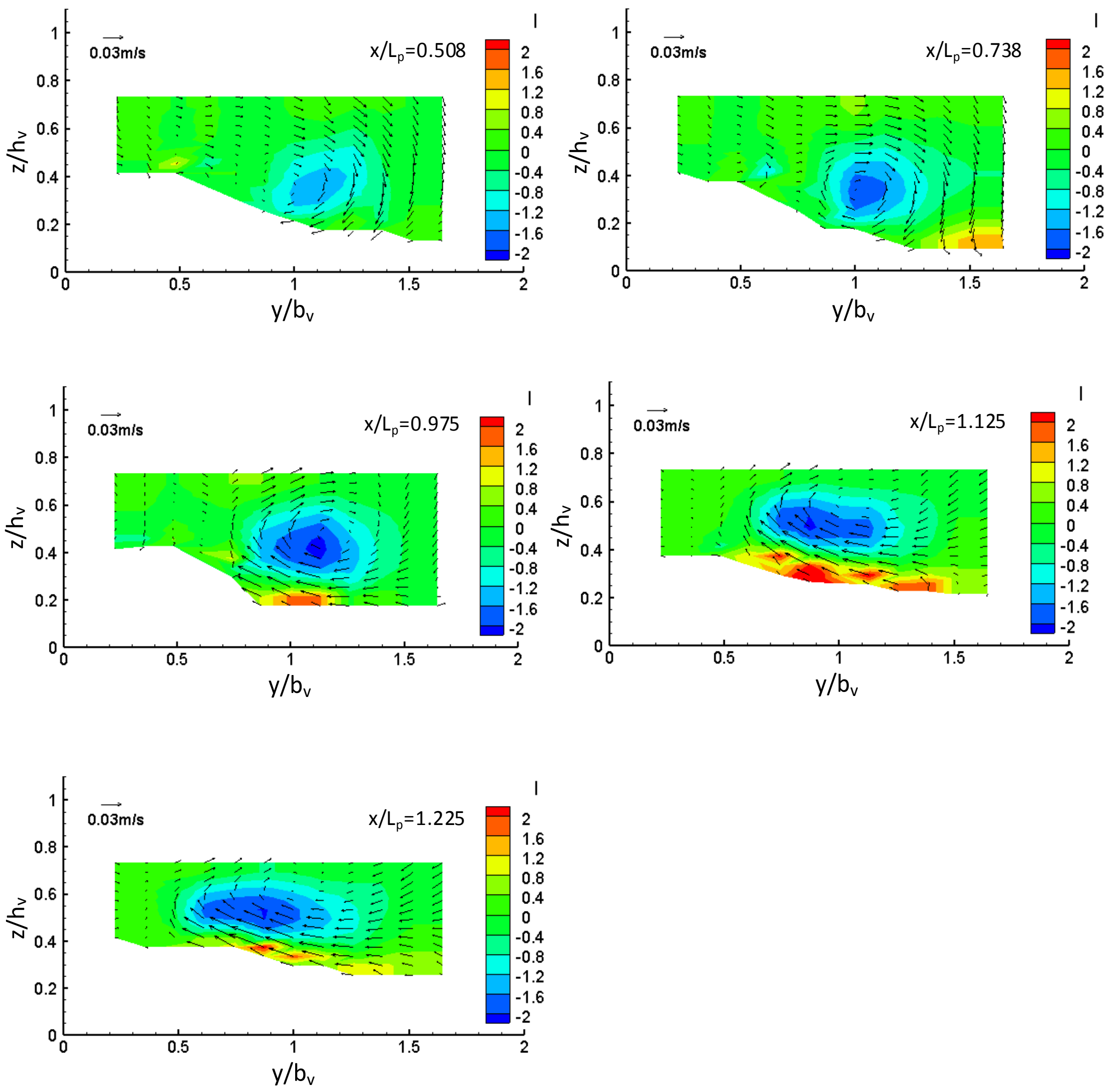

Figure 5.23 Secondary flow vectors and intensity at different cross sections along the channel.

Apart from the clockwise secondary flows generated as a role in mass and momentum transverse transport in the junction, horizontal coherent vortices are examined here regarding transverse Reynolds stress ($-\overline{u'v'}$). Figure 5.24 shows $-\overline{u'v'}$ at different cross-sections along the channel. As the flow enters the vegetated reach, $-\overline{u'v'}$ is observed to be negligible in the NOWR but relatively large in the VR. This is probably attributed to the interaction between the transverse flow motion and vegetation elements. Downstream of the channel, a remarkable positive core is found in the junction region and continuously grows downstream. The maximum occurs near the trailing edge of the vegetation canopy and remains constant at the downstream reach adjacent to the vegetation canopy wake.

It should be noted that the maximum at a certain cross-section shifts to the NOWR (roughly at y/b_v=1.25) rather than on the lateral edge of the vegetation canopy. In addition, $-\overline{u'v'}$ is negligible near the bed and gradually increases along the vertical distance from the bed. With respect to the same cross-section, $-\overline{u'v'}$ also develops as the primary flow propagates downstream. However, due to the resistance of the vegetation canopy, the transverse extension of transverse Reynolds stress toward the VR is limited by a transverse distance (y/b_v=0.8). A further transverse extension toward the vegetated side is observed in the near-bed region in the canopy wake region.

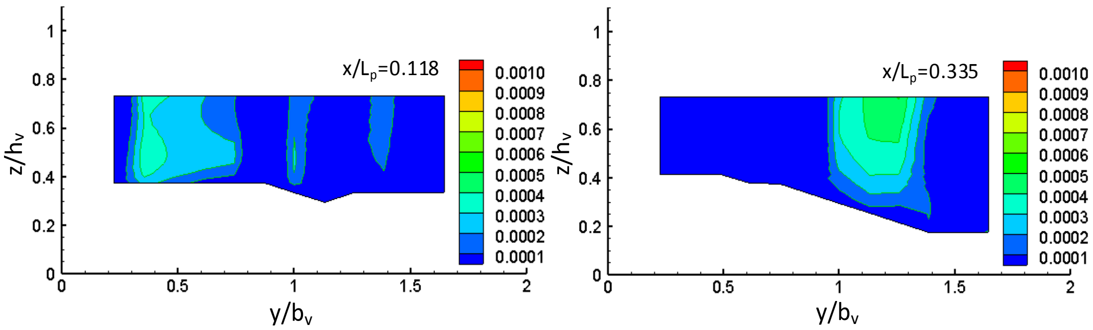

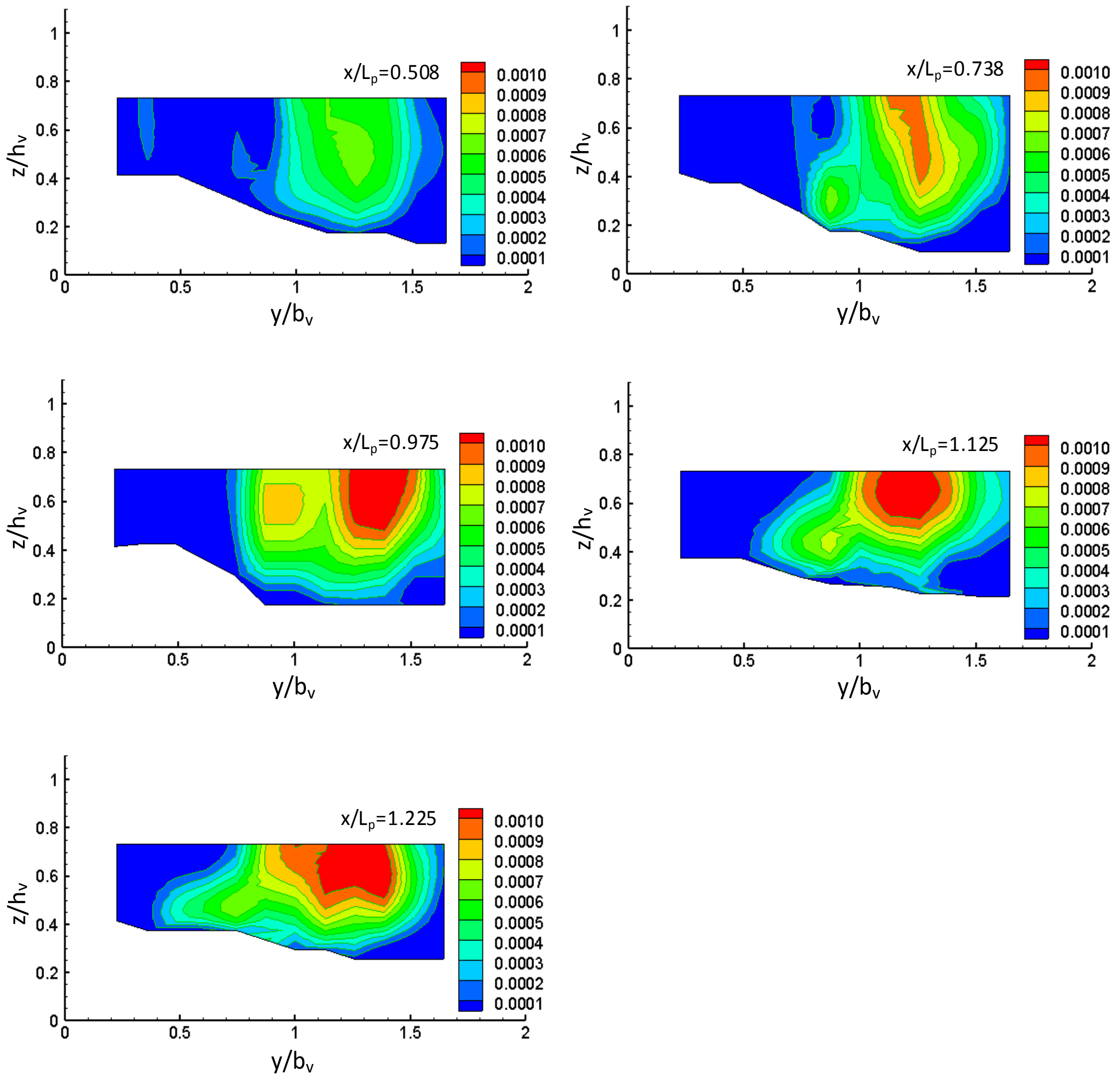

Figure 5.24 Transverse Reynolds stress at different cross sections along the channel

The vertical Reynolds stress $(-\overline{u'w'})$ along the entire channel is fairly small as shown in Figure 5.25. Downstream the channel, a negative core occurs in the junction region and continuously develops. Different from the positive value generated in wall-bounded flow, the negativity indicates the direction reversal in the vertical transfer of flow momentum. This is also observed in the flat-bed channel. More specifically, the high momentum of flow from the lower layer (near-bed region) is transported to the upper layer. This phenomenon is also reflected by the negative gradient on the vertical profile of longitudinal velocity. However, different from the flow over the flat bed, secondary flows may play a role in generating the negative vertical Reynolds stress.

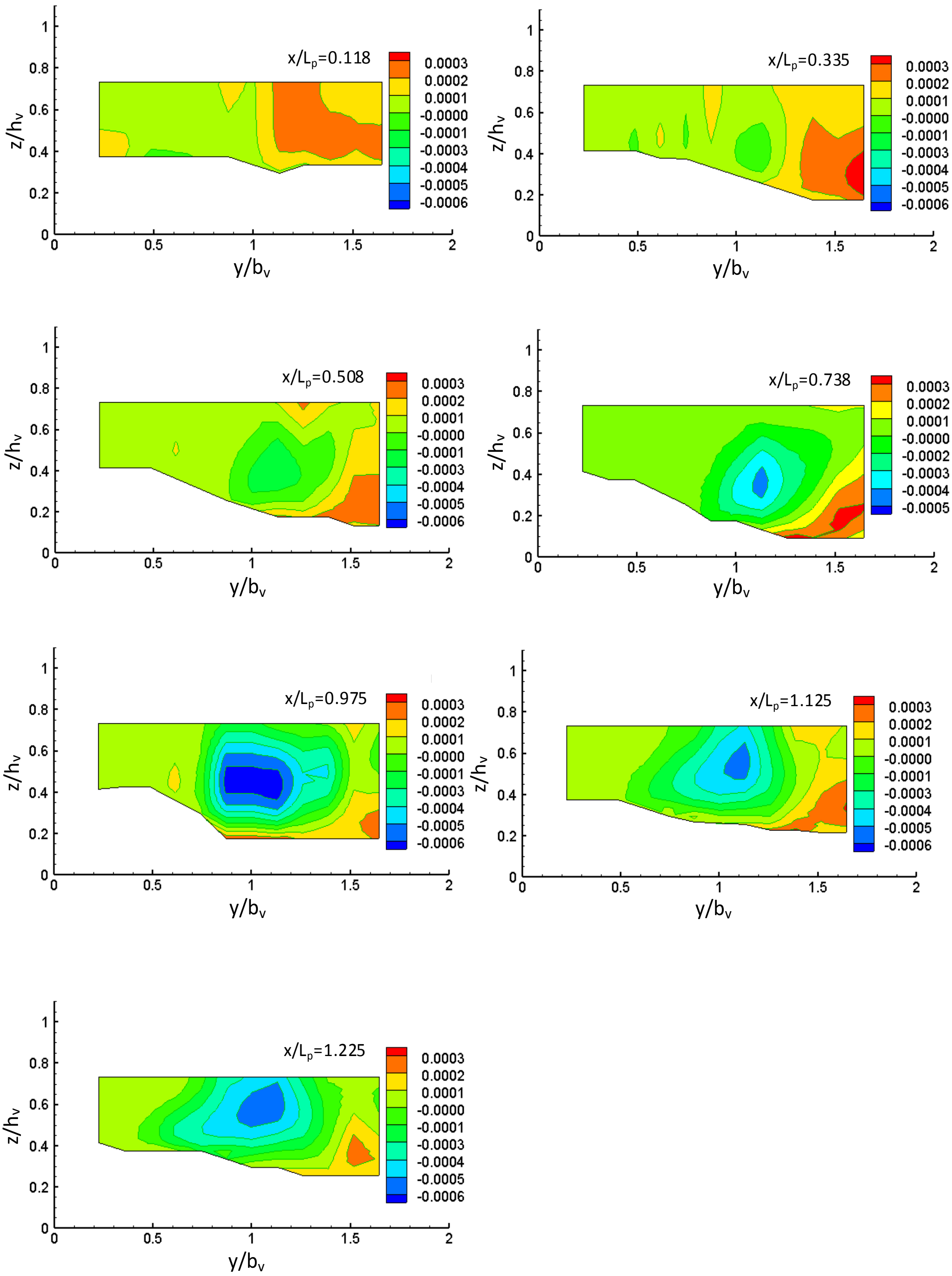

Figure 5.25 Vertical Reynolds stress at different cross-sections along the channel.

As discussed above, the generation of horizontal coherent vortices along the lateral edge of vegetation canopy dominates the turbulent momentum exchange horizontally. Turbulent kinetic energy (TKE) contour is presented to enhance the interpretation of turbulence characteristics over the equilibrium bed as shown in Figure 5.26. As clearly noted, although no large-scale vortices are found at the entry of vegetation canopy, significant TKE is observed in the VR. Similar identification is demonstrated by existing literature at the entry of FOCVC (Zeng et al, 2013). It is contributed by the longitudinal turbulent activity and can be explained by significant kinetic energy exchange of flow through a short distance in the VR. The main flow kinetic energy decays due to both the vegetative drag and turbulence dissipation in the longitudinal direction.

Downstream of the channel, TKE decreases quickly due to the dramatic reduction of flow velocity in the VR and greatly increases in the NOWR corresponding to the growth of transverse Reynolds stress owing to the generation of horizontal coherent vortices. It should be noted that TKE is not noticeable in the very-close-to-bed region. The significant TKE, therefore, should have negligible effect on bed-load transport and the associated bed morphology evolution. However, Chen et al. (2012b) still addressed that the suspended load transport characteristics must be significantly influenced when suspended load transport is considered.

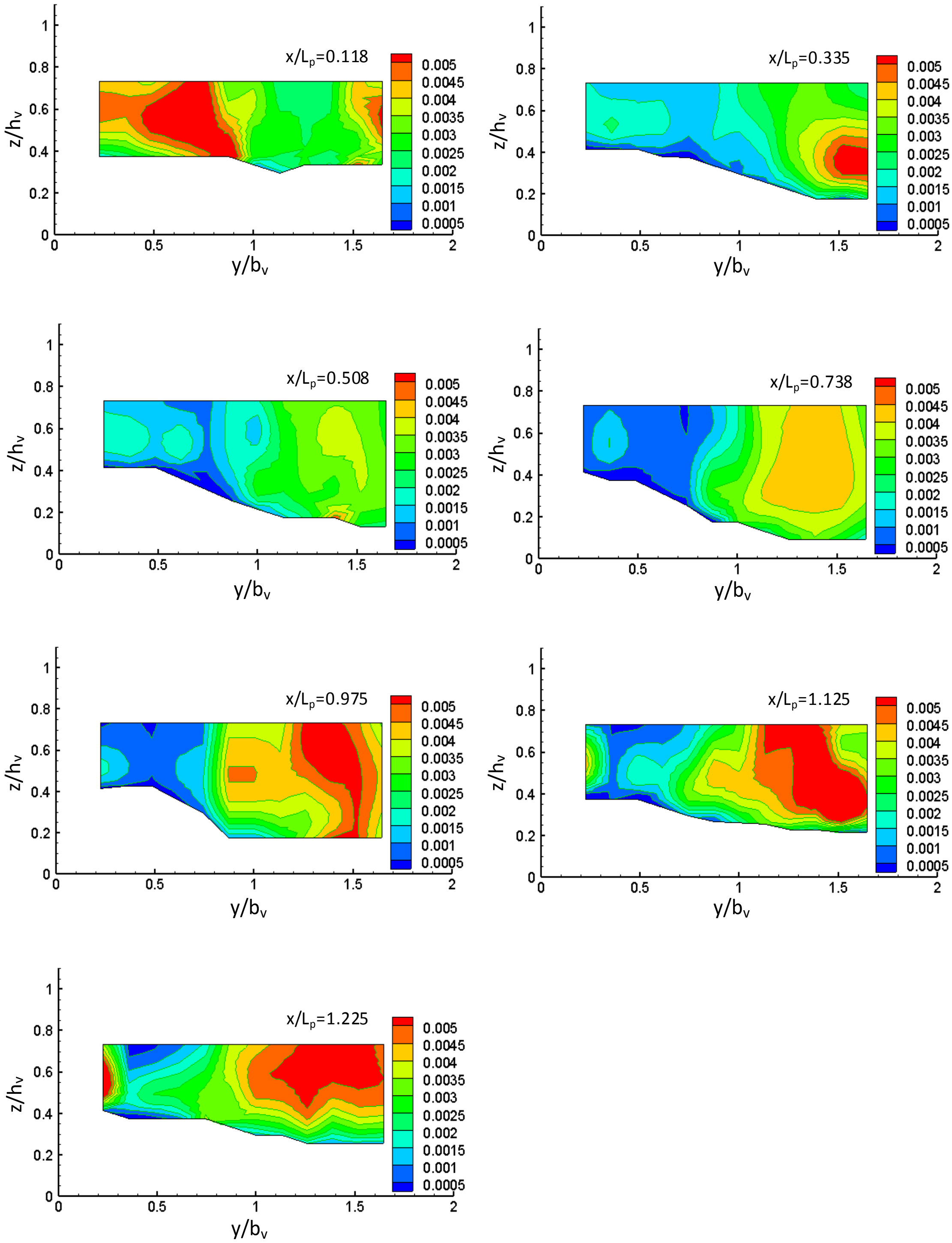

Figure 5.26 Turbulent kinetic energy at different cross sections along the channel

5.3.4 Analysis of the relationship between flow characteristics and bed morphology

In this section, the relationship between the generated equilibrium bed morphology and flow characteristics in the POCVC is examined. From the experiment, with the combination of water level (z_w) and bed elevation (z_b), the water depth in the entire channel can be obtained.

$$h(y) = z_w(y) - z_b(y) \tag{5.2}$$

Thus the cross-section area for flow passage can be calculated,

$$A = \sum_{y=0}^{b_v} h(y)\Delta y \tag{5.3}$$

Then the cross-sectional averaged flow velocity (U_m) reads,

$$U_m = \frac{Q}{A} \tag{5.4}$$

The associated Reynolds number (Re) is derived,

$$\mathrm{Re} = \frac{U_m \dfrac{A}{b}}{\nu_m} \tag{5.5}$$

Figure 5.27 shows the longitudinal distribution of cross-sectional area, cross-sectional velocity, and Reynolds number along the vegetation canopy. The origin of x-coordinate is set at the leading edge of the vegetation canopy. Clearly, there are two stages in the entire vegetated reach for the flow development. From the leading edge, the cross-sectional averaged velocity and Reynolds number increase downstream of the channel, corresponding to the decrease in the cross-section area. The onset location of flow being fully-developed with respect to the three parameters is coincident. It is noted that the onset location for Case1 (the small flow rate) is around x=0.615m and for Case2 (the large flow rate) is around x=0.81m. Of importance is the linear relationship between each parameter and longitudinal distance in the flow adjustment stage. This identity is beneficial to the prediction of associated flow development in the POCVC.

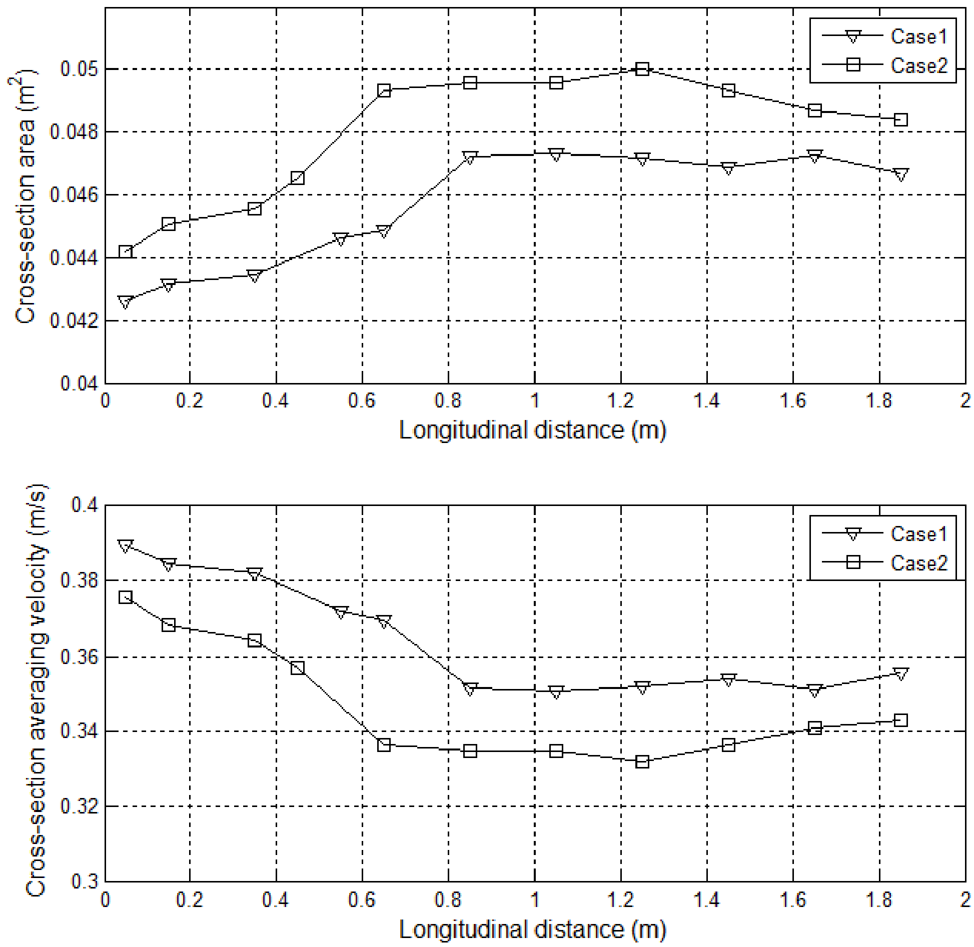

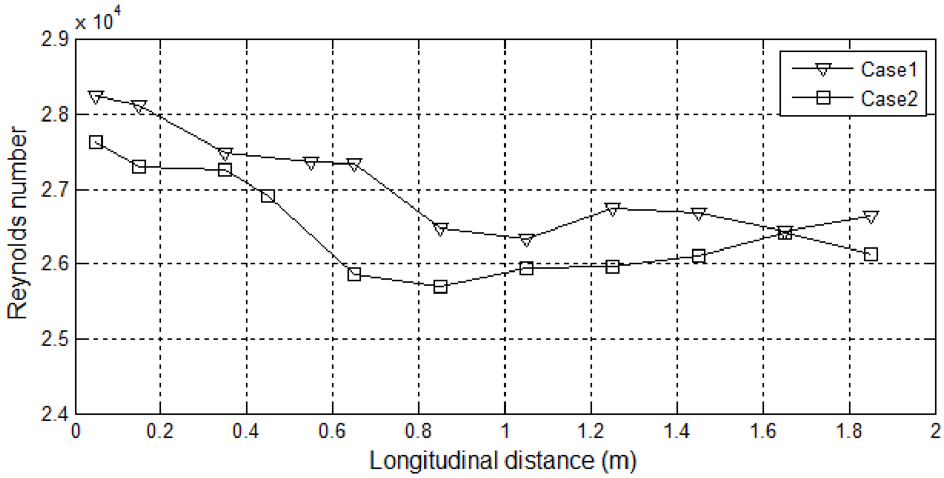

Figure 5.27 Different properties along the vegetation canopy.

As previously mentioned, the transverse bed profile along the vegetated reach gradually develops into a hyperbolic-tangent-like curve. On the basis of the observation, the characteristic lengths can be defined for the transverse bed profile as shown in Figure 5.28. Bound by the canopy edge, the bed curve can be divided into the inner and outer parts in the VR and NOWR. It is recognized that an inner extension length (Δ_{in}) and an outer extension length (Δ_{out}) characterize the hyperbolic-tangent-like bed curve in the junction region. The inner extension length is the difference between the transverse coordinate of canopy lateral edge (y_{ed}) and the transverse coordinate of the onset location (y_{in}) of the minimum vertical scour [$T_{in}=Z_{ini}-Z_b(y_{in})$] in the VR. The outer extension length is the difference between the transverse coordinate of canopy lateral edge (y_{ed}) and the transverse coordinate of the onset location (y_{out}) of the maximum vertical scour [$T_{out}=Z_{ini}-Z_b(y_{out})$] in the NOWR.

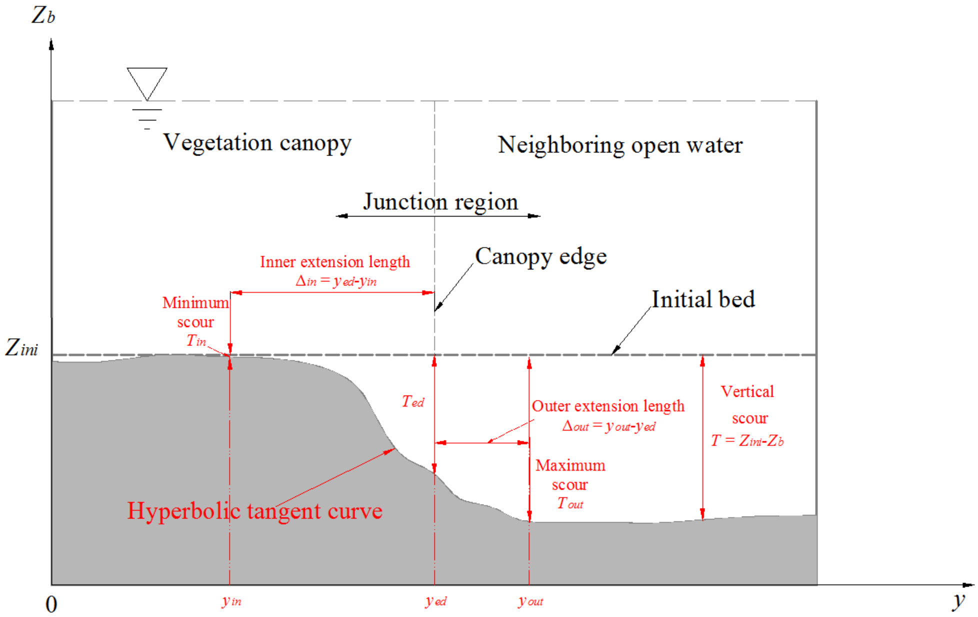

Figure 5.28 Characteristic transverse scouring bed morphology in a partially-vegetated channel. The bed topographic surface is observed as a hyperbolic-tangent-like curve. Bound by the canopy edge, the bed curve can be divided into the inner branch and outer branch in the VR and NOWR. Respectively, it is recognized that an inner extension length and an outer extension length characterize the hyperbolic-tangent-like bed curve.

Figure 5.29 shows the longitudinal distribution of maximum scour thickness in the neighboring open water region. It can be observed that the maximum scour thickness has a similar pattern with the cross-sectional area of the flow passage. The local maximum scour thickness linearly increases in the longitudinal direction before reaching the global maximum value. It then remains constant as flow propagates downstream. The onset locations of the global maximum scour thickness for Case1 and Case2 are also at x=0.625m and x=0.82m.

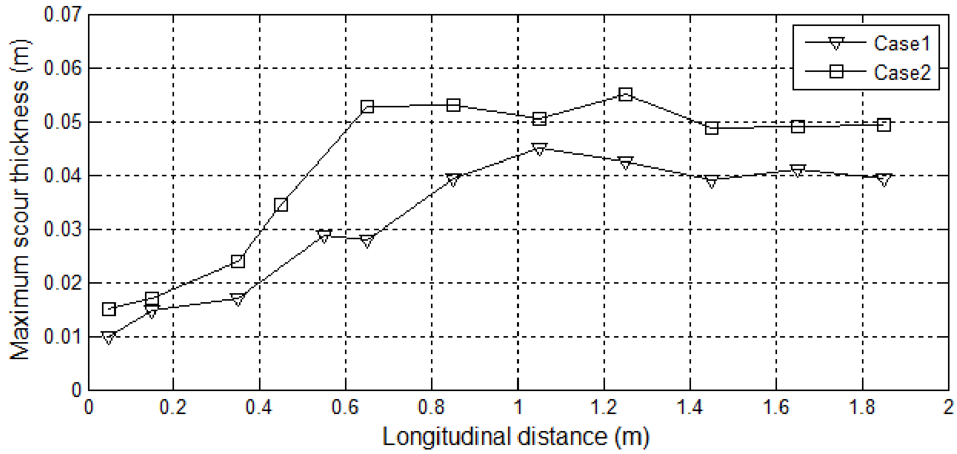

Figure 5.29 Maximum scour thickness along the vegetation canopy

By definition, the inner extension length and outer extension length describe the characteristics of the transverse bed profile in the junction region. As shown in Figure 5.30, the inner extension length linearly increases in the longitudinal direction. The value is similarly equal under two different flow rates. The inner extension length nearly peaks at *x*=0.82m for a smaller flow rate (Case1) and *x*=1.22m for larger flow rate (Case2). The development distance is both larger than the distance for the maximum scour thickness, say *x*=0.625m and *x*=0.82m. The space lag between the vertical length and transverse length of the bed scour could be attributed to secondary flow evolution. Regarding the neighboring open water region, the outer extension length rapidly develops within a short longitudinal length (*x*=0.32m) and almost remains constant as the flow propagates downstream. This indicates the outer extension length is only determined by primary flow evolution.

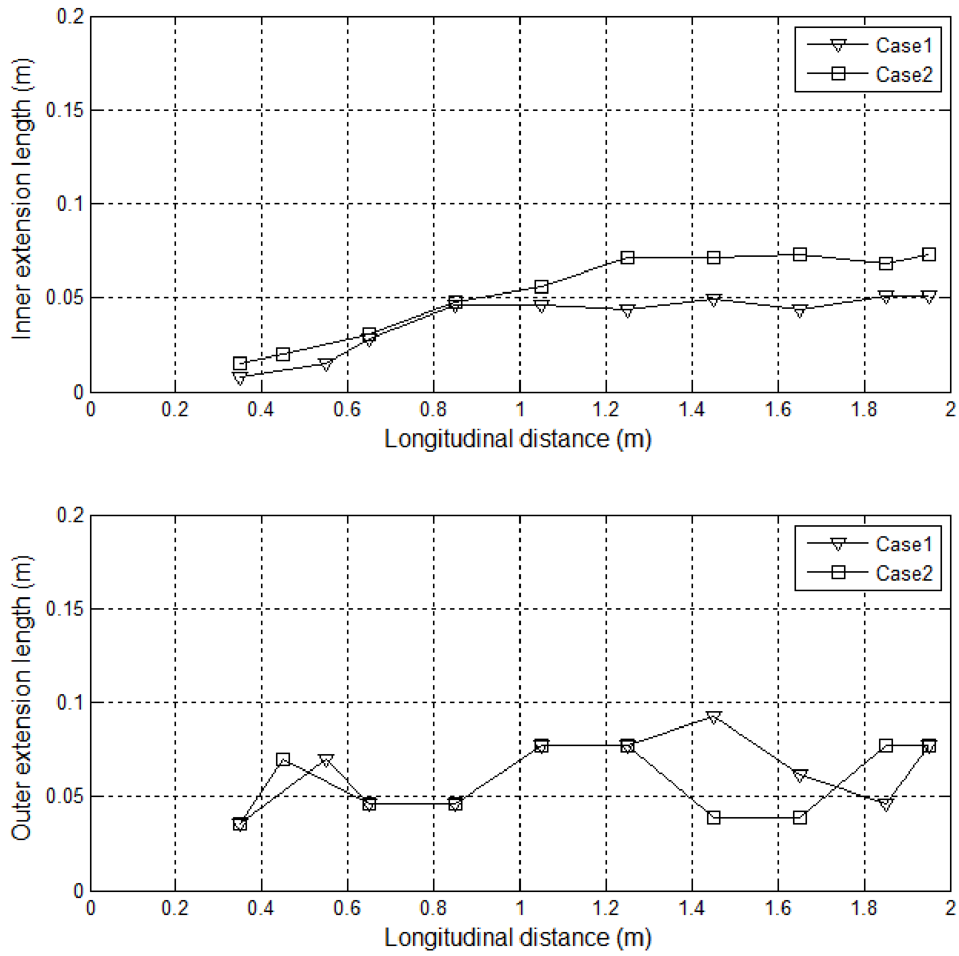

Figure 5.30 Characteristic transverse extension length of the bed profile

Further, the relation between the cross-sectional averaged flow parameters and the maximum scour thickness at the same longitudinal location is presented in Figure 5.31. The maximum scour thickness decreases perfectly with the increasing cross-sectional averaged velocity and Reynolds number. A linear regression formula can be used to describe the relation between the maximum scour thickness and the cross-sectional averaged velocity or Reynolds number as below,

$$T = -0.8U_m + 0.3214 \tag{5.6}$$

$$T = -0.0000191\mathrm{Re} + 0.5473 \tag{5.7}$$

The regression formulas are useful in predicting the basic bed morphology on the basis of the measurable flow velocity.

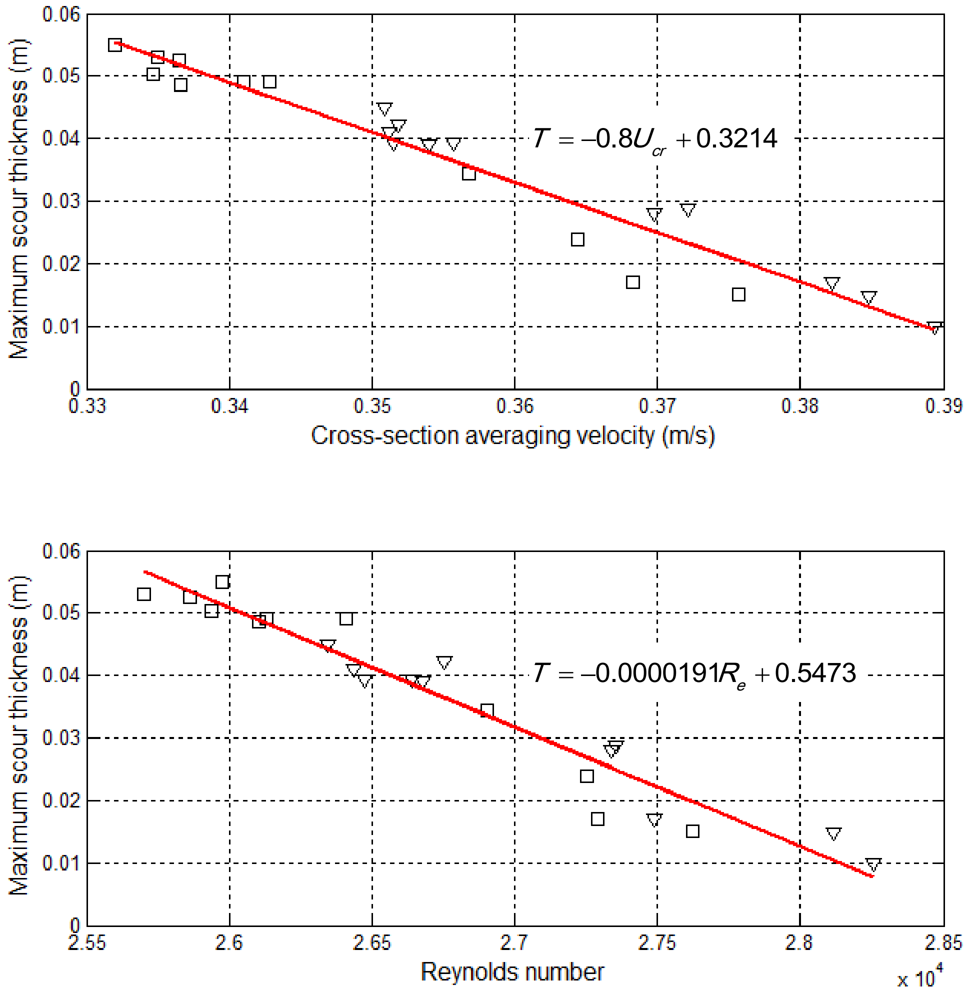

Figure 5.31 Linear relationships between the maximum scour thickness and the flow properties along vegetation canopy.

Obviously, as flow passes through the partial vegetation canopy, bed erosion occurs both in vertical and transverse directions, indicating the development process of local maximum scour thickness and inner extension length at the same cross-section. Figure

5.32 shows the pair of local maximum scour thicknesses and inner extension lengths in the vegetated reach. It shows increasing local maximum scour thickness corresponding to increasing inner extension length as the flow propagates along the vegetation canopy. For both cases, a linear relationship exists between maximum scour thickness and inner transverse extension length. The linear relationship almost satisfies all maximum scour thickness/inner extension length pair for the smaller flow rate (Case1). However, for the larger flow rate (Case2), the linear relation only satisfies the smaller inner extension length. As the inner length continues to increase, the inner extension length remains constant. It should be noted that the ratio of inner extension length to maximum scour thickness in the linear stage decreases with an increasing flow rate.

The variation of the inner extension length relative to maximum scour thickness well describes the space property of bed morphology evolution due to partial obstruction of the vegetation canopy. The increasing flow rate leads to maximum vertical downward bed erosion in a shorter longitudinal distance but maximum transverse bed erosion towards the inner vegetation canopy in a longer longitudinal distance.

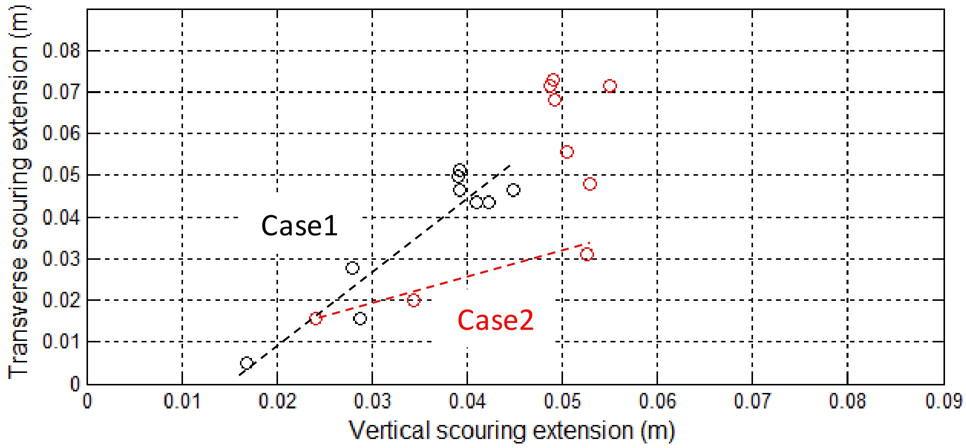

Figure 5.32 Relationship between the local maximum scour thickness and the inner extension length.

The characteristic length can be calculated by measured transverse bed profiles. It should be noted that the transverse bed profile is analogous to the hyperbolic tangent curve which may tend to be not standard. This nonstandard property can be confirmed by the inequality of the inner extension length and outer extension length [$(y_{ed}-y_{in})/(y_{out}-y_{in})\neq 1$). Therefore, the scaling between scour thickness (T) and the transverse coordinate (y) in the junction region should be classified as the canopy region and neighboring open water region as follows.

Canopy region

$$\frac{T_{ed}-T}{T_{ed}-T_{in}}=\tanh\left(\frac{y_{ed}-y}{\Delta_{in}}\right) \tag{5.8}$$

Neighboring open water region

$$\frac{T - T_{ed}}{T_{out} - T_{ed}} = \tanh\left(\frac{y - y_{ed}}{\Delta_{out}}\right) \quad (5.9)$$

Figure 5.33 shows the comparison of bed scouring thickness in the transverse direction due to the scaling theory in vegetation region. The estimated bed scouring thickness by the hyper tangent formula agrees well with the experimental data. However, scatters occur in regions further away from the vegetation lateral edge for both flow configurations. Interestingly, the scattering effect becomes more pronounced in the front region of the vegetation canopy. It should be noted that the larger flow rate (Case2) leads to larger scattering of data. In the entry region, the scaling theory underestimates the bed scouring. The underestimation is obviously greater for the larger flow rate (i.e., Case2).

As discussed previously, the transverse bed scouring is mostly caused by the combination of the main flow and the secondary flow. This leads to a transverse scouring extension region in the vegetation canopy. Beyond this extension region, the secondary flow effect significantly declines and the main flow velocity decreases due to vegetative drag. The resulting bed shear stress is so small that the sediment cannot be moved by the flow. Nevertheless, at the entry of the vegetation canopy, the main flow velocity, on the contrary, increases due to the reduction of the flow passage area leading to the local bed scouring as shown in the figure. Local bed scouring in Case2 exceeds the scouring in Case1. This explains the underestimation of bed scouring by the scaling relationship.

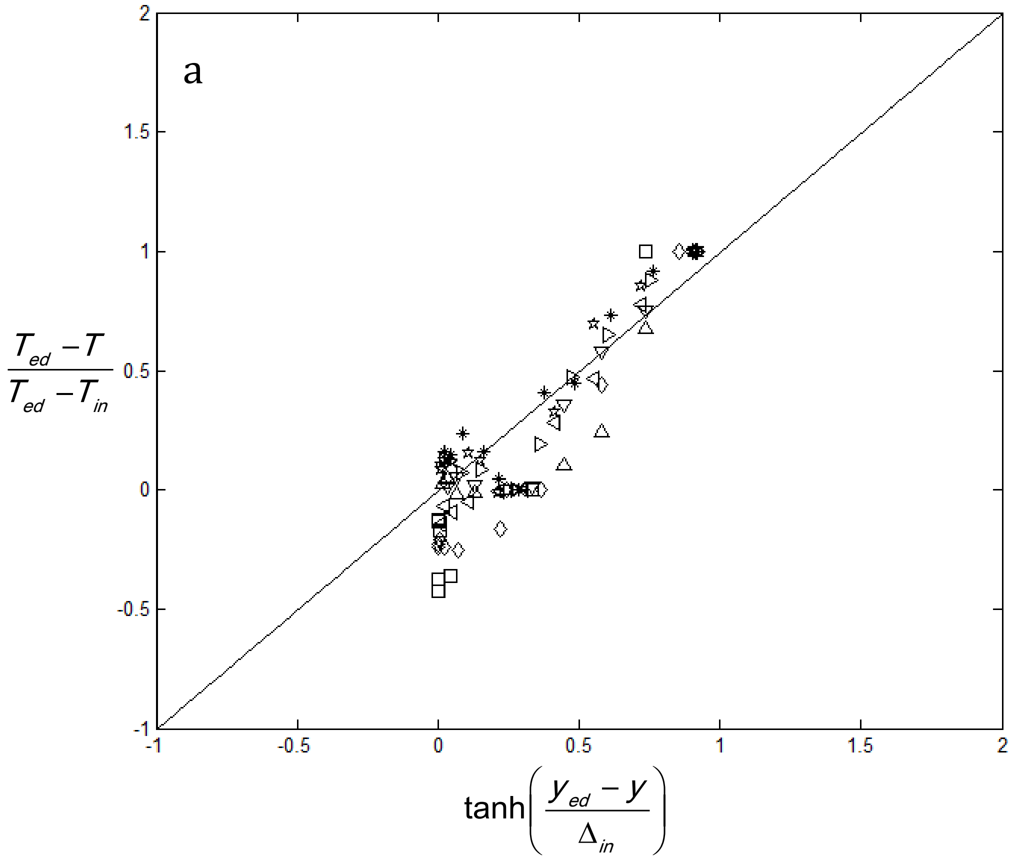
a
2
1.5
1
0.5
0
-0.5
-1
-1
-0.5
0
0.5
1
1.5
2
$\frac{T_{ed}-T}{T_{ed}-T_{in}}$
$\tanh\left(\frac{y_{ed}-y}{\Delta_{in}}\right)$

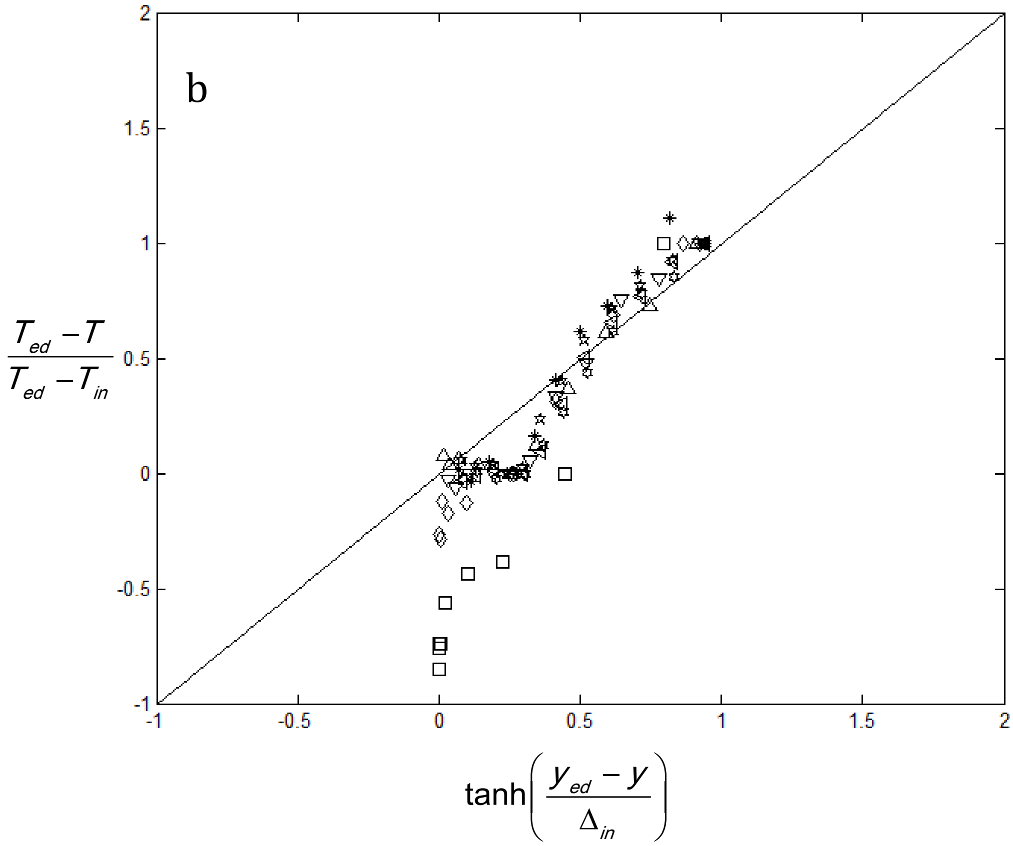
b
2
1.5
1
0.5
0
-0.5
-1
-1
-0.5
0
0.5
1
1.5
2
$\frac{T_{ed}-T}{T_{ed}-T_{in}}$
$\tanh\left(\frac{y_{ed}-y}{\Delta_{in}}\right)$

Figure 5.33 Geometric scaling of the bed scouring thickness in the transverse direction for the vegetation region in (a) Case1 and (b) Case2. Circle (○) x=0.55m (Case1) or 0.45m (Case2); square (□) x=0.65m; diamond (◇) x=0.85m; upward-pointing triangle (△) x=1.05m; downward-pointing triangle (▽) x=1.25m; left-pointing triangle (◁) x=1.45m; right-pointing triangle (▷) x=1.65m; pentagram (☆) x=1.85m; asterisk (*) x=1.95m.

Figure 5.34 shows the comparison of bed scouring thickness in the transverse direction in accordance with the scaling theory in the NOWR. The scaling formula can well describe the relationship between the outer extension length and scour thickness. Compared with the bed profile in the vegetation region, the range of scatters is narrower and deviated against the standard line. The cause might be attributed to the difference in flow characteristics between the VR and the NOWR.

For both cases, relatively high deviated data is observed in regions farther away from the lateral edge of the vegetation canopy. The deviation is higher for larger flow rate, at which the bed scour is more significant. The results are generally overestimated, which suggests that the predicted scour thickness is larger than the experimental data. The possible reason is that in those regions, the sidewall tends to inhibit the bed erosion. Despite the deviation, due to the sidewall effect, the proposed formula can provide a reasonable prediction of bed scour thickness or transverse bed profile.

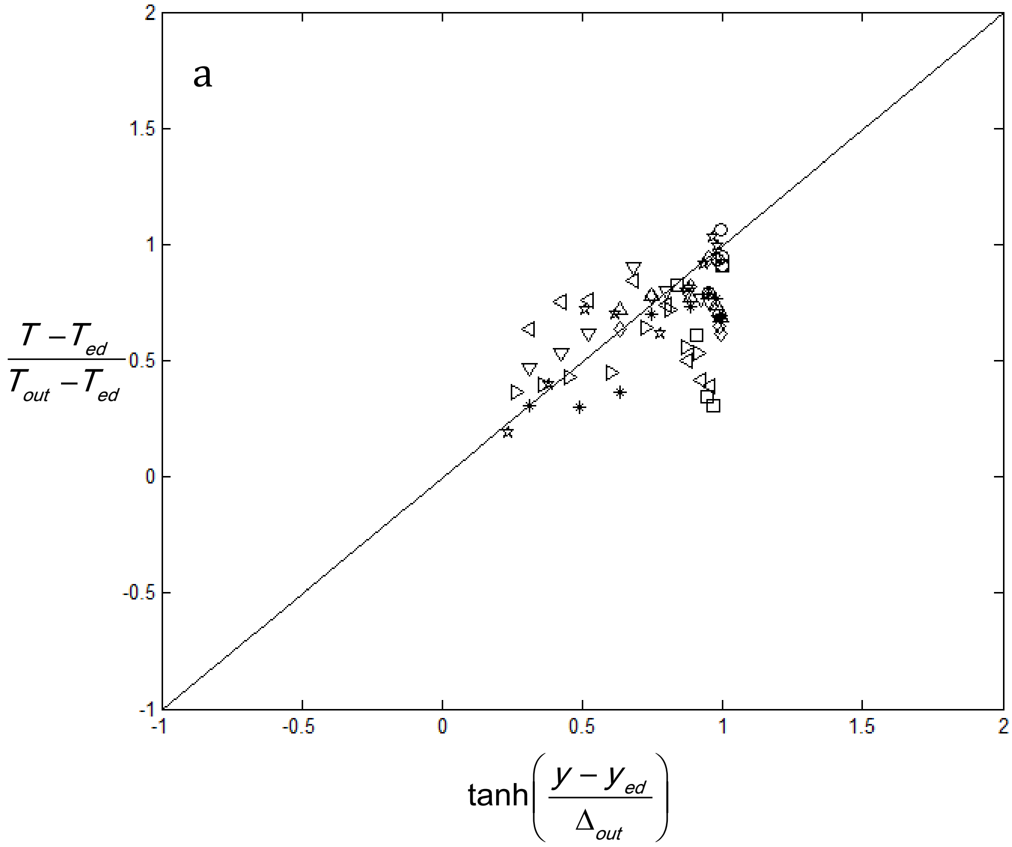
a
2
1.5
1
0.5
0
-0.5
-1
-1
-0.5
0
0.5
1
1.5
2
$\frac{T - T_{ed}}{T_{out} - T_{ed}}$
$\tanh\left(\frac{y - y_{ed}}{\Delta_{out}}\right)$

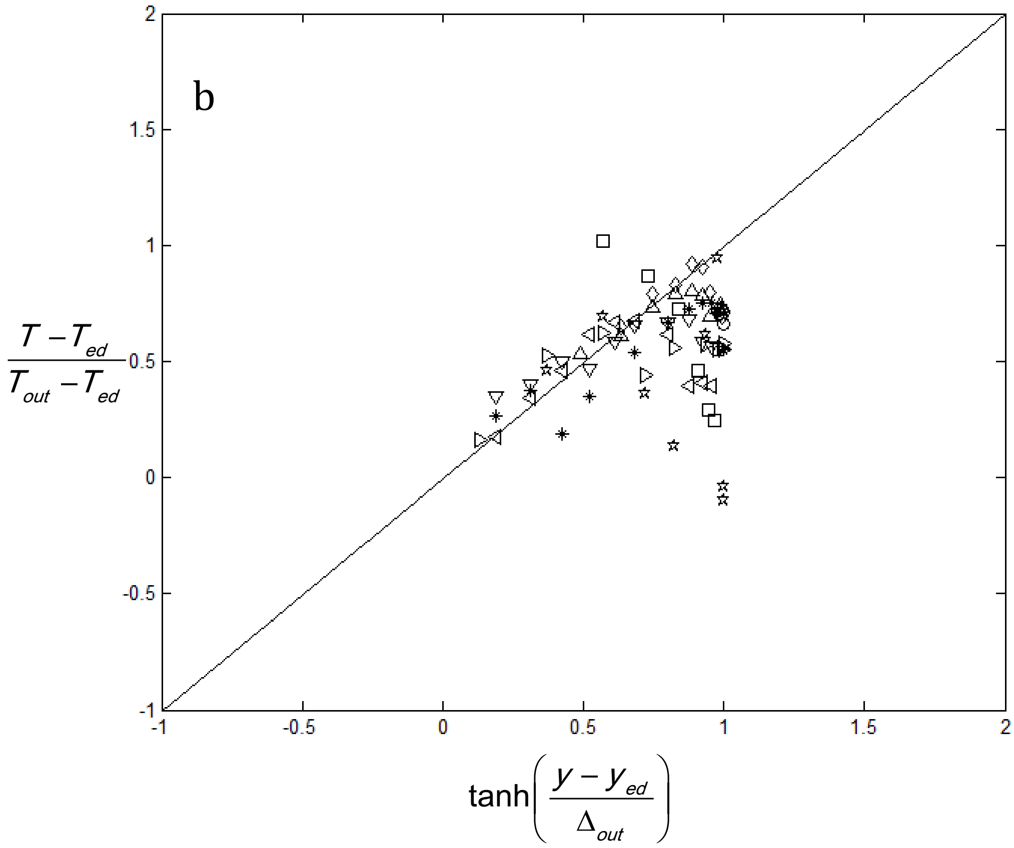
b
2
1.5
1
0.5
0
-0.5
-1
-1
-0.5
0
0.5
1
1.5
2
$\frac{T - T_{ed}}{T_{out} - T_{ed}}$
$\tanh\left(\frac{y - y_{ed}}{\Delta_{out}}\right)$

Figure 5.34 Geometric scaling of bed scouring thickness in the transverse direction for non-vegetation region in (a) Case1 and (b) Case2. Circle (○) x=0.55m (Case1) or 0.45m (Case2); square (□) x=0.65m; diamond (◇) x=0.85m; upward-pointing triangle (△) x=1.05m; downward-pointing triangle (▽) x=1.25m; left-pointing triangle (◁) x=1.45m; right-pointing triangle (▷) x=1.65m; pentagram (☆) x=1.85m; asterisk (*) x=1.95m.

5.4 Conclusions

Bed scour experiments were conducted to investigate the characteristics of bed-load transport and bed morphology evolution in the POCVC in the absence of upstream sediment supply. To approach real situations, gradated sediment was used as bed materials. Meanwhile, to interpret the complex flow effect on the alluvial process, the associated flow structure over the equilibrium bed was measured. The investigation shows that due to the partial obstruction by the finite vegetation canopy, massive sediment transport was observed in the neighboring open water region. A significant peak occurs in the sediment transport rate variation as the sand wave from the neighboring open water region propagates to the downstream collection point. The sediment transport rate fluctuates as bed roughness changes with bed morphology evolution. The fluctuation of sediment transport is greater for larger flow rate. During the sediment transport process, the sediment sorting effect is evident.

As the bed morphology becomes fully-developed, important characteristic bedforms can be identified due to bed scour in the NOWR in association with flow intensity.

These bedforms include (A) water pool induced by flow convergence in the NOWR, (B) slightly-eroded bed protected by the vegetation canopy in the VR, (C) slightly-eroded bed at upstream of vegetation canopy, (D) local bed scour near the leading edge of vegetation canopy, (E) sediment bar with surface fining extending downstream after the vegetation canopy, and (F) riffle downstream of the vegetated reach. Of significance is that the scour pool and the downstream deposition bedform compose the famous pool-riffle morphology that is suggested to be able to contribute to river restoration. In comparison of the long vegetation canopy and the short vegetation canopy, it is noted that the canopy length tends to affect the bed morphology pattern including the scale and spatial distribution.

Over the generated equilibrium bed, the mean flow and turbulence structure were investigated for a better understanding of the formation mechanism of bed morphology in the POCVC. Apart from the generation of horizontal coherent vortices, secondary flows are induced along the vegetation canopy to drive the transverse motion of flow, directly governing the transverse bed surface sediment sorting. Although sediment transport and bed morphology evolution occur in experiments, flow adjustment is similar to that in the non-sediment channel. Velocity deflection and negative vertical Reynolds stress in the near-bed region are also identified. The distribution of secondary flows in the canopy wake can well account for the generation of longitudinal sediment bar with surface fining.

Finally, along the vegetation canopy, the relationship between bed morphology and flow characteristics was analyzed with the scaling approach. Linear relations can be found among the longitudinal bed profiles, longitudinal flow propagation distance, mean flow velocity and the transverse inner extension of bed erosion. In the vegetated reach, the transverse bed profile is displayed in the curve of the tangent hyperbolic function. The proposed tangent hyperbolic formulas can predict well the transverse bed profile with defined inner and outer extension lengths.

In summary, alluvial process (i.e., sediment transport, bed morphology evolution and flow characteristics) in the POCVC has been rarely studied and not well understood. This study contributes fundamental recognition and understanding of behaviors of the flow and sediment motion in the POCVC.

Chapter 6 Morphological Modeling in the Partially-obstructed Open Channel with Vegetation Canopy

6.1 Introduction

The three-dimensional numerical simulation technique, undoubtedly, is an ideal method to predict the sediment transport and alluvial processes in rivers. In real situations, the flow structure is three dimensional and complex. Due to turbulence anisotropy and the irregularity of bed geometry, secondary flows tend to be produced in the streamwise direction. According to the sediment mass balance equation, secondary flows control the transverse component of sediment transport. Further, compared to the depth-averaged flow model, the near-bed flow calculated by the full three-dimensional flow model directly acts on the bed surface sediment, which determines the movement status of sediment on the bed surface. Therefore, the calculation of three-dimensional flow field, especially the derivation of near-bed flow velocities, is beneficial for a more accurate prediction of sediment transport and bed deformation.

As mentioned above in the Introduction, the significant computational expense, however, is a critical limiting factor in the numerical simulation of sediment transport and bed morphology evolution based on the simulated three-dimensional flow field. The essential cause is the distinct time scale in the evolution of flow and bed morphology. Even in laboratory flumes, the evolutionary timescale for the latter is far greater than that for the former (as demonstrated in the last section, the evolutionary time for bed morphology is about three hours, while the computational time for pure water flow is only 100 seconds). Therefore, it is not realistic to employ the fully three-dimensional model to predict the relatively long-term sediment transport and bed morphology evolution.

An alternative compromise is to couple the governing equations of sediment transport and bed deformation into the two-dimensional depth-averaged shallow water flow model. Even though this treatment might sacrifice some accuracy in predicted results, for instance, uncertainty in reproducing minor bedforms due to secondary flows, it is still expected that the two-dimensional flow-sediment coupled model can predict the correct patterns of sediment transport and bed morphology in the partly-obstructed channel with a finite vegetation canopy.

6.2 2D numerical simulation of morphological model Nays2DH-IRIC

For convenience, all donations used here are consistent with original ones in the menu of Nays2DH-IRIC.

6.2.1 Governing equations of flow motions

Continuity equation

$$\frac{\partial h}{\partial t}+\frac{\partial (hU)}{\partial x}+\frac{\partial (hV)}{\partial y}=0 \tag{6.1}$$

Momentum equations

$$\frac{\partial (hU)}{\partial t}+\frac{\partial (hU^2)}{\partial x}+\frac{\partial (hUV)}{\partial y}=-gh\frac{\partial H}{\partial x}-\frac{\tau_{bx}}{\rho}+T_x+\frac{F_x}{\rho} \tag{6.2}$$

$$\frac{\partial (hV)}{\partial t}+\frac{\partial (hUV)}{\partial x}+\frac{\partial (hV^2)}{\partial y}=-gh\frac{\partial H}{\partial y}-\frac{\tau_{by}}{\rho}+T_y+\frac{F_y}{\rho} \tag{6.3}$$

$$\tau_{bx}=\rho C_f U\sqrt{U^2+V^2}, \qquad \tau_{by}=\rho C_f V\sqrt{U^2+V^2} \tag{6.4}$$

$$T_x=\frac{\partial}{\partial x}\left(\nu_t h\frac{\partial U}{\partial x}\right)+\frac{\partial}{\partial y}\left(\nu_t h\frac{\partial U}{\partial y}\right) \tag{6.5}$$

$$T_y=\frac{\partial}{\partial x}\left(\nu_t h\frac{\partial V}{\partial x}\right)+\frac{\partial}{\partial y}\left(\nu_t h\frac{\partial V}{\partial y}\right) \tag{6.6}$$

$$F_x=\frac{1}{2}\rho C_d a h_v U\sqrt{U^2+V^2}, \qquad F_y=\frac{1}{2}\rho C_d a h_v V\sqrt{U^2+V^2} \tag{6.7}$$

where h is the water depth, t is the time, U and V are the depth-averaged velocities in *x*- and *y*-directions, respectively, g is the gravitational acceleration, H is the water surface, x and y are the components of the shear stress of river bed in *x*- and y-directions, F_x and F_y are the components of drag force by vegetation in the *x*- and y-direction, C_f is the drag coefficient of the bed shear stress, C_μ is the eddy viscosity coefficient, C_d is the drag coefficient of vegetation, a_s is the area of interception by vegetation per unit volume, and h_v is the height of vegetation. ν_t is the depth-averaged eddy viscosity and can be calculated by the depth-averaged *k*-*ε* model, which can be referred to the menu of Nays2DH.

River bed friction

In Nays2DH, the friction of river bed is set using Manning's roughness parameter. For Manning's roughness parameter, the user can define this parameter locally in each computational cell.

In Eq. (4), bed shear forces τ_{bx} and τ_{by} are expressed by using the coefficient of bed shear force C_f . The coefficient of bed shear force C_f is estimated by Manning's roughness parameter n_m as follows:

$$C_f = \frac{gn_m^2}{h^{1/3}} \tag{6.7}$$

This Manning's roughness parameter can be estimated from the relative roughness height, k_s , by using the Manning-Strickler equation,

$$n_m = \frac{k_s^{1/6}}{7.66\sqrt{g}} \tag{6.8}$$

where k_s is the relative roughness height which is defined as γd_s , d_s is sediment diameter, γ is an empirical constant in the range of 1 to 3, and g is the gravitational acceleration.

Dimensionless river bed shearing force

Composite velocity V_m is defined by the following equation:

$$V_m = \sqrt{U^2 + V^2} \tag{6.9}$$

Hence, the Shields number Θ exerted on the riverbed is as follows,

$$\Theta = \frac{C_f V_m^2}{(\rho_s - \rho) d_s} = \frac{n_m^2 V_m^2}{(\rho_s - \rho) d_s h^{1/3}} \tag{6.10}$$

where ρ_s is the density of bed materials in fluid and d_s is the grain size of bed materials which can be represented by the median diameter of the grain.

6.2.2 Governing equations of sediment motions

6.2.2.1 Sediment mass balance equation

Since in this study, only the bed-load transport is taken into consideration to simulate the bed morphology evolution, the continuity equation of sediment transport is as follows,

$$(1-\lambda)\frac{\partial z_b}{\partial t} + \frac{\partial q_{bx}}{\partial x} + \frac{\partial q_{by}}{\partial y} = 0 \tag{6.11}$$

where q_{bx} and q_{by} are the bed-load transport rates in the longitudinal and transverse directions, z_b is the bed elevation and λ is the porosity of bed materials pre-specified in the current model. With bed-load transport rate known, bed deformation can be calculated by Eq.6.11.

6.2.2.2 Bed-load transport equation

The formulas of bed-load transport rate have been summarized in the chapter of the literature review. Relations between bed shear stress and bed-load transport rate were empirically derived based on flume data. In this present model, the total bed-load transport rate in the depth-averaged velocity direction can be estimated by either Meyer-Peter and Müller formula or Ashida and Michiue formula,

Meyer-Peter and Müller formula,

$$q_b = 8\left(\Theta - \Theta_{cr}\right)^{1.5} \sqrt{\rho_s g d_s^{\,3}}\, r_b \tag{6.12}$$

Ashida and Michiue formula

$$q_b = 17\Theta_e^{1.5}\left(1 - K_c \frac{\Theta_{cr}}{\Theta}\right)^{1.5}\left(1 - \sqrt{K_c \frac{\Theta_{cr}}{\Theta}}\right)\sqrt{\rho_s g d_s^{\,3}}\, r_b \tag{6.13}$$

where Θ_e is the effective Shields number calculated as follows:

$$\Theta_e = \frac{V_m^2}{(\rho_s - \rho) g d_s \left(6 + 2.5\ln \dfrac{h}{d_s(1+2\Theta)}\right)^2} \tag{6.14}$$

where Θ_{cr} is the critical Shields number and can be determined by the Shield diagram.

K_c is the modification function of the effect of the local bed slope on the sediment transport as follows,

$$K_c = 1 + \frac{1}{\mu_s}\left[\left(\frac{\rho}{\rho_s - \rho} + 1\right)\cos\vartheta \tan\theta_x + \sin\vartheta \tan\theta_y\right] \tag{6.15}$$

where ϑ is the angle of deviation of near-bed flow from *x*-direction and defined as follows:

$$\vartheta = \arctan\left(\frac{v_b}{u_b}\right) \tag{6.16}$$

μ_s is the static friction coefficient of bed materials. θ_x and θ_y are bed inclinations in the x and y-directions, respectively, and can be calculated by the local bed topography. r_b is the function exchange layer thickness.

6.2.2.3 Correction of large gradient by Slope collapse model

As presented in the experimental results, the transverse bed profile around the lateral edge vegetation canopy is in great gradient. For this scenario, the computation requires particular treatment to the computed bed profile greater than the angle of repose of sediment. In fact, this slope usually occurs between the low water channel and the floodplain, or near obstacles. Nays2DH adopts a simple slope collapse model. This model assumes that if the computed bed slope exceeds the angle of repose, the bed is instantaneously corrected to satisfy the critical angle considering the mass balance. The basic mechanism is illustrated in Figure 6.1.

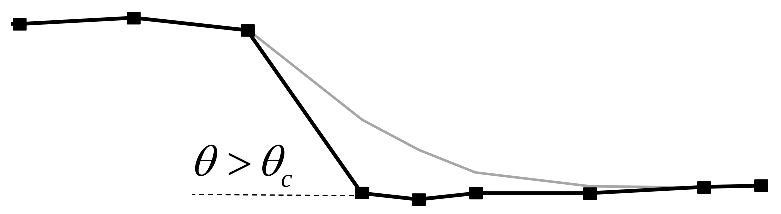

Figure 6.1 Description of slope collapse model. The grey line is the computed bed

curve after correction by the slope collapse model.

6.2.3 Boundary conditions

In the numerical simulation of the flow-sediment process, a couple of boundary conditions need to be specified for governing equations of flow and sediment transport, respectively. For the flow part, water discharge is set at the inlet cross-section, which can be transformed into flow velocity. At the outlet cross section, water depth is specified. For the sediment transport part, no sediment supply is at the inlet cross section for the present study. At the outlet cross-section, the bed is fixed so that neither erosion nor deposition exists. In another word, this boundary specification is equivalent to the radiation boundary condition.

In Nays2DH, in order to enable a better generality of the application in different geometric boundaries, Cartesian coordinate system, employed in the above equations, is transformed into the moving boundary-fitted coordinate system in coordinates. The details can be referred to the solver menu of Nays2DH-IRIC.

6.3 Results of two-dimensional flow-sediment model

6.3.1 Validation of Nays2DH-IRIC

6.3.1.1 Depth-averaged (DA) flow velocity *U*

Figure 6.2 shows the comparison of the depth-averaged longitudinal velocity between experimental and simulated results. Three transverse transects, representing vegetation region (VR), junction and neighboring open water region (NOWR), are selected for presentation. Results show that the 2D Nays2DH model can generally simulate *U* over deformed bed morphology in the POCVC. Particularly, the agreement is better at the downstream reach for the fully-developed flow. For the non-developed flow, the result is overestimated for the NOWR. Underestimation in result can be observed near the leading edge of vegetation canopy. For the junction region, the simulated result well fits the measurement.

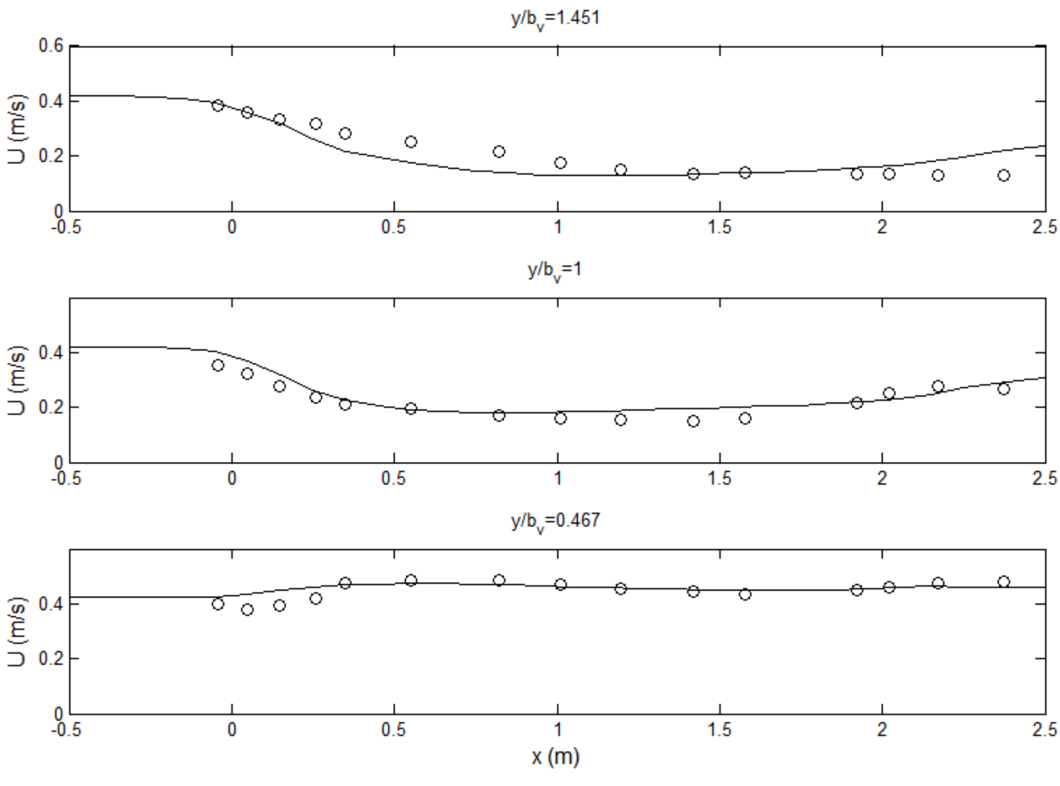

Figure 6.2 Comparison of the longitudinal distribution of depth-averaged longitudinal velocity the between the measurement (open circle) and simulation (solid line).

In addition, the simulation is examined with respect to the transverse profile of the depth-averaged flow velocity as shown in Figure 6.3. Seven different cross-sections along the vegetation canopy are presented for comparison. It is shown that the transverse profile of longitudinal velocity can be well fitted by the simulation. However, near the leading edge of vegetation canopy (x=0.162m), U is slightly underestimated. The inflection property of the tangent hyperbolic profile is accurately captured along the vegetation canopy. It is also noted that at the patch wake the longitudinal velocity is overestimated. In the region, the flow separation may contribute to the underestimation. It can be simply concluded that the 2D Nays2DH-IRIC model can well reproduce the depth-averaged longitudinal velocity at the reach of fully-developed flow. Either overestimation or underestimation is found for reaches of non-developed flow such as the entry region and wake region of vegetation canopy.

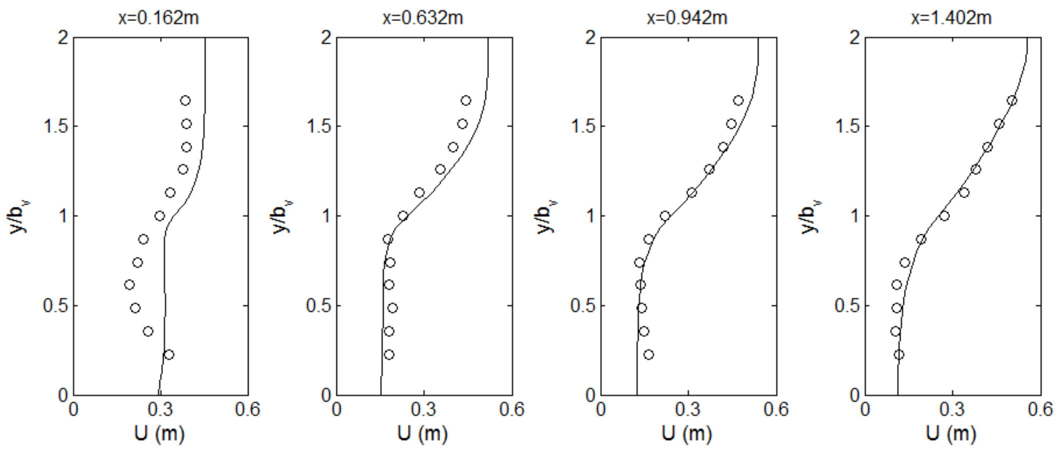

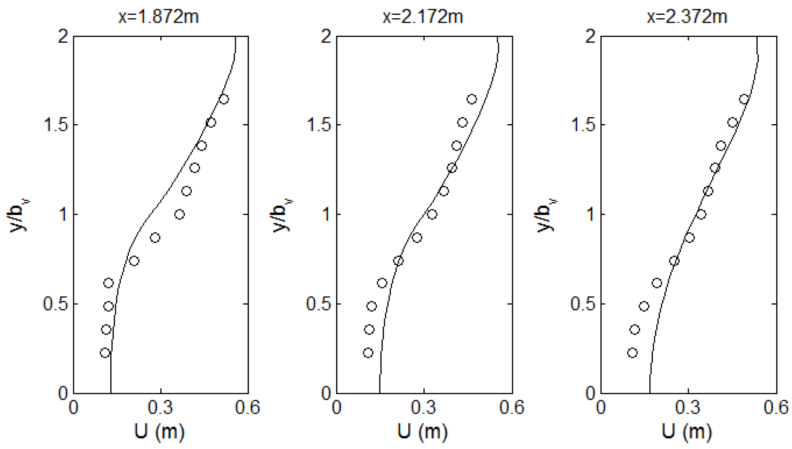

Figure 6.3 Comparison of transverse profile of depth-averaged longitudinal velocity between the measurement (open circle) and simulation (solid line).

6.3.1.2 Validation of bed morphology

The capability of 2D Nays2DH-IRIC in simulating of bed morphology evolution is examined against the measurement.

Figure 6.4 shows transverse bed profile for different cross-sections. Along the vegetation canopy, it is clearly noted that the 2D Nays2DH-IRIC can successfully produce the transverse bed profile in the partially-obstructed channel with a finite vegetation canopy. To be more precise, the simulated bed deformation in the neighboring open water region agrees well with the measurement. However, in the vegetation region, the simulation slightly underestimates the bed erosion. This might be because the real sediment mixture is non-uniform and fine sediment could be initiated. In addition, the local variation of the flow velocity around vegetation stems cannot be modeled by the drag-force method, which may also result in the underestimation of bed erosion. Near the trailing edge of vegetation canopy, bed erosion in the vegetation canopy in the junction region is relatively underestimated. As known, in that region secondary flows are well developed and might promote the bed erosion in the vegetation canopy. The Nays2DH takes the effect of secondary flows into consideration with a submodel in the governing equations. However, the simulated results show that the secondary flow effect might still be underestimated.

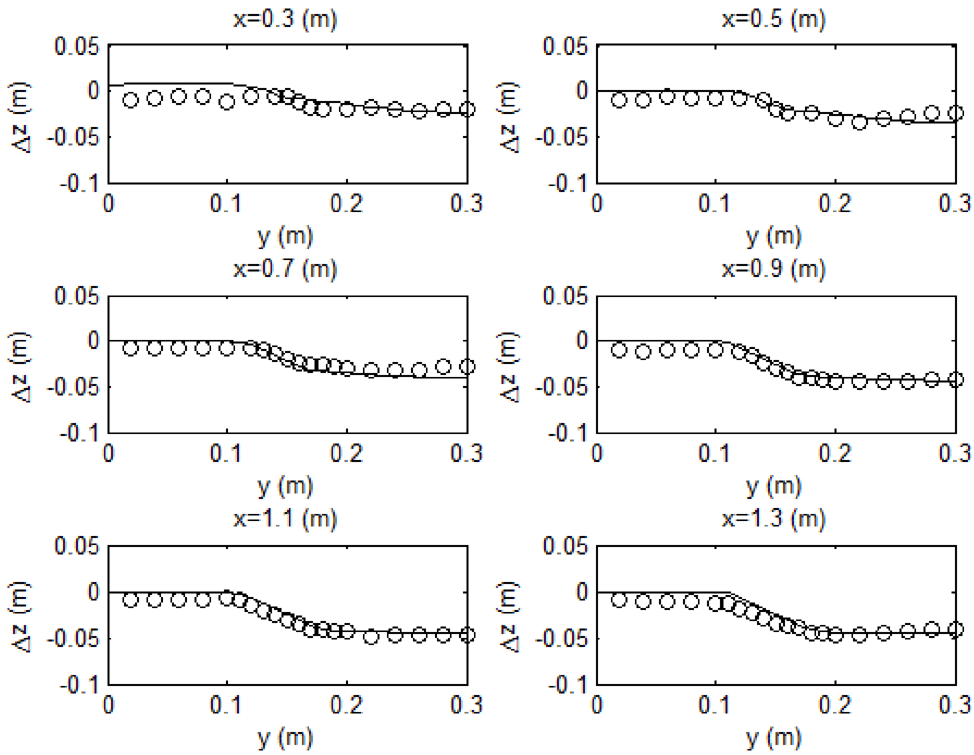

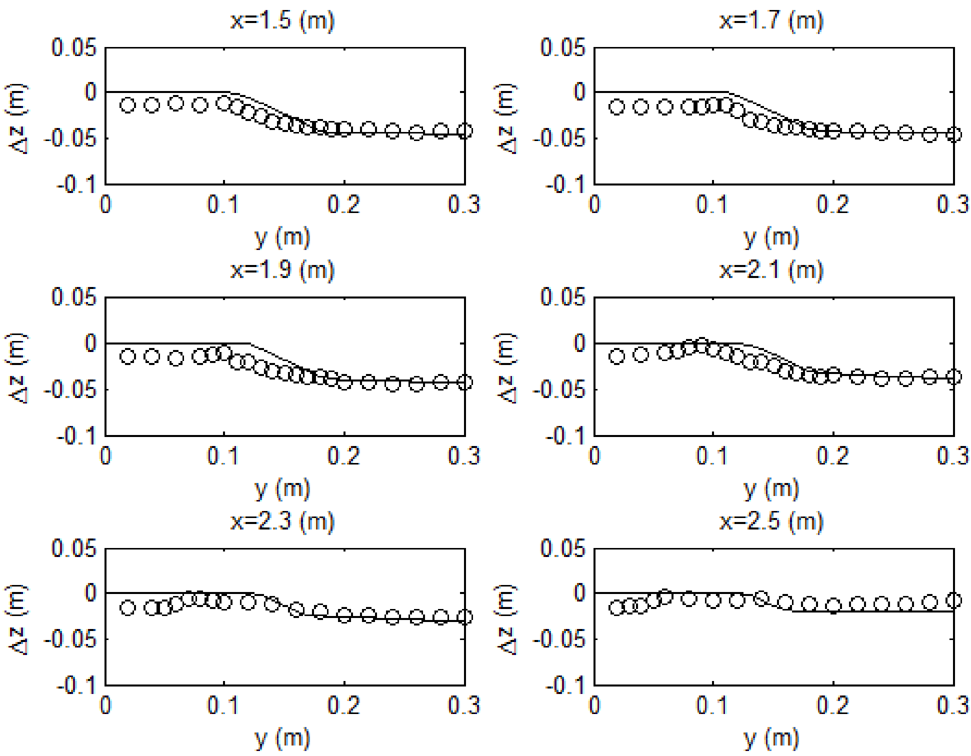

Figure 6.4 Transverse profiles of bed elevation change between the measurement (open circle) and simulation (solid line) for Case1.

Figure 6.5 shows longitudinal bed profile for five different transverse locations. In general, the morphological model is able to reproduce the right pattern of longitudinal bed profile with respect to the sediment erosion and deposition. At the non-vegetated side ($y/b_v \geqq 1$), the simulated results perfectly agree with the measurement. The simulated entire profile at the vegetated reach accurately fits the measurement. The deviation between measurement and simulation is found at the vegetated side (y/b_v < 1). The possible reason is the drag-force method incorporated in the 2D numerical model to simulate the vegetated flow cannot capture the accurate and specific flow structure in the vegetation canopy. However, it is also worth noticing that the deviation is insignificant as the vegetation canopy effectively protects the bed from being eroded.

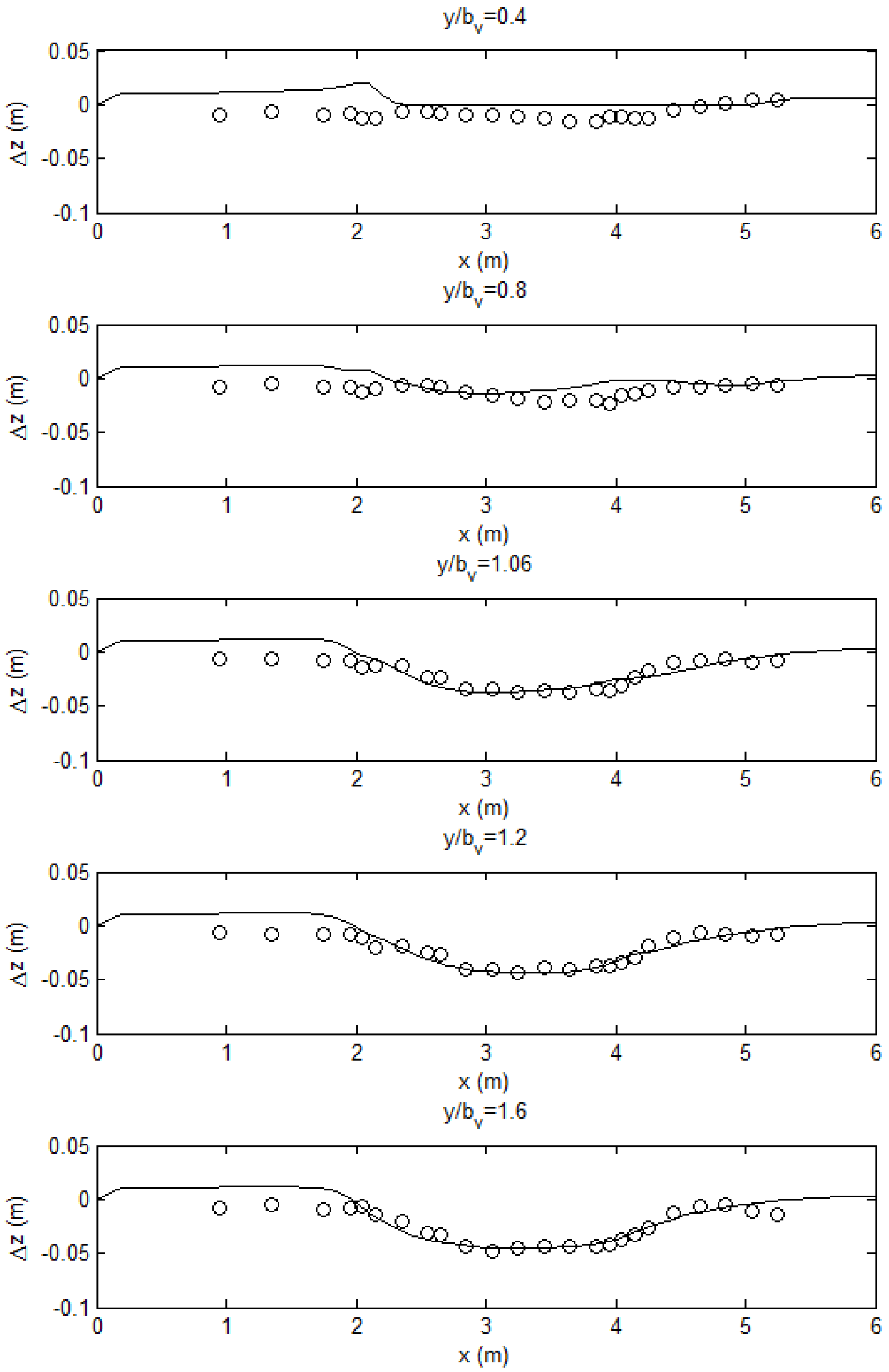

Figure 6.5 Longitudinal profiles of bed elevation change for observation (open circle) and simulation (solid line) for Case1.

6.3.2 Numerical experiments in POCVC: case study

Because the 2D morphological model Nays2DH-IRIC has been proved to be able to simulate the flow velocity and bed morphology evolution, it is used to investigate impacts of different parameters on the bed morphology pattern in the POCVC to achieve a general recognition of alluvial process characteristics due to near-bank vegetation canopies.

Table 6.1 shows details of different runs in numerical experiments. Four major factors which are considered to affect the evolution of the bed morphology are investigated by the 2D flow-sediment-vegetation coupled model. The four factors are the angle of repose value of bed materials (RAV), vegetation density (VD), patch length (CL) and patch width (CW), respectively. For reference, the configuration setting of Runf1 is used as the basic run and only one factor is changed for each run. It is presented that altogether four groups which are (Run1, Run2, Run3), (Run1, Run4, Run5), (Run1, Run6, Run7) and (Run1, Run8, Run9).

Table 6.1 List of different parameters in parameter study

	Water discharge Q (m3/s)	Angle of repose value RAV	Vegetation density VD (m^{-2})	Patch length CL (m)	Patch width CW (m)	Remarks parameter variation
Run1	**0.0125**	**0.6**	**5.56**	**2**	**0.15**	**Basic run**
Run2	0.0125	**0.45**	5.56	2	0.15	RAV
Run3	0.0125	**0.3**	5.56	2	0.15	
Run4	0.0125	0.6	**3**	2	0.15	VD
Run5	0.0125	0.6	**8**	2	0.15	
Run6	0.0125	0.6	5.56	**1**	0.15	CL
Run7	0.0125	0.6	5.56	**0.5**	0.15	
Run8	0.0125	0.6	5.56	2	**0.1**	CW
Run9	0.0125	0.6	5.56	2	**0.2**	

6.3.2.1 RAV of bed materials on bed morphology evolution

Three RAVs of bed materials, 0.6, 0.45 and 0.3, are used for the numerical study. The three values are generally acceptable regarding submerged sands with an angle of repose in the range of 15-30 degrees. Figure 6.6 shows simulated contours of bed morphology for runs with the variation of RAV of bed materials. It is clearly noted that by changing RAV of bed materials no significant difference is induced, particularly for regions of maximum erosion and deposition. And for three runs, the sediment bar at the downstream of vegetation canopy has a similar pattern with respect to orientation and scale.

However, as we know RAV influences the local slope of the bed surface, therefore, it is found that in the junction, bed morphology changes a lot due to different RAVs of bed materials. For larger RAV, isolines of the contour are denser, vice versa. This indicates that the transverse slope becomes steep due to the large RAV. In other words, with smaller RAV, the bed erosion is transversely extended to the deeper inner region of vegetation canopy, which overestimates flow erosion ability due to partial obstruction of the vegetation canopy.

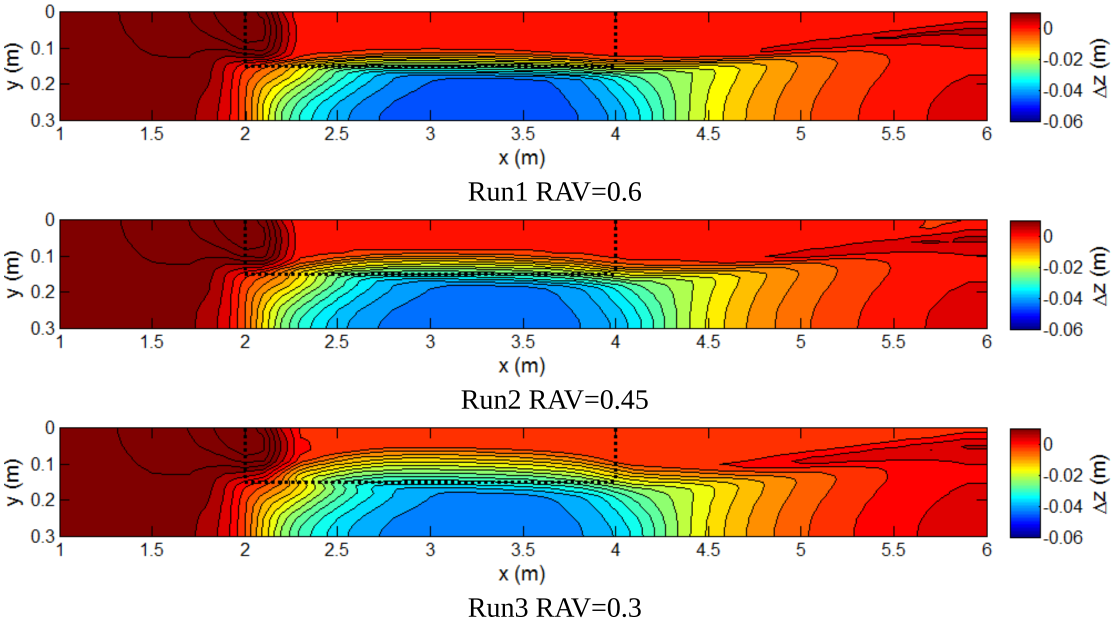

Figure 6.6 Contour of bed morphology under different RAVs of bed materials. The rectangular area bounded by dotted lines donates the vegetation canopy.

Transverse bed profiles at different cross-sections along the channel are shown in Figure 6.7. More clearly, with different RAVs of materials, except for the junction region, transverse bed profiles show perfect agreement. More specifically, in the deeper inner vegetation region the bed is very stable with no bed elevation change while the bed is greatly eroded in the neighboring open water region. Larger RAV produces steeper transverse bed slope in the transitional region. The difference of simulated results is distinguishable. With respect to bed profile in the junction, the simulation with RAV=0.3 nearly produces an increase of 0.06m out of patch width

0.15m compared to the simulation with RAV=0.6 (see *x*=3m and *x*=3.5m). Therefore, smaller RAV results in the larger volume of bed erosion.

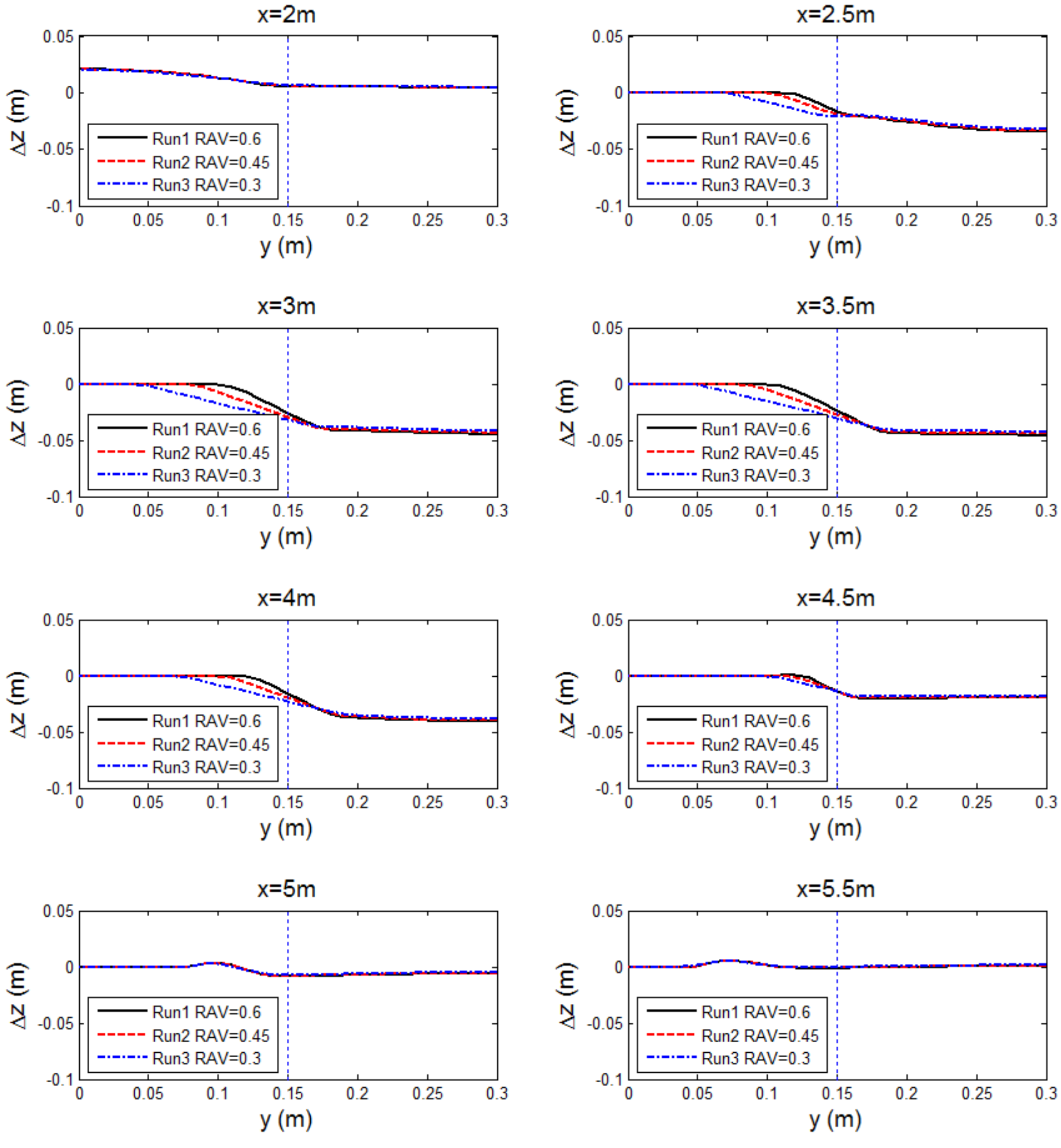

Figure 6.7 Transverse bed profiles under different RAVs of bed materials. The lateral edges of vegetation canopy for three runs overlap at *y*=0.15m, indicated by vertical dotted lines.

Figure 6.8 shows longitudinal bed profiles. For the three given transverse transects (y=0.05m, 0.15m, 0.25m) indicating the VR, junction and NOWR, simulated longitudinal bed profiles along the entire channel under different RAVs of bed materials are almost the same. But as discussed above the difference occurs at the transitional junction region.

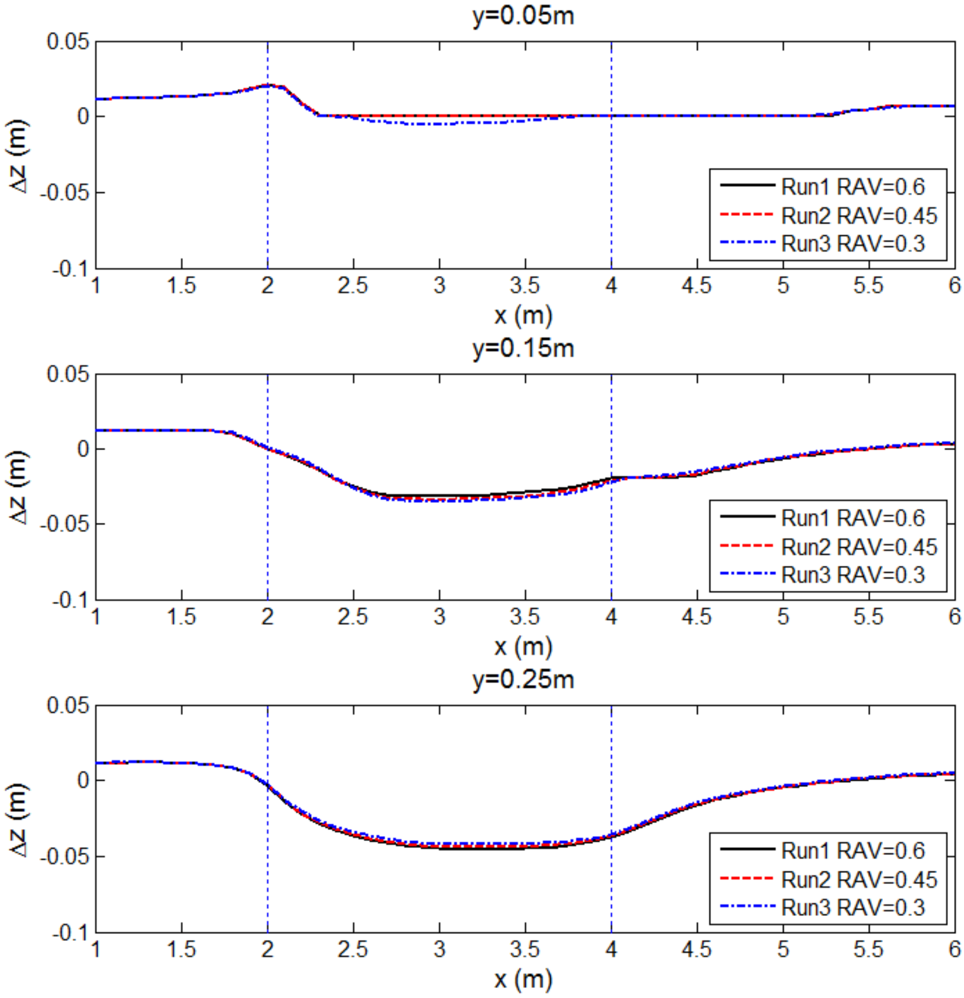

Figure 6.8 Longitudinal bed profiles under different RAVs of bed materials. The leading and trailing edges of vegetation canopy for three runs overlap at x=2m and 4m indicated by vertical dotted lines.

6.3.2.2 VD on bed morphology evolution

Figure 6.9 shows the simulated contour of bed morphology under different VDs. It is found that VD greatly affects bed erosion in the NOWR along the vegetation canopy. As expected, larger VD leads to larger scour depth. Meanwhile, the existence of vegetation canopy effectively protects the bed from surface erosion even for Run4 which is under smallest vegetation density. Unlike that RAVs of bed materials sensitively affects transverse erosion in the junction region, smaller VD (Run4 VD=3m^{-2}) leads to smaller transverse erosion toward the VR. However, in comparison with Run1 (VD=5.56m^{-2}) and Run5 (VD=8m^{-2}), the transverse bed erosion shows the insignificant difference. In regard to the sediment bar, the morphology does not change with VD. But the deposition at the sediment bar seems to decrease as VD increases. Still, the difference is not remarkable.

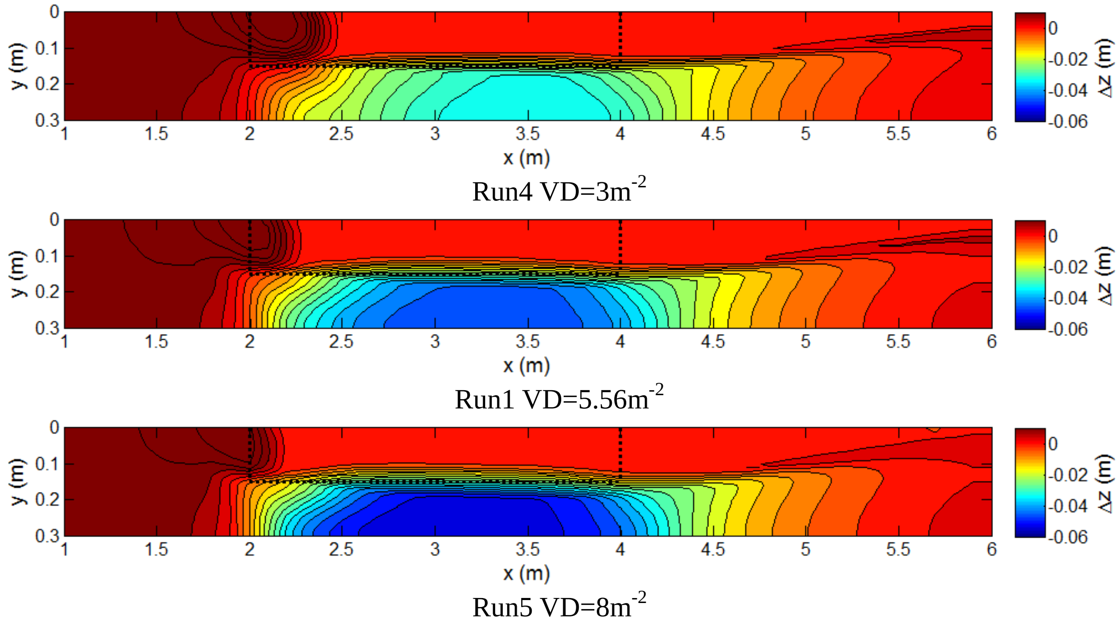

Figure 6.9 Contour of bed morphology under different VDs. The rectangular area bounded by dotted lines donates the vegetation canopy.

Figure 6.10 shows transverse bed profiles at different cross-sections along the channel.

Larger VD leads to larger bed erosion in the NOWR owing to the increase in flow velocity. The transverse bed erosion toward the VR is nearly the same along the channel except for the cross section at x=3m, where smaller VD (Run4 VD=3m^{-2}) leads to smaller transverse bed erosion. However, with larger VD, the transitional bed profile extends remarkably toward the NOWR with a simultaneous larger degradation. This property is very obvious at the vegetated reach. Interestingly, the numerical simulation illustrates that the transitional profile for three VDs are almost of a same slope, which should be confirmed by further supportive evidences such as experimental results.

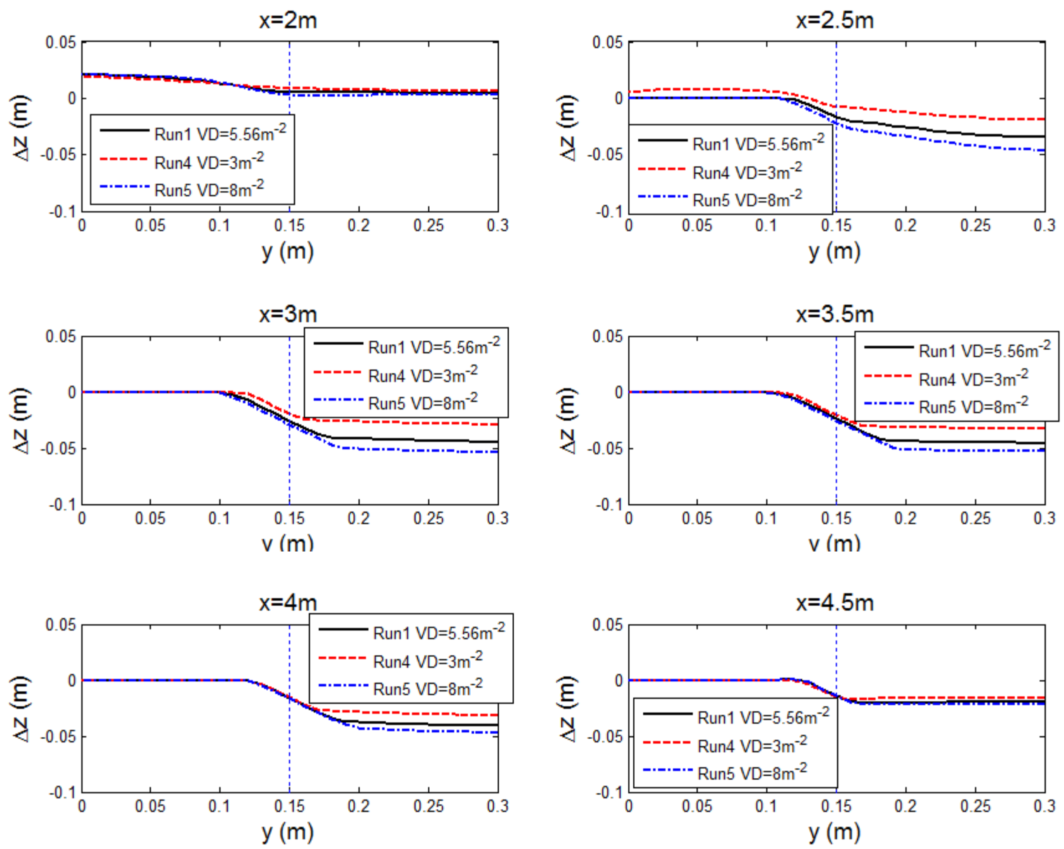

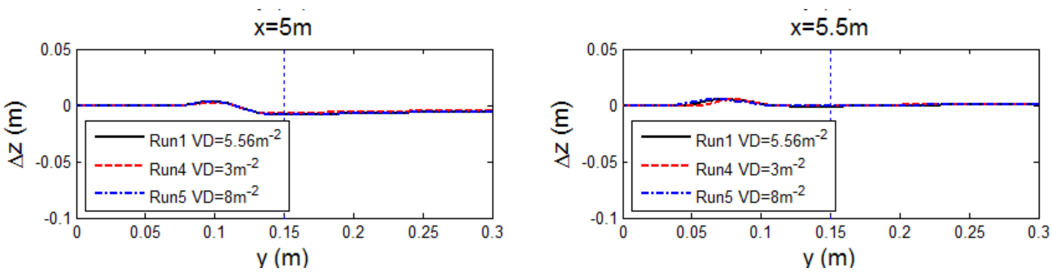

Figure 6.10 Transverse bed profiles under different VDs. The lateral edges of vegetation canopy for three runs overlap at *y*=0.15m indicated by vertical dotted lines.

Figure 6.11 shows simulated longitudinal bed profiles under different vegetation densities. In the deeper inner vegetation region, no erosion and deposition occur. This extends to the downstream of the vegetation canopy. However, due to the nature of the mathematical model, the sediment deposition happens at the leading edge other than the local scour observed in laboratory experiments. The smaller vegetation density leads to the larger sediment deposition due to the smaller flow resistance. In the neighboring open water region, as the vegetation density increases, the bed degradation (erosion) is not only greater but also extends further toward the upstream.

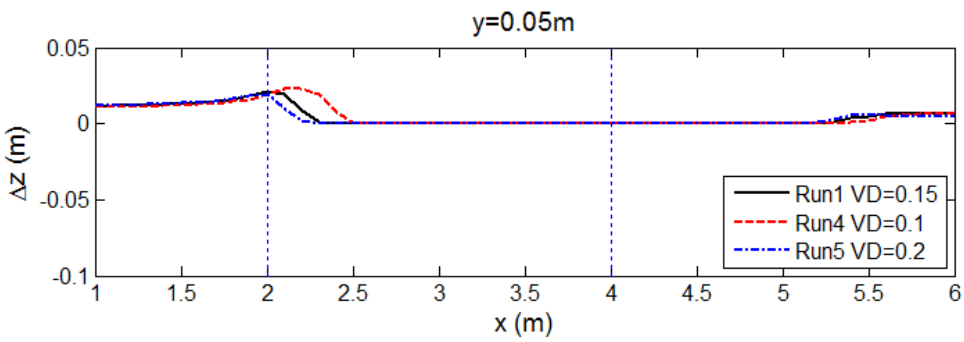

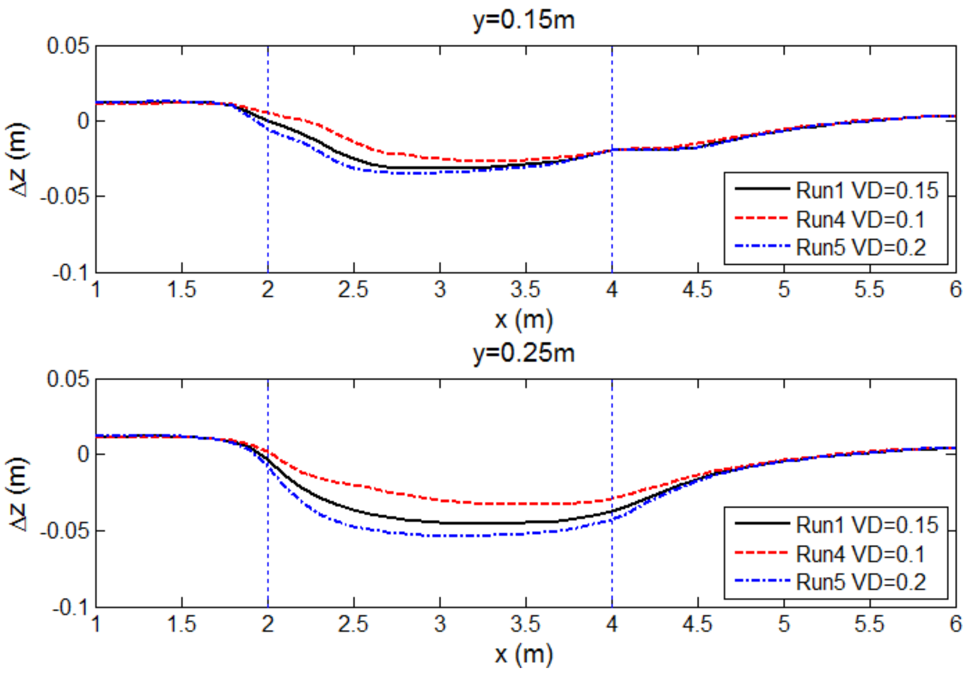

Figure 6.11 Longitudinal bed profiles under different VDs. The leading and trailing edges of vegetation canopy for three runs overlap at x=2m and 4m, indicated by vertical dotted lines.

6.3.2.3 CL on bed morphology evolution

In real situations, the geometric morphology of vegetation canopy is of diversity. CL in the streamwise direction is an important one. Figure 6.12 shows the simulated contour of bed morphology with different CLs. The pattern of bed morphology, in general, does not change, but an apparent difference in geometry can be found in the simulated results. As CL increases, bed erosion in the NOWR increases correspondingly. This may be attributed to that a longer vegetation canopy can lead to larger flow velocity in the NOWR, resulting in greater scouring. Transversely, the longer vegetation canopy also leads to greater transverse erosion toward the VR. Due to the difference in CL, the morphology of sediment bar also differs. For the longest vegetation canopy (Run1 CL=2m), the sediment bar clearly forms at the downstream of vegetation canopy. However, as the vegetation canopy becomes shorter, the sediment bar tends to degrade and forms at further downstream. This is probably owing to the better development of secondary flows for longer vegetation canopy compared to shorter vegetation canopy.

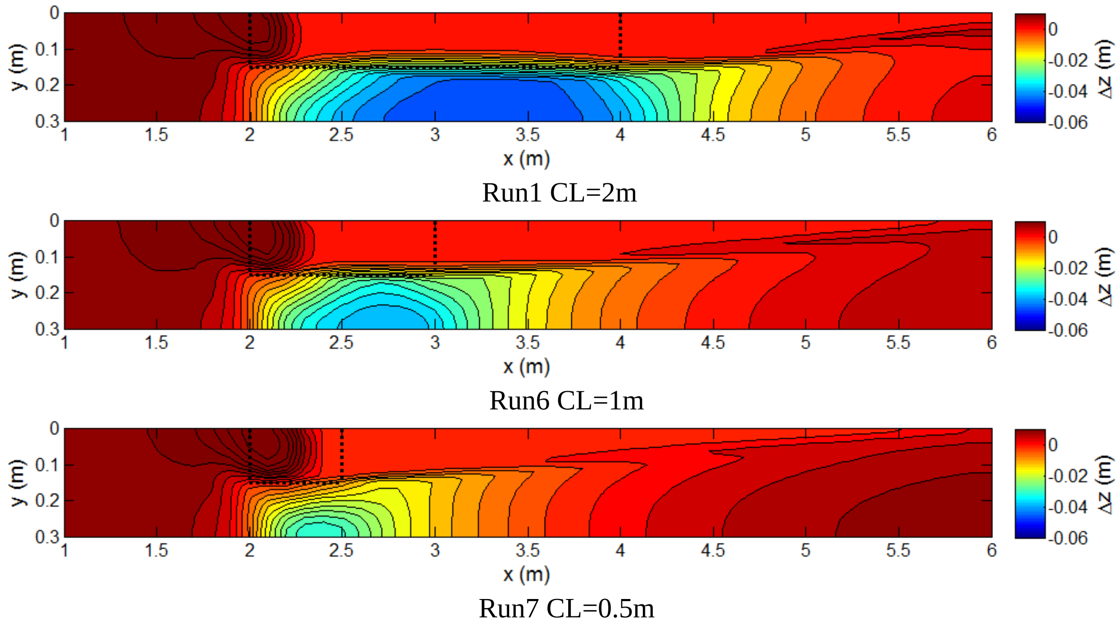

Figure 6.12 Contour of bed morphology under different CLs. The rectangular area bounded by dotted lines donates the vegetation canopy.

Figure 6.13 shows transverse bed profiles at different cross-sections along the channel. As shown above, larger CL leads to larger overall maximum of bed erosion on the non-vegetated side at different cross-sections. However, before flow exits the vegetated reach, transverse bed profile under different CLs is not quite distinct (e.g., Run1, Run6 and Run7 at x=2.5m, Run1 and Run6 at x=3m). An obvious difference in transverse bed profile only can be observed in the junction. Under larger CL bed erosion in the junction is more pronounced (see bed profiles at x=2.5m and x=3m).

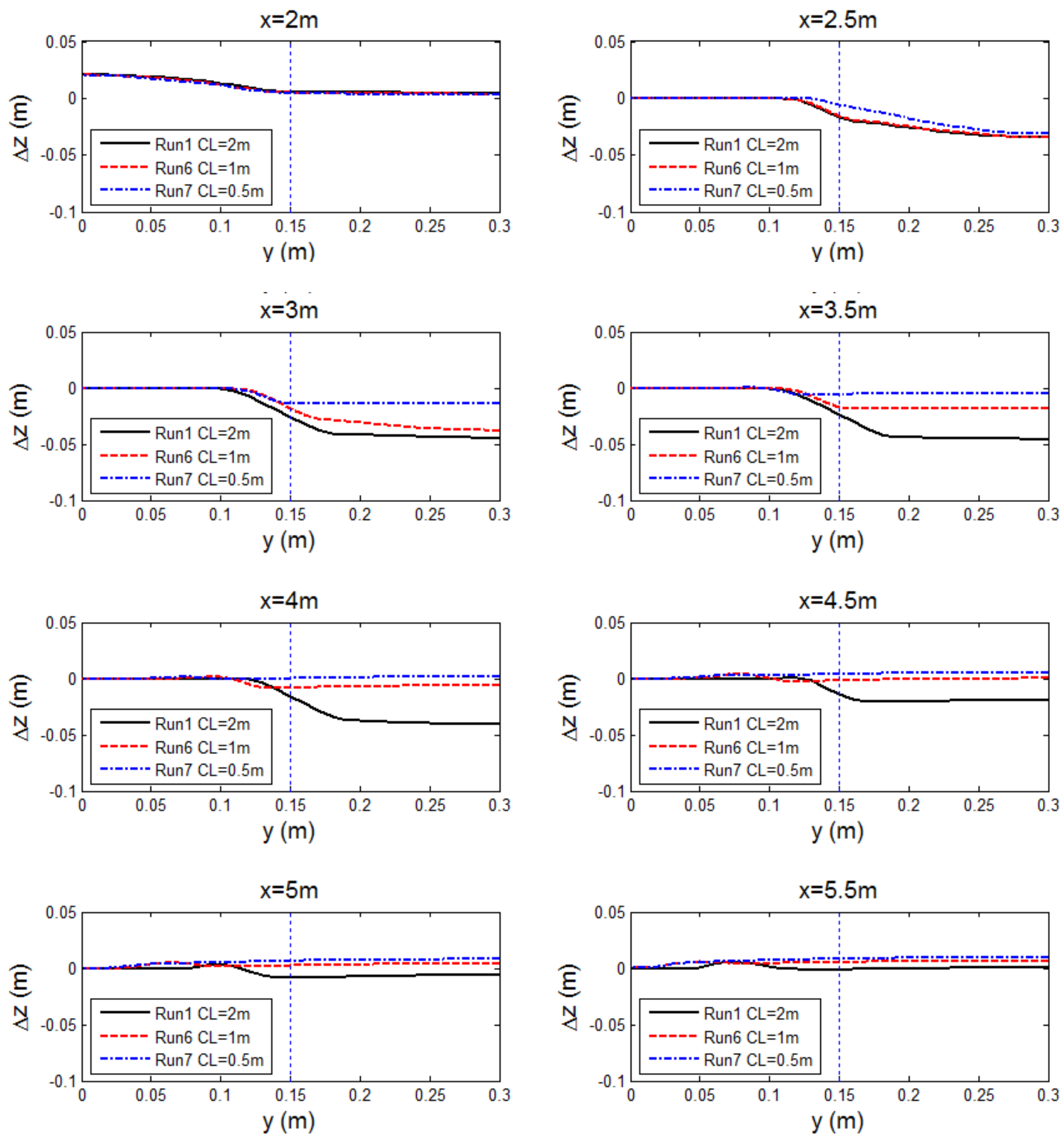

Figure 6.13 Transverse bed profiles under different CLs. The lateral edges of vegetation canopy overlap at y=0.15m indicated by vertical dotted lines.

Figure 6.14 shows longitudinal bed profiles under different CLs. It is certain that maximum scour depth occurs at the upstream of trailing edge of vegetation canopy for all runs (see y=0.25m). This differs from the observation by Kim (2015) that maximum scour depth occurs at the downstream of the trailing edge. The disagreement is still under uncertainty. The reason might be the 2D numerical model calculates sediment transport and bed deformation with the depth-averaged flow velocity information. It is clearly known that the depth-averaged flow velocity would decrease immediately due to the disappearance of the vegetative obstruction at the downstream. This could lead to the sediment deposition rather than erosion. Therefore, the model also offers the reasonable simulated results. However, for the present study, bed-load transport as the dominant sediment transport phenomenon is in fact directly related to the near-bed flow velocity. Therefore, further experimental investigation of short vegetation canopy is required for a complete recognition of bed morphology evolution due to partial obstruction of vegetation canopy. Probably, a fully three-dimensional sediment transport model is satisfactory for the numerical simulation of bed morphology evolution if the above argument is reasonable.

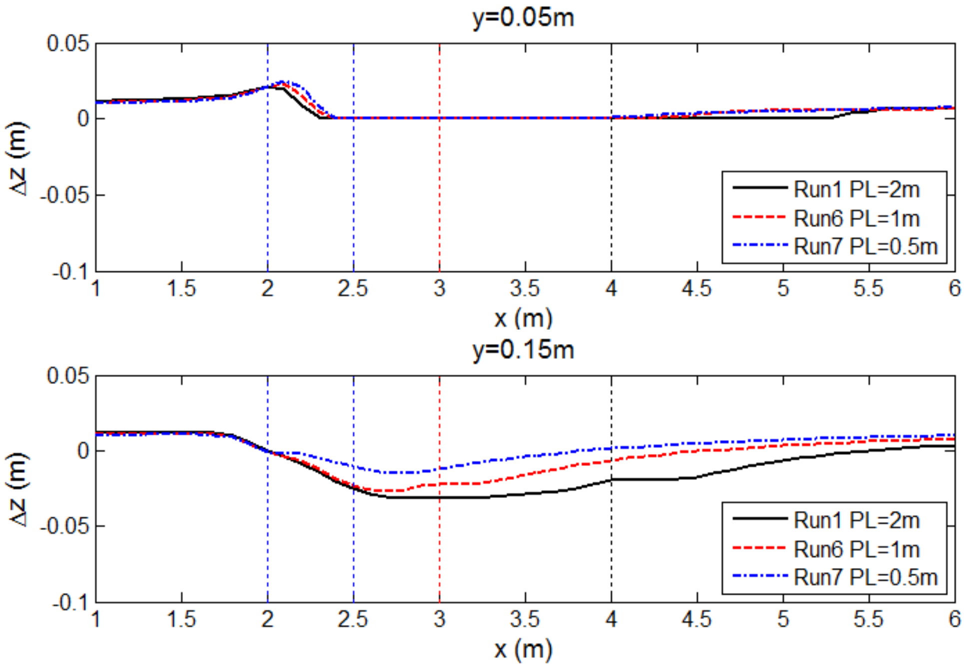

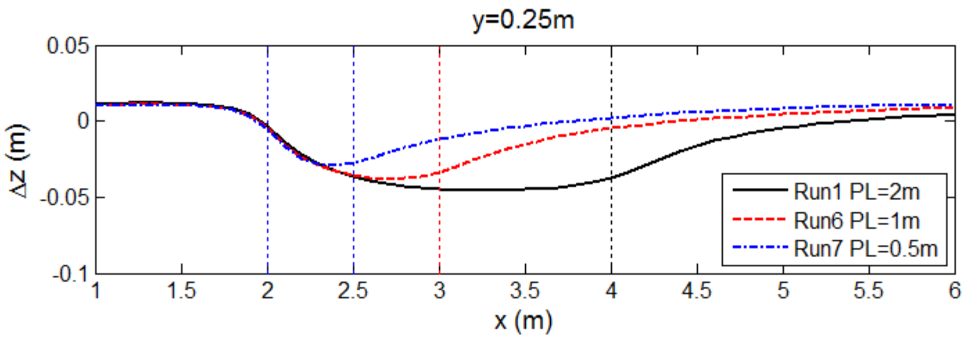

Figure 6.14 Longitudinal bed profiles under different CLs. The lateral edges of vegetation canopy for three runs are at *x*=2m and 4m, *x*=2m and 3m and *x*=2m and 2.5m indicated by vertical black, red and blue dotted lines.

6.3.2.4 Vegetation canopy blockage on bed morphology evolution

The colonization of vegetation on the channel bed can flourish and degrade in different seasons periodically. Obstruction proportion of vegetation across the channel is expected to impact flow structure and thus alluvial process. In order to investigate the blockage effect of vegetation canopy on channel bed morphology evolution, three vegetation canopy widths (Run8 CW=0.1m, Run1 CW=0.15m and Run9 CW=0.2m) are used in the numerical experiments. In other words, the blockage ratio in the channel (canopy width/channel width) is 33%, 50% and 67%.

Figure 6.15 shows the simulated contour of bed morphology with different CWs. It is clearly shown that the blockage effect of vegetation canopy significantly affects bed morphology pattern. Along the vegetation canopy, bed scour in the NOWR under larger blockage ratio is much greater than that under smaller blockage ratio. Meanwhile, maximum scour core under the largest blockage ratio (Run9 CW=0.2m) of vegetation canopy occurs at the upstream in the vegetated reach (x=2-4m). However, for the other two runs (Run8 CW=0.1m and Run1 CW=0.15m), maximum sour cores extend to the downstream in the vegetated reach. This might be attributed to that the larger vegetation blockage ratio can lead to a quicker adjustment of flow in the NOWR, thus resulting in the quicker adjustment of bed morphology.

The blockage ratio of vegetation canopy also affects transverse bed erosion toward the VR. Clearly, larger blockage ratio can lead to greater transverse erosion. Roughly, no transverse bed erosion toward the vegetation region occurs for Run8 (CW=0.1m) of the smallest vegetation blockage ratio. For three runs, the sediment bar can be found at the downstream of the vegetation canopy, and its morphology is not much different.

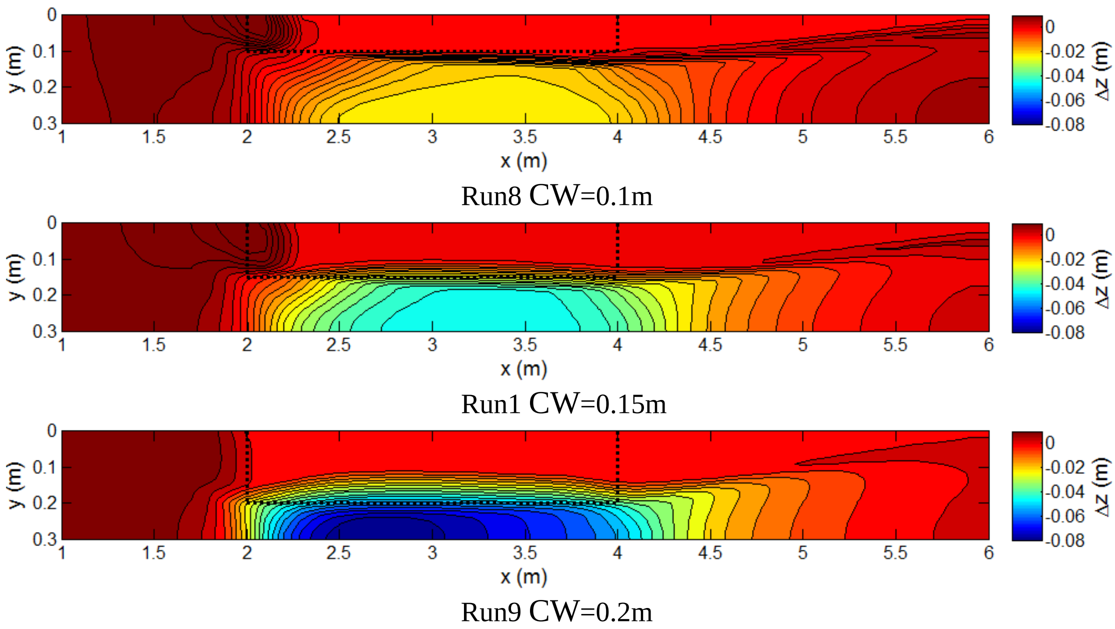

Figure 6.15 Contour of bed morphology under different CWs. The rectangular area bounded by dotted lines donates the vegetation canopy.

Figure 6.16 shows transverse bed profiles at different cross-sections along the channel.

Again, larger blockage ratio of vegetation canopy leads to the greater bed erosion in the NOWR at the vegetated reach. Larger blockage ratio also leads to longer transverse transitional bed profile in the junction region. It is interestingly noted that the slope of transitional bed profile is almost the same for all three runs. Therefore, the RAV of bed materials might be one of the most important factors to shape the morphology of the transitional bed profiles based on the simulated results. But this conclusion is still speculative and should be confirmed by laboratory experiments.

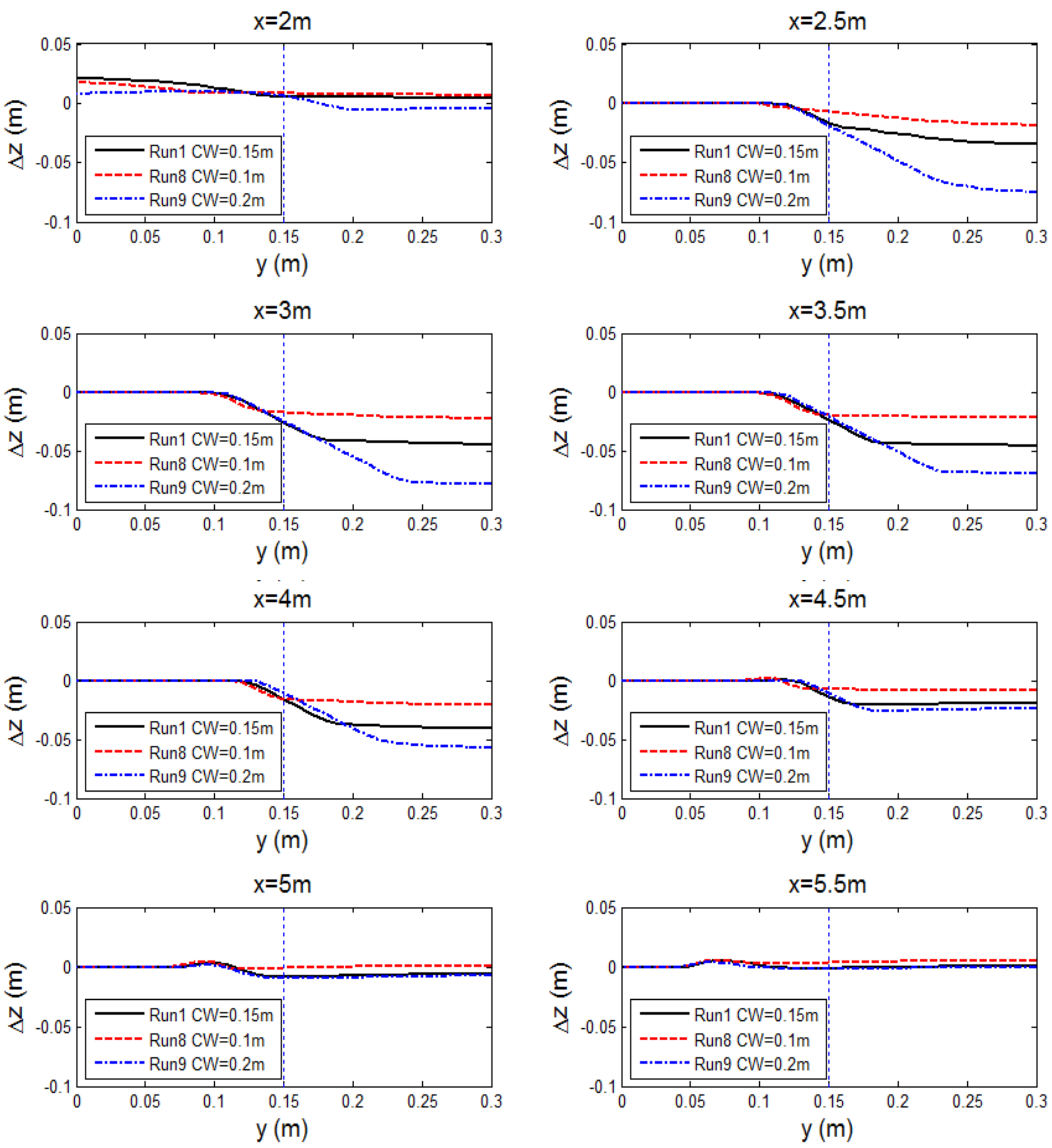

Figure 6.16 Transverse bed profiles under different CWs. The lateral edges of vegetation canopy for three runs are at *y*=0.1m, 0.15m and 0.2m indicated by vertical red, black and blue dotted lines.

Figure 6.17 shows longitudinal bed profiles at three transects across the channel. As discussed previously, maximum scour depth occurs at *x*=2.5m at the upstream in the vegetated reach due to larger vegetation blockage ratio. The bed profile then slightly increases along the channel. However, for the other two smaller blockage ratios of vegetation canopy, the maximum scour depth occurs behind *x*=2.5m and then tends to remain constant along the channel.

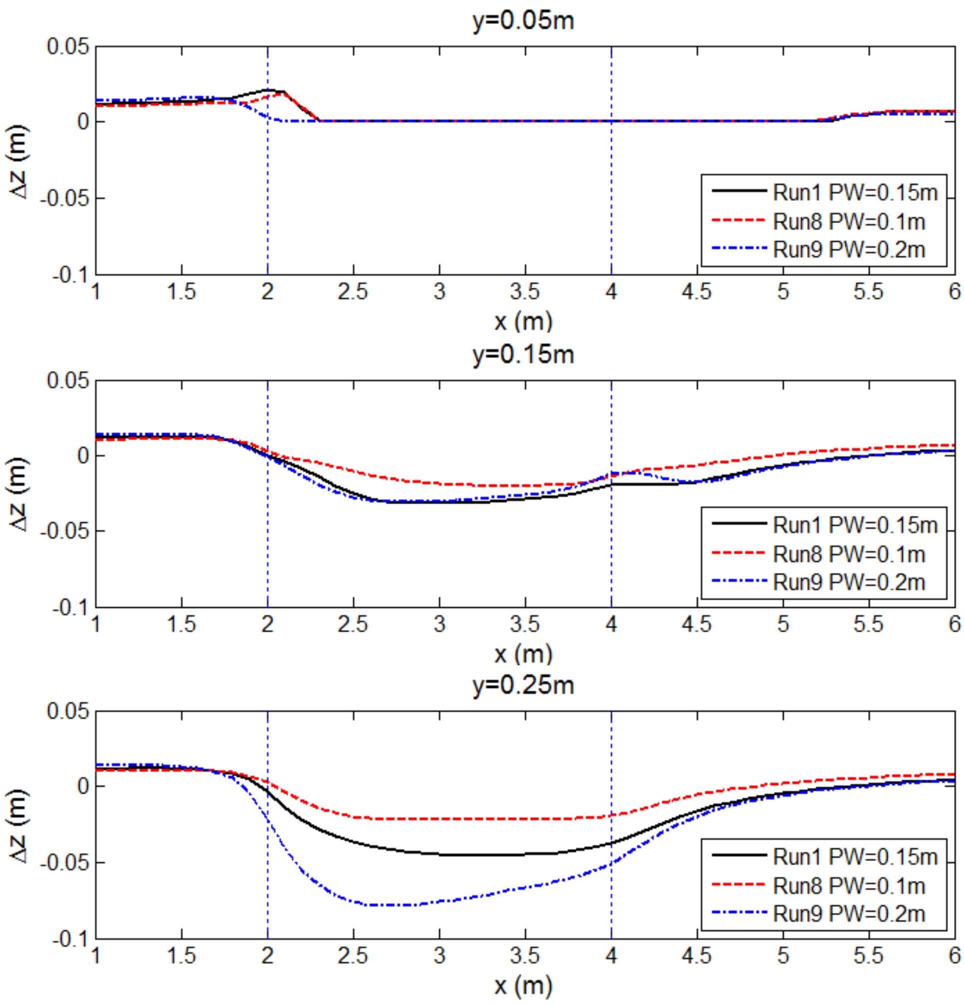

Figure 6.17 Longitudinal bed profiles under different CWs. The leading and trailing edges of the vegetation canopy for three runs overlap at *x*=2m and 4m, indicated by vertical dotted lines.

6.4 Conclusions

This chapter aims to study the effects of different flow-vegetation configurations on bed morphology evolution, and the 2D morphological model Nays2DH-IRRIC was employed to model the alluvial process in the POCVC. The validation of the numerical model was carried out with the experimental depth-averaged flow velocity and bed morphology, respectively. It is shown that Nays2DH-IRIC can well reproduce flow characteristics and bed morphology in the POCVC with acceptable accuracy. Then factors including angle of repose value (RAV) of sediment, vegetation density (VD), canopy length (CL) and canopy width (CW) (representing canopy blockage effect) of vegetation canopy were adopted in the parameter study. It is found that above factors all have significant influences on bed morphology evolution. Numerical results show that the RAV of sediment parameterized in the slope failure model only dominates the transverse bed profile in the junction. Larger RAV leads to steeper transverse bed profile. The increase in VD, CL and CW is able to induce deeper pool region at the vegetated reach. Besides above, larger VD tends to induce upstream expansion in pool and bed erosion inside vegetation canopy. Larger CL induces larger pool region along vegetation canopy in the longitudinal dimension. With the increase in CW, the location of the deepest core in the pool tends to shift upstream.

Chapter 7 Conclusions and Future work

7.1 Introduction

The recognition of the significance of vegetation canopy on water management, alluvial process, and river restoration has been raised by the public for decades. Extensive efforts have been made to understand the flow-vegetation-sediment interaction mechanism. Particularly, investigations of mean flow and turbulence characteristics due to sole flow-vegetation interaction have been extended to a variety of vegetation canopy configurations, which offers knowledge and guidelines to practical activities.

The existing knowledge for the flow-vegetation interaction mechanism is frequently limited to simple boundaries, over which flow characteristics are not complex. The existing knowledge of the junction between the vegetation canopy and the neighboring open water concentrates on the depth-averaged flow features and lacks detailed three-dimensional flow descriptions. The high anisotropy across the junction is likely to induce uncertainties when the existing two-dimensional depth-averaged flow knowledge is applied to the practice. Therefore, of great significance is to investigate the three-dimensional flow characteristics so as to gain a complete understanding of flow behaviors in the partially-obstructing channel with vegetation canopy (POCVC).

To date, studies including experimental investigations and numerical simulations on the three-dimensional flow characteristics and the associated sediment transport and bed morphology evolution of flow in the POCVC are insufficient and incomplete. Two main contributions were made in this dissertation. One is the experimental investigation and numerical simulation of three-dimensional flow characteristics in the POCVC. The other is the experimental investigation and two-dimensional numerical simulation of bed morphology evolution in the POCVC.

7.2 Flow structure and turbulence in the partially-obstructed channel with vegetation canopy

7.2.1 Experimental study

The latest-generation acoustic Doppler velocimeter (ADV) profiler, namely Vectrino-II, was employed for its high efficiency in measuring 3D instantaneous velocities. The flow adjustment in the vegetation region (VR) ($y/b_v \ll 1$) was examined in terms of depth-averaged (DA) and three-dimensional flow characteristics. For the DA longitudinal velocity (U), the flow adjustment distance approximates 70% of the canopy length ($0.7L_p$) under the same vegetation density. In the neighboring open water region (NOWR) ($y/b_v \gg 1$), the flow adjustment distance is much shortened in particular for the large-submergence canopy. The flow adjustment distance in terms of DA flow characteristics also meets the adjustment of the vertical profile of longitudinal velocity ($\overline{u}$) except for the near-bed region. Other turbulent properties such as vertical Reynolds stress ($-\overline{u'w'}$) and transverse Reynolds stress ($-\overline{u'v'}$), however, require a longer adjustment distance in consistency with previous studies.

One significant finding is that the vertical profile of longitudinal velocity is deflected in the near-bed region of the outer-side junction. Vertical Reynolds stress correspondingly becomes negative in the same region. Velocity deflection and negativity in vertical Reynolds stress are attributed to the generation of horizontal coherent vortices, which transport the low momentum from the vegetation canopy to the neighboring open water. The generation of those coherent vortices, however, is inhibited by the bed resistance confirmed by the vertical growth of transverse Reynolds stress above the bed. It is shown that vegetation density and vegetation submergence essentially influence the 3D distribution pattern of flow characteristics. More specifically, velocity deflection and negativity in vertical Reynolds stress in the near-bed region can be enhanced by larger vegetation density and vegetation submergence.

Subsequently, a term-by-term analysis of turbulent kinetic energy (TKE) transport equation for the fully-developed flow was carried out to look into the energy transfer between the vegetation canopy and neighboring open water. The turbulence production and transport both in the vertical and transverse directions are taken into consideration. Results show the turbulent kinetic energy inside the deeper vegetation canopy is predominantly produced by the vegetation stem wake and is balanced by the combination of dissipation and pressure transport. The low vegetation density is found to promote vegetation stem wake owing to the large spacing between stems benefitting the wake development. In the junction region, the shear production due to the vertical/transverse coherent vortices positively contributes a large proportion together with the wake production (deep inside the vegetation canopy). Apart from the energy dissipation and pressure transport, the turbulent transport negatively contributes to the turbulent kinetic energy. In the NOWR farther away from the canopy edges, the turbulent transport makes the larger positive contribution instead of the shear production, indicating massive TKE transport from the junction.

With such implication, a hydrodynamic model was proposed for the description of vortex pattern rising from flow-vegetation interaction, which can be used to explain vertical distribution of flow characteristics in the POCVC and to provide the fundamental for improving the accuracy of the 3D numerical simulation.

7.2.2 Numerical simulation

The Spalart-Allmaras (SA) model can efficiently model shear flows due to the nature of eddy viscosity transport equation in characterizing the turbulence length of the large-scale vortex (Zeng and Li, 2013). However, the standard one-equation SA model is highly isotropic due to the specification of one turbulence length scale, making it difficult in describing mean flow and turbulence characteristics in the POCVC.

This study improved the SA model on the basis of the vortex pattern in the POCVC: vertical coherent vortices, horizontal coherent vortices and vegetation stem wake. The predominant turbulence length scale of local eddies was specified so that the simulated eddy viscosity becomes highly anisotropic through the entire water body, which essentially reflects the turbulent flow mixing in the POCVC. The validation shows that the vortex-based SA model accurately simulates flow characteristics in the VR except for the entry region. In the junction region, flow velocity deflection in coincidence with negative vertical Reynolds stress in the near-bed region can be well reproduced, while the standard SA model failed to do so.

A parameter study shows that the two parameters α_y and β_y for describing the spatial distribution of horizontal coherent vortices have distinct impacts on the simulated flow behaviors in the junction. The impact of α_y on the flow behavior is negligible while β_y characterizing the development of horizontal coherent vortices away from the bed pronouncedly contributes to the degree of velocity deflection and the negativity of vertical Reynolds stress in the near-bed region. The characteristic transverse turbulence length δ_y dominates the transverse extension of horizontal coherent vortices in the NOWR. As δ_y decreases, the outer region farther away from the junction is negligibly affected by horizontal coherent vortices accompanied by momentum exchange between the VR and the NOWR. The increase in vegetation density tends to result in an increase in the degree of velocity deflection and negativity in vertical Reynolds stress, since the vegetation density essentially promotes the generation of coherent vortices.

7.3 Alluvial process in the partially-obstructed channel with vegetation canopy

7.3.1 Experimental study

This study demonstrates the experimental investigations of bed-load transport and bed morphological evolution in the POCVC. Clean water scours in the absence of upstream sediment supply were conducted. To approach real situations, the sorted sediment was used as bed materials. The flow characteristics over the equilibrium bed were measured for understanding the role of the generated bed morphology in the development of flow characteristics in the POCVC, which might be useful for further improvement of morphological modeling of alluvial process affected by the in-stream vegetation.

Results show that due to partial obstruction of the vegetation canopy, intensive sediment transport occurred owing to the significant increase in bed shear stress in the NOWR. A significant peak occurred for the sediment transport rate variation when the downstream-propagating sand wave reached the sediment collection section. The curve of sediment transport rate fluctuates as bed roughness changes with the propagation of the sand wave. Meanwhile, the obvious sediment sorting effect is coincident during the sediment transport process.

As the equilibrium bed morphology is reached, characteristic bed morphology was developed and can be identified as (A) water pool induced by flow convergence in the

NOWR, (B) slightly-eroded bed protected by the vegetation canopy in the VR, (C) slightly-eroded bed at upstream of vegetation canopy, (D) local bed scour near the leading edge of vegetation canopy, (E) sediment bar with surface fining extending downstream after the vegetation canopy, and (F) riffle downstream of the vegetated reach. Of significance is that the scour pool and the downstream deposition bed morphology compose typical pool-riffle morphology, which is suggested to be crucial for river restoration and species rehabilitation. By comparing equilibrium bed morphologies due to long vegetation canopy with short vegetation canopy in previous studies, canopy length might affect the bed morphology pattern such as scale and spatial distribution.

Flow characteristics over the equilibrium bed in the POCVC were measured. Apart from the generation of horizontal coherent vortices, secondary flows were induced along the vegetation canopy to drive the transverse motion of flow as well as transverse bed surface sediment sorting. Although sediment transport and bed morphology evolution happen in experiments, flow adjustment is similar to the counterpart in the non-sediment flat channel. Velocity deflection and negative vertical Reynolds stress in the near-bed region were also identified in the junction.

Finally, along the vegetation canopy, the relationship between bed morphology and flow characteristics was analyzed with scaling concept. Linear relations can be found among the longitudinal bed profile, longitudinal flow propagation distance, mean flow velocity and the transverse inner extension of bed erosion. At the vegetated reach, transverse bed profile displays in the curve of the tangent hyperbolic function. The proposed tangent hyperbolic equations can well predict the transverse bed profile with well-defined transverse extension lengths. Future work on more experimental and simulated data under different flow configurations is required to validate the generality of the tangent hyperbolic equations.

7.3.2 Morphological modeling

In order to study effects of different flow-vegetation configurations on bed morphology evolution, the depth-averaged morphological model Nays2DH-IRIC was employed to model the alluvial process in the POCVC. The vegetation resistance effect was adopted into the drag force term. The validation shows that the depth-averaged flow velocity and bed morphology predicted by Nays2DH-IRIC well agree with the experimental data. The depth-averaged flow characteristics and bed morphology in the POCVC can be reproduced. Then important factors including angle of repose value (RAV) of sediment, vegetation density (VD), canopy length (CL) and canopy width (CW) (representing canopy blockage effect) of vegetation canopy were adopted in the parameter study. It is found that above factors all have significant influences on bed morphology evolution. Numerical results show that the RAV of sediment parameterized in the slope failure model only dominates the transverse bed profile in the junction. Larger RAV leads to steeper transverse bed profile. The increase in VD, CL and CW is able to induce deeper pool region at the vegetated reach. Besides above, larger VD tends to induce upstream expansion in pool and bed erosion inside vegetation canopy. Larger CL induces larger pool region along vegetation canopy in the longitudinal dimension. With the increase in CW, the location of the deepest core in the pool tends to shift upstream.

7.4 Future works

Fundamental experimental work has been made for a better understanding of flow and sediment motion behaviors due to the flow-vegetation and flow-vegetation-sediment interaction in the POCVC. It is observed that the generation of multi-dimensional coherent vortices substantially determines the flow behaviors. The inspiring concept of vortex pattern from experimental investigations was adopted into the three-dimensional numerical simulation of flow in the POCVC and important flow characteristics were successfully reproduced. However, limitations still exist for applications of the obtained results to other channels since the present small-width channel holds a relatively small aspect ratio (=width/depth), where uncertainty might be brought from the side wall on behaviors of horizontal coherent vortices. The knowledge needs to be examined when applied to studies on large-width channels. The distribution pattern of horizontal coherent vortices is a dominant factor for the flow velocity deflection and negativity in vertical Reynolds stress in the near-bed region in the junction. But currently, it is difficult to find their direct relation with quantitative evidence. Therefore, one direction is to focus on detailed investigations on the geometric property of vortex structure.

Similarly, the channel geometry might influence the scour bed pattern through the boundary effect of the side wall. Bed morphology in the large-width channel might differ from the obtained results in this study since the flow velocity in the large-width channel tends to decline due to the boundary effect leading to less bed erosion. Therefore, extra experiments in large-width channels are required for developing a more general pattern of the alluvial process in the POCVC. Moreover, though the 2D morphological model was able to reproduce major bed morphologies, some characteristic secondary bedforms such as the sediment bar, in fact, are underestimated or overestimated. Those secondary bedforms are believed to be induced by the growth of secondary flows, which cannot be simulated by Nays2DH. Therefore, a full 3D morphological model is desirable to take the secondary flow effect into account for the computation of sediment transport and bed deformation.

Appendix A Flow Measurement and Data Post-process

A.1 Acoustic Doppler velocimeter (ADV) profiler: Vectrion-II

The Vectrino-II (ADV profiler) uses a technique often used in Doppler radar known as dual pulse repetition frequency (PRF) to extend the velocity range. With this technique, two alternating ping intervals are used to collect a single profile. This technique has the advantage of producing an extended velocity measurement for all cells in the profile (unlike the coarse/fine pulse-pairs technique). Signal noise effectively limits the minimum usable time difference.

The adaptive interval algorithm selects ping intervals based upon the acoustic environment. Acoustic coherent Doppler systems can suffer from data degradation due to reflections from previous pulse(s) interfering with the current pulse. This interference can cause significant velocity errors and detection and removal of these so-called "weak spot" regions within a Doppler system can be notoriously difficult given that the environmental geometry plays a significant role in how these weak spots manifest.

The Vectrino-II (ADV profiler) uses adaptive ping interval algorithms to help alleviate these issues. The instrument measures the channel impulse response between the transmit transducer and all four receive transducers by collecting long profiles from each receiver beam. These profiles are then scanned to determine the temporal position of the relevant energy in the backscatter. In environments which exhibit large amounts of acoustic interference, ping rates are chosen that are long enough to avoid all reflections by constraining the ping rates to values larger than the duration of the channel impulse response.

In environments that exhibit less acoustic interference a more sophisticated approach can be employed to avoid weak spots while at the same time allow fast ping rates for the measurement of faster and more turbulent flows. In this case, the instrument predicts the temporal position of all relevant interferers for a large number of ping intervals. A minimum ping rate is then selected that satisfies the conditions of range, ambiguity velocity and weak spots. In this case, every attempt is made to place the profiles between relevant reflections rather than after all of them.

More details about the design principle and characterization of Vectrino-II (ADV profiler) can be referred to user's guide series (SW User Guide and Vectrino Profiler User Guide), Craig et al. (2011), Zedel and Hay (2011) and Leng and Chanson (2016).

The signal-noise ratio (SNR) is an important parameter indicates the similarity of two-pulses. The higher SNR value implies more coherence of the transmitted and received signals and thus the more reliable measurements. For previous versions (i.e., Vectrino and Vectrino Plus), the SNR above 70% for the ADV measurement is commonly acceptable in open channel flow investigations (Voulgaris and Trowbridge, 1998).

As demonstrated by MacVicar et al. (2014), the great weakness of Vectrino-II profiler is that the SNR is not constant over the 35-milimeter profiling distance. Specifically, there exists a subregion (roughly 1 cm in height) with a relatively high constant signal-noise-ration (SNR) value, which is referred to as the 'sweet spot'. In this subregion of one single profiling region, the three-dimensional statistical flow velocity components and the related temporal and spatial correlations with good quality are in consistency with a high value of constant SNR. Therefore, in order to avoid the 'sweet spot' subregion, the first and last 5 points are not used for analysis.

The three instantaneous velocity components (u, v, w) are measured using a new generation of 3D NORTEX acoustic Doppler velocimeter (ADV) (Vectrino-II). Vectrino-II measures a velocity profile within a sampled water volume of 35mm with a resolution of 1mm. It works much more efficiently than the conventional ADV which can only measure velocity at a single point. The sampling profile spans from 40mm to 74mm beneath the probe. The sampling rate can be set to 100Hz. The calibration of Vectrino-II against other flow velocimetries (i.e. PIV and ADV Vectrino) has been reported (Craig et al., 2011; Nezu and Nakagawa, 1993; Zedel and Hay, 2011). In the present work, to ensure the capture of high-frequency turbulence, the sampling rate and number are respectively set to be 75 Hz and 5000 as recommended by Nezu and Nakagawa (1993) and Chanson et al. (2007). We also compared the time-averaged velocity and Reynolds stress obtained 5000 samples and 10000 samples, and very good agreement between the two sets of results have been observed, as shown in Figure A.1. The ensemble averaging of 5000 instantaneous velocity samples recorded by Vectrino-II are thus reliable to capture the time-averaging characteristics. The total sampling duration, therefore, is roughly 66.7s for each single point measurement.

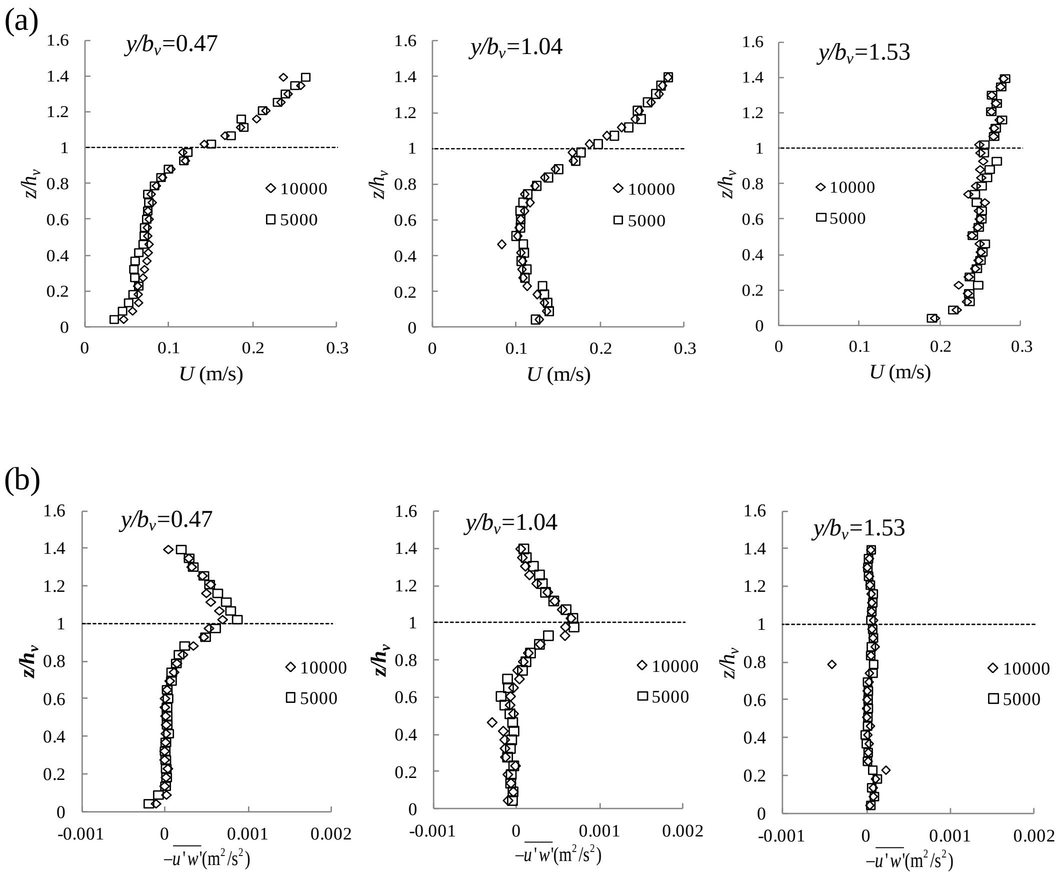

Figure A.1 Comparison of $\bar{u}$ and $-\overline{u'w'}$ with respect to 5000 and 10000 samples for Q50H25N1. The dashed line indicates the vegetation top.

A.2 Despiking ADV data

Another factor to determine the quality of instantaneous velocities is the degree of spikes produced by phase shift between the outgoing and incoming pulse. Figure A.2 shows measurements of the longitudinal instantaneous velocity process within a certain period of 10s-60s. The measurement of vertical line was conducted in the vegetation region near the lateral edge of submerged vegetation canopy. It is clear that periodical large-scale fluctuations of velocity can be observed at different water layer level, which indicates the formation of coherent vortices. Further, above the CTL, the velocity scale is much greater than that in the vegetation canopy. For all sampling records, spikes occur for measurements of different water depths, while the number and magnitude differ a lot. The spikes of samplings at near-bed region are more numerous and larger. These spikes in velocity data may not impact the mean statistics of flows but can dominate high-order correlations of velocity components such as turbulence intensities, Reynolds stresses and turbulent kinetic energy.

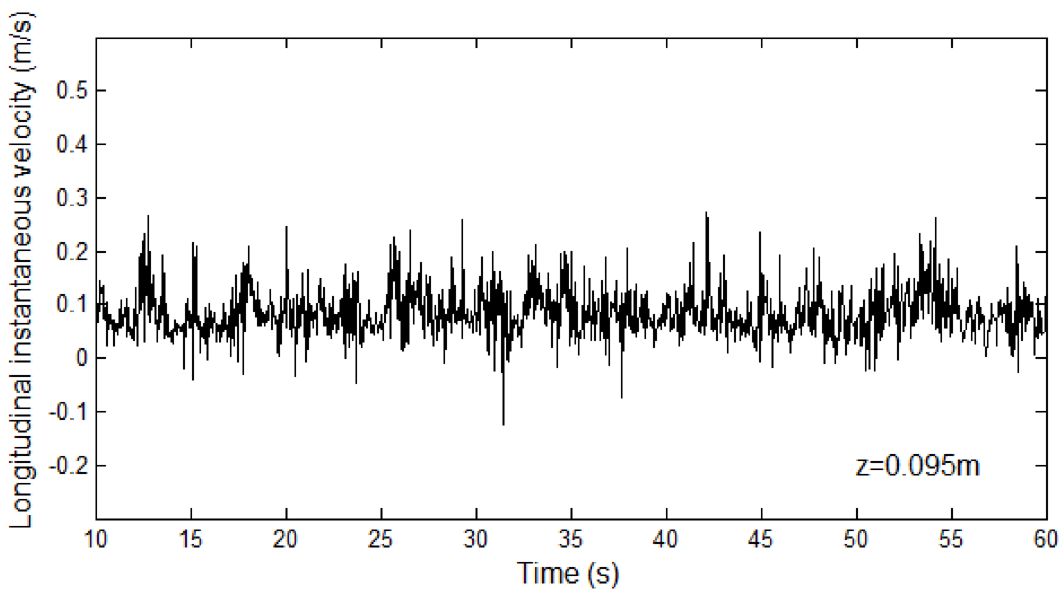

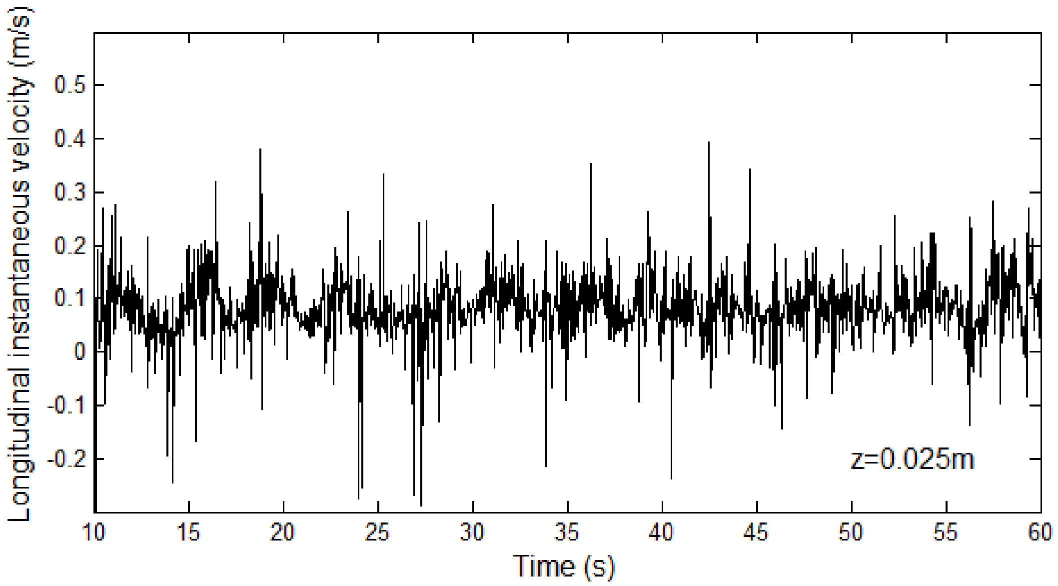

Figure A.2 Multipoint spike events (black line) and the refinements (red line) using the phase-space thresholding method for longitudinal flow velocity data at different water depths for partially vegetated flow. The location of the vertical line is at the neighboring open water region near the vegetation canopy.

In order to remove undesired spikes during measurements, the phase-space thresholding technique developed by Goring and Nikora (2002) is applied to refine spurious spikes in the data set. The technique procedures are simple and straightforward and can be easily coded in Matlab. The details are not demonstrated here, can be referred to the paper of Goring and Nikora (2002). Applying the phase-space thresholding technique, the refinement of velocity signals is shown in Figure A.3. The detection and replacement of the spikes from the phase-space thresholding technique are satisfactory. As shown, the property of the phase-space thresholding technique is that the relatively short-period and large-scale spikes and the non-spike data can be effectively detected. The latter then is maintained and the spikes are replaced by reasonable values such as mean velocity and the accurate neighboring non-spike data.

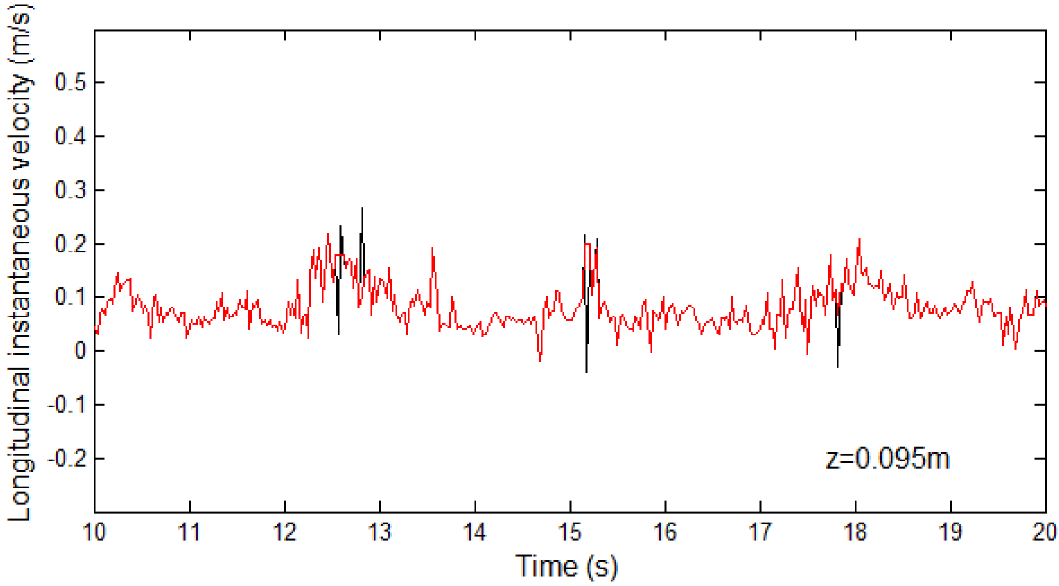

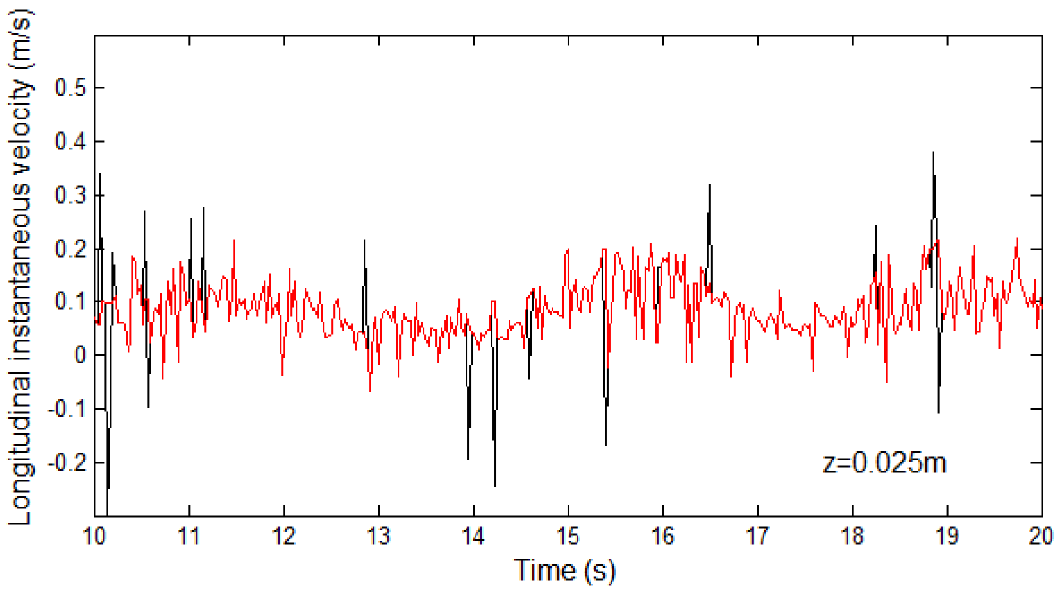

Figure A.3 Multipoint spike events (black line) and the refinements (red line) using the phase-space thresholding method for longitudinal flow velocity data at different water depths for partially vegetated flow. The location of the vertical line is at the neighboring open water region near the vegetation canopy.

A.3 Smoothing in spatial distribution of flow data

The phase-space thresholding technique can effectively refine the time-related instantaneous velocity data. However, the flow data scattering in spatial distribution also dramatically influence in-depth flow analysis like the mass, momentum and energy flux as well as the result presentation. The fake information of in-depth flow property is frequently induced by the incorrect gradient of flow data due to scattering in spatial distribution. In order to conduct a good result presentation and correct in-depth flow analysis, the forward-backward three-point smoothing technique is applied to refine the space-related flow data.

Figure A.4 shows the refinement of longitudinal velocity and vertical Reynolds stress by forward-backward three-point smoothing. It is noted that the scattering of data can be well refined. However, the trend of the vertical profile is not modified after smoothing. The result demonstrates that the forward-backward three-point smoothing can effectively refined the data scattering without losing the nature of the original data.

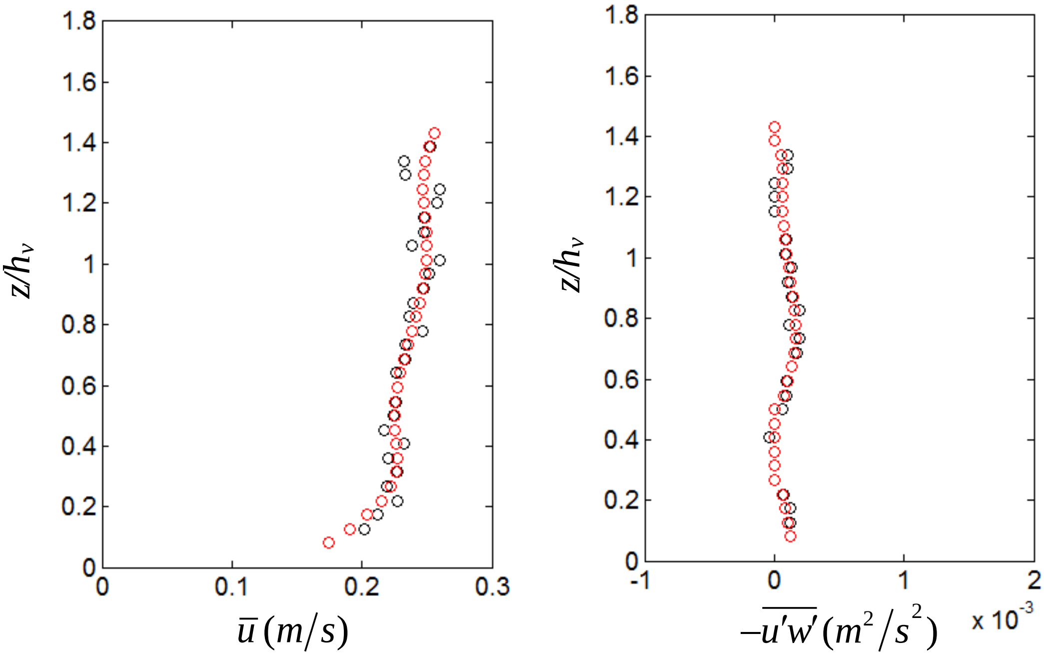

Figure A.4 Forward-backward three-point smoothing: original data (black circle) and refined data (red circle).

References

Baptist MJ. 2005. Modelling floodplain biogeomorphology.

Bennett SJ, Pirim T, Barkdoll BD. 2002. Using simulated emergent vegetation to alter stream flow direction within a straight experimental channel. *Geomorphology*, **44** (1): 115-126.

Bennett SJ, Wu W, Alonso CV, Wang SSY. 2008. Modeling fluvial response to in-stream woody vegetation: implications for stream corridor restoration. *Earth Surface Processes and Landforms*, **33** (6): 890-909.

Berenbrock C, Tranmer AW, 2008, Simulation of flow, sediment transport, and sediment mobility of the lower Coeur d'Alene River, Idaho: Geological Survey (US), 2328-0328.

Biron PM, Robson C, Lapointe MF, Gaskin SJ. 2004. Deflector designs for fish habitat restoration. *Environmental Management*, **33** (1): 25-35.

Brunet Y, Finnigan J, Raupach M. 1994. A wind tunnel study of air flow in waving wheat: single-point velocity statistics. *Boundary-Layer Meteorology*, **70** (1): 95-132.

Chanson H, Trevethan M, Koch C. 2007. Discussion of “turbulence measurements with acoustic doppler velocimeters” by Carlos M. García, Mariano I. Cantero, Yarko Niño, and Marcelo H. García. *Journal of Hydraulic Engineering*, **133** (11): 1286-1289.

Chen SC, Chan HC, Li YH. 2012a. Observations on flow and local scour around submerged flexible vegetation. *Advances in Water Resources*, **43**: 28-37.

Chen Z, Ortiz A, Zong L, Nepf H. 2012b. The wake structure behind a porous obstruction and its implications for deposition near a finite patch of emergent vegetation. *Water Resources Research*, **48** (9): n/a-n/a.

Cheng NS, Nguyen HT, Tan SK, Shao S. 2012. Scaling of Velocity Profiles for Depth-Limited Open Channel Flows over Simulated Rigid Vegetation. *Journal of Hydraulic Engineering*, **138** (8): 673-683.

Cheng NS. 2013. Calculation of Drag Coefficient for Arrays of Emergent Circular Cylinders with Pseudofluid Model. *Journal of Hydraulic Engineering*, **139** (6): 602-611.

Choi SU, Kang H. 2004. Reynolds stress modeling of vegetated open-channel flows. *Journal of Hydraulic Research*, **42** (1): 3-11.

Choi SU, Kang H . 2006. Numerical investigations of mean flow and turbulence structures of partly-vegetated open-channel flows using the Reynolds stress model. *Journal of Hydraulic Research*, **44** (2): 203-217.

Chu V, Wu JH, Khayat R. 1991. Stability of transverse shear flows in shallow open channels. *Journal of Hydraulic Engineering*, **117** (10): 1370-1388.

Craig RG, Loadman C, Clement B, Rusello PJ, Siegel E, Characterization and testing of a new bistatic profiling acoustic doppler velocimeter: The vectrino-ii, *in* Proceedings Current, Waves and Turbulence Measurements (CWTM), 2011 IEEE/OES 10th2011, IEEE, p. 246-252.

Crosato A, Saleh MS. 2011. Numerical study on the effects of floodplain vegetation on river planform style. *Earth Surface Processes and Landforms*, **36** (6): 711-720.

de Lima AC, Izumi N. 2013. Linear stability analysis of open-channel shear flow generated by vegetation. *Journal of Hydraulic Engineering*, **140** (3): 231-240.

Dunn WC, Milne BT, Mantilla R, Gupta VK. 2011. Scaling relations between riparian vegetation and stream order in the Whitewater River network, Kansas, USA. *Landscape Ecology*, **26** (7): 983-997.

Einstein HA, 1950, The bed-load function for sediment transportation in open channel flows, US Department of Agriculture Washington DC.

Euler T, Zemke J, Rodrigues S, Herget J. 2014. Influence of inclination and permeability of solitary woody riparian plants on local hydraulic and sedimentary processes. *Hydrological Processes*, **28** (3): 1358-1371.

Fetherston KL, Naiman RJ, Bilby RE. 1995. Large woody debris, physical process, and riparian forest development in montane river networks of the Pacific Northwest. *Geomorphology*, **13** (1-4): 133-144.

Finnigan J. 2000. Turbulence in plant canopies. *Annual Review of Fluid Mechanics*, **32** (1): 519-571.

Follett EM, Nepf HM. 2012. Sediment patterns near a model patch of reedy emergent vegetation. *Geomorphology*, **179**: 141-151.

Güneralp İ, Abad JD, Zolezzi G, Hooke J. 2012. Advances and challenges in meandering channels research. *Geomorphology*, **163**: 1-9.

Gao W, Shaw R, Paw U K. 1989. Observation of organized structure in turbulent flow within and above a forest canopy. *Boundary-Layer Meteorology*, **47** (1): 349-377.

Ghidaoui MS, Kolyshkin AA. 1999. Linear stability analysis of lateral motions in compound open channels. *Journal of Hydraulic Engineering*, **125** (8): 871-880.

Ghisalberti M. 2002. Mixing layers and coherent structures in vegetated aquatic flows. *Journal of Geophysical Research*, **107** (C2).

Ghisalberti M . 2009. Obstructed shear flows: similarities across systems and scales. *Journal of Fluid Mechanics*, **641**: 51.

Ghisalberti M, Nepf H. 2006. The Structure of the Shear Layer in Flows over Rigid and Flexible Canopies. *Environmental Fluid Mechanics*, **6** (3): 277-301.

Ghisalberti M, Nepf H. 2004. The limited growth of vegetated shear layers. *Water Resources Research*, **40** (7).

Gomez B, Church M. 1989. An assessment of bed load sediment transport formulae for gravel bed rivers. *Water Resources Research*, **25** (6): 1161-1186.

Goring DG, Nikora VI. 2002. Despiking acoustic Doppler velocimeter data. *Journal of Hydraulic Engineering*, **128** (1): 117-126.

Harvey JW, Conklin MH, Koelsch RS. 2003. Predicting changes in hydrologic retention in an evolving semi-arid alluvial stream. *Advances in Water Resources*, **26** (9): 939-950.

Hauer C, Unfer G, Tritthart M, Formann E, Habersack H. 2011. Variability of mesohabitat characteristics in riffle‐pool reaches: Testing an integrative evaluation concept (FGC) for MEM‐application. *River Research and Applications*, **27** (4): 403-430.

Hu Y, Huai W, Han J. 2013. Analytical solution for vertical profile of streamwise velocity in open-channel flow with submerged vegetation. *Environmental Fluid Mechanics*, **13** (4): 389-402.

Huai W, Xu Z, Yang Z, Zeng Y. 2008. Two dimensional analytical solution for a partially vegetated compound channel flow. *Applied Mathematics and Mechanics*, **29**: 1077-1084.

Huai W, Xue W, Qian Z. 2015. Large-eddy simulation of turbulent rectangular open-channel flow with an emergent rigid vegetation patch. *Advances in Water Resources*, **80**: 30-42.

Huai WX, Zeng YH, Xu ZG, Yang ZH. 2009. Three-layer model for vertical velocity distribution in open channel flow with submerged rigid vegetation. *Advances in Water Resources*, **32** (4): 487-492.

Hupp CR, Osterkamp W. 1996. Riparian vegetation and fluvial geomorphic processes. *Geomorphology*, **14** (4): 277-295.

James C, Jordanova A, Nicolson C. 2002. Flume experiments and modelling of flow-sediment-vegetation interactions. *International Association of*

Hydrological Sciences, Publication, **276**: 3-9.

Jamieson E, Rennie C, Townsend R. 2013. 3D flow and sediment dynamics in a laboratory channel bend with and without stream barbs. *Journal of Hydraulic Engineering*, **139** (2): 154-166.

Jordanova AA, James C. 2003. Experimental study of bed load transport through emergent vegetation. *Journal of Hydraulic Engineering*, **129** (6): 474-478.

Julien PY, 2002, River mechanics, Cambridge University Press.

Khosronejad A, Kang S, Sotiropoulos F. 2012. Experimental and computational investigation of local scour around bridge piers. *Advances in Water Resources*, **37**: 73-85.

Kim HS, Kimura I, Shimizu Y. 2015. Bed morphological changes around a finite patch of vegetation. *Earth Surface Processes and Landforms*, **40** (3): 375-388.

López F, García MH. 2001. Mean flow and turbulence structure of open-channel flow through non-emergent vegetation. *Journal of Hydraulic Engineering*, **127** (5): 392-402.

Le Bouteiller C, Venditti JG. 2015. Sediment transport and shear stress partitioning in a vegetated flow. *Water Resources Research*: 2901-2922.

Leng X, Chanson H, Steady and unsteady turbulent velocity profiling in open channel flows using the ADV Vectrino II profiler, *in* Proceedings 6th International Symposium on Hydraulic Structures: Hydraulic Structures and Water System Management, ISHS 20162016, Utah State University, p. 305-314.

Leonard BP. 1979. A stable and accurate convective modelling procedure based on quadratic upstream interpolation. *Computer Methods in Applied Mechanics and Engineering*, **19** (1): 59-98.

Li CW. 1990. advection simulation by mlnimax-Characteristics Method. *Journal of Hydraulic Engineering*, **116** (9): 1138-1144.

Li CW, Zeng C. 2009. 3D Numerical modelling of flow divisions at open channel junctions with or without vegetation. *Advances in Water Resources*, **32** (1): 49-60.

Li CW, Zhang ML. 2010. Numerical modeling of shallow water flow around arrays of emerged cylinders. *Journal of Hydro-Environment Research*, **4** (2): 115-121.

Lin P, Li CW. 2002. A σ - coordinate three - dimensional numerical model for surface wave propagation. *International Journal for Numerical Methods in Fluids*, **38** (11): 1045-1068.

Liu C, Luo X, Liu X, Yang K. 2013. Modeling depth-averaged velocity and bed shear stress in compound channels with emergent and submerged vegetation. *Advances in Water Resources*, **60**: 148-159.

Liu D, Diplas P, Fairbanks JD, Hodges CC. 2008. An experimental study of flow through rigid vegetation. *Journal of Geophysical Research*, **113** (F4).

Liu Z, Chen Y, Zhu D, Hui E, Jiang C. 2012. Analytical model for vertical velocity profiles in flows with submerged shrub-like vegetation. *Environmental Fluid Mechanics*, **12** (4): 341-346.

Luhar M, Rominger J, Nepf H. 2008. Interaction between flow, transport and vegetation spatial structure. *Environmental Fluid Mechanics*, **8** (5-6): 423-439.

MacVicar B, Dilling S, Lacey R, Hipel K, A quality analysis of the Vectrino II instrument using a new open-source MATLAB toolbox and 2D ARMA models to detect and replace spikes, *in* Proceedings River Flow2014, p. 1951-1959.

Meftah MB, De Serio F, Mossa M. 2014. Hydrodynamic behavior in the outer shear layer of partly obstructed open channels. *Physics of Fluids (1994-present)*, **26** (6): 065102.

Messina MG, Schoenholtz SH, Lowe MW, Wang Z, Gunter DK, Londo AJ. 1997. Initial responses of woody vegetation, water quality, and soils to harvesting intensity in a Texas bottomland hardwood ecosystem. *Forest Ecology and Management*, **90** (2-3): 201-215.

Millar RG. 2000. Influence of bank vegetation on alluvial channel patterns. *Water Resources Research*, **36** (4): 1109-1118.

Moltchanov S, Bohbot-Raviv Y, Duman T, Shavit U. 2015. Canopy edge flow: A momentum balance analysis. *Water Resources Research*, **51**(4): 2081-2095.

Neary VS, Constantinescu SG, Bennett SJ, Diplas P. 2012. Effects of Vegetation on Turbulence, Sediment Transport, and Stream Morphology. *Journal of Hydraulic Engineering*, **138** (9): 765-776.

Nepf H, Ghisalberti M, White B, Murphy E. 2007. Retention time and dispersion associated with submerged aquatic canopies. *Water Resources Research*, **43** (4).

Nepf H, Vivoni E. 2000. Flow structure in depth‐limited, vegetated flow. *Journal of Geophysical Research: Oceans (1978–2012)*, **105** (C12): 28547-28557.

Nezu I, Nakagawa H. 1993. Turbulence in open channel flows, IAHR. Balkema, Rotterdam.

Nezu I, Onitsuka K. 2001. Turbulent structures in partly vegetated open-channel flows with LDA and PI V measurements. *Journal of Hydraulic Research*, **39** (6): 629-642.

Nezu I, Sanjou M. 2008. Turburence structure and coherent motion in vegetated canopy open-channel flows. *Journal of Hydro-Environment Research*, **2** (2): 62-90.

Okamoto TA, Nezu I. 2009. Turbulence structure and “Monami” phenomena in flexible vegetated open-channel flows. *Journal of Hydraulic Research*, **47** (6): 798-810.

Osborne LL, Kovacic DA. 1993. Riparian vegetated buffer strips in water‐quality restoration and stream management. *Freshwater Biology*, **29** (2): 243-258.

Palmer MA, Bernhardt E, Allan J, Lake P, Alexander G, Brooks S, Carr J, Clayton S, Dahm C, Follstad Shah J. 2005. Standards for ecologically successful river restoration. *Journal of Applied Ecology*, **42** (2): 208-217.

Phillips BC, Sutherland AJ. 1989. Spatial lag effects in bed load sediment transport. *Journal of Hydraulic Research*, **27** (1): 115-133.

Phillips NA. 1957. A coordinate system having some special advantages for numerical forecasting. *J. Meteor.*, **14**: 184-185.

Poggi D, Porporato A, Ridolfi L, Albertson J, Katul G. 2004. The effect of vegetation density on canopy sub-layer turbulence. *Boundary-Layer Meteorology*, **111** (3): 565-587.

Pollen‐Bankhead N, Simon A. 2009. Enhanced application of root‐reinforcement algorithms for bank‐stability modeling. *Earth Surface Processes and Landforms*, **34** (4): 471-480.

Pollen N, Simon A. 2005. Estimating the mechanical effects of riparian vegetation on stream bank stability using a fiber bundle model. *Water Resources Research*, **41** (7).

Pope SB, 2000, Turbulent flows, Cambridge university press.

Raupach M, Coppin P, Legg B. 1986. Experiments on scalar dispersion within a model plant canopy part I: The turbulence structure. *Boundary-Layer Meteorology*, **35** (1): 21-52.

Raupach MR, Finnigan J, Brunei Y. 1996. Coherent eddies and turbulence in vegetation canopies: the mixing-layer analogy. *Boundary-Layer Meteorology*, **78** (3-4): 351-382.

Reynolds O. 1894. On the dynamical theory of incompressible viscous fluids and the determination of the criterion. *Proceedings of the Royal Society of London*, **56** (336-339): 40-45.

Rominger JT, Nepf HM. 2011. Flow adjustment and interior flow associated with a rectangular porous obstruction. *Journal of Fluid Mechanics*, **680**: 636-659.

Shields A. 1936. Application of similarity principles and turbulence research to bed-load movement. *CalTech library*.

Shimizu Y, Tsujimoto T. 1993. Comparison ofFlood Flow Structure Between Compound Channel andChannel with Vegetation Zone. *Proceedings of 25thIAHR Congress, Delft, The Netherlands*.

Simpson RL, Good RE, Walker R, Frasco BR. 1983. The role of Delaware River freshwater tidal wetlands in the retention of nutrients and heavy metals. *Journal of Environmental Quality*, **12** (1): 41-48.

Siniscalchi F, Nikora VI, Aberle J. 2012. Plant patch hydrodynamics in streams: Mean flow, turbulence, and drag forces. *Water Resources Research*, **48** (1).

Spalart PR, Allmaras SR. 1992. A one-equation turbulence model for aerodynamic flows.

Stoesser T, Kim S, Diplas P. 2010. Turbulent flow through idealized emergent vegetation. *Journal of Hydraulic Engineering*, **136** (12): 1003-1017.

Stoesser T, Neary V, Wilson C, Modeling vegetated channel flows: Challenges and opportunities, *in* Proceedings WSEAS (The World Scientific and Engineering Academy and Society) Conference on Fluid Mechanics, Corfu, Greece2005.

Sukhodolov AN, Sukhodolova TA. 2012. Vegetated mixing layer around a finite-size patch of submerged plants: Part 2. Turbulence statistics and structures. *Water Resources Research*, **48** (12).

Sukhodolova TA, Sukhodolov AN. 2012. Vegetated mixing layer around a finite-size patch of submerged plants: 1. Theory and field experiments. *Water Resources Research*, **48** (10).

Sweeney BW, Bott TL, Jackson JK, Kaplan LA, Newbold JD, Standley LJ, Hession WC, Horwitz RJ. 2004. Riparian deforestation, stream narrowing, and loss of stream ecosystem services. *Proceedings of the National Academy of Sciences of the United States of America*, **101** (39): 14132-14137.

Tang H, Wang H, Liang DF, Lv SQ, Yan L. 2013. Incipient motion of sediment in the presence of emergent rigid vegetation. *Journal of Hydro-Environment Research*, **7** (3): 202-208.

Tang X, Knight D, Sterling M. 2011. Analytical model for streamwise velocity in vegetated channels. *Proceedings of the ICE-Engineering and Computational Mechanics*, **164** (2): 91-102.

Tanino Y, Nepf HM. 2008. Laboratory investigation of mean drag in a random array of rigid, emergent cylinders. *Journal of Hydraulic Engineering*, **134** (1): 34-41.

Thomas T, Williams J. 1995. Large eddy simulation of turbulent flow in an asymmetric compound open channel. *Journal of Hydraulic Research*, **33** (1): 27-41.

Tooth S, Nanson GC. 2000. The role of vegetation in the formation of anabranching channels in an ephemeral river, Northern plains, arid central Australia. *Hydrological Processes*, **14** (16 - 17): 3099-3117.

Tsujimoto T. 1999. Fluvial processes in streams with vegetation. *Journal of Hydraulic*

Research, **37** (6): 789-803.

Tsujimoto T, Kitamura T. 1992. Appearance of organized fluctuations in open channel flow with vegetated zone. *KHL Progressive Rep., Hydr. Lab., Kanazawa Univ., Kanazawa, Japan, Dec., 37-45.*

Van der Vorst HA. 1992. Bi-CGSTAB: A fast and smoothly converging variant of Bi-CG for the solution of nonsymmetric linear systems. *SIAM Journal on scientific and Statistical Computing*, **13** (2): 631-644.

Van Rijn LC. 1987. Mathematical modelling of morphological processes in the case of suspended sediment transport.

Vorst HA, Sonneveld P, 1990, CGSTAB: A more smoothly converging variant of CG-S, Delft University of Technology.

Voulgaris G, Trowbridge JH. 1998. Evaluation of the acoustic Doppler velocimeter (ADV) for turbulence measurements. *Journal of Atmospheric and Oceanic Technology*, **15** (1): 272-289.

Ward JV, Tockner K, Uehlinger U, Malard F. 2001. Understanding natural patterns and processes in river corridors as the basis for effective river restoration. *River Research and Applications*, **17** (4 - 5): 311-323.

White BL, Nepf HM. 2007. Shear instability and coherent structures in shallow flow adjacent to a porous layer. *Journal of Fluid Mechanics*, **593**.

White BL, Nepf HM . 2008. A vortex-based model of velocity and shear stress in a partially vegetated shallow channel. *Water Resources Research*, **44** (1).

Windham L, Weis J, Weis P. 2003. Uptake and distribution of metals in two dominant salt marsh macrophytes, Spartina alterniflora (cordgrass) and Phragmites australis (common reed). *Estuarine, Coastal and Shelf Science*, **56** (1): 63-72.

Wohl E, Angermeier PL, Bledsoe B, Kondolf GM, MacDonnell L, Merritt DM, Palmer MA, Poff NL, Tarboton D. 2005. River restoration. *Water Resources Research*, **41** (10).

Wu W, He Z. 2009. Effects of vegetation on flow conveyance and sediment transport capacity. *International Journal of Sediment Research*, **24** (3): 247-259.

Wu W, Rodi W, Wenka T. 2000. 3D numerical modeling of flow and sediment transport in open channels. *Journal of Hydraulic Engineering*, **126** (1): 4-15.

Wu W, Shields FD, Bennett SJ, Wang SSY. 2005. A depth-averaged two-dimensional model for flow, sediment transport, and bed topography in curved channels with riparian vegetation. *Water Resources Research*, **41** (3).

Wu W, Wang SS. 2004. A Depth‐Averaged Two‐Dimensional Numerical Model of Flow and Sediment Transport in Open Channels with Vegetation. *Riparian Vegetation and Fluvial Geomorphology*: 253-265.

Xiaohui S, Li C. 2002. Large eddy simulation of free surface turbulent flow in partly vegetated open channels. *International Journal for Numerical Methods in Fluids*, **39** (10): 919-937.

Xie Z-T, Coceal O, Castro IP. 2008. Large-Eddy Simulation of Flows over Random Urban-like Obstacles. *Boundary-Layer Meteorology*, **129** (1): 1-23.

Yager E, Schmeeckle M. 2013. The influence of vegetation on turbulence and bed load transport. *Journal of Geophysical Research: Earth Surface*, **118** (3): 1585-1601.

Yan X-F, Wai W-HO, Li C-W. 2016. Characteristics of flow structure of free-surface flow in a partly obstructed open channel with vegetation patch. *Environmental Fluid Mechanics*, **16** (4): 807-832.

Yang JQ, Kerger F, Nepf HM. 2015. Estimation of the bed shear stress in vegetated and bare channels with smooth beds. *Water Resources Research*, **51** (5): 3647-3663.

Yang S-Q, Han Y, Lin P, Jiang C, Walker R. 2014. Experimental study on the validity of flow region division. *Journal of Hydro-Environment Research*, **8** (4): 421-427.

Zedel L, Hay A, Turbulence measurements in a jet: Comparing the Vectrino and VectrinoII, *in* Proceedings Current, Waves and Turbulence Measurements (CWTM), 2011 IEEE/OES 10th2011, IEEE, p. 173-178.

Zeng C, Li CW. 2012. Modeling flows over gravel beds by a drag force method and a modified S–A turbulence closure. *Advances in Water Resources*, **46**: 84-95.

Zeng C, Li CW. 2013. Measurements and modeling of open-channel flows with finite semi-rigid vegetation patches. *Environmental Fluid Mechanics*, **14** (1): 113-134.

Zong L, Nepf H. 2010. Flow and deposition in and around a finite patch of vegetation. *Geomorphology*, **116** (3-4): 363-372.

Zong L, Nepf H . 2012. Vortex development behind a finite porous obstruction in a channel. *Journal of Fluid Mechanics,* **691**: 368-391.

List of Publication

Yan XF, Wai WHO, Li CW. 2016. Characteristics of flow structure of free-surface flow in a partly obstructed open channel with vegetation patch. *Environmental Fluid Mechanics*, **16** (4): 807-832.

Gomes PI, Wai WHO, Yan XF. 2017. Eco‐hydraulic evaluation of herbaceous ecosystems below headwater dams without a base flow: Observing below dam reaches as new stream sources. *Ecohydrology*, **10** (1).